UNIVERSITAT DE BARCELONA

Two-dimensional modeling and inversion of the controlled-source electromagnetic and magnetotelluric methods using finite elements and full-space PDE-constrained optimization strategies

Savitri Galiana Blanch

Two-dimensional modeling and inversion of the controlled-source electromagnetic and magnetotelluric methods using finite elements and full-space PDE-constrained optimization strategies

A thesis submitted to

Universitat de Barcelona

in partial fulfillment for the award of the degree of

Doctor of Philosophy

in

Earth Sciences

presented by

Savitri Galiana Blanch

supervised by

Dr. Xavier Garcia
Institut de Cienciès del Mar, CSIC, Barcelona, Spain

tutored by

Prof. Dr. Pilar Queralt
Departament de Geodinàmica i Geofísica, Universitat de Barcelona, Spain

examined by

Prof. Dr. Àlex Marcuello
Departament de Geodinàmica i Geofísica, Universitat de Barcelona, Spain
Prof. Dr. Mark E. Everett
Department of Geology and Geophysics, Texas A&M University, Texas
Prof. Dr. Klaus Spitzer
Institut für Geophysik und Geoinformatik, TU Bergakademie Freiberg, Germany

with substitute examination members

Dr. Valentí Sallarés
Institut de Cienciès del Mar, CSIC, Barcelona, Spain
Prof. Dr. Jaume Pous
Departament de Geodinàmica i Geofísica, Universitat de Barcelona, Spain

July 2016

Signature page

Savitri Galiana Blanch
Barcelona, 20*th* July 2016

Abstract

The controlled-source electromagnetics (CSEM) and magnetotellurics (MT) methods are common geophysical tools for imaging the electrical properties of the Earth's subsurface and are employed independently, jointly, and in combination with other geophysical techniques. In order to appreciate measured data, both methods require forward and inverse modeling of the electrically conductive subsurface with the ultimate goal of finding a feasible model for which the simulated data reasonably fits the observations. Naturally, the potential goodness of this fit not only depends on the error in the measured data and on the numerical error but also on the degree of physical approximation inferred by numerical modeling. Therefore, active research focuses on new methods for modeling and inversion to obtain accurate and reliable models of the Earth's structure in increasingly complex scenarios.

A first step is to enhance modeling approximations by taking into account physical factors such as anisotropy, topography or realistic sources. Second, in order to accommodate these factors in a modeling and inversion program and to deal with typically large data sets, numerical methods need to be assessed in terms of solution accuracy, time efficiency and memory demand. The finite elements (FE) modeling methods are known to offer most flexibility in model geometry and contain quality control mechanisms for the solution, like shape function order and adaptive mesh refinement. Most emerging modeling programs are based on FE, appreciating significant advantages, but nearly all inverse modeling programs to date are still based on finite differences (FD) or integral equation (IE) methods.

Furthermore, inverse modeling developed for electromagnetic (EM) data is generally based on gradient methods and is formulated in a reduced space, where the only optimization variables are the model parameters, that is the electric conductivity of the subsurface. Originally, the inverse problem is stated for the EM fields and the conductivity parameter, and constrained by partial differential equations (PDEs) governing the EM field variables. The reduced-space strategy eliminates the field variables by applying equality constraints and solving then, the unconstrained problem in the reduced-space of model parameters. A common drawback of such methods is the repeated costly computation of the solution of the forward problem and of the Jacobian matrix of sensitivities (for Newton's based methods). In contrast, it is also possible to solve the inverse problem in the full-space of model parameters, including both the EM field variables and the electric conductivity parameter. Solving the PDE-constrained optimization problem directly (full-space) has the advantage that it is only necessary to solve exactly the PDEs at the very end of the optimization pro-

cess but it comes at the cost of many more optimization variables and of the presence of equality constraints. Also, in particular, within a FE framework, the PDE-constrained optimization problem provides the additional benefit to include sophisticated FE techniques in the inversion process, such as adaptive mesh refinement.

This thesis develops a robust and versatile adaptive unstructured mesh FE program to numerically model the total field for two-dimensional (2-D) anisotropic CSEM and MT data, allowing for arbitrarily oriented, three-dimensional (3-D) sources. To represent 3-D CSEM sources for a 2-D physical model, a two-and-a-half-dimensional (2.5-D) approximation is employed. The FE formulations are derived for both methods, for isotropic and anisotropic subsurface conductivity structures. Although the anisotropic case is not general, it includes vertical and dipping anisotropy. The accuracy of the solution is controlled and improved by an adaptive mesh refinement algorithm using *a-posteriori* error estimator methods.

Exhaustive numerical experiments validate the adaptive FE program for both CSEM and MT methods and on land and marine environments. The influence of the model dimensions, mesh design and order of shape functions on the solution accuracy is studied and notably, an outperformance of quadratic shape functions is found compared to linear or cubic realizations. Several examples demonstrate the effect of complex scenarios on EM data, in particular, a model with bathymetry, a land and marine model with oriented and finite-length sources, a vertical anisotropic media with an embedded reservoir and another one with a reservoir within an anticline structure. These examples showcase the importance of adequate consideration (in terms of forward modeling) of physical features such as the topography, the geometry and orientation of the source and the anisotropy of the media, which are very common in real world data.

Further, a formulation for the 2.5-D CSEM inverse problem as a PDE-constrained optimization in full-space is derived within a FE framework following two different strategies: *discretize-optimize* and *optimize-discretize*. The discretize-optimize strategy considers the inverse problem to be present in discretized form and the Lagrangian optimization conditions and the Newton's step are derived based on the discretized inverse problem. Contrarily, the optimize-discretize approach, first derives the optimization conditions and the Newton's step or an approach of it, and after discretizes the resulting equations. The performance of the implementation of the discretize-optimize formulation is demonstrated through two examples, a canonical reservoir model and a more realistic marine model with topography, using a general-purpose optimization program, which is an implementation of a sequential quadratic programming (SQP) algorithm. Although, without explicit regularization, different meshes for the model parameters and for the field variables allow recovery of the main structures of the model within an acceptable data misfit. However, the time and memory efficiency of the program should be improved.

Finally, the 2.5-D CSEM inverse problem is formulated as a PDE-constrained optimization in full-space and within a FE framework using an optimize-discretize strategy as a first step of the development of an inversion scheme using adaptive FE meshes.

Resum

El mètode de font electromagnètica controlada (CSEM) i el mètode magnetotel.lúric (MT) són tècniques geofísiques usades habitualment per obtenir una imatge de les propietats elèctriques del subsòl terrestre i s'utilitzen independentment, conjuntament i en combinació amb altres tècniques geofísiques. Per poder interpretar les dades, ambdós mètodes necessiten la modelització directa i inversa de la conductivitat elèctrica del subsòl amb l'objectiu final d'obtenir un model coherent per al qual les dades simulades s'ajustin de forma raonable a les observacions. Naturalment, la qualitat d'aquest ajust no només depèn de l'error en les dades mesurades i de l'error numèric, sinó també del grau en l'aproximació física inferit per la modelització numèrica. D'aquesta manera, les recerques actuals se centren a investigar noves metodologies per a la modelització i inversió, per tal d'obtenir models acurats i fiables de les estructures de la Terra en escenaris cada cop més complexos.

Un primer pas és millorar les aproximacions en la modelització tenint en compte factors físics com ara l'anisotropia, la topografia o fonts més realistes. En segon lloc, per tal d'acomodar aquests factors en un programa de modelització i inversió i per poder tractar els conjunts de dades típicament llargs, els mètodes numèrics han de ser avaluats en termes de la precisió de la solució, l'eficiència en temps i la demanda en memòria. Els mètodes de modelització en elements finits (FE) són coneguts per oferir una major flexibilitat en la modelització de la geometria i contenen mecanismes de control de la solució, com ara l'ordre de les funcions forma i la tècnica de refinament adaptatiu de la malla. La majoria de programes de modelització emergents estan basats en els FE, i mostren avantatges significatius, però gairebé tots els programes de modelització inversa, encara avui dia, estan basats en el mètode de les diferències finites (FD) o en el mètode de l'equació integral (IE).

A més a més, la modelització inversa desenvolupada per a dades electromagnètiques (EM) es basa generalment en mètodes del gradient i es formula en un espai reduït, on les úniques variables d'optimització són els paràmetres del model, és a dir, la conductivitat elèctrica del subsòl. Originalment, el problema invers es formula per als camps EM i per al paràmetre conductivitat, i està constret per les equacions diferencials en derivades parcials (PDEs) que governen les variables camps EM. L'estratègia d'espai reduït elimina les variables camps aplicant lligams d'igualtat i soluciona, doncs, el problema no constret en l'espai reduït dels paràmetres del model. Un desavantatge general d'aquests mètodes és la costosa repetició del càlcul de la solució del problema directe i de la matriu jacobiana de sensibilitats (per mètodes basats en Newton). D'altra banda, també és possible de solucionar el problema invers en l'espai complet de les variables camps EM i del

paràmetre conductivitat. Solucionar-hi el problema d'optimització constret per les PDEs té l'avantatge que només és necessari de solucionar exactament el problema directe al final del procés d'optimització, però això comporta el cost addicional de tenir moltes més variables d'optimització i de la presència de lligams d'igualtat. També, en particular, en el marc dels FE, el problema d'optimització constret per les PDEs té l'avantatge afegit d'incloure tècniques sofisticades pròpies dels FE en el procés d'inversió, com ara el refinament adaptatiu de la malla.

Aquesta tesi desenvolupa un programa robust i versàtil amb FE i malles irregulars adaptatives per modelar numèricament el camp total de dades CSEM i MT bidimensionals (2D) i anisòtropes, que permet l'ús de fonts tridimensionals (3D) orientades arbitràriament. Per tal de representar fonts CSEM 3D en un model físic 2D, s'utilitza una aproximació dos i mig dimensional (2.5D). Les formulacions FE es deriven per a ambdós mètodes, per a estructures de conductivitat del subsòl isòtropes i anisòtropes. Encara que el cas anisòtrop no és general, inclou anisotropia vertical i de cabussament. La precisió en la solució es controla i millora amb un algoritme de refinament adaptatiu de la malla utilitzant mètodes d'estimació de l'error *a posteriori*.

Una sèrie exhaustiva d'experiments numèrics valida el programa de FE adaptatius per ambdós mètodes, CSEM i MT, i en escenaris terrestres i marins. S'estudia la influència de les dimensions del model, del disseny de la malla i de l'ordre de les funcions forma en l'exactitud de la solució i es troba un comportament notablement superior de les funcions forma quadràtiques comparades amb les lineals o cúbiques. Diferents exemples mostren l'efecte d'escenaris complexos sobre les dades EM, en particular, un model amb batimetria, un model terrestre i un de marí amb fonts orientades i de dimensió finita, un medi amb anisotropia vertical amb un reservori encastat i un altre amb un reservori encastat en una estructura anticlinal. Aquests exemples demostren la importància de considerar adequadament (en termes de modelització directa) característiques físiques com la topografia, l'orientació i geometria de la font i l'anisotropia del medi, que sovint es troben en mesures reals.

Juntament amb això, es deriva una formulació per al problema invers 2.5D CSEM com una optimització constreta per les PDEs en l'espai complet i en un marc de FE, seguint dues estratègies diferents: *discretització-optimització* i *optimització-discretització*. L'estratègia de discretització-optimització considera que el problema invers es troba en forma discretitzada i deriva les condicions d'optimitat de la Lagrangiana i el pas de Newton. Contràriament, l'aproximació optimització-discretització deriva primer les condicions d'optimitat i el pas de Newton o una aproximació d'aquest, i després discretitza les equacions resultants. La implementació de la formulació discretització-optimització es mostra en dos exemples, un model canònic de reservori i un model marí més realista amb topografia, utilitzant un programa d'optimització de propòsit general, que és una implementació d'un algoritme de programació quadràtica seqüencial (SQP). Encara que no s'utilitza una regularització explícita, l'ús de diferents malles per al paràmetre del model i per a les variables camps, permet recuperar les principals estructures del model i obtenir

un ajust de les dades acceptable. Cal dir, però, que l'eficiència en temps i memòria del programa hauria de millorar-se.

Finalment, el problema invers 2.5D CSEM es formula com un problema d'optimització constret per les PDEs en l'espai complet i en un marc de FE utilitzant una estratègia d'optimització-discretització i com un primer pas per al desenvolupament d'un esquema d'inversió que utilitzi malles adaptatives de FE.

Contents

List of Figures

List of Tables

List of Acronyms

MT magnetotelluric . . . 1

EM Electromagnetic . . . 1

RHS right-hand-side . . . 27

LHS left-hand-side . . . 19

CSEM controlled-source electromagnetic . . . 1

IE integral equation . . . 3

FD finite differences . . . 3

FE finite elements . . . 3

1-D one-dimensional . . . 2

2-D two-dimensional . . . 2

3-D three-dimensional . . . 2

2.5-D 2.5-dimensional . . . 5

PDE partial differential equation . . . 4

TE transverse electric . . . 20

TM transverse magnetic . . . 20

SI International System of Units . . . 6

BVP boundary value problem . . . 11

DOFs degrees of freedom . . . 29

HED horizontal electric dipole . . . 21

HEPD horizontal electric point dipole . . . 139

HMD horizontal magnetic dipole . . . 22

VED vertical electric dipole . . . 22

VMD vertical magnetic dipole . . . 23

DWR dual-weighted residual . . . 65

TIV transverse isotropy with a vertical axis of symmetry . . . 148

TIH transverse isotropy with a horizontal axis of symmetry . . . 148

Acknowledgments

The demanding path of authoring a thesis would not have been possible without the advice, support and love of many individuals.

First, I would like to thank my supervisor Dr. Xavier Garcia for his advice and encouragement and for giving me the freedom to develop my own ideas.

The work for this thesis was funded within the project CODOS financed by REPSOL, which I acknowledge. I also want to thank the whole group at the Barcelona-Center for Subsurface Imaging and in particular Prof. César R. Ranero for giving me the opportunity to work on this project. My special thanks are extended to Estelle Roux, Agnese Muñoz, Adrià Meléndez, Manel Prada, Alejandra Lago, Sara Martínez, and everyone in the past and present of the group, with best regards to Naiara Korta and Ivan de la Cruz Vargas by countless discussions and life experiences.

I would like to offer my special thanks to my tutor at the University of Barcelona, Prof. Pilar Queralt, for her support during the development of this thesis and especially for my time in their EM group during the development of my Master's thesis, and extend my gratitude to Prof. Àlex Marcuello and Prof. Juanjo Ledo, because all together have suceeded on creating an enjoyable working atmosphere. I also want to use this opportunity to thank the students from my time there: Xènia Ogaya, Joan Campanyà, Perla Piña and Eloi Vilamajó and with special thanks to Lena Escalas.

I am particularly grateful to Prof. Klaus Spitzer for the great opportunity to stay at the Institute of Geophysics and Geoinformatics in the TU Bergakademie Freiberg in February and March of 2013, and extend my gratitude to Wenke Wilhelms, Jana Börner, Feiyan Wang, Antje Franke-Börner and Ralph Börner for their warm welcome during my stay there and for taking the time to explain their work to me.

I would also use the opportunity to thank Dr. Juan José Curto from the Ebre Observatory for giving me the opportunity to have my first contact with geophysics and geomagnetics when I was still in my Diploma studies.

I am most grateful to Ivan Latella for his loyal friendship and for the time we spend together studying Physics.

A les meves amigues tortosines, Montse Novella, Joana Andreu i Maite Martí, donar-los les gràcies per sempre ser-hi de cor.

Quiero darle mi más profundo agradecimiento a Jorge Belenguer, porque gran parte de este camino lo hicimos juntos y desde luego no hubiera podido hacerlo sin su dedicación. Gracias de corazón.

A la meva familia agrair-los per sempre ser-hi, per donar-me tant amor i per creure en mi; a la meva mare, Trini, al meu pare, Alfonso, als meus germans: Satyavan, Shankar i Björn, a la meva 'tata', Conxita, i a Albert, a les meves iaies, Maria Cinta i Mercedes i al meu iaio, Alfonso, que des d'aquest any vola lliure pel Mediterrani.

My most sincere thanks to my love Maik Neukirch, for all his patience and support, for his time spent on revisiting this thesis, for his good advices, for great discussions, for all.

CHAPTER 1

Introduction

Electromagnetic (EM) induction methods are used in geophysics to measure the electric properties of geologic formations. Propagation of EM fields depends on the electrical conductivity of the medium, which mainly depends on a combination of rock composition, porosity and pore-fluid content. This relation is used by EM methods that measure and study the EM fields, usually on the Earth's surface, and try to reconstruct a subsurface conductivity model which explains the observed data. Two different EM induction methods are the controlled-source electromagnetic (CSEM) and the magnetotelluric (MT) methods. CSEM uses an artificial EM source to excite induced currents in the subsurface and measure the induced EM fields for distinct source-receiver configurations and frequencies or transient decays for time-domain methods. On the other hand, MT is a natural-source method that exploits time variations of the Earth's magnetic field (Chave and Jones, 2012), caused at low frequencies ($< 10Hz$) by the interaction of the solar plasma with the ionosphere and the magnetosphere as sources, and at high frequencies ($> 10Hz$) by global lightning activity (Garcia and Jones, 2002). In both cases, the fluctuating magnetic field induces electric currents in the ground dependent on in-depth conductivity structure and MT analyses the resulting time variations of the EM fields to infer the conductivity distribution.

The MT method was first introduced in the 1950s (Cagniard, 1953) and since then it has developed fast. It has been used successfully on land and on marine environments to study large-scale features of the litosphere (Chave and Jones, 2012). In MT surveys time variations of the electric and magnetic field components are recorded simultaneously on the surface, at a sampling interval between $1 \times 10^{-3} - 1 \times 10^{5} s$. The frequency dependent transfer function between the electric and magnetic fields, which physically represents the electrical conductivity structure, is statistically appreciated. The depth of signal penetration can easily reach mid-mantle depths and is solely limited by the frequency range of the observed signal. MT has been proven to be particularly useful for mapping salt, volcanics and carbonates which present challenges to seismic methods. The reason is that MT is primarily sensitive to electrically conductive material, where electric currents are preferentially induced, and thus can detect the sediments below resistive volcanics or carbonates,

where seismic methods experience difficulties. However, this technique alone is not useful for hydrocarbon fluid detection, because MT currents within the Earth are generated mostly in the horizontal plane and the thin sub-horizontal, resistive formations typical for the presence of hydrocarbons are almost invisible to the method. In this context, CSEM is a complementary technique to MT, because common EM transmitters used in marine CSEM generate vertical electric fields which are sensitive to horizontal resistors of sufficient size.

The deepwater marine CSEM method used today for hydrocarbon exploration was first proposed by Cox (1981) and the first experiment was carried out to measure the conductivity of the lithosphere. On subsequent experiments, marine CSEM methods were focused on detecting magma chambers and hydrothermal systems at mid-ocean ridges (e.g. Young and Cox, 1981; Evans et al., 1991; MacGregor et al., 2001). It has been in the past decade that the CSEM method has been widely recognized as an exploration tool for detecting and delineating hydrocarbon reservoirs (e.g. Edwards, 2005).

Even though, CSEM methods can employ electric or magnetic dipole transmitters, a typical frequency-domain marine CSEM survey uses a high powered horizontal electric dipole to transmit a low-frequency EM signal through the seafloor to an array of multicomponent EM receivers. The direct signal is rapidly attenuated within the conductive sea water, and already at source-receivers separations of more than a few hundred meters, the received signal is dominated by fields that have interacted with the Earth. Transmission frequencies are typical between 0.01 and $10Hz$ and the depth of investigation ranges between a few tens of meters to depths of several kilometers.

The fast progress of these techniques had been supported by advances of the theory, field instrumentation and interpretation tools. At present, the interpretation process consists mainly in a processing phase and in a modeling (also called forward modeling) and inversion phases. For data processing, the spectral responses are estimated from the measured time series. The spectral responses in MT are impedances, or more specifically the relation between the electric and magnetic fields in the frequency domain, and in CSEM the spectral response relates the received EM fields with the transmitted source signal in the frequency domain, thus normalized EM fields. The modeling phase calculates EM fields or impedances for a given synthetic model solving the Maxwell's equations, and these fields are compared to the real measurements (after processing) through an inversion process in which the misfit between synthetic and real data is minimized iteratively by varying the synthetic model. The resulting synthetic model from the optimization process is taken as the best model to represent the measurements, and ultimately as an image of the subsurface conductivity model.

Modeling and inversion codes have been improved continuously along with the ongoing advances in computer performance. The programs evolved from approximating the Earth as a one-dimensional (1-D) model to consider the full problem of a three-dimensional (3-D) Earth. However, the two-dimensional (2-D) approach is still the standard tool for inversion.

1.1 Modeling

The different numerical methods in use for MT and CSEM modeling include variations of the integral equation (IE), finite differences (FD) and finite elements (FE) methods. We will give more details on these techniques on the next chapter and an overview of their application to EM methods is provided, for example, by Avdeev (2005) and Börner (2010). Amongst these techniques, the FE method has been proven to be the more flexible with respect to model geometry (e.g. Avdeev, 2005). The reason is that FE methods in combination with the use of unstructured grids, allow for a better representation of the topography and of the different resistivity boundaries than for example, FD techniques, and are able to accommodate both small and large structures in the same grid. Moreover, FE accepts superior order spatial approximations in contrast to FD, which is usually derived using first or second order approximations, and enables extensive error estimation analysis.

Recently, with the improvement of computer technology and the availability of high-quality mesh generators and robust and efficient numerical solvers, a number of modeling programs using FE have been developed for MT (e.g. Mogi, 1996; Farquharson and Miensopust, 1993; Key and Ovall, 2011; Ren et al., 2013) and for CSEM (e.g. Badea et al., 2001; Schwarzbach et al., 2011; Mukherjee and Everett, 2011; Key and Ovall, 2011).

Many of these FE codes are developed for the 3-D problem and are fast and memory efficient if only a limited number of forward modeling solutions is required. However, they are still impractical for inversion, where a large number of simulations is essential. Thus, it is easier to investigate on new techniques for modeling and inversion on 2-D problems, where the time and memory requirements are in a more reasonable level for the existing computational resources. Moreover, most MT and CSEM data is collected along a profile (Constable, 2010) and in many geological situations the subsurface conductivity structure can be assumed invariant in one horizontal dimension and described as 2-D.

Last advances in FE modeling incorporate adaptive mesh refinement techniques to control solution accuracy and program efficiency (e.g. Franke et al., 2007; Li and Pek, 2008; Key and Ovall, 2011; Schwarzbach et al., 2011). Adaptive mesh refinement methods estimate the error contribution of each mesh element to the solution error or to the error of a certain functional, and based on this error select a subset of elements to refine. The grid is then refined in these regions and the entire process is repeated iteratively improving the solution or functional accuracy until a stopping criteria is reached.

On the other hand, only a few of the state-of-the-art codes allow for simulations on an electrically anisotropic media. However, it is widely known by the EM community that anisotropy is an important factor to consider when interpreting EM geophysical data (e.g. Wannamaker, 2005; Martí, 2014). In 2-D modeling the few codes that allow for anisotropy and are based on FE are proposed by Li and Pek (2008), for MT and generally anisotropic media, and by Li and Dai (2011) for CSEM and dipping anisotropic structures.

1.2 Inversion

Inversion of EM geophysical data is a specially challenging and computationally intense task. The EM inverse problem is nonlinear and underdetermined with unstable solutions. These features make the inverse problem ill-posed. Furthermore, the problem is also large-scale with thousands of data points to be inverted in the tens of thousands of model parameters (Avdeev, 2005).

Usually, inverse programs include a regularization function to deal with the instability and non-uniqueness of the problem. Then, the inverse problem is generally solved numerically, minimizing a functional which penalizes both misfit to the data and model roughness, using derivative-based optimization methods, such as non-linear conjugate gradients (e.g. Newman and Alumbaugh, 2000; Rodi and Mackie, 2001; Commer and Newman, 2008), quasi-Newton (e.g. Haber, 2005; Avdeev and Avdeeva, 2009) or Gauss-Newton (e.g. Mackie and Madden, 1993; Siripunvaraporn et al., 2004). For further details of the application of these optimizations methods to solve EM inverse problems we refer to the reviews of Avdeev (2005) and Siripunvaraporn (2012). These methods present different benefits and drawbacks when applied to the EM inverse problem, however, in most of them the computation of the forward solution and of the sensitivities constitute the most expensive part (e.g. Siripunvaraporn, 2012; Egbert and Kelbert, 2012).

On the other hand, most of the inversion codes to date are based on the FD method for discretization or on the IE method. Only very recently, a few 3-D codes have appeared that implement a FE framework in the inversion scheme (Schwarzbach and Haber, 2013; Grayver, 2015). Schwarzbach and Haber (2013) give a novel formulation for the regularization function in a FE framework, and Grayver (2015) include in their code the possibility to use different meshes for the forward and inverse problems, and to additionally calculate the optimal mesh in each case and in each iteration of the inversion process. This last point allows to calculate accurate EM responses on a suitable fine mesh and at the same time avoids overparametrization of the model parameter variable with a coarser mesh that represents imaged subsurface structure.

All the mentioned inversion schemes shear a common initial approximation which consists of eliminating the partial differential equation (PDE) that constraints the forward solution variables from the optimization problem, by substituting it, using equality constraints, in the predicted variable of the objective function misfit term. Then, the only variable in the optimization is the model parameter. Methods using this approach are called *reduced-space* methods, because they reduce the space of optimization variables, and are also sometimes referred to as *black-box* methods (Herzog and Kunisch, 2010), since they treat the state equation as a black-box, embedding it into an optimization loop. By contrast, there is a developed mathematical theory in the full-space, in which the PDE-constrained optimization problem is addressed directly (e.g. Nocedal and Wright, 1999; Biros and Ghattas, 2005), treating the state and model parameters variables as independent optimization variables, which are coupled through the PDE constraint. These methods are

sometimes called *all-at-once* methods (e.g. Haber et al., 2004; Bangerth, 2008).

The main advantage of the *all-at-once* approach over *black-box* methods is that while the latter require the repeated costly solution of the (nonlinear) state equation for each evaluation of the objective function and of the adjoint equation to evaluate the sensitivities and the gradients, the former avoid these calculations and only need to solve exactly the state equation at the very end of the optimization process. This advantage comes at the cost of many more optimization variables and of the presence of equality constraints. *All-at-once* inversion schemes have already been applied to solve EM inverse problems in a FD framework (Haber et al., 2000, 2004; Wilhelms et al., 2013), and Haber et al. (2004) concluded that this procedure has potential for a solution to be reached faster than in traditional unconstrained optimization approaches.

Recent research has formulated algorithms using *all-at-once* methods in a FE framework and using a continuous function space setting to allow for discretizations that are adaptively refined as nonlinear iterations proceed (Bangerth, 2008; Herzog and Kunisch, 2010; Günther, 2010). In these optimizations schemes, the common techniques in *all-at-once* approaches are first formulated on continuous function spaces and then discretized. This has the advantage that then, the finite dimensional norms usually used for estimating the error of the variables in the meshes, are independent of the mesh size and individual steps of the algorithm are comparable even if they used differently refined meshes (Bangerth, 2008). This can reduce significantly the numerical effort to solve the inverse problem because it allows to use independent adaptive meshes for the model parameter variables and for the field variables. The mesh for the model parameter can then be coarser where we lack information, making the inverse problem better posed, and the mesh for the fields variables can be fine only in the required regions for accuracy.

1.3 Objectives of the Thesis

This thesis is concerned with the development of a robust and versatile unstructured mesh FE program to numerically model the total field for 2-D anisotropic CSEM and MT data, allowing for arbitrarily oriented 3-D sources. To represent 3-D CSEM sources for a 2-D physical model, a 2.5-dimensional (2.5-D) approximation will be considered. We will derive and implement the FE formulations for both methods, for isotropic and anisotropic subsurface conductivity structures. Moreover, we investigate on adaptive mesh refinement techniques to control the accuracy of the solution.

Further, we study a framework for the 2.5-D CSEM inverse problem as a PDE-constrained optimization in full-space with a FE discretization and demonstrate viability of this scheme.

1.4 Outline

Chapter 2 begins by reviewing the numerical techniques to model CSEM and MT data using 2-D and 3-D approaches, states the isotropic and anisotropic 2.5-D frequency-domain

CSEM and 2-D MT problems, and derives their FE formulation. The adaptive mesh refinement techniques are introduced as a method to control and improve the quality of the FE solution. These FE formulations form the basis of the development of an algorithm presented in Chapter 3, where used packages and different techniques for the implementation are described and the capabilities of the program discussed. Then, Chapter 4, assesses the performance and accuracy of the developed modeling software. The results of conducted numerical experiments are presented to illustrate and validate the main characteristics and numerical strategies of the software for MT and CSEM and on 1-D and 2-D synthetic models. In particular, the influence of the model dimensions and the mesh design on the accuracy of the solution is studied, which justifies the need of an adequate mesh design. Then, the performance of the adaptive mesh refinement is benchmarked and the influence of shape function order and choice of error estimator method is studied with respect to solution accuracy. Additionally, advantages of this technique for modeling topography are illustrated. Finally, numerical experiments demonstrate the importance firstly, to realistically model sources in certain situations and secondly, to appropriately treat anisotropy.

Work on a PDE-constrained full-space optimization scheme to the solution of the 2.5-D CSEM inverse problem using the FE method for the discretization is presented in Chapter 5, beginning by briefly reviewing contributions on EM inversion. Then, two different strategies on formulating the PDE-constrained optimization problem in full-space are discussed: a *discretize-optimize* strategy and an *optimize-discretize* strategy. Formulation for the 2.5-D CSEM PDE-constrained optimization problem using the discretize-optimize strategy are derived and implemented by using a general-purpose optimization algorithm. Synthetic inversion examples verify the program. At the end of the Chapter the PDE-constrained full-space optimization formulation is derived to solve the 2.5-D CSEM inverse problem by using the FE method for the discretization. This formulation of an optimize-discretize strategy offers the potential to use adaptive FE meshes during the inversion. Chapter 6 discusses the contributions of the thesis and Chapter 7 summarizes the major conclusions and suggests directions for future work.

1.5 Remark on the basic notation

In this thesis, vectors, matrices and tensors are distinguished from scalars by the use of bold typeface. All variables and parameters are in the International System of Units (SI).

The reference frame for the equations and Figures we show in the thesis is not the conventional one used in geophysics. Our reference frame, S', is related to the conventional one in geophysics, S, by:

$$
\begin{aligned}
x' &= y \\
y' &= -z \\
z' &= -x,
\end{aligned}
$$

thus, the horizontal right-hand-side axis is denoted x (instead of y); the depth is defined as $-y$ (typically z) and finally, the strike axis is represented by z (usually x). The reason for the different reference frame compared to a typically accepted standard in geophysics, is that our program uses COMSOL (COMSOL, 2015) and S' is the reference frame in COMSOL. Therefore, all the equations presented in this thesis are derived in this particular reference frame. The output of the program could be easily rotated to the reference frame S, and then, the Figures we show in this thesis would be on the typical system. However, we preferred to keep the same reference frame for both the equations and the Figures, to maintain consistency and avoid confusion throughout the work.

References

D. Avdeev and A. Avdeeva. 3D magnetotelluric inversion using a limited-memory quasi-newton optimization. *Geophysics*, 74(3):F45–F57, 2009.

D. B. Avdeev. Three-dimensional electromagnetic modelling and inversion from theory to application. *Surveys in Geophysics*, 26:767–799, 2005.

E. A. Badea, M. E. Everett, G. A. Newman, and O. Biro. Finite-element analysis of controlled-source electromagnetic induction using Coloumb-gauged potentials. *Geophysics*, 66(3):786–799, 2001.

W. Bangerth. A framework for the adaptive finite element solution of large-scale inverse problems. *SIAM Journal on Scientific Computing*, 30(6):2965–2989, 2008.

G. Biros and O. Ghattas. Parallel Lagrange-Newton–Krylov–Schur methods for PDE-constrained optimization. Part I: The Krylov–Schur solver. *SIAM Journal on Scientific Computing*, 27(2):687–713, 2005.

R.-U. Börner. Numerical modelling in geo-electromagnetics: advances and challenges. *Surveys in Geophysics*, 31:225–245, 2010.

L. Cagniard. Basic theory of the magnetotelluric method of geophysical prospecting. *Geophysics*, 18:605–635, 1953.

A. D. Chave and A. G. Jones. *The magnetotelluric method: Theory and practice*. Cambridge University Press, 2012.

M. Commer and G. A. Newman. New advances in three-dimensional controlled-source electromagnetic inversion. *Geophysical Journal International*, 172:513–535, 2008.

COMSOL. Comsol Multiphysics 5.1 User's Guide. *COMSOL, Burlington, MD*, 2015. URL `https://www.comsol.com/`.

S. Constable. Ten years of marine CSEM for hydrocarbon exploration. *Geophysics*, 75(5): 75A67–75A81, 2010.

C. Cox. On the electrical-conductivity of the oceanic litosphere. *Physics of the Earth and Planetary Interiors*, 25(3):196–201, 1981.

N. Edwards. Marine controlled source electromagnetics: principles, methodologies, future commercial applications. *Surveys in Geophysics*, 26(6):675–700, 2005.

G. D. Egbert and A. Kelbert. Computational recipes for electromagnetic inverse problems. *Geophysical Journal International*, 189:251–267, 2012.

R. L. Evans, S. C. Constable, M. C. Sinha, and C. S. Cox. Upper crustal resistivity structure of the East Pacific Rise near 13°N. *Geophysical Research Letters*, 18(10):1917–1920, 1991.

C. G. Farquharson and M. P. Miensopust. Three-dimensional finite-element modelling of magnetotelluric data with a divergence correction. *Journal of Applied Geophysics*, 75(4): 699–710, 1993.

A. Franke, R.-U. Börner, and K. Spitzer. Adaptive unstructured grid finite element simulation of two-dimensional magnetotelluric fields for arbitrary surface and seafloor topography. *Geophysical Journal International*, 171:71–86, 2007.

X. Garcia and A. G. Jones. Atmospheric sources for audio-magnetotelluric (AMT) sounding. *Geophysics*, 67(2):448, 2002.

A. V. Grayver. Parallel three-dimensional magnetotelluric inversion using adaptive finite-element method. Part I: theory and synthetic study. *Geophysical Journal International*, 202:584–603, 2015.

A. Günther. *Structure exploiting Galerkin schemes for optimal control of PDEs with constraints on the involved variables*. PhD thesis, University of Hamburg, 2010.

E. Haber. Quasi-Newton methods for large-scale electromagnetic inverse problems. *Inverse Problems*, 21:305–323, 2005.

E. Haber, U. M. Ascher, and D. W. Oldenburg. On optimization techniques for solving nonlinear inverse problems. *Inverse Problems*, 16:1263–1280, 2000.

E. Haber, U. M. Ascher, and D. W. Oldenburg. Inversion of 3D electromagnetic data in frequency and time domain using an inexact all-at-once approach. *Geophysics*, 69(5): 1216–1228, 2004.

R. Herzog and K. Kunisch. Algorithms for PDE-constrained optimization. *GAMM-Mitteilungen*, 33:163–176, 2010.

K. Key and J. Ovall. A parallel goal-oriented adaptive finite element method for 2.5-D electromagnetic modelling. *Geophysical Journal International*, 186:137–154, 2011.

Y. Li and S. Dai. Finite element modelling of marine controlled-source electromagnetic responses in two-dimensional dipping anisotropic conductivity structures. *Geophysical Journal International*, 185(2):622–636, 2011.

Y. Li and J. Pek. Adaptive finite element modelling of two-dimensional magnetotelluric fields in general anisotropic media. *Geophysical Journal International*, 175:942–954, 2008.

L. M. MacGregor, M. Sinha, and S. Constable. Electrical resistivity structure of the Valu Fa Ridge, Lau Basin, from marine controlled-source electromagnetic sounding. *Geophysical Journal International*, 146(1):217–236, 2001.

R. L. Mackie and T. R. Madden. Three-dimensional magnetotelluric inversion using conjugate gradients. *Geophysical Journal International*, 115:215–229, 1993.

A. Martí. The role of electrical anisotropy in magnetotelluric responses: from modelling and dimensionality analysis to inversion and interpretation. *Surveys in Geophysics*, 35 (1):179–218, 2014.

T. Mogi. Three-dimensional modeling of magnetotelluric data using finite element method. *Journal of Applied Geophysics*, 35:185–189, 1996.

S. Mukherjee and M. E. Everett. 3D controlled-source electromagnetic edge-based finite element modeling of conductive and permeable heterogeneities. *Geophysics*, 76(4):F215–F226, 2011.

G. A. Newman and D. L. Alumbaugh. Three-dimensional magnetotelluric inversion using non-linear conjugate gradients. *Geophysical Journal International*, 140:410–424, 2000.

J. Nocedal and S. J. Wright. *Numerical Optimization*. Springer-Verlag, 1999.

Z. Ren, T. Kalscheuer, S. Greenhalgh, and H. Maurer. A goal-oriented adaptive finite-element approach for plane wave 3-D electromagnetic modelling. *Geophysical Journal International*, 194(2):700–718, 2013.

W. Rodi and R. L. Mackie. Nonlinear conjugate gradients algorithm for 2-D magnetotelluric inversion. *Geophysics*, 66(1):174–187, 2001.

C. Schwarzbach and E. Haber. Finite element based inversion for time-harmonic electromagnetic problems. *Geophysical Journal International*, 193:615–634, 2013.

C. Schwarzbach, R.-U. Börner, and K. Spitzer. Three-dimensional adaptive higher order finite element simulation for geo-electromagnetics - a marine CSEM example. *Geophysical Journal International*, 187:63–74, 2011.

W. Siripunvaraporn. Three-dimensional magnetotelluric inversion: An introductory guide for developers and users. *Surveys in Geophysics*, 33:5–27, 2012.

W. Siripunvaraporn, G. Egbert, Y. Lenbury, and M. Uyeshima. Three-dimensional magnetotelluric inversion: data-space method. *Physics of the Earth and Planetary Interiors*, 150: 3–14, 2004.

P. E. Wannamaker. Anisotropy versus heterogeneity in continental solid earth electromagnetic studies: fundamental response characteristics and implications for physicochemical state. *Surveys in Geophysics*, 26:733–765, 2005.

W. Wilhelms, R.-U. Börner, and K. Spitzer. Preparation for a 3D magnetotelluric inversion - specific characteristics of the all-at-once approach. In *5th International Symposium on Three-Dimensional Electromagnetics*, 2013.

P. D. Young and C. S. Cox. Electromagnetic active source sounding near the East Pacific Rise. *Geophysical Research Letters*, 8(10):1043–1046, 1981.

CHAPTER 2

CSEM and MT Finite Elements modeling in 2-D

2.1 Introduction

The process of forward modeling consists in solving a mathematical boundary value problem (BVP), that is, solving the PDE that describe some physical phenomena in some media/model. When this model presents a simple geometry, i.e. it only varies in depth, that is a 1-D approach, an analytical or semi-analytical solution exists for the MT (e.g. Wait, 1953; Yin, 2006) and CSEM (e.g. Løseth and Ursin, 2007; Key, 2009; Streich and Becken, 2011) governing equations. In particular, 1-D CSEM modeling is a fast and simple tool that has showed its usefulness in the interpretation of tabular bodies when both source and receiver are over the target (Constable, 2010). However, for more complex geometries numerical methods are required. Usually the problem is split in smaller regions, in a process known as discretization, and solved within each one of them with appropriate boundary conditions. The numerical solution needs the computational domain to be finite and bounded, but the original BVP is located naturally in an infinite 3-D space and an artificial boundary is added so the fields in the truncated domain reproduce the problem in the original infinite domain.

The accuracy of the numerical solution and the efficiency of its computation in terms of time and memory are principal concerns of the modeling process and depend mainly on the numerical methods used for the BVP solution. However, other determinant factors to obtain realistic synthetic MT and CSEM responses are a suitable approximation of boundary conditions and EM sources, and of the conductivity model, keeping it as simple as possible. That is, in certain geologic and experimental scenarios, to model the orientation and geometry of the sources or to mesh accurately the topography or the small and large structures of a complex geological formation. Another component which can have an impact on the EM observations are electrically anisotropic structures in the model, for which suitable considerations on the conductivity tensor need to be performed.

Numerical techniques in use for EM induction methods modeling include variations of the IE, FD and FE methods.

The IE method is suitable when the model consists of an anomalous region (e.g., a min-

eral deposit) incrusted in an homogeneous model. Discretization is only applied in the anomalous region and consequently the number of unknowns and equations is smaller than with other techniques. At the beginning, when the computational resources where limited, IE methods were the most practical for modeling the full 3-D problem (e.g. Weidelt, 1975; Wannamaker et al., 1984).

Advances in computational resources has promoted the use of FD methods which are more appropriate for more complex and generalized models in MT (e.g. Jones and Pascoe, 1972; Smith and Booker, 1991; Mackie et al., 1993) and CSEM (e.g. Newman and Alumbaugh, 1995; Haber et al., 2000; Weiss and Constable, 2006; Streich, 2009) modeling. In parallel, research on efficient IE codes has continued (e.g. Zhdanov and Fang, 1996; Avdeev et al., 1997). Using FD methods the discretization is generally in all the model so the unknowns and equations involved are larger than for the IE method. Furthermore, the discretization is commonly based on a structured rectangular grid and fine-scale discretization required to handle topography in the central region of a model leads to thin cells that extend laterally and vertically throughout the entire domain, often resulting in highly elongated cells and poor convergence in the resulting numerical linear system (Key and Ovall, 2011).

Amongst the different numerical methods the FE method provides the greatest flexibility in accounting for model geometry (e.g. Avdeev, 2005). Latest programs incorporate unstructured grids which allow for a better representation of the topography and of the different resistivity boundaries than FD and are able to accommodate both small and large structures in the same grid. Moreover, FE accepts superior order spatial approximations in contrast to FD, which is usually derived using first or second order approximations, and enables extensive error estimation analysis. Although the first 3-D FE algorithm appeared in Pridmore et al. (1981), it was not since recently, with the emergence of more powerful computers, that new algorithms were developed for MT (e.g. Mogi, 1996; Farquharson and Miensopust, 1993; Ren et al., 2013) and CSEM (e.g. Badea et al., 2001; Börner et al., 2008; Schwarzbach et al., 2011; Mukherjee and Everett, 2011). The reason is that FE techniques are more difficult to implement than FD and require more complex calculations, which translate in larger computational time.

Further details on EM applications of these techniques is provided, for example, in the reviews of Avdeev (2005) and Börner (2010).

Three-dimensional simulations can now be fast and memory efficient if only a limited number of forward modeling solutions is required. However, 3-D modeling can become impractical if a large number of simulations is essential, i.e. for parameter testing or resolution studies in inversion (Streich et al., 2011). In addition, most MT and CSEM data is collected along a profile (Constable, 2010) and in many geological situations the subsurface conductivity structure can be assumed invariant in one horizontal dimension and described as 2-D.

The 2-D approach of the CSEM problem can not be applied through a direct 2-D formulation of the problem because of the 3-D nature of the source fields. Rather a 2.5-D

formulation is considered. In this approach, the geology is 2-D and the 3-D Maxwell's equations are Fourier transformed in the strike direction coordinate onto the wavenumber domain, resulting in a formulation that captures the 3-D physics but is substantially more efficient to compute than the full 3-D solution (Unsworth et al., 1993; Streich et al., 2011). Discretization is necessary only over a cross-section, rather than throughout a volume, but the problem needs to be solved for a number of wavenumber values in order to perform the inverse Fourier transform of the solution fields back to the spatial domain.

Stoyer and Greenfield (1976) published one of the first solutions to the 2.5-D CSEM problem using FD and Lee and Morrisson (1985) reported the first 2.5-D FE modeling scheme. However, the number of publications that succeed their work is very limited (Leppin, 1992; Everett and Edwards, 1992; Unsworth et al., 1993). The main reason is that advances in computational resources made the fully 3-D problem as tractable as the 2.5-D, even though it may require significantly more computer power, and research focused on it (Everett and Edwards, 1992). Recently, interest in the 2.5-D approach has resurged and solutions have been published using both FD (e.g. Abubakar et al., 2008; Streich et al., 2011) and FE methods (e.g. Mitsuhata, 2000; Kong et al., 2008; Li and Dai, 2011; Key and Ovall, 2011).

Otherwise, most of the mentioned IE, FD and FE state-of-the-art algorithms assume that the 2-D or 3-D subsurface is electrically isotropic and can not model electrically anisotropic structures. Contrarily, it is widely known by the EM community that anisotropy is an important factor to consider when interpreting EM geophysical data (e.g. Wannamaker, 2005; Martí, 2014). First modeling programs dealing with anisotropy were published at the same time as the isotropic ones (e.g. Reddy and Rankin, 1971, 1975), but not as many have been developed in subsequent years. Among the most known, for different 1-D scenarios are e.g. Pek and Santos (2002) and Yin (2006) for MT and Li and Pedersen (1992) and Løseth and Ursin (2007) for controlled-source in land and marine media, respectively. In 2-D the most recognized and used code for MT is the one of Pek and Verner (1997) for arbitrary anisotropy using the FD method based on the FE algorithm of Reddy and Rankin (1975). More recently, Li and Pek (2008) presented a 2-D MT FE program for generally anisotropic media and Li and Dai (2011) a 2.5-D CSEM FE algorithm for dipping anisotropic structures. Research on MT modeling of 3-D anisotropic media has been also published (e.g. Weidelt, 1999; Weiss and Newman, 2002).

Last advances in both 2-D and 3-D FE modeling increase time efficiency and solution accuracy incorporating *a posteriori* adaptive mesh refinement techniques (e.g. Franke et al., 2007; Li and Pek, 2008; Key and Ovall, 2011; Schwarzbach et al., 2011; Grayver and Bürg, 2014). Adaptive methods seek to increase the solution accuracy by iteratively refining the grid. At each iteration, is calculated an estimation of the error contribution by the mesh elements. Posterior, it is selected a subset of elements for refinement based on this estimate and finally, the grid is refined by creating new smaller elements in these regions.

One of the goals of this thesis is the development of a robust and efficient forward modeling program, which has to be able to model MT and CSEM responses in complex

2-D geometries and electrically anisotropic structures. For this purpose we develop a 2.5-D CSEM and 2-D MT frequency-domain adaptive unstructured FE program which is additionally able to model arbitrary oriented magnetic and electric sources. Many of the newest discussed 2-D adaptive FE codes incorporate some of the characteristics of our program, but only last versions of the forward algorithm of MARE2DEM (Key and Ovall, 2011) present similar features regarding versatility in: method (CSEM and MT), sources (electrical and magnetic arbitrarily oriented) and including anisotropy of the conductivity.

In this Chapter, we state the 2.5-D frequency-domain CSEM and 2-D MT problems and we derive their FE formulation. We first extract the 2.5-D CSEM governing equations for an isotropic conductivity model and then we apply to this BVP the FE method. Then, we extend the derived problem to the dipping electrically anisotropic case. Finally, we present the MT problem as a particular case of the 2.5-D CSEM equations. Original contributions of this Chapter are the derivation of the 2.5-D CSEM problem and its FE formulation for dipping anisotropic conductivity structures using the total field formulation.

2.2 The 2.5-D frequency-domain CSEM problem

The fundamental equations of classical electrodynamics are Maxwell's equations, which describe how electric and magnetic fields are generated and altered by each other and by charges and currents in a macroscopic media. The 2.5-D CSEM problem consists of a mathematical approximation for the solution of the 3-D Maxwell's equations on a 2-D conductivity model with 3-D sources. The conductivity does not vary in the strike direction (z), but the source is finite, as in the case of a loop or grounded wire (Figure 2.1). The approximation is the Fourier transformation of the equations in along-strike spatial direction onto the wavenumber domain $xy\kappa_z$. The problem is solved over a cross-section in the $xy\kappa_z$–domain. Many solutions are required for several wavenumber values κ_z to transform the fields back to the spatial domain. In this section the 2.5-D CSEM BVP is stated by deriving its governing equations and the harmonic source equations are specified.

2.2.1 Governing equations

Time domain Maxwell's equations in a region free of sources are:

$$\nabla \times \mathbf{E} + \frac{\partial \mathbf{B}}{\partial t} = 0, \tag{2.1a}$$

$$\nabla \times \mathbf{H} - \frac{\partial \mathbf{D}}{\partial t} = \mathbf{J}, \tag{2.1b}$$

$$\nabla \cdot \mathbf{D} = \rho_v, \tag{2.1c}$$

$$\nabla \cdot \mathbf{B} = 0, \tag{2.1d}$$

where $\boldsymbol{E}$ is the electric field intensity, $\boldsymbol{H}$ is the magnetic field intensity, $\boldsymbol{D}$ is the electric flux density (or dielectric displacement), $\boldsymbol{B}$ is the magnetic flux density (or magnetic in-

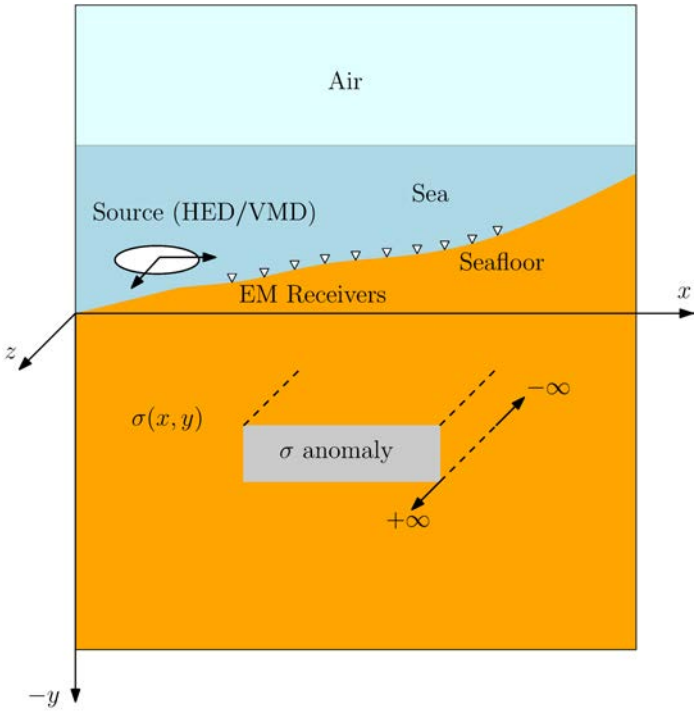

Figure 2.1: *Two and a half dimensional (2.5-D) CSEM problem scheme. The conductivity (σ) model varies in the two-dimensional (2-D) $xy-$plane and extends to infinity in the $z-$ direction; the sources are finite and can be oriented in any of the three-dimensional (3-D) space directions. In this picture we show a representation of an horizontal electric dipole (HED) or a vertical magnetic dipole (VMD). The reference frame in the picture is the one we use in all this thesis.*

duction), $\boldsymbol{J}$ is the electric current density and ρ_v is the volume electric charge density. All field quantities are function of space and time.

If there is conservation of charge, the charge density is related to the current density by the continuity equation:

$$\nabla \cdot \mathbf{J} + \frac{\partial \rho_v}{\partial t} = 0. \tag{2.2}$$

Furthermore, the field quantities are related by the constitutive relations:

$$\mathbf{D} = \boldsymbol{\epsilon} * \mathbf{E}, \tag{2.3a}$$

$$\mathbf{B} = \boldsymbol{\mu} * \mathbf{H}, \tag{2.3b}$$

$$\mathbf{J} = \boldsymbol{\sigma} * \mathbf{E}, \tag{2.3c}$$

in which $\boldsymbol{\epsilon}$ is the electrical permittivity, $\boldsymbol{\mu}$ is the magnetic permeability and $\boldsymbol{\sigma}$ is the electrical conductivity of the media. The asterisk denotes convolution in time and when the equations are transformed to the frequency-domain becomes a product.

For the frequency-domain CSEM method, the following general assumptions are made:

- The electrical properties in the earth are independent of time, temperature or pressure.
- Due to attenuation in the earth and use of low frequencies, fields propagate only by

diffusion (quasi-static approximation): $\frac{\partial \mathbf{D}}{\partial t} \approx 0$ and $\frac{\partial \rho_v}{\partial t} \approx 0$.

- There are external electric and magnetic harmonic sources which generate an electric current $\boldsymbol{J}^s$ and a magnetization $\boldsymbol{M}^s$ respectively.

- The EM fields are time-harmonic with time dependence $e^{i\omega t}$ and with constant angular frequency ω.

Additionally, we consider the simplest case and assume for the remainder of this work, that:

- The media is isotropic for the electromagnetic properties: $\boldsymbol{\epsilon} = \epsilon\mathbb{I}$ and $\boldsymbol{\mu} = \mu\mathbb{I}$.

- The electrical permittivity and the magnetic permeability can be approximated by their value in the free space ϵ_0 and μ_0, leaving the information of the media only through the electrical conductivity property σ.

Moreover, for the following derivations we also assume an electrically isotropic conductivity: $\boldsymbol{\sigma} = \sigma\mathbb{I}$.

With the assumptions above, Maxwell's equations can be expressed in complex form as (Ward and Hohmann, 1988):

$$\nabla \times \mathbf{E} + i\omega\mu_0\mathbf{H} = -i\omega\mu_0\mathbf{M}^s \tag{2.4a}$$

$$\nabla \times \mathbf{H} - (\sigma + i\epsilon_0\omega)\mathbf{E} = \mathbf{J}^s, \tag{2.4b}$$

where $\boldsymbol{E}$ and $\boldsymbol{H}$ are now the frequency-domain electric and magnetic fields, complex-valued vector functions of position but not time. The use of the same nomenclature for the time-domain and frequency-domain fields is ambiguous, but is restricted to this section. Only the frequency-domain quantities will be considered throughout in the remainder of this work.

Equations (2.4) are only valid within a material and if there is more than one material, both equations hold separately within each.

Continuity conditions that must be satisfied as the fields traverses the boundary between conductor I and II (Figure 2.2) are (Ward and Hohmann, 1988):

- **Normal B**. The normal component of $\boldsymbol{B}$ is continuous across an interface separating medium I from medium II:

$$\hat{\mathbf{n}} \cdot (\mathbf{B}_I - \mathbf{B}_{II}) = 0. \tag{2.5}$$

- **Normal D**. The normal component of $\boldsymbol{D}$ is discontinuous at an interface due to the accumulation of a surface-charge density ρ_s:

$$\hat{\mathbf{n}} \cdot (\mathbf{D}_I - \mathbf{D}_{II}) = \rho_s. \tag{2.6}$$

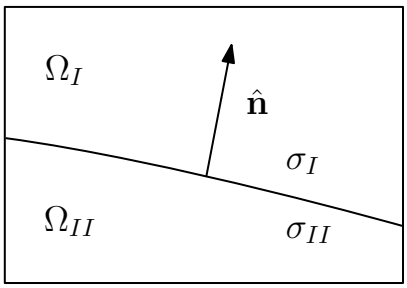

Figure 2.2: *Interior boundary separating domain Ω_I with conductivity σ_I from domain Ω_{II} with conductivity σ_{II}, where continuity conditions are imposed. The vector $\hat{\mathbf{n}}$ is the unitary normal vector to the boundary.*

- **Tangential E**. The tangential component of $\boldsymbol{E}$ is continuous across an interface:

$$\hat{\mathbf{n}} \times (\mathbf{E}_I - \mathbf{E}_{II}) = 0. \tag{2.7}$$

- **Tangential H**. The tangential component of $\boldsymbol{H}$ is continuous across an interface if there is no surface current:

$$\hat{\mathbf{n}} \times (\mathbf{H}_I - \mathbf{H}_{II}) = 0. \tag{2.8}$$

- **Current density J**. If displacement currents are neglected, the normal component of the electric current density $\boldsymbol{J}$ is continuous across an interface:

$$\hat{\mathbf{n}} \cdot (\mathbf{J}_I - \mathbf{J}_{II}) = 0. \tag{2.9}$$

It follows from this last condition together with (2.3c) in frequency-domain that in regions where σ is discontinuous, the normal component of $\boldsymbol{E}$ to the discontinuity will be also discontinuous. A comment on (2.6) is that in static equilibrium, the surface electric charge density ρ_s at the interface between two conductors may be different from zero despite the fact that the volume charge density ρ_v vanishes everywhere.

Particularizing for the 2.5-D CSEM problem, we consider a 2-D space and define a Cartesian xy–coordinate system with y vertically upwards and x horizontally right, the conductivity is invariant in the z–direction: $\sigma = \sigma(x,y)$ (Figure 2.1). Despite the 2-D conductivity distribution, the source terms $\boldsymbol{M}^s$ and $\boldsymbol{J}^s$ contain 3-D variations and consequently the EM fields are also 3-D and we have to solve the complete Maxwell's equations.

Following the 2.5-D approximation, equations (2.4) are Fourier transformed along the strike direction z onto the wavenumber-domain.

We define the 1-D Fourier transformation as:

$$\mathcal{F}\left[\mathbf{F}(x,y,z))\right](\kappa_z) = \hat{\mathbf{F}}(x,y,\kappa_z) = \int_{-\infty}^{+\infty} \mathbf{F}(x,y,z) e^{-i\kappa_z z} dz, \tag{2.10}$$

and the corresponding inverse transform as:

$$\mathcal{F}^{-1}\left[\hat{\mathbf{F}}(x,y,\kappa_z)\right](z) = \mathbf{F}(x,y,z) = \frac{1}{2\pi}\int_{-\infty}^{+\infty}\hat{\mathbf{F}}(x,y,\kappa_z)e^{i\kappa_z z}d\kappa_z, \tag{2.11}$$

where κ_z is the along-strike wavenumber.

We transform equations (2.4) with (2.10) and using:

$$\mathcal{F}\left[\frac{\partial\mathbf{F}(x,y,z)}{\partial z}\right](\kappa_z) = \int_{-\infty}^{+\infty}\frac{\partial\mathbf{F}(x,y,z)}{\partial z}e^{-i\kappa_z z}dz = i\kappa_z\hat{\mathbf{F}}(x,y,\kappa_z), \tag{2.12}$$

for the transformation of the derivatives of the fields with respect to the along-strike coordinate. After applying some algebra, we obtain a system of PDEs for the electric and magnetic along-strike field components $\hat{E}_z$ and $\hat{H}_z$ (Stoyer and Greenfield, 1976; Mitsuhata, 2000):

$$-\partial_x(\hat{y}\kappa_e^{-2}\partial_x\hat{E}_z) - \partial_y(\hat{y}\kappa_e^{-2}\partial_y\hat{E}_z) + i\kappa_z\partial_x(\kappa_e^{-2}\partial_y\hat{H}_z) - i\kappa_z\partial_y(\kappa_e^{-2}\partial_x\hat{H}_z) + \hat{y}\hat{E}_z = \hat{f}_1, \tag{2.13a}$$
$$-\partial_x(\hat{z}\kappa_e^{-2}\partial_x\hat{H}_z) - \partial_y(\hat{z}\kappa_e^{-2}\partial_y\hat{H}_z) - i\kappa_z\partial_x(\kappa_e^{-2}\partial_y\hat{E}_z) + i\kappa_z\partial_y(\kappa_e^{-2}\partial_x\hat{E}_z) + \hat{z}\hat{H}_z = \hat{f}_2, \tag{2.13b}$$

where we introduce the impedivity $\hat{z} = i\mu_0\omega$ and the admittivity $\hat{y} = \sigma + i\epsilon_0\omega$ (Ward and Hohmann, 1988), with the admittivity approximated as: $\hat{y} \approx \sigma$, because of the quasi-static assumption; κ_e^2 is defined as $\kappa_e^2 = \kappa_z^2 + \hat{z}\hat{y}$ (Hohmann, 1988) and $\hat{f}_1$ and $\hat{f}_2$ are the source terms which in the most general case include electric and magnetic sources oriented in the three space directions and can be expressed as:

$$\hat{f}_1 = -\hat{J}_z^s + i\kappa_z\partial_x(\kappa_e^{-2}\hat{J}_x^s) + i\kappa_z\partial_y(\kappa_e^{-2}\hat{J}_y^s) - \partial_x(\hat{z}\hat{y}\kappa_e^{-2}\hat{M}_y^s) + \partial_y(\hat{z}\hat{y}\kappa_e^{-2}\hat{M}_x^s), \tag{2.14a}$$
$$\hat{f}_2 = -\hat{z}\hat{M}_z^s + i\kappa_z\partial_x(\hat{z}\kappa_e^{-2}\hat{M}_x^s) + i\kappa_z\partial_y(\hat{z}\kappa_e^{-2}\hat{M}_y^s) + \partial_x(\hat{z}\kappa_e^{-2}\hat{J}_y^s) - \partial_y(\hat{z}\kappa_e^{-2}\hat{J}_x^s). \tag{2.14b}$$

Equations (2.14) can be written in a more compact form (Key and Ovall, 2011) and introducing Dirichlet boundary conditions in the outer boundary yields:

$$-\nabla\cdot(\hat{y}\kappa_e^{-2}\nabla\hat{E}_z) - i\kappa_z\nabla\cdot(\kappa_e^{-2}\mathbf{R}\nabla\hat{H}_z) + \hat{y}\hat{E}_z = \hat{f}_1 \tag{2.15a}$$
$$-\nabla\cdot(\hat{z}\kappa_e^{-2}\nabla\hat{H}_z) + i\kappa_z\nabla\cdot(\kappa_e^{-2}\mathbf{R}\nabla\hat{E}_z) + \hat{z}\hat{H}_z = \hat{f}_2 \text{ in } \Omega \tag{2.15b}$$
$$\hat{E}_z, \hat{H}_z = 0 \text{ on } \partial\Omega \tag{2.15c}$$

with

$$\hat{f}_1 = -\hat{J}_z^s + i\kappa_z\nabla\cdot(\kappa_e^{-2}\hat{\mathbf{J}}_t^s) + \nabla\cdot(\hat{z}\hat{y}\kappa_e^{-2}\mathbf{R}\hat{\mathbf{M}}_t^s), \tag{2.16a}$$
$$\hat{f}_2 = -\hat{z}\hat{M}_z^s + i\kappa_z\nabla\cdot(\hat{z}\kappa_e^{-2}\hat{\mathbf{M}}_t^s) - \nabla\cdot(\hat{z}\kappa_e^{-2}\mathbf{R}\hat{\mathbf{J}}_t^s), \tag{2.16b}$$

where the field variations are only in the $xy-$plane, $\nabla = (\partial_x, \partial_y)$, and $\Omega \subset \mathbb{R}^2$ is the bounded computational domain with outer boundary $\partial\Omega$. The vectors $\hat{\mathbf{J}}_t^s$ and $\hat{\mathbf{M}}_t^s$ are the source currents transverse to z, i.e. $\hat{\mathbf{J}}_t^s = (\hat{J}_x^s, \hat{J}_y^s)$ and $\hat{\mathbf{M}}_t^s = (\hat{M}_x^s, \hat{M}_y^s)$; and $\boldsymbol{R}$ is a rotation matrix for a rotation of $\pi/2$:

$$\mathbf{R} = \begin{pmatrix} 0 & -1 \\ 1 & 0 \end{pmatrix}. \tag{2.17}$$

With the introduction of the domain Ω and the enforcement of boundary conditions on $\partial\Omega$ the real physical problem naturally posed on an infinite domain is approximated to a problem restricted on an artificial finite domain, which can be solved numerically. The quality of this approximation depends on how good the external boundary conditions approximate the solution in infinity. The physical justification for Dirichlet boundary conditions is that the EM fields decay away from the transmitter source, such that at a sufficient distance satisfy (2.15c) sufficiently well. However for this to be true, Ω must be chosen sufficiently large that the approximation due to the inexact boundary condition posed on $\partial\Omega$ is not larger than the discretization error. Besides, the domain Ω is partitioned in non-overlapping subdomains Ω_i, $\Omega = \bigcup_i \Omega_i$, such that within each subdomain the constitutive parameters and source terms are continuous functions of space. The discontinuities of the fields coincide with interfaces between subdomains, where continuity conditions are imposed.

Equations (2.15) together with continuity conditions of the tangential field components in the interior boundaries, define the 2.5-D frequency-domain CSEM BVP in its continuous form.

The two PDEs (2.15a) and (2.15b) for $\hat{E}_z$ and $\hat{H}_z$ are coupled through the middle terms on the left-hand-side (LHS) and are proportional to κ_z. Therefore, these equations must be solved simultaneously for $\hat{E}_z$ and $\hat{H}_z$. Once the system (2.15) is solved, the other EM field components are obtained from space derivatives of $\hat{E}_z$ and $\hat{H}_z$ using:

$$\hat{E}_x = \kappa_e^{-2}\left(-i\kappa_z\partial_x\hat{E}_z + \hat{z}\partial_y\hat{H}_z - \hat{z}\hat{J}_x^s + i\kappa_z\hat{z}\hat{M}_y^s\right), \tag{2.18a}$$

$$\hat{E}_y = \kappa_e^{-2}\left(-i\kappa_z\partial_y\hat{E}_z - \hat{z}\partial_x\hat{H}_z - \hat{z}\hat{J}_y^s - i\kappa_z\hat{z}\hat{M}_x^s\right), \tag{2.18b}$$

$$\hat{H}_x = \kappa_e^{-2}\left(-\hat{y}\partial_y\hat{E}_z - i\kappa_z\partial_x\hat{H}_z - i\kappa_z\hat{J}_y^s - \hat{z}\hat{y}\hat{M}_x^s\right), \tag{2.18c}$$

$$\hat{H}_y = \kappa_e^{-2}\left(\hat{y}\partial_x\hat{E}_z - i\kappa_z\partial_y\hat{H}_z + i\kappa_z\hat{J}_x^s - \hat{z}\hat{y}\hat{M}_y^s\right), \tag{2.18d}$$

or in more compact form (Key and Ovall, 2011):

$$\hat{\mathbf{E}}_t = \kappa_e^{-2}\left(-i\kappa_z\nabla\hat{E}_z - \hat{z}\mathbf{R}\nabla\hat{H}_z - \hat{z}\hat{\mathbf{J}}_t^s - i\kappa_z\hat{z}\mathbf{R}\hat{\mathbf{M}}_t^s\right), \tag{2.19a}$$

$$\hat{\mathbf{H}}_t = \kappa_e^{-2}\left(\hat{y}\mathbf{R}\nabla\hat{E}_z - i\kappa_z\nabla\hat{H}_z + i\kappa_z\mathbf{R}\hat{\mathbf{J}}_t^s - \hat{z}\hat{y}\hat{\mathbf{M}}_t^s\right), \tag{2.19b}$$

with $\hat{\mathbf{E}}_t = (\hat{E}_x, \hat{E}_y)$ and $\hat{\mathbf{H}}_t = (\hat{H}_x, \hat{H}_y)$ and we assumed the more general situation with electric and magnetic sources oriented in the three space directions.

In the limit, when κ_z is 0, the coupling terms in (2.15) disappear, and the resulting PDEs separate into two independent modes, transverse electric (TE) and transverse magnetic (TM), as in MT or for an infinitely long wire source (Unsworth et al., 1993; Everett and Edwards, 1992):

$$-\nabla\cdot(\hat{z}^{-1}\nabla\hat{E}_z)+\hat{y}\hat{E}_z=-\hat{J}_z^s-\nabla\cdot(\mathbf{R}\hat{\mathbf{M}}_t^s) \tag{2.20a}$$

$$-\nabla\cdot(\hat{y}^{-1}\nabla\hat{H}_z)+\hat{z}\hat{H}_z=-\hat{z}\hat{M}_z^s-\nabla\cdot(\hat{y}^{-1}\mathbf{R}\hat{\mathbf{J}}_t^s). \tag{2.20b}$$

The TE mode is defined by equation (2.20a) and the electric field is only in the along-strike direction, while the magnetic field is in the $xy-$plane. The TM is defined by equation (2.20b) and, in this case, it is the magnetic field that has only the along-strike direction component, while the electric field is in the $xy-$plane.

To compute the response for a finite source ($\kappa_z \neq 0$), the coupled equations (2.15a) and (2.15b) must be considered for a range of κ_z values to represent the fields in the 3-D space. Then (2.11) is used to transform the fields back to the spatial domain.

It is important to note that equations (2.15) are formulated in terms of the transformed total $\boldsymbol{E}$ and $\boldsymbol{H}$ fields. The same formulation has been used by e.g. Stoyer and Greenfield (1976); Mitsuhata (2000); Key and Ovall (2011). Nevertheless, equivalent formulations have appeared in the literature for 2.5-D CSEM modeling applying the primary (background)/secondary (scattered) field approach to the $\boldsymbol{E}$ and $\boldsymbol{H}$ equations (e.g. Unsworth et al., 1993; Li and Key, 2007); and formulations for only one of the EM secondary fields ($\boldsymbol{E}$ or $\boldsymbol{H}$) within the $xy\kappa_z$ domain vector Helmholtz equation (e.g. Streich et al., 2011). We chose the total field formulation because although source terms are singular and difficult to model numerically it is more suitable for complex structures. On the other hand, comparing the $\boldsymbol{E}$ - $\boldsymbol{H}$ formulation (equations 2.15) with the $\boldsymbol{E}$ or $\boldsymbol{H}$ formulation (Helmholtz equations), the $\boldsymbol{E}$ - $\boldsymbol{H}$ approach is advantageous, because the number of unknowns is reduced from 3 to 2 and because the along-strike field components are continuous in the interfaces.

2.2.2 Harmonic sources

There is a variety of EM sources used in CSEM methods. In land-based surveys, magnetic loops or long horizontal wires are grounded, and in marine surveys, they are deployed at the seafloor or towed through the water. In both cases there is also the possibility to use vertical electrical sources. Commonly, the sources are approximated as point electric and magnetic dipoles, assuming a sufficiently large distance between source and receiver. When this approximation is not valid the source is approximated as a line of point dipoles and their response is calculated independently and after integrated.

In the following we give the equations for electric and magnetic point dipoles oriented in any of the three space directions and we derive their form after applying the Fourier

transform in the strike-parallel direction.

Harmonic electric dipole

The electric dipole is a straight conducting filament of length Δs carrying a current I. The dipole is grounded at both ends to the surroundings conductors. At a sufficient distance from the source the electric dipole can be modeled as an electric point dipole. If point sources, such as an electric or magnetic dipole, are to be modeled, the source term is not a classical function any more but a distribution, the Dirac delta distribution δ.

The current density in a x–directed electric dipole (a small current element of length Δs) at the origin can be represented by (Ward and Hohmann, 1988):

$$J_x^s = I\Delta s\left[\frac{u\,(x+\Delta s/2)-u\,(x-\Delta s/2)}{\Delta s}\right]\delta(y)\delta(z), \tag{2.21}$$

where $u(x \pm \Delta s/2)$ is the Heaviside step function.

Letting $\Delta s \to ds$:

$$J_x^s = Ids\delta(x)\delta(y)\delta(z), \tag{2.22}$$

using that the derivative of the step function is the delta distribution, $\frac{du}{dx} = \delta(x)$. This result applies to a current density in any given direction, so in general:

$$\mathbf{J}^s = p\delta(x-x_0)\delta(y-y_0)\delta(z-z_0)\frac{\mathbf{r}}{|\mathbf{r}|}, \tag{2.23}$$

where p is the dipole moment:

$$p = Ids \quad [A\cdot m]. \tag{2.24}$$

Transforming (2.23) to the κ_z–wavenumber domain reads:

$$\hat{\mathbf{J}}^s = \int_{-\infty}^{+\infty} p\delta(x-x_0)\delta(y-y_0)\delta(z-z_0)e^{-i\kappa_z(z-z_0)}dz\frac{\mathbf{r}}{|\mathbf{r}|} = p\delta(x-x_0)\delta(y-y_0)e^{-i\kappa_z z_0}\frac{\mathbf{r}}{|\mathbf{r}|}, \tag{2.25}$$

where we have used the Dirac delta property $\mathcal{F}_z[\delta(z-z_0)](\kappa_z) = e^{-i\kappa_z z_0}$.

An horizontal electric dipole (HED) will generate a $\mathbf{J}_t^s$ current in the xz–plane, thus it will be decomposed in a combination of J_x^s and J_z^s.

In the case in which there is only a x–directed HED source $\mathbf{J}_t^s = (J_x^s, 0)$, equations (2.16) will reduce to:

$$\hat{f}_1 = i\kappa_z\nabla\cdot(\kappa_e^{-2}\hat{\mathbf{J}}_t^s), \tag{2.26a}$$

$$\hat{f}_2 = -\nabla\cdot(\hat{z}\kappa_e^{-2}\mathbf{R}\hat{\mathbf{J}}_t^s), \tag{2.26b}$$

and equations (2.19) to:

$$\hat{\mathbf{E}}_t = \kappa_e^{-2}\left(-i\kappa_z\nabla\hat{E}_z - \hat{z}\mathbf{R}\nabla\hat{H}_z - \hat{z}\hat{\mathbf{J}}_t^s\right), \tag{2.27a}$$

$$\hat{\mathbf{H}}_t = \kappa_e^{-2}\left(\hat{y}\mathbf{R}\nabla\hat{E}_z - i\kappa_z\nabla\hat{H}_z + i\kappa_z\mathbf{R}\hat{\mathbf{J}}_t^s\right). \tag{2.27b}$$

A z–directed HED source generates a J_z^s current and equations (2.16) reduce to:

$$\hat{f}_1 = -\hat{J}_z^s, \tag{2.28a}$$

$$\hat{f}_2 = 0, \tag{2.28b}$$

and equations (2.19) to:

$$\hat{\mathbf{E}}_t = \kappa_e^{-2}\left(-i\kappa_z\nabla\hat{E}_z - \hat{z}\mathbf{R}\nabla\hat{H}_z\right), \tag{2.29a}$$

$$\hat{\mathbf{H}}_t = \kappa_e^{-2}\left(\hat{y}\mathbf{R}\nabla\hat{E}_z - i\kappa_z\nabla\hat{H}_z\right). \tag{2.29b}$$

A vertical electric dipole (VED) generates a J_y^s current and equations (2.16) and (2.19) will read as (2.26) and (2.27), respectively, with $\hat{\mathbf{J}}_t^s = (0, \hat{J}_y^s)$.

Harmonic magnetic dipole

A small loop of current I at the origin and in the xy–plane can be represented by an infinitesimal magnetic dipole with moment (Ward and Hohmann, 1988):

$$m = IS, \tag{2.30}$$

where S is the area of the loop. The magnetization vector is given by:

$$M_z^s = m\delta(x)\delta(y)\delta(z). \tag{2.31}$$

The magnetization vector in a general direction will read:

$$\mathbf{M}^s = m\delta(x-x_0)\delta(y-y_0)\delta(z-z_0)\frac{\mathbf{r}}{|\mathbf{r}|}. \tag{2.32}$$

Transforming it to the κ_z–wavenumber domain yields:

$$\hat{\mathbf{M}}^s = \int_{-\infty}^{+\infty} m\delta(x-x_0)\delta(y-y_0)\delta(z-z_0)e^{-i\kappa_z(z-z_0)}dz\frac{\mathbf{r}}{|\mathbf{r}|} = m\delta(x-x_0)\delta(y-y_0)e^{-i\kappa_z z_0}\frac{\mathbf{r}}{|\mathbf{r}|}, \tag{2.33}$$

where, again, we have used the Dirac delta property $\mathcal{F}_z[\delta(z-z_0)](\kappa_z) = e^{-i\kappa_z z_0}$.

An horizontal magnetic dipole (HMD) will be generated from a loop in the xy–plane, M_z^s, or a yz–plane, M_x^s.

For M_x^s magnetization $\mathbf{M}_t^s = (M_x^s, 0)$, equations (2.16) reduce to:

$$\hat{f}_1 = +\nabla\cdot(\hat{z}\hat{y}\kappa_e^{-2}\mathbf{R}\hat{\mathbf{M}}_t^s), \tag{2.34a}$$

$$\hat{f}_2 = +i\kappa_z\nabla\cdot(\hat{z}\kappa_e^{-2}\hat{\mathbf{M}}_t^s), \tag{2.34b}$$

and equations (2.19) to:

$$\hat{\mathbf{E}}_t = \kappa_e^{-2}\left(-i\kappa_z\nabla\hat{E}_z - \hat{z}\mathbf{R}\nabla\hat{H}_z - i\kappa_z\hat{z}\mathbf{R}\hat{\mathbf{M}}_t^s\right), \tag{2.35a}$$

$$\hat{\mathbf{H}}_t = \kappa_e^{-2}\left(\hat{y}\mathbf{R}\nabla\hat{E}_z - i\kappa_z\nabla\hat{H}_z - \hat{z}\hat{y}\hat{\mathbf{M}}_t^s\right). \tag{2.35b}$$

For a M_z^s magnetization the sources terms are:

$$\hat{f}_1 = 0, \tag{2.36a}$$

$$\hat{f}_2 = -\hat{z}\hat{M}_z^s, \tag{2.36b}$$

and the transverse field components:

$$\hat{\mathbf{E}}_t = \kappa_e^{-2}\left(-i\kappa_z\nabla\hat{E}_z - \hat{z}\mathbf{R}\nabla\hat{H}_z\right), \tag{2.37a}$$

$$\hat{\mathbf{H}}_t = \kappa_e^{-2}\left(\hat{y}\mathbf{R}\nabla\hat{E}_z - i\kappa_z\nabla\hat{H}_z\right). \tag{2.37b}$$

A vertical magnetic dipole (VMD) will have a M_y^s magnetization and equations (2.16) and (2.19) will reduce to (2.34) and (2.35) respectively with $\hat{\mathbf{M}}_t^s = (0, \hat{M}_y^s)$.

2.3 The Finite element method for 2.5-D CSEM

The FE method is a numerical technique to calculate an approximate solution to a BVP. The basis of the method consists of transforming the problem to a weak form or variational problem that involves an integration of the governing differential equations over the problem domain, in contrast to other methods, e.g. FD, which approximate the PDEs directly. Using the FE method, the model domain is partitioned into a number of subdomains called finite elements and the solution of the PDEs is approximated by piecewise polynomial functions in each element in the overall domain, compared to FD where the solution is approximated within a set of points. The variational problem is spatially discretized, and the integration in the whole domain, translates into a sum of integrals on each finite element, reducing the BVP to a system of linear equations. Moreover, a measure of the quality of the numerical solution is obtained that quantifies the discretization and solution errors, and can be iteratively improved up to a desired accuracy.

In this section we will apply the Galerkin method (a type of weighted residual method) to derive the FE linear system of equations approximating the 2.5-D CSEM BVP (equation 2.15 and continuity conditions). Equivalently, variational theory could be used. For more details on theoretical aspects of FE methods for Maxwell's equations we address the reader to e.g. Silvester and Ferrari (1996) and Monk (2003).

2.3.1 The weak form

The weak form or variational problem is the basis for the method of FE. The equivalence of the weak and strong formulations (differential equations) is a fundamental property of Euler-type second-order partial differential equations (Badea et al., 2001) and will not be discussed in this thesis. Only let us stress that the weak formulation relaxes smoothness and derivability conditions on $\hat{E}_z$ and $\hat{H}_z$.

In the previous section, we obtained second order governing PDEs for the 2.5-D CSEM problem, while the original Maxwell's equations are first order. The second order PDE requires the electric field to be differentiable twice while the original Maxwell system requires only the first derivative to be defined. In the weak formulation of the BVP governed by equations (2.15) only first order derivatives are required, as it will be shown later.

To construct the weak form, the equality in equations (2.15) is only required in an inner product sense, that is, after applying the inner product to equation (2.15) with a test function v, the equality needs to be preserved for every possible choice of v.

We consider two complex valued scalar functions u and v to be square-integrable, belong to $L^2(\Omega)$, with the inner product defined as:

$$(u,v)_{L_2(\Omega)} = \int_\Omega \bar{v} u \, d^2r, \tag{2.38}$$

where $\bar{v}$ denotes the complex conjugate of v. Then, equations (2.15) read in the weak sense as an $L^2(\Omega)$ square-integrability:

$$\int_\Omega \bar{v}_1 \left(-\nabla\cdot(\hat{y}\kappa_e^{-2}\nabla\hat{E}_z) - i\kappa_z\nabla\cdot(\kappa_e^{-2}\mathbf{R}\nabla\hat{H}_z) + \hat{y}\hat{E}_z\right) d^2r = \int_\Omega \bar{v}_1 \hat{f}_1 \, d^2r, \tag{2.39a}$$

$$\int_\Omega \bar{v}_2 \left(-\nabla\cdot(\hat{z}\kappa_e^{-2}\nabla\hat{H}_z) + i\kappa_z\nabla\cdot(\kappa_e^{-2}\mathbf{R}\nabla\hat{E}_z) + \hat{z}\hat{H}_z\right) d^2r = \int_\Omega \bar{v}_2 \hat{f}_2 \, d^2r. \tag{2.39b}$$

From the divergence theorem:

$$\int_\Omega \nabla\cdot\mathbf{A}\, d^2r = \oint_{\partial\Omega} \mathbf{A}\cdot\hat{\mathbf{n}}\, dr, \tag{2.40}$$

where $\partial\Omega$ is a closed contour enclosing the surface $\Omega \subset \mathbb{R}^2$ and $\hat{\mathbf{n}}$ is a unit vector normal to the closed contour $\partial\Omega$; and using the vector formula:

$$U(\nabla\cdot\mathbf{A}) = -(\nabla U)\cdot\mathbf{A} + \nabla\cdot(U\mathbf{A}), \tag{2.41}$$

we obtain the following result:

$$\int_\Omega \bar{v}\nabla\cdot(p\nabla u)d^2r = -\int_\Omega \nabla\bar{v}\cdot(p\nabla u)d^2r + \oint_{\partial\Omega} \bar{v}(p\nabla u)\cdot\hat{\mathbf{n}}\, dr, \tag{2.42}$$

where $p = p(x,y) > 0$.

Using (2.42), the integrals in equations (2.39) can be transformed to:

$$\begin{aligned}
&\int_\Omega \Big(\nabla\bar{v}_1\cdot(\hat{y}\kappa_e^{-2}\nabla\hat{E}_z)+\nabla\bar{v}_1\cdot(i\kappa_z\kappa_e^{-2}\mathbf{R}\nabla\hat{H}_z)+\bar{v}_1\hat{y}\hat{E}_z\Big)d^2r\\
&\quad-\int_\Omega\Big(-\bar{v}_1\hat{J}_z^s-\nabla\bar{v}_1\cdot(i\kappa_z\kappa_e^{-2}\hat{\mathbf{J}}_t^s)-\nabla\bar{v}_1\cdot(\hat{z}\hat{y}\kappa_e^{-2}\mathbf{R}\hat{\mathbf{M}}_t^s)\Big)d^2r \qquad (2.43a)\\
&\quad+\oint_{\partial\Omega}\bar{v}_1\kappa_e^{-2}\Big(-\hat{y}\nabla\hat{E}_z-i\kappa_z\mathbf{R}\nabla\hat{H}_z-i\kappa_z\hat{\mathbf{J}}_t^s-\hat{z}\hat{y}\mathbf{R}\hat{\mathbf{M}}_t^s\Big)\cdot\hat{\mathbf{n}}dr=0,\\
&\int_\Omega\Big(\nabla\bar{v}_2\cdot(\hat{z}\kappa_e^{-2}\nabla\hat{H}_z)-\nabla\bar{v}_2\cdot(i\kappa_z\kappa_e^{-2}\mathbf{R}\nabla\hat{E}_z)+\bar{v}_2\hat{z}\hat{H}_z\Big)d^2r\\
&\quad-\int_\Omega\Big(-\bar{v}_2\hat{z}\hat{M}_z^s-\nabla\bar{v}_2\cdot(i\kappa_z\hat{z}\kappa_e^{-2}\hat{\mathbf{M}}_t^s)+\nabla\bar{v}_2\cdot(\hat{z}\kappa_e^{-2}\mathbf{R}\hat{\mathbf{J}}_t^s)\Big)d^2r \qquad (2.43b)\\
&\quad+\oint_{\partial\Omega}\bar{v}_2\kappa_e^{-2}\Big(-\hat{z}\nabla\hat{H}_z+i\kappa_z\mathbf{R}\nabla\hat{E}_z-i\kappa_z\hat{z}\hat{\mathbf{M}}_t^s+\hat{z}\mathbf{R}\hat{\mathbf{J}}_t^s\Big)\cdot\hat{\mathbf{n}}dr=0,
\end{aligned}$$

where we have used (2.16a) and (2.16b) for $\hat{f}_1$ and $\hat{f}_2$ respectively.

At this point, we need to define the space where $\hat{E}_z$ and $\hat{H}_z$, and the test functions v_1 and v_2 are well-defined in equations (2.43). We require the Sobolev space of complex valued once-differentiable functions on Ω, $H^1(\Omega)$, such that both the functions and its first-order weak derivatives are square-integrable (belong to L^2, see equation 2.38).

The Sobolev space H^1 has the inner product and norm:

$$(u,v)_1=(u,v)+(\nabla u,\nabla v)=\int_\Omega(\hat{v}u+\nabla\hat{v}\cdot\nabla u)d\mathbf{r}, \qquad (2.44)$$

$$\|u\|_1=\left[\int_\Omega(u^2+(\nabla u)^2)d\mathbf{r}\right]^{1/2}, \qquad (2.45)$$

where $\hat{v}$ is the complex conjugate of v. For a further discussion on Sobolev spaces, see Monk (2003).

On the other hand, focusing now only on the boundary integral terms in (2.43), multiplying them by the identity matrix $\mathbf{R}^T\mathbf{R}$ and using the relation $\mathbf{RR}=-\mathbb{I}$, we obtain:

$$\oint_{\partial\Omega}\bar{v}_1\kappa_e^{-2}\mathbf{R}^T\Big(-\hat{y}\mathbf{R}\nabla\hat{E}_z+i\kappa_z\nabla\hat{H}_z-i\kappa_z\mathbf{R}\hat{\mathbf{J}}_t^s+\hat{z}\hat{y}\hat{\mathbf{M}}_t^s\Big)\cdot\hat{\mathbf{n}}dr, \qquad (2.46a)$$

$$\oint_{\partial\Omega}\bar{v}_2\kappa_e^{-2}\mathbf{R}^T\Big(-\hat{z}\mathbf{R}\nabla\hat{H}_z-i\kappa_z\nabla\hat{E}_z-i\kappa_z\hat{z}\mathbf{R}\hat{\mathbf{M}}_t^s-\hat{z}\hat{\mathbf{J}}_t^s\Big)\cdot\hat{\mathbf{n}}dr, \qquad (2.46b)$$

where by comparing with equations (2.19), the transverse components $\hat{\mathbf{E}}_t$ and $\hat{\mathbf{H}}_t$ are exposed. Substituting them in (2.46), together with the relation $-\mathbf{R}^T=\mathbf{R}$, we obtain:

$$\oint_{\partial\Omega}\bar{v}_1\mathbf{R}\hat{\mathbf{H}}_t\cdot\hat{\mathbf{n}}dr, \qquad (2.47a)$$

$$-\oint_{\partial\Omega}\bar{v}_2\mathbf{R}\hat{\mathbf{E}}_t\cdot\hat{\mathbf{n}}dr. \qquad (2.47b)$$

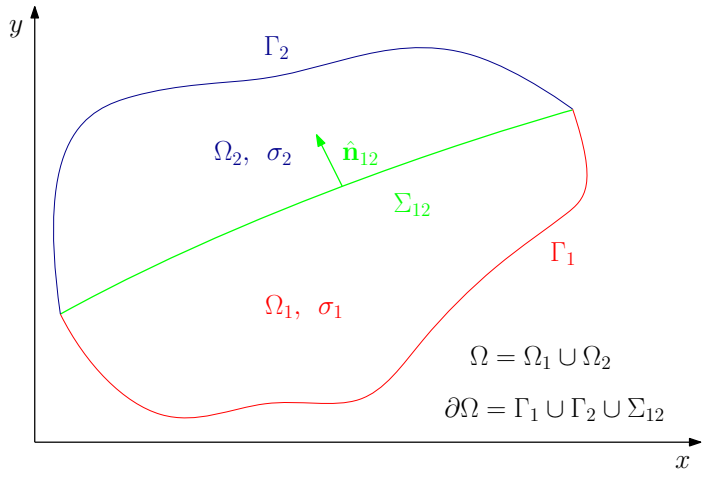

Figure 2.3: *Partitioning of domain boundaries. The domain Ω splits in two subdomains, Ω_1 and Ω_2 characterized by the conductivities σ_1 and σ_2. Besides, the boundary $\partial\Omega$ of Ω splits in two boundaries resulting from its intersection with each subdomain outer boundary, Γ_1 and Γ_2. As a consequence of the partitioning, an additional boundary, Σ_{ij}, between subdomains Ω_1 and Ω_2 must be considered.*

As explained in the last section, the PDEs (2.15) are only defined on subdomains Ω_i and $\Omega = \bigcup_{i=1}^{n_s} \Omega_i$. Then, integrations in (2.47) are split into the sum over all n_s subdomains. The boundary of Ω_i is composed of an outer boundary part $\Gamma_i = \partial\Omega \cap \partial\Omega_i$ and an inner boundary part $\partial\Omega_i \setminus \Gamma_i = \bigcup_{i\neq j} \Sigma_{ij}$ which is the union of all interfaces with adjacent subdomains Ω_j (Figure 2.3).

With this in mind, equations (2.47) read:

$$\oint_{\partial\Omega} \bar{v}_1 \mathbf{R}\hat{\mathbf{H}}_t \cdot \hat{\mathbf{n}} dr = \sum_{i=1}^{n_s} \left(\oint_{\partial\Omega_i \setminus \Gamma_i} \bar{v}_1 \mathbf{R}\hat{\mathbf{H}}_t \cdot \hat{\mathbf{n}} dr + \oint_{\Gamma_i} \bar{v}_1 \mathbf{R}\hat{\mathbf{H}}_t \cdot \hat{\mathbf{n}} dr \right), \tag{2.48a}$$

$$-\oint_{\partial\Omega} \bar{v}_2 \mathbf{R}\hat{\mathbf{E}}_t \cdot \hat{\mathbf{n}} dr = -\sum_{i=1}^{n_s} \left(\oint_{\partial\Omega_i \setminus \Gamma_i} \bar{v}_2 \mathbf{R}\hat{\mathbf{E}}_t \cdot \hat{\mathbf{n}} dr + \oint_{\Gamma_i} \bar{v}_2 \mathbf{R}\hat{\mathbf{E}}_t \cdot \hat{\mathbf{n}} dr \right). \tag{2.48b}$$

Considering the inner boundaries and the normal vector $\hat{\mathbf{n}}$ on Σ_{ij} pointing from subdomain i to subdomain j yields:

$$\sum_{i=1}^{n_s} \oint_{\partial\Omega_i \setminus \Gamma_i} \bar{v}_1 \mathbf{R}\hat{\mathbf{H}}_t \cdot \hat{\mathbf{n}} dr = \sum_{\substack{i,j=1 \\ i\neq j}}^{n_s} \int_{\Sigma_{ij}} \bar{v}_1 \mathbf{R}\hat{\mathbf{H}}_t \cdot \hat{\mathbf{n}} dr = \sum_{\substack{i,j=1 \\ i<j}}^{n_s} \int_{\Sigma_{ij}} \bar{v}_1 \left[\mathbf{R}\hat{\mathbf{H}}_t \cdot \hat{\mathbf{n}} \right]_\Sigma dr = 0, \tag{2.49a}$$

$$-\sum_{i=1}^{n_s} \oint_{\partial\Omega_i \setminus \Gamma_i} \bar{v}_2 \mathbf{R}\hat{\mathbf{E}}_t \cdot \hat{\mathbf{n}} dr = -\sum_{\substack{i,j=1 \\ i\neq j}}^{n_s} \int_{\Sigma_{ij}} \bar{v}_2 \mathbf{R}\hat{\mathbf{E}}_t \cdot \hat{\mathbf{n}} dr = -\sum_{\substack{i,j=1 \\ i<j}}^{n_s} \int_{\Sigma_{ij}} \bar{v}_2 \left[\mathbf{R}\hat{\mathbf{E}}_t \cdot \hat{\mathbf{n}} \right]_\Sigma dr = 0, \tag{2.49b}$$

where we have used that the tangential components of $\boldsymbol{E}$ and $\boldsymbol{H}$ are continuous across an interface (equations 2.7 and 2.8) also known as natural boundary conditions. For the outer

boundary integrals, the Dirichlet boundary condition (equation 2.15c) will be enforced explicitly as an essential boundary condition. That means that the test functions are chosen such that they are null in Γ_i and the corresponding boundary integrals vanish, thus the space of the dependent variables and test functions is redefined to a subspace $H_0^1(\Omega) \subset H^1(\Omega)$ of functions that vanish on the boundary.

Finally, the BVP problem can be restated as the variational problem:

Find $\hat{E}_z, \hat{H}_z \in \mathcal{H} = [H_0^1(\Omega)]^2$ *such that*

$$\int_\Omega \left(\nabla \bar{v}_1 \cdot (\hat{y}\kappa_e^{-2}\nabla \hat{E}_z) + \nabla \bar{v}_1 \cdot (i\kappa_z \kappa_e^{-2}\mathbf{R}\nabla \hat{H}_z) + \bar{v}_1 \hat{y}\hat{E}_z\right) d^2r = \int_\Omega \bar{v}_1 \hat{f}_1 d^2r \tag{2.50a}$$

$$\int_\Omega \left(\nabla \bar{v}_2 \cdot (\hat{z}\kappa_e^{-2}\nabla \hat{H}_z) - \nabla \bar{v}_2 \cdot (i\kappa_z \kappa_e^{-2}\mathbf{R}\nabla \hat{E}_z) + \bar{v}_2 \hat{z}\hat{H}_z\right) d^2r = \int_\Omega \bar{v}_2 \hat{f}_2 d^2r \tag{2.50b}$$

for all $v_1, v_2 \in \mathcal{H}$ *and with*

$$\int_\Omega \bar{v}_1 \hat{f}_1 d^2r = \int_\Omega \left(-\bar{v}_1 \hat{f}_z^s - \nabla \bar{v}_1 \cdot (i\kappa_z \kappa_e^{-2}\hat{\mathbf{J}}_t^s) - \nabla \bar{v}_1 \cdot (\hat{z}\hat{y}\kappa_e^{-2}\mathbf{R}\hat{\mathbf{M}}_t^s)\right) d^2r \tag{2.50c}$$

$$\int_\Omega \bar{v}_2 \hat{f}_2 d^2r = \int_\Omega \left(-\bar{v}_2 \hat{z}\hat{M}_z^s - \nabla \bar{v}_2 \cdot (i\kappa_z \hat{z}\kappa_e^{-2}\hat{\mathbf{M}}_t^s) + \nabla \bar{v}_2 \cdot (\hat{z}\kappa_e^{-2}\mathbf{R}\hat{\mathbf{J}}_t^s)\right) d^2r. \tag{2.50d}$$

Here $\mathcal{H} = [H_0^1(\Omega)]^2$ is the space where the functions and its first order weak derivatives are square integrable in Ω and vanish in the outer boundary $\partial\Omega$.

It is necessary at this point to emphasize that boundary conditions have been absorbed into the function space and that integration by parts has eliminated second derivatives terms from the formulation, relaxing the smoothness requirements of $\hat{E}_z$ and $\hat{H}_z$ in (2.15), as already anticipated. It is also important to note, that in the derivation of the BVP weak form, (2.50), the inner product is taken in the whole domain Ω, but actually, as mentioned in the last section and in the analysis of boundary integrals, the PDEs are only defined on subdomains where the constitutive parameters are continuous functions of space. Thus, although not explicitly written for simplicity, the integrals in (2.50) split into the sum over all subdomains.

The significance of the weak formulation lies in the guarantee that considering a bilinear form $a(u,v)$ (as the LHS of 2.50a or of 2.50b) with exact solution $u \in \mathcal{H}$ and test function $v \in \mathcal{H}$, an approximate solution $u_h \in \mathcal{H}_h \subset \mathcal{H}$ is the closest possible solution to u in $\mathcal{H}_h$ when measured by the corresponding bilinear form and $v \in \mathcal{H}_h$. This guarantee is possible without explicit *a priori* knowledge of u. The reason is because choosing $v \in \mathcal{H}_h$, both $a(u,v) = (f,v)$ and $a(u_h,v) = (f,v)$ (with (f,v) the right-hand-side (RHS) of 2.50a or of 2.50b) hold true for all $v \in \mathcal{H}_h$ and their subtraction yields $a(u - u_h, v) = 0$ for all $v \in \mathcal{H}_h$.

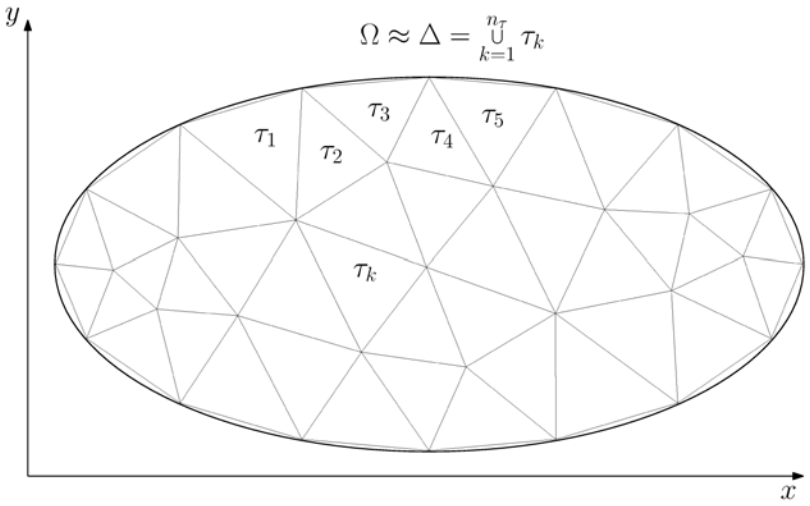

Figure 2.4: *Elemental decomposition of the model domain. The model domain Ω is divided into n_τ elements τ_k, triangles, forming a FE mesh Δ. The model domain Ω does not coincide exactly with the approximated domain Δ in the boundaries. The quality of the approximation can be improved, e.g. by mesh refinement.*

This means, the error between the approximate solution u_h and the exact solution u is orthogonal to the space $\mathcal{H}_h$ with respect to $a(\cdot,\cdot)$.

2.3.2 Spatial discretization using finite elements

In the variational problem (2.50), derived in the previous section, the function space $\mathcal{H}$ is infinite dimensional, but in numerical computation it is not possible to treat infinite dimensional function spaces. The fundamental step of the FE method is to approximate the infinite dimensional function spaces by finite dimensional subspaces $\mathcal{H}_h$ of piecewise polynomial functions, such that it is feasible to compute an approximate solution of the variational problem. In this section we apply the FE analysis to derive a system of linear equations to be solved computationally.

First, the model domain Ω is divided into n_τ simple geometrical elements τ, e.g. triangles (Figure 2.4),

$$\Omega \approx \Delta = \bigcup_{k=1}^{n_\tau} \tau_k. \tag{2.51}$$

If Ω consists of several subdomains the elemental decomposition has to respect the subdomain interfaces. The set of elements, Δ, is known as the FE mesh or grid. For our FE discretization we use a triangular mesh of non overlapping elements, $\bigcap_{k=1}^{n_\tau} \tau_k = \emptyset$. The model domain Ω does not generally need to exactly coincide with the discretized domain Δ, because of the error introduced when discretizing complex boundaries with triangles. However, the approximation can be accurate and in complex situations can be improved using unstructured grids and fine meshing.

The FE space, $\mathcal{P}^p(\Delta)$, can be constructed with the following constraints (Schwarzbach, 2009): (a) it is a subspace of $\mathcal{H}$, i.e. it satisfies the same continuity conditions, (b) its mem-

bers are piecewise polynomial (c) its basis functions have a compact support, i.e. its scope of influence is limited only to neighboring elements, and (d) it forms an exact sequence. We use a subscript h in members from $\mathcal{P}^p(\Delta)$ to indicate the dependency on some discretization parameter h. We define the FE space $\mathcal{P}^p(\Delta)$ of functions $u_h \in \mathcal{H} = [H_0^1]^2$, which are polynomials of degree p in each finite element, that is:

$$\mathcal{P}^p(\Delta) = \left\{ u_h \in \mathcal{H} = [H_0^1(\Omega)]^2 : u_h|_\tau \text{ polynomial of degree } p < \infty \right\}, \tag{2.52}$$

where $u_h|_\tau$ denotes the restriction of u_h onto element τ.

The approximated variable $u_h \in \mathcal{P}^p(\Delta)$ can be written as a linear combination of a finite number of basis functions:

$$u_h(\mathbf{r}) = \sum_{i=1}^{n_u} U_i \phi_i(\mathbf{r}), \tag{2.53}$$

for $\mathbf{r} \in \tau$ where $\{\phi_i\}_{i=1}^{n_u}$ is a basis of $\mathcal{P}^p(\Delta)$ and $n_u = \dim \mathcal{P}^p(\Delta)$. The basis function ϕ_i is associated with mesh entity indexed by i and the degrees of freedom (DOFs) are the linear coefficients U_i of the basis function expansion of u_h in $\mathcal{P}^p(\Delta)$ and fulfill:

$$U_i(\phi_j) = \delta_{ij}, \quad i, j = 1, \ldots, n_u, \tag{2.54}$$

where δ_{ij} is the Kronecker delta.

The field variables and test functions of the continuous BVP are chosen from the finite dimensional $\mathcal{P}^p \subset \mathcal{H}$ of piecewise polynomial functions. The approximation of the dependent variable functions, $\hat{E}_{z,h}$ and $\hat{H}_{z,h}$, are called trial functions.

Substituting them and the test functions approximations $v_{1,h}$ and $v_{2,h}$ in (2.50), the discrete variational problem reads:

Find $\hat{E}_{z,h}, \hat{H}_{z,h} \in \mathcal{H}_h$ such that

$$\int_\Delta \left(\nabla \bar{v}_{1,h} \cdot (\hat{y} \kappa_e^{-2} \nabla \hat{E}_{z,h}) + \nabla \bar{v}_{1,h} \cdot (i \kappa_z \kappa_e^{-2} \mathbf{R} \nabla \hat{H}_{z,h}) + \bar{v}_{1,h} \hat{y} \hat{E}_{z,h} \right) d^2 r = \int_\Delta \bar{v}_{1,h} \hat{f}_1 d^2 r \tag{2.55a}$$

$$\int_\Delta \left(\nabla \bar{v}_{2,h} \cdot (\hat{z} \kappa_e^{-2} \nabla \hat{H}_{z,h}) - \nabla \bar{v}_{2,h} \cdot (i \kappa_z \kappa_e^{-2} \mathbf{R} \nabla \hat{E}_{z,h}) + \bar{v}_{2,h} \hat{z} \hat{H}_{z,h} \right) d^2 r = \int_\Delta \bar{v}_{2,h} \hat{f}_2 d^2 r \tag{2.55b}$$

for all $v_{1,h}, v_{2,h} \in \mathcal{H}_h$,

where the finite dimensional space of trial and test functions, $\mathcal{H}_h$, is defined as

$$\mathcal{H}_h = \{ \mathbf{u}_h, \mathbf{v}_h \in \mathcal{P}^p(\Delta) : \mathbf{u}_h = 0, \mathbf{v}_h = 0 \text{ on } \partial\Delta \} \tag{2.56}$$

with $\mathbf{u}_h = (\hat{E}_{z,h}, \hat{H}_{z,h})$, and $\mathbf{v}_h = (v_{1,h}, v_{2,h})$.

The use of the same function space for test and trial functions is a characteristic of the Galerkin method.

As in (2.53), the trial functions are a linear combination of a set of basis functions $\{\phi_{u,i}\}_{i=1}^{n_u}$ from $\mathcal{H}_h$:

$$\hat{E}_{z,h}(x,y) = \sum_{i=1}^{n_E} \hat{E}_i \phi_{E,i}(x,y), \tag{2.57a}$$

$$\hat{H}_{z,h}(x,y) = \sum_{i=1}^{n_H} \hat{H}_i \phi_{H,i}(x,y). \tag{2.57b}$$

Following the Galerkin method, we choose the test function $\mathbf{v}$ to be a linear combination of the same n_u basis function used for $\hat{E}_{z,h}$ and $\hat{H}_{z,h}$:

$$v_{1,h}(x,y) = \sum_{i=1}^{n_E} \phi_{E,i}(x,y) \tag{2.58a}$$

$$v_{2,h}(x,y) = \sum_{i=1}^{n_H} \phi_{H,i}(x,y); \tag{2.58b}$$

and we also choose the same basis function for $\hat{E}_{z,h}$ and for $\hat{H}_{z,h}$, thus:

$$\phi_{E,i} = \phi_{H,i} \equiv \phi_i,$$
$$n_E = n_H \equiv n.$$

Replacing (2.58) and (2.57) in (2.55) gives a well-determined system of $2n$ linear equations with $2n$ unknowns:

$$\sum_{i=1}^{n}\sum_{j=1}^{n}\int_\Delta \left(\nabla\bar{\phi}_i \cdot \left(\hat{y}\kappa_e^{-2}\nabla(\hat{E}_j\phi_j)\right) + \nabla\bar{\phi}_i \cdot \left(i\kappa_z\kappa_e^{-2}\mathbf{R}\nabla(\hat{H}_j\phi_j)\right) + \bar{\phi}_i\hat{y}\hat{E}_j\phi_j\right)d^2r = \sum_{i=1}^{n}\sum_{j=1}^{n}\int_\Delta \bar{\phi}_i\hat{f}_1 d^2r, \tag{2.59a}$$

$$\sum_{i=1}^{n}\sum_{j=1}^{n}\int_\Delta \left(\nabla\bar{\phi}_i \cdot \left(\hat{z}\kappa_e^{-2}\nabla(\hat{H}_j\phi_j)\right) - \nabla\bar{\phi}_i \cdot \left(i\kappa_z\kappa_e^{-2}\mathbf{R}\nabla(\hat{E}_j\phi_j)\right) + \bar{\phi}_i\hat{z}\hat{H}_j\phi_j\right)d^2r = \sum_{i=1}^{n}\sum_{j=1}^{n}\int_\Delta \bar{\phi}_i\hat{f}_2 d^2r, \tag{2.59b}$$

which is a consequence of choosing the same basis for trial and test functions.

Written in matrix form:

$$\mathbf{AU} = \mathbf{F}, \tag{2.60}$$

where $\mathbf{A}$ is a $n \times n$ matrix with elements $\mathbf{A}_{ij}$, 2×2 matrices,

$$\mathbf{A}_{ij} = \begin{pmatrix} \int_\Delta \hat{y}\left(\kappa_e^{-2}\nabla\bar{\phi}_i \cdot \nabla\phi_j + \bar{\phi}_i\phi_j\right)d^2r & i\kappa_z \int_\Delta \kappa_e^{-2}\nabla\bar{\phi}_i \cdot \mathbf{R}\nabla\phi_j d^2r \\ -i\kappa_z \int_\Delta \kappa_e^{-2}\nabla\bar{\phi}_i \cdot \mathbf{R}\nabla\phi_j d^2r & \int_\Delta \hat{z}\left(\kappa_e^{-2}\nabla\bar{\phi}_i \cdot \nabla\phi_j + \bar{\phi}_i\phi_j\right)d^2r \end{pmatrix} \quad \text{for } i,j = 1,2,\dots n, \tag{2.61}$$

$\mathbf{U}$ is the vector of unknowns of dimension $n \times 1$ where elements $\mathbf{U}_j$ associated to mesh entity j read:

$$\mathbf{U}_j = \begin{pmatrix} \hat{E}_j \\ \hat{H}_j \end{pmatrix}, \quad \text{for } j = 1,2,\dots n, \tag{2.62}$$

and finally, $\mathbf{F}$ is a $n \times 1$ vector, with vector elements:

$$\mathbf{F}_i = \begin{pmatrix} \int_\Delta \bar{\phi}_i \hat{f}_1 d^2r \\ \int_\Delta \bar{\phi}_i \hat{f}_2 d^2r \end{pmatrix}, \quad \text{for } i = 1,2,\dots n. \tag{2.63}$$

In the linear system (2.60) we have not specified the shape of the piecewise polynomials functions. A variety of piecewise polynomials basis functions have been studied and applied to different problems; below we describe the Lagrange shape functions which are appropriate for our problem. With the use of these functions we derive an elementwise system of equations which is more appropriate for a computer implementation.

2.3.3 Lagrange shape functions

In the FE method, basis functions are constructed elementwise in terms of shape functions. A shape function is the restriction of a basis function to an element. We consider the quadratic Lagrange shape functions on triangles. Lagrange shape functions are basis functions of $\mathcal{P}^p(\Delta)$ and are the standard type used to approximate scalar functions which are globally continuous. Using quadratic Lagrange shape functions the nodes (coordinate locations of the DOFs) are placed at the vertices and midsides of a triangular element (Figure 2.5 left).

The FE basis is constructed such that: (1) if ϕ_i is associated with node indexed by i, then is unity at node i and vanishes at all other nodes and (2) ϕ_i is only nonzero on those elements containing node i (Figure 2.5 right):

$$\phi_i(x_j, y_j) = \delta_{ij}, \quad \text{for } i,j = 1,\dots,n. \tag{2.64}$$

Thereby, the quadratic Lagrange shape function $N^k_{i_k}(x,y)$ associated with local node i_k in an arbitrary element τ_k with local nodes indexed by $1,2,\dots 6$ (Figure 2.5 left), satisfies:

$$N^k_{i_k}(x_{j_k}, y_{j_k}) = \delta_{i_k j_k}, \quad i_k, j_k = 1,2,\dots 6, \tag{2.65}$$

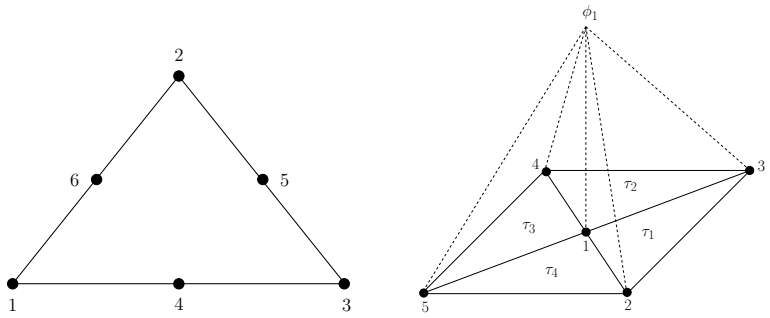

Figure 2.5: *Triangular element with vertices* $1,2,3$*, and nodes* $1-6$*, on the vertices and on the midsides of the triangle, for quadratic Lagrange FE approximations (left); and linear nodal basis functions* ϕ_1 *for a cluster of four FE at node* 1 *(right).*

and has the form:

$$N_{i_k}^k = d_1 + d_2 x + d_3 y + d_4 x^2 + d_5 xy + d_6 y^2, \tag{2.66}$$

where the value of the coefficients d_l, $l = 1,2,\dots 6$ can be determined from (2.65). Then, the restriction of the approximated function $\hat{E}_{z,h}$ (or $\hat{H}_{z,h}$) to element τ_k reads:

$$\hat{E}_{z,h}(x,y) = \sum_{i_k=1}^{6} \hat{E}_{i_k} N_{i_k}^k(x,y), \quad (x,y) \in \tau_k. \tag{2.67}$$

With this definition of the shape functions, the continuity of the approximated fields is fulfilled by construction, because the nodes are placed on vertex elements and midsides edges.

It is important to note that we are using local indexes $i_k = 1,\dots,n_k$ for the Lagrange shape functions on element k, $N_{i_k}^k$; and global indexes $i = 1,\dots,n$ for the basis functions $\phi_i \in \mathcal{P}^p(\Delta)$. It is necessary a discrete mapping between local indexes $i_k = 1,\dots,n_k$ and global indexes $i = i(k,i_k) = 1,\dots,n$ (Figure 2.6) such that:

- The local basis function $N_{i_k}^k$ is part of the global basis function ϕ_i,
  i.e. $\phi_i(x,y) = N_{i_k}^k(x,y)$ for $x,y \in \tau_k$, $\quad k = 1,\dots,n_\tau$.

- The global basis function satisfy global continuity conditions.

- $U_i = U_{i_k}^k$.

If more than one element contribute to a global basis function there are several local indexes $i_{k_1}, i_{k_2},\dots$ that map to the same global index i. If the global DOFs are to be defined unambiguously, the local DOFs that are mapped to the same global **DOF!** (**DOF!**) need to be evaluated for the same value. For this reason, they cannot be defined on all geometric entities of an element. If we use the same shape functions for $\hat{E}_{z,h}$ and $\hat{H}_{z,h}$ (then $v_{1,h} = v_{2,h} = v_h$) and we substitute the global basis functions by the local Lagrange shape

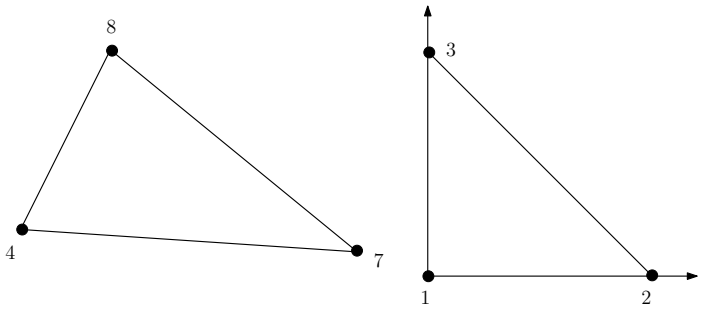

Figure 2.6: *The same triangular element with global nodes (i indexes)* $4,7,8$ *and local nodes (*i_k *indexes)* $1,2,3$ *respectively.*

functions in (2.57) and (2.58), we obtain:

$$\hat{E}_{z,h}(x,y) = \sum_{i_k=1}^{n_k} \hat{E}_{i_k} N_{i_k}^k(x,y), \quad (x,y) \in \tau_k, \tag{2.68a}$$

$$\hat{H}_{z,h}(x,y) = \sum_{i_k=1}^{n_k} \hat{H}_{i_k} N_{i_k}^k(x,y), \quad (x,y) \in \tau_k, \tag{2.68b}$$

$$v_h(x,y) = \sum_{i_k=1}^{n_k} N_{i_k}^k(x,y), \quad (x,y) \in \tau_k, \tag{2.68c}$$

where n_k are the total number of nodes in the triangle (6 for quadratic Lagrange polynomials), $N_{i_k}^k$ is the shape function associated with node i_k in element τ_k, and $\hat{E}_{i_k}$ and $\hat{H}_{i_k}$ are unknown coefficients on the nodes of element τ_k to be found by the FE method.

2.3.4 System of linear equations

The substitution of the trial and test functions by the local Lagrange shape functions, equations (2.68), in the discrete variational problem (2.55) results in:

$$\begin{aligned}\sum_{k=1}^{n_\tau}\sum_{j_k=1}^{6}\Bigg[\int_{\tau_k}\Big(&\hat{E}_{j_k}^k \nabla\bar{N}_{i_k}^k\cdot(\hat{y}\kappa_e^{-2}\nabla N_{j_k}^k) + \hat{H}_{j_k}^k \nabla\bar{N}_{i_k}^k\cdot(i\kappa_z\kappa_e^{-2}\mathbf{R}\nabla N_{j_k}^k)\\ &+\hat{E}_{j_k}^k \bar{N}_{i_k}^k \hat{y} N_{j_k}^k\Big)d^2r\Bigg] = \sum_{k=1}^{n_\tau}\sum_{j_k=1}^{6}\left[\int_{\tau_k}\bar{N}_{i_k}^k \hat{f}_1 d^2r\right];\quad i_k = 1,2,\ldots,6,\end{aligned} \tag{2.69a}$$

$$\begin{aligned}\sum_{k=1}^{n_\tau}\sum_{j_k=1}^{6}\Bigg[\int_{\tau_k}\Big(&\hat{H}_{j_k}^k \nabla\bar{N}_{i_k}^k\cdot(\hat{z}\kappa_e^{-2}\nabla N_{j_k}^k) - \hat{E}_{j_k}^k \nabla\bar{N}_{i_k}^k\cdot(i\kappa_z\kappa_e^{-2}\mathbf{R}\nabla N_{j_k}^k)\\ &+\hat{H}_{j_k}^k \bar{N}_{i_k}^k \hat{z} N_{j_k}^k\Big)d^2r\Bigg] = \sum_{k=1}^{n_\tau}\sum_{j_k=1}^{6}\left[\int_{\tau_k}\bar{N}_{i_k}^k \hat{f}_2 d^2r\right];\quad i_k = 1,2,\ldots,6.\end{aligned} \tag{2.69b}$$

Written in matrix form:

$$\sum_{k=1}^{n_\tau}[\mathbf{A}^k]\{\mathbf{U}^k\} = \sum_{k=1}^{n_\tau}\{\mathbf{F}^k\}, \tag{2.70}$$

where $[\mathbf{A}^k]$ is a 6×6 matrix with components:

$$\mathbf{A}^k_{i_k j_k} = \begin{pmatrix} \hat{y}\int_{\tau_k}\left(\kappa_e^{-2}\nabla\bar{N}^k_{i_k}\cdot\nabla N^k_{j_k} + \bar{N}^k_{i_k}N^k_{j_k}\right)d^2r & i\kappa_z\kappa_e^{-2}\int_{\tau_k}\nabla\bar{N}^k_{i_k}\cdot\mathbf{R}\nabla N^k_{j_k}d^2r \\ -i\kappa_z\kappa_e^{-2}\int_{\tau_k}\nabla\bar{N}^k_{i_k}\cdot\mathbf{R}\nabla N^k_{j_k}d^2r & \hat{z}\int_{\tau_k}\left(\kappa_e^{-2}\nabla\bar{N}^k_{i_k}\cdot\nabla N^k_{j_k} + \bar{N}^k_{i_k}N^k_{j_k}\right)d^2r \end{pmatrix} \tag{2.71}$$

$$\text{for } i_k, j_k = 1, 2, \dots 6,$$

with medium properties $\hat{y}, \kappa_e^{-2}$ and $\hat{z}$ assumed constant inside an element. $\{\mathbf{U}^k\}$ is the 6×1 vector of unknowns on the nodes of triangle τ_k, with vector elements:

$$\mathbf{U}^k_{j_k} = \begin{pmatrix} \hat{E}_{j_k} \\ \hat{H}_{j_k} \end{pmatrix} \quad \text{for } j_k = 1, 2, \dots 6; \tag{2.72}$$

and $\{\mathbf{F}^k\}$ is a 6×1 vector with components:

$$\mathbf{F}^k_{i_k} = \begin{pmatrix} \int_{\tau_k}\bar{N}^k_{i_k}\hat{f}_1 d^2r \\ \int_{\tau_k}\bar{N}^k_{i_k}\hat{f}_2 d^2r \end{pmatrix} \quad \text{for } i_k = 1, 2, \dots 6. \tag{2.73}$$

The three integrals that appear in the element matrix $\mathbf{A}^k_{i_k j_k}$ (2.71) are:

$$\int_{\tau_k}\nabla\bar{N}^k_{i_k}\cdot\nabla N^k_{j_k}d^2r, \tag{2.74a}$$

$$\int_{\tau_k}\bar{N}^k_{i_k}N^k_{j_k}d^2r, \tag{2.74b}$$

$$\int_{\tau_k}\nabla\bar{N}^k_{i_k}\cdot\mathbf{R}\nabla N^k_{j_k}d^2r. \tag{2.74c}$$

Note that, these integrals only depend on the geometry, so they can be reused for calculations with different frequencies, different wavenumber values κ_z and different source-receiver geometries. They can be calculated by Gaussian quadrature or more precisely, quadrature rules.

Element matrices $[\mathbf{A}^k]$ and element vectors $\{\mathbf{U}^k\}$ and $\{\mathbf{F}^k\}$ are generated for all elements in the mesh and assembled into their proper locations in the global matrix and vectors. The positions of the elemental matrices and vectors in their global counterparts are determined by their indexing.

The assembly process avoids the explicit summations in (2.69) and yields the general expression:

$$\mathbf{AU} = \mathbf{F}, \tag{2.75}$$

where $\mathbf{A}$ is a $2n\times 2n$ global matrix; $\mathbf{U}$ is a global $2n\times 1$ vector of 2 unknowns, E_j and H_j, on each mesh node j; $\mathbf{F}$ is a global $2n\times 1$ vector containing the source terms and n is the dimension of the trial space (the number of DOFs).

The FE matrix $\mathbf{A}$ is sparse because the nodal basis function ϕ_i vanishes outside the

triangles containing node i as a vertex, implying that integrals in equations (2.74) are zero if node i is not connected to node j.

2.3.5 Finite element solution

The last step to construct a FE solution for the 2.5-D CSEM BVP is the solution of the linear system (2.75) obtaining the values of the approximated along strike field components, $\hat{E}_{z,h}$ and $\hat{H}_{z,h}$, on the mesh nodes. Then, the solution in all the computational domain Δ is approximated using the interpolation piecewise polynomial functions on each mesh element.

The matrix system (2.75) is large and sparse, since each shape function is nonzero only on adjacent elements sharing a certain node. There are a number of techniques to solve it which essentially can be differentiated into iterative and direct. Iterative methods need relatively little memory compared to direct methods, because they require to store only matrix-vector products. However, ill-conditioning of matrices can lead to poor iterative results. Direct techniques need to store the whole matrices, but sparse factorization techniques can reduce the memory requirements. Additionally, direct solution methods are less affected by ill-conditioning, if sufficient numerical precision is used. As we will describe in the next Chapter, we use a direct solver for the solution of (2.75).

The remaining EM field components, $\hat{E}_x, \hat{E}_y, \hat{H}_x$ and $\hat{H}_y$, are derived from $\hat{E}_{z,h}$ and $\hat{H}_{z,h}$ using (2.19). However, the resulting EM fields are in the κ_z-wavenumber domain, hence an inverse Fourier transformation to the spatial domain is required. To compute the inverse Fourier transform (2.11) numerically, it is necessary to calculate a set of solutions for several wavenumbers κ_z.

In the next Chapter we give further details on the solution of the FE linear system and on the numerical technique we use to calculate the inverse Fourier transform.

2.4 Analysis of the finite element method

When solving a BVP using a numerical technique it is important to provide a measure of the quality of the approximate solution. Errors in the FE solution can be differentiated between FE approximation errors, $\|u-u_h\|$, where $\|\cdot\|$ is some appropriate norm, and perturbation errors generated from: a) numerical integration; b) interpolated Dirichlet boundary conditions by functions in $\mathcal{P}^p$; and c) errors caused by the approximation of the external boundary domain $\partial\Delta$ by piecewise-polynomial functions.

Analysis of the FE approximation error consists, essentially, on two steps (Flaherty):

1. Show that u_h is optimal in the sense that the error of discretization satisfies:

$$\|u - u_h\| \leq C \min_{w_h \in \mathcal{H}^h} \|u - w_h\|, \tag{2.76}$$

in an appropriate norm and $C > 1$.

2. Find an upper bound for the RHS of (2.76) (convergence rate).

With the FE numerical method accurate *a priori* and *a posteriori* estimates of discretization errors and convergence rates are possible. *A priori* estimations can, without computation, infer that FE solutions converge at a certain rate depending on the exact solution's smoothness. Otherwise, *a posteriori* error estimates, obtain the error from a computed FE solution. The *a posteriori* estimate can give more quantitative information about the accuracy of the solution than *a priori* estimates, for which error bounds are expressed in terms of unknown constants which are difficult, if not impossible, to determine.

As a part of this thesis we included in our algorithm a mesh refinement technique based on *a posteriori* error estimators. Technical details are given in Chapter 3. We have also performed some numerical experiments using two different *a posteriori* error estimation techniques to generate an optimal mesh, which will be discussed in Chapter 4. In the following section, we will summarize some principal ideas about the subject, however error estimators of Maxwell's equations are nontrivial and are the topic of active research. For a thorough details on FE error estimation techniques we refer to Babuška and Strouboulis (2001).

2.4.1 *A priori* error estimates

The *a priori* error estimates utilize information about the smoothness of the exact solution, the input data, the span of the FE basis functions, and the geometry of the elements to infer the convergence rate of the FE solution. All these quantities are known prior to the computation of the FE solution for the problem of interest. The *a priori* estimates are important because they guarantee that, in principle, the FE solution u_h can approximate the exact solution u, with arbitrarily high accuracy, and because they characterize the factors on which the accuracy depends on. *A priori* estimates however cannot be used effectively, for the quantitative estimation of the error.

First of all, let us consider a Galerkin problem for a second-order differential equation, find $u \in H_0^1$ such that:

$$A(u, v) = F(v), \quad \forall v \in H_0^1, \tag{2.77}$$

where A is the FE operator and v is the test function, and we have changed the notation respect equation (2.75), to clarify the following exposition. Also we consider its FE counterpart, find $u_h \in \mathcal{P}^p$ such that:

$$A(u_h, v_h) = F(v_h), \quad \forall v_h \in \mathcal{P}^p. \tag{2.78}$$

Second, we define the discretization error as:

$$e(x, y) = u(x, y) - u_h(x, y), \tag{2.79}$$

and the global norm as a square root of the strain energy of the error:

$$\|e\|_A := \sqrt{A(e,e)}, \tag{2.80}$$

with the L^2 norm:

$$\|e\|_0 := \left[\int e^2\right]^{1/2}. \tag{2.81}$$

Additionally, we consider a family of uniform FE meshes Δ for which all angles of all elements are bounded away from 0 and π and all aspect ratios are bounded away from zero as the element size $h \to 0$. Uniformity ensures that transformations from the physical to the computational space are well behaved. Thus, with uniform meshes the error in interpolating a function $u \in H^{p+1}$ by a complete polynomial w_h of degree p satisfies (2.76).

We also assume that $u \in H_0^1$ and $u_h \in S_0^N \subset H_0^1$ satisfy (2.77) and (2.78), respectively, where $A(u,v)$ is a symmetric, continuous, and H^1–elliptic bilinear form; S_0^N consists of complete piecewise-polynomial functions of degree p with respect to a uniform family of meshes τ_h; and $u \in H_0^1 \cap H^{p+1}$. Then we find:

$$\|u - u_h\|_1 \leq Ch^p \|u\|_{p+1}, \tag{2.82}$$

and

$$A(u - u_h, u - u_h) \leq Ch^{2p} \|u\|_{p+1}^{2p}, \tag{2.83}$$

with h^Δ the maximum element size for the mesh Δ.

The convergence of the approximate solution can be addressed by letting $n \to \infty$. For the Galerkin FE method $n = pN(\Delta)$, and the convergence can be achieved in one of the following three ways (Babuška and Strouboulis, 2001):

1. By refining the mesh such that the mesh size h^Δ tends to zero as the number of elements $N(\Delta)$ diverges to infinity, while keeping p fixed. This is the h version of the FE methods.

2. By increasing p while keeping the mesh Δ fixed. This is the p version of the FE methods.

3. By letting h^Δ tend to zero, and increasing p simultaneously. This is the hp version of the FE method.

in this thesis we address the h and p versions with $p = 1, 2, 3$.

The FE solution converges to the exact solution by establishing asymptotic estimates for the energy norm, the L^2 norm, and various other norms of the error (Babuška and Strouboulis, 2001).

2.4.2 *A posteriori* error estimates

A posteriori error estimates utilize a computed FE solution to estimate quantitatively the discretization error. There are several techniques available, which can be divided into four categories (Flaherty):

1. Residual error estimates. Local FE problems are created on either an element or a subdomain and solved for the error estimate. The data depend on the residual of the FE solution.

2. Flux-projection error estimates. A new flux is calculated by post processing the FE solution. This flux is smoother than the original FE flux and an error estimate is obtained from the difference of the two fluxes.

3. Extrapolation error estimates. Two FE solutions having different orders or different meshes are compared and their differences are used to provide an error estimate.

4. Interpolation error estimates. Interpolation error bounds are used with estimates of the unknown constants.

It is also important to differentiate between error estimator and element error indicator (Babuška and Strouboulis, 2001):

- The error estimator gives an estimate for the error in a solution quantity, and serves as criterion for the acceptance of the results, whether the desired accuracy in the outputs of interest has been achieved. Thus the estimator is used as a stopping criteria.

- The error indicator is a tool for the adaptive construction of the approximation. In many cases an error indicator is the contribution of the element in an estimate for a quantity of interest, e.g. the global energy norm of the error, but often the indicator is based on heuristics, for example, the indicator which employs the gradient of the computed solution, or some function of the residual.

A major requirement is that the computation of the *a posteriori* estimates should have reasonable cost. Another important requirement is that the *a posteriori* estimates must be accurate.

In this thesis we will use in the adaptive mesh refinement technique *a posteriori* error estimator methods. In particular, we will use some form of the residual error estimate.

2.5 2.5-D CSEM in an electrically anisotropic media

In an electrically anisotropic media, the conductivity varies with the direction of the applied electric field. Anisotropy in the Earth observed using EM methods can be originated in a microscopic scale (e.g. preferred orientations within crystals) or in a macroscopic scale due to the inability of EM methods to resolve oriented structures smaller than the

averaged volume (Martí, 2014). Electrical anisotropy is recognized by the EM community as an important factor to consider in order to understand EM observations (e.g. Li and Pek, 2008; Martí, 2014). However, most of the modeling programs used today assume that the subsurface is electrically isotropic and only recent publications report anisotropic modeling studies for 2-D marine CSEM. In 2.5-D CSEM, Kong et al. (2008) included diagonal anisotropy in their marine modeling program, and Li and Dai (2011) presented a more complete FE algorithm to model 2-D dipping anisotropic conductivity structures.

In the program we develop in this thesis we have implemented the possibility to model 2-D dipping anisotropic conductivity structures. In the sections above we have derived the 2.5-D CSEM modeling equations for an electric isotropic conductivity model. The derivation is simpler for the isotropic case and it is helpful for a clear description of the FE analysis. In the following we derive the governing equations and weak form of the 2.5-D CSEM problem considering anisotropy. We follow the derivation of Li and Dai (2011), but only partly since they use the primary/secondary field approach whereas we consider the total field. In the derivation we concentrate only in the differences with the above described isotropic case: the governing equations and the weak form equations in the FE context.

2.5.1 Governing equations

In this section we derive and give the governing equations for the 2.5-D CSEM electrically anisotropic problem. The starting point are equations (2.4), Maxwell's equations in complex form. All the previous assumptions to these equations are still valid, except the one concerning the electrical conductivity, which now we assume to be more general where the media has dipping electrical conductivity anisotropy:

$$\boldsymbol{\sigma} = \begin{pmatrix} \sigma_{xx} & \sigma_{xy} & 0 \\ \sigma_{yx} & \sigma_{yy} & 0 \\ 0 & 0 & \sigma_{zz} \end{pmatrix}. \tag{2.84}$$

In the Earth the conductivity tensor is symmetric and positive definite (e.g. Martí, 2014). Accordingly, $\sigma_{xy} = \sigma_{yx}$ and the conductivity tensor (2.84) is characterized only by four components. The conductivity tensor above (2.84) and even the more general one where σ_{xz} and σ_{yz} are non-zero, can be rotated, because of the symmetry and positive definiteness properties, into their principal axes using Euler's elementary rotations and then be described by its three principal values, σ_x, σ_y and σ_z, and the corresponding three Euler angles, α_s (strike), α_d (dipping) and α_l (slant) (e.g. Martí, 2014), as shown in Figure 2.7. The tensor above describes the dipping anisotropic case for which the diagonal elements can be all different, $\sigma_x \neq \sigma_y \neq \sigma_z \neq \sigma_x$, and $\alpha_d \neq 0$ and $\alpha_s = \alpha_l = 0$ (Figure 2.8 left). When all the angles are null and the tensor is diagonal in the measuring reference frame, the anisotropy is vertical for a vertical axis of symmetry (Figure 2.8 right).

We rewrite equations (2.4) substituting the isotropic conductivity variable σ ($\sigma\mathbb{I}$) with

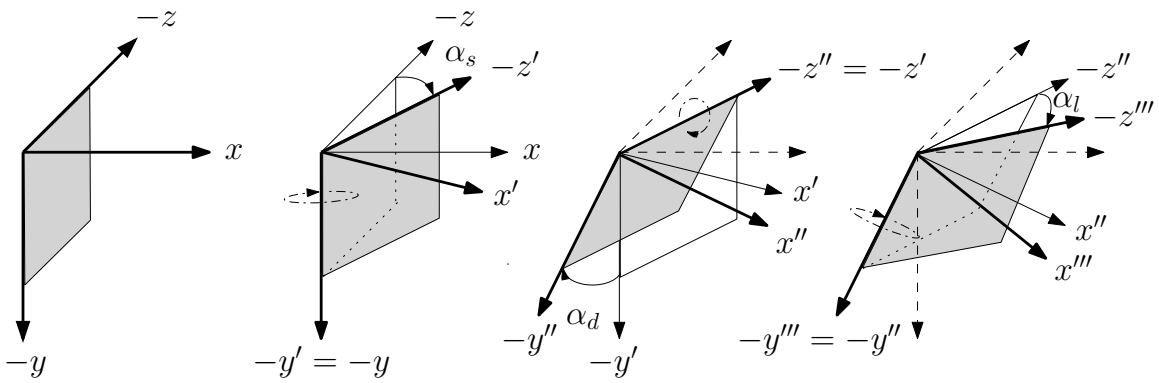

Figure 2.7: *Euler's elementary rotations applied to the 3×3 conductivity tensor to define it by its three principal values, σ_x, σ_y and σ_z, and by three rotation angles: α_s (strike), α_d (dip) and α_l (slant). Three rotations are successively applied to the diagonal principal form of the conductivity tensor; first, around the vertical axis by the anisotropy strike α_s, then around the new strike axis by the anisotropy dip α_d, and finally, around the latest vertical axis by the slant angle α_l. In this way, any orientation of the conductivity tensor in space can be achieved. Redrawn and modified from Martí (2014).*

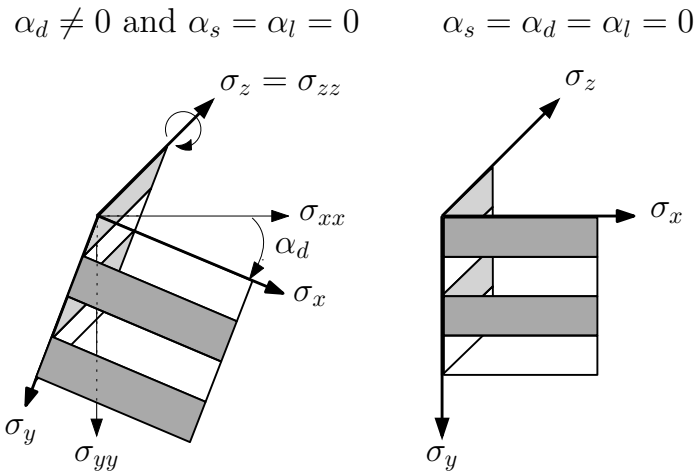

Figure 2.8: *Left: Dipping anisotropy; the three principal values of the conductivity can be all different $\sigma_x \neq \sigma_y \neq \sigma_z$, and $\alpha_d \neq 0$ and $\alpha_s = \alpha_l = 0$. Right: Vertical anisotropy; the three principal values of the conductivity can be all different $\sigma_x \neq \sigma_y \neq \sigma_z$, and $\alpha_d = \alpha_s = \alpha_l = 0$. Redrawn and modified from Martí (2014).*

the anisotropic tensor $\boldsymbol{\sigma}$:

$$\nabla \times \mathbf{E} + i\omega\mu_0 \mathbf{H} = -i\omega\mu_0 \mathbf{M}^s, \tag{2.85a}$$

$$\nabla \times \mathbf{H} - (\boldsymbol{\sigma} + i\epsilon_0\omega)\mathbf{E} = \mathbf{J}^s. \tag{2.85b}$$

We apply, as before, the 2.5-D approximation and we Fourier transform the equations using equation (2.10) and equation (2.12). After some algebra, we obtain a system of coupled PDEs for the electric and magnetic along-strike field components, $\hat{E}_z$ and $\hat{H}_z$, in a bounded domain $\Omega \subset \mathbb{R}^2$ with conductivity $\boldsymbol{\sigma}$:

$$-\nabla \cdot (\boldsymbol{\sigma}_2 \boldsymbol{\Lambda}^{-1} \nabla \hat{E}_z) - i\kappa_z \nabla \cdot (\boldsymbol{\Lambda}^{-1} \mathbf{R} \nabla \hat{H}_z) + \sigma_{zz} \hat{E}_z = \hat{f}_{a,1} \tag{2.86a}$$

$$-\nabla \cdot (\hat{z}\mathbf{R}\boldsymbol{\Lambda}^{-1}\mathbf{R}^T \nabla \hat{H}_z) + i\kappa_z \nabla \cdot (\mathbf{R}\boldsymbol{\Lambda}^{-1}\mathbf{R}^T \mathbf{R} \nabla \hat{E}_z) + \hat{z}\hat{H}_z = \hat{f}_{a,2} \text{ in } \Omega \tag{2.86b}$$

$$\hat{E}_z, \hat{H}_z = 0 \text{ on } \partial\Omega, \tag{2.86c}$$

with

$$\hat{f}_{a,1} = -\hat{J}^s_z + i\kappa_z \nabla \cdot (\boldsymbol{\Lambda}^{-1} \hat{\mathbf{J}}^s_t) + \nabla \cdot (\hat{z}\boldsymbol{\sigma}_2 \boldsymbol{\Lambda}^{-1} \mathbf{R} \hat{\mathbf{M}}^s_t), \tag{2.87a}$$

$$\hat{f}_{a,2} = -\hat{z}\hat{M}^s_z + i\kappa_z \nabla \cdot (\hat{z}\mathbf{R}\boldsymbol{\Lambda}^{-1}\mathbf{R}^T \hat{\mathbf{M}}^s_t) - \nabla \cdot (\hat{z}\mathbf{R}\boldsymbol{\Lambda}^{-1}\mathbf{R}^T \mathbf{R} \hat{\mathbf{J}}^s_t), \tag{2.87b}$$

and

$$\nabla = (\partial_x, \partial_y); \quad \boldsymbol{\sigma}_2 \equiv \begin{pmatrix} \sigma_{xx} & \sigma_{xy} \\ \sigma_{xy} & \sigma_{yy} \end{pmatrix}; \quad \hat{z} = i\mu_0\omega; \quad \mathbf{R} = \begin{pmatrix} 0 & -1 \\ 1 & 0 \end{pmatrix};$$

$$\boldsymbol{\Lambda} \equiv \hat{z}\boldsymbol{\sigma}_2 + \kappa_z^2 \mathbb{I} = \begin{pmatrix} \gamma_x^2 & \hat{z}\sigma_{xy} \\ \hat{z}\sigma_{xy} & \gamma_y^2 \end{pmatrix}; \quad \boldsymbol{\Lambda}^{-1} = \frac{1}{det(\Lambda)} \mathbf{R}\Lambda^T \mathbf{R}^T;$$

$$\gamma_x^2 = \hat{z}\sigma_{xx} + \kappa_z^2;$$

$$\gamma_y^2 = \hat{z}\sigma_{yy} + \kappa_z^2;$$

$$\gamma_{xy}^2 = \gamma_x^2\gamma_y^2 - \hat{z}^2\sigma_{xy}^2 = det(\boldsymbol{\Lambda}).$$

In the outer boundary, $\partial\Omega$, Dirichlet boundary conditions are imposed. The vectors $\hat{\mathbf{J}}^s_t$ and $\hat{\mathbf{M}}^s_t$ are, as before, the transformed source currents transverse to z, i.e. $\hat{\mathbf{J}}^s_t = (\hat{J}^s_x, \hat{J}^s_y)$ and $\hat{\mathbf{M}}^s_t = (\hat{M}^s_x, \hat{M}^s_y)$.

Writing the governing equations using the variables we defined above helps to see the equations of the electrically anisotropic problem as a generalization of the isotropic problem given by equations (2.15). Equation (2.15a) is directly recovered from (2.86a) if $\sigma_{xx} = \sigma_{yy} = \sigma_{zz} = \sigma$ and $\sigma_{xy} = 0$ since in this case $\boldsymbol{\sigma}_2 = \hat{y} = \sigma\mathbb{I}$, $\sigma = \sigma_{zz}$, and $\Lambda^{-1} = \kappa_e^2 = \hat{z}\hat{y}\mathbb{I} + \kappa_z^2\mathbb{I}$. Equation (2.15b) is also readily found from equation (2.86b) with the mentioned substitutions, but with, $\mathbf{R}\Lambda^{-1}\mathbf{R}^T = \kappa_e^2 = \hat{z}\hat{y}\mathbb{I} + \kappa_z^2\mathbb{I}$, where the identity $\mathbf{R}\mathbb{I}\mathbf{R}^T = \mathbb{I}$ has been used.

The other EM field components can be obtained from space derivatives of $\hat{E}_z$ and $\hat{H}_z$

using:

$$\hat{\mathbf{E}}_t = \boldsymbol{\Lambda}^{-1}\left(-i\kappa_z\nabla\hat{E}_z - \hat{z}\mathbf{R}\nabla\hat{H}_z - \hat{z}\hat{\mathbf{J}}_t^s - i\kappa_z\hat{z}\mathbf{R}\hat{\mathbf{M}}_t^s\right), \tag{2.88a}$$

$$\hat{\mathbf{H}}_t = \mathbf{R}\boldsymbol{\Lambda}^{-1}\mathbf{R}^T\left(\mathbf{R}\boldsymbol{\sigma}_2\mathbf{R}^T\mathbf{R}\nabla\hat{E}_z - i\kappa_z\nabla\hat{H}_z + i\kappa_z\mathbf{R}\hat{\mathbf{J}}_t^s - \hat{z}\mathbf{R}\boldsymbol{\sigma}_2\mathbf{R}^T\hat{\mathbf{M}}_t^s\right), \tag{2.88b}$$

with $\hat{\mathbf{E}}_t = \left(\hat{E}_x, \hat{E}_y\right)$ and $\hat{\mathbf{H}}_t = \left(\hat{H}_x, \hat{H}_y\right)$.

2.5.2 Finite elements formulation

To derive the FE formulation of the electrically anisotropic 2.5-D CSEM problem we follow the same scheme as for the isotropic case. In this section we focus mainly on the derivation of the weak form of the governing equations.

Considering the inner product $L^2(\Omega)$ of two complex valued scalar functions (equation 2.38) and applying it to equations (2.86), with test functions v_1 and v_2, reads:

$$\int_\Omega \bar{v}_1\left(-\nabla\cdot(\boldsymbol{\sigma}_2\boldsymbol{\Lambda}^{-1}\nabla\hat{E}_z) - i\kappa_z\nabla\cdot(\boldsymbol{\Lambda}^{-1}\mathbf{R}\nabla\hat{H}_z) + \sigma_{zz}\hat{E}_z\right)d^2r = \int_\Omega \bar{v}_1\hat{f}_{a,1}d^2r, \tag{2.89a}$$

$$\int_\Omega \bar{v}_2\left(-\nabla\cdot(\hat{z}\mathbf{R}\boldsymbol{\Lambda}^{-1}\mathbf{R}^T\nabla\hat{H}_z) + i\kappa_z\nabla\cdot(\mathbf{R}\boldsymbol{\Lambda}^{-1}\mathbf{R}^T\mathbf{R}\nabla\hat{E}_z) + \hat{z}\hat{H}_z\right)d^2r = \int_\Omega \bar{v}_2\hat{f}_{a,2}d^2r. \tag{2.89b}$$

Using equation (2.42), the integrals above can be transformed to:

$$\begin{aligned}
&\int_\Omega\left(\nabla\bar{v}_1\cdot(\boldsymbol{\sigma}_2\boldsymbol{\Lambda}^{-1}\nabla\hat{E}_z) + \nabla\bar{v}_1\cdot(i\kappa_z\boldsymbol{\Lambda}^{-1}\mathbf{R}\nabla\hat{H}_z) + \bar{v}_1\sigma_{zz}\hat{E}_z\right)d^2r\\
&\quad-\int_\Omega\left(-\bar{v}_1\hat{J}_z^s - \nabla\bar{v}_1\cdot(i\kappa_z\boldsymbol{\Lambda}^{-1}\hat{\mathbf{J}}_t^s) - \nabla\bar{v}_1\cdot(\hat{z}\boldsymbol{\sigma}_2\boldsymbol{\Lambda}^{-1}\mathbf{R}\hat{\mathbf{M}}_t^s)\right)d^2r\\
&\quad+\oint_{\partial\Omega}\bar{v}_1\boldsymbol{\Lambda}^{-1}\left(-\boldsymbol{\sigma}_2\nabla\hat{E}_z - i\kappa_z\mathbf{R}\nabla\hat{H}_z - i\kappa_z\hat{\mathbf{J}}_t^s - \hat{z}\boldsymbol{\sigma}_2\mathbf{R}\hat{\mathbf{M}}_t^s\right)\cdot\hat{\mathbf{n}}dr = 0,
\end{aligned} \tag{2.90a}$$

$$\begin{aligned}
&\int_\Omega\left(\nabla\bar{v}_2\cdot(\hat{z}\mathbf{R}\boldsymbol{\Lambda}^{-1}\mathbf{R}^T\nabla\hat{H}_z) - \nabla\bar{v}_2\cdot(i\kappa_z\mathbf{R}\boldsymbol{\Lambda}^{-1}\mathbf{R}^T\mathbf{R}\nabla\hat{E}_z) + \bar{v}_2\hat{z}\hat{H}_z\right)d^2r\\
&-\int_\Omega\left(-\bar{v}_2\hat{z}\hat{M}_z^s - \nabla\bar{v}_2\cdot(i\kappa_z\hat{z}\mathbf{R}\boldsymbol{\Lambda}^{-1}\mathbf{R}^T\hat{\mathbf{M}}_t^s) + \nabla\bar{v}_2\cdot(\hat{z}\mathbf{R}\boldsymbol{\Lambda}^{-1}\mathbf{R}^T\mathbf{R}\hat{\mathbf{J}}_t^s)\right)d^2r\\
&\quad+\oint_{\partial\Omega}\bar{v}_2\mathbf{R}\boldsymbol{\Lambda}^{-1}\mathbf{R}^T\left(-\hat{z}\nabla\hat{H}_z + i\kappa_z\mathbf{R}\nabla\hat{E}_z - i\kappa_z\hat{z}\hat{\mathbf{M}}_t^s + \hat{z}\mathbf{R}\hat{\mathbf{J}}_t^s\right)\cdot\hat{\mathbf{n}}dr = 0,
\end{aligned} \tag{2.90b}$$

where we have used (2.87a) and (2.87b) for $\hat{f}_{a,1}$ and $\hat{f}_{a,2}$ respectively.

Analyzing the boundary integral terms in (2.90), we multiply by the identity matrix $\mathbf{R}^T\mathbf{R}$ and use the relations $-\mathbf{R}^T = \mathbf{R}$ and $\mathbf{R}\mathbf{R} = -\mathbb{I}$ to obtain

$$\oint_{\partial\Omega}\bar{v}_1\mathbf{R}^T\mathbf{R}\boldsymbol{\Lambda}^{-1}\mathbf{R}^T\left(-\mathbf{R}\boldsymbol{\sigma}_2\nabla\hat{E}_z + i\kappa_z\nabla\hat{H}_z - i\kappa_z\mathbf{R}\hat{\mathbf{J}}_t^s + \hat{z}\mathbf{R}\boldsymbol{\sigma}_2\mathbf{R}^T\hat{\mathbf{M}}_t^s\right)\cdot\hat{\mathbf{n}}dr, \tag{2.91a}$$

$$\oint_{\partial\Omega}\bar{v}_2\mathbf{R}\boldsymbol{\Lambda}^{-1}\left(\hat{z}\mathbf{R}\nabla\hat{H}_z + i\kappa_z\nabla\hat{E}_z + i\kappa_z\hat{z}\mathbf{R}\hat{\mathbf{M}}_t^s + \hat{z}\hat{\mathbf{J}}_t^s\right)\cdot\hat{\mathbf{n}}dr, \tag{2.91b}$$

where we can identify the transverse components $\hat{\mathbf{E}}_t$ (equation 2.88a) and $\hat{\mathbf{H}}_t$ (equation 2.88b) and substitute them in (2.91) together with the relation $-\mathbf{R}^T = \mathbf{R}$, obtaining

$$\oint_{\partial\Omega} \bar{v}_1 \mathbf{R}\hat{\mathbf{H}}_t \cdot \hat{\mathbf{n}} dr \tag{2.92a}$$

$$-\oint_{\partial\Omega} \bar{v}_2 \mathbf{R}\hat{\mathbf{E}}_t \cdot \hat{\mathbf{n}} dr. \tag{2.92b}$$

This result is exactly the same as for the isotropic case, equation (2.47). The integrals in the boundaries are 0, by natural boundary conditions (continuity conditions in internal boundaries) and by explicitly enforcing essential boundary conditions. Therefore, the test functions are chosen null in the external boundary.

Finally, the electrically anisotropic BVP can be restated as the variational problem:

Find $\hat{E}_z, \hat{H}_z \in \mathcal{H} = [H_0^1(\Omega)]^2$ *such that*

$$\int_\Omega \left(\nabla\bar{v}_1 \cdot (\boldsymbol{\sigma}_2 \boldsymbol{\Lambda}^{-1} \nabla\hat{E}_z) + \nabla\bar{v}_1 \cdot (i\kappa_z \boldsymbol{\Lambda}^{-1} \mathbf{R} \nabla\hat{H}_z) + \bar{v}_1 \sigma_{zz} \hat{E}_z\right) d^2r = \int_\Omega \bar{v}_1 \hat{f}_{a,1} d^2r, \tag{2.93a}$$

$$\int_\Omega \left(\nabla\bar{v}_2 \cdot (\hat{z}\mathbf{R}\boldsymbol{\Lambda}^{-1}\mathbf{R}^T \nabla\hat{H}_z) - \nabla\bar{v}_2 \cdot (i\kappa_z \mathbf{R}\boldsymbol{\Lambda}^{-1}\mathbf{R}^T \mathbf{R}\nabla\hat{E}_z) + \bar{v}_2 \hat{z}\hat{H}_z\right) d^2r = \int_\Omega \bar{v}_2 \hat{f}_{a,2} d^2r, \tag{2.93b}$$

for all $v_1, v_2 \in \mathcal{H}$ *and with*

$$\int_\Omega \bar{v}_1 \hat{f}_{a,1} d^2r = \int_\Omega \left(-\bar{v}_1 \hat{J}_z^s - \nabla\bar{v}_1 \cdot (i\kappa_z \boldsymbol{\Lambda}^{-1} \hat{\mathbf{J}}_t^s) - \nabla\bar{v}_1 \cdot (\hat{z}\boldsymbol{\sigma}_2 \boldsymbol{\Lambda}^{-1} \mathbf{R}\hat{\mathbf{M}}_t^s)\right) d^2r, \tag{2.93c}$$

$$\int_\Omega \bar{v}_2 \hat{f}_{a,2} d^2r = \int_\Omega \left(-\bar{v}_2 \hat{z}\hat{M}_z^s - \nabla\bar{v}_2 \cdot (i\kappa_z \hat{z}\mathbf{R}\boldsymbol{\Lambda}^{-1}\mathbf{R}^T \hat{\mathbf{M}}_t^s) + \nabla\bar{v}_2 \cdot (\hat{z}\mathbf{R}\boldsymbol{\Lambda}^{-1}\mathbf{R}^T \mathbf{R}\hat{\mathbf{J}}_t^s)\right) d^2r. \tag{2.93d}$$

The space $\mathcal{H} = [H_0^1(\Omega)]^2$ is, as before, the space where the functions and its first order weak derivatives are square integrable in Ω and vanish in the outer boundary $\partial\Omega$.

The next steps are, as for the isotropic problem, to approximate the infinite dimensional function spaces, $\mathcal{H}$, by finite dimensional ones, $\mathcal{H}_h$, and to spatially discretize the model domain. Then, the dependent variables are approximated by a linear combination

of a set of basis functions $\{\phi_i\}_{i=1}^n$ from $\mathcal{H}_h$:

$$\hat{E}_{z,h}(x,y) = \sum_{i=1}^{n} \hat{E}_i \phi_i(x,y), \tag{2.94a}$$

$$\hat{H}_{z,h}(x,y) = \sum_{i=1}^{n} \hat{H}_i \phi_i(x,y), \tag{2.94b}$$

and the test function $\mathbf{v}$ as a linear combination of the same n basis function used for $\hat{E}_{z,h}$ and $\hat{H}_{z,h}$:

$$v_{1,h}(x,y) = v_{2,h}(x,y) = \sum_{i=1}^{n} \phi_i(x,y). \tag{2.95}$$

The discretized FE problem reads then,

$$\begin{aligned}\sum_{i=1}^{n}\sum_{j=1}^{n}\int_\Delta \Big(\nabla\bar{\phi}_i\cdot\Big(\boldsymbol{\sigma}_2\boldsymbol{\Lambda}^{-1}\nabla(\hat{E}_j\phi_j)\Big)+\nabla\bar{\phi}_i\cdot\Big(i\kappa_z\boldsymbol{\Lambda}^{-1}\mathbf{R}\nabla(\hat{H}_j\phi_j)\Big)\\ +\bar{\phi}_i\sigma_{zz}\hat{E}_j\phi_j\Big)d^2r=\sum_{i=1}^{n}\sum_{j=1}^{n}\int_\Delta\bar{\phi}_i\hat{f}_{a,1}d^2r,\end{aligned} \tag{2.96a}$$

$$\begin{aligned}\sum_{i=1}^{n}\sum_{j=1}^{n}\int_\Delta \Big(\nabla\bar{\phi}_i\cdot\Big(\hat{z}\mathbf{R}\boldsymbol{\Lambda}^{-1}\mathbf{R}^T\nabla(\hat{H}_j\phi_j)\Big)-\nabla\bar{\phi}_i\cdot\Big(i\kappa_z\mathbf{R}\boldsymbol{\Lambda}^{-1}\mathbf{R}^T\mathbf{R}\nabla(\hat{E}_j\phi_j)\Big)\\ +\bar{\phi}_i\hat{z}\hat{H}_j\phi_j\Big)d^2r=\sum_{i=1}^{n}\sum_{j=1}^{n}\int_\Delta\bar{\phi}_i\hat{f}_{a,2}d^2r,\end{aligned} \tag{2.96b}$$

which has a similar form as for the isotropic case (2.59), and again can be expressed in matrix form as a linear system of matrices:

$$\mathbf{AU} = \mathbf{F}, \tag{2.97}$$

where $\mathbf{A}$ is a $n\times n$ matrix with elements $\mathbf{A}_{ij}$, 2×2 matrices,

$$\mathbf{A}_{ij} = \begin{pmatrix} \int_\Delta\Big(\nabla\bar{\phi}_i\cdot\Big(\boldsymbol{\sigma}_2\boldsymbol{\Lambda}^{-1}\nabla\phi_j\Big)+\sigma_{zz}\bar{\phi}_i\phi_j\Big)d^2r & i\kappa_z\int_\Delta\nabla\bar{\phi}_i\cdot\Big(\boldsymbol{\Lambda}^{-1}\mathbf{R}\nabla\phi_j\Big)d^2r \\ -i\kappa_z\int_\Delta\nabla\bar{\phi}_i\cdot\Big(\mathbf{R}\boldsymbol{\Lambda}^{-1}\mathbf{R}^T\mathbf{R}\nabla\phi_j\Big)d^2r & \int_\Delta\hat{z}\Big(\nabla\bar{\phi}_i\cdot\Big(\mathbf{R}\boldsymbol{\Lambda}^{-1}\mathbf{R}^T\nabla\phi_j\Big)+\bar{\phi}_i\phi_j\Big)d^2r\end{pmatrix}$$

$$\text{for } i,j=1,2,\dots n, \tag{2.98}$$

$\mathbf{U}$ is the vector of unknowns of dimension $n\times 1$ where elements $\mathbf{U}_j$ associated to mesh entity j read:

$$\mathbf{U}_j = \begin{pmatrix}\hat{E}_j\\ \hat{H}_j\end{pmatrix}, \quad \text{for } j=1,2,\dots n; \tag{2.99}$$

and finally, $\mathbf{F}$ is a $n \times 1$ vector, with vector elements:

$$\mathbf{F}_i = \begin{pmatrix} \int_\Delta \bar{\phi}_i \hat{f}_{a,1} d^2r \\ \int_\Delta \bar{\phi}_i \hat{f}_{a,2} d^2r \end{pmatrix}, \quad \text{for } i = 1, 2, \dots n. \tag{2.100}$$

We use again Lagrange shape functions for the trial functions above, and then, the integrals in $\mathbf{A}$ are evaluated on each element, reducing to the same ones as for the isotropic case. Therefore:

$$\int_{\tau_k} \partial_x \bar{N}^k_{i_k} \partial_x N^k_{j_k} d^2r, \tag{2.101a}$$

$$\int_{\tau_k} \partial_y \bar{N}^k_{i_k} \partial_y N^k_{j_k} d^2r, \tag{2.101b}$$

$$\int_{\tau_k} \partial_x \bar{N}^k_{i_k} \partial_y N^k_{j_k} d^2r, \tag{2.101c}$$

$$\int_{\tau_k} \partial_y \bar{N}^k_{i_k} \partial_x N^k_{j_k} d^2r, \tag{2.101d}$$

$$\int_{\tau_k} \bar{N}^k_{i_k} N^k_{j_k} d^2r. \tag{2.101e}$$

In the integrals above, the dependency with $\boldsymbol{\sigma}$ has been moved out of the integration. Functions of the conductivity tensor components: $\sigma_{xx}, \sigma_{yy}, \sigma_{zz}$ and σ_{xy}, resulting from products between the vectors and matrices: ∇, $\boldsymbol{\sigma}_2$, $\boldsymbol{\Lambda}^{-1}$ and $\mathbf{R}$, are constant inside each element and can be moved out of the integrals. The linear system in (2.97) is solved using a direct solver, as in the previous case.

2.6 The Magnetotellurics modeling problem

In the MT method, the natural EM fields at the surface of the Earth can be approximated as plane waves with most of their energy reflected but with a small amount propagating vertically downward into the subsurface. For plane waves, $\kappa_z = 0$ and the sources terms are also null because the sources are not located in the model, but at infinity. However it is necessary to generate these EM plane waves, and this can be achieved through boundary conditions (e.g. Franke et al., 2007).

When modeling MT in 2-D structures, it is necessary to solve the problem for two independent polarizations: the E-polarization or TE mode and the H-polarization or TM mode (Figure 2.9). In the TE mode, the electric field, $\mathbf{E}$, points in the strike direction and the magnetic field, $\mathbf{H}$, lies in the plane orthogonal to the strike. In contrast, in the TM mode, $\mathbf{H}$ points in the strike direction and $\mathbf{E}$ is oriented in the horizontal plane orthogonal to the strike.

These two modes of MT excitation are described by two uncoupled differential equations for $\hat{E}_z$ and $\hat{H}_z$, respectively, which can be derived directly from Maxwell's equations.

However, in the following, we derive them from the 2.5-D CSEM equations (2.15) or (2.86), for an electrically anisotropic media, as a particular case when $\kappa_z = 0$ and $\mathbf{J}_t^s = 0$, $\mathbf{M}_t^s = 0$, $J_z^s = 0$, $M_z^s = 0$.

We consider the MT governing equations for an electrically anisotropic media starting from (2.86), and show the governing equations for the particular case when the media can be approximated as isotropic. Below, we develop the FE analysis for MT, concentrating strictly on the differences with the described 2.5-D CSEM FE formulation, principally, the weak form of the governing equations.

We excite the model giving appropriate Dirichlet conditions in the outer boundaries following Franke et al. (2007). These conditions are constructed from 1-D solutions for the corresponding layered media at the left and right lateral sides of the model. Solutions for plane waves diffusing in a 1-D media can be calculated analytically applying a matrix propagation method to the vector composed of the horizontal components of the MT field. In the top and bottom boundaries, a cosine taper is applied between the 1-D values at the left and right margins of the model.

2.6.1 Governing equations

The MT governing equations can be derived as a particular case of the 2.5-D CSEM equations when $\kappa_z = 0$, and $\mathbf{J}_t^s = 0,\ \mathbf{M}_t^s = 0,\ J_z^s = 0,\ M_z^s = 0$. The basic assumptions are the same as for CSEM; the conditions in the inner boundaries are again: continuity of the tangential component of the electric field, continuity of the normal component of the current density and continuity of all components of the magnetic field.

Considering the 2.5-D CSEM equations for an electrically anisotropic media (2.86), and imposing $\kappa_z = 0$, and $\mathbf{J}_t^s = 0,\ \mathbf{M}_t^s = 0,\ J_z^s = 0,\ M_z^s = 0$, we obtain:

$$-\nabla\cdot\left(\frac{1}{\hat{z}}\nabla E_z\right)+\sigma_{zz}E_z = 0 \tag{2.102a}$$

$$-\nabla\cdot\left(\mathbf{R}\boldsymbol{\sigma}_2^{-1}\mathbf{R}^T\nabla H_z\right)+\hat{z}H_z = 0 \text{ in } \Omega \tag{2.102b}$$

$$E_z, H_z = g(x,y) \text{ on } \partial\Omega, \tag{2.102c}$$

with

$$\nabla = (\partial_x, \partial_y);\ \ \hat{z} = i\mu_0\omega;\ \ \mathbf{R} = \begin{pmatrix} 0 & -1 \\ 1 & 0 \end{pmatrix};$$

$$\boldsymbol{\sigma}_2 \equiv \begin{pmatrix} \sigma_{xx} & \sigma_{xy} \\ \sigma_{xy} & \sigma_{yy} \end{pmatrix};\ \ \boldsymbol{\sigma}_2^{-1} = \frac{1}{det(\boldsymbol{\sigma}_2)}\mathbf{R}\boldsymbol{\sigma}_2^T\mathbf{R}^T;\ \ det(\boldsymbol{\sigma}_2) = \sigma_{xx}\sigma_{yy} - \sigma_{xy}^2.$$

The PDEs (2.102) are the governing equations for MT; two uncoupled equations for the electric and magnetic strike-parallel field components E_z and H_z in a bounded domain

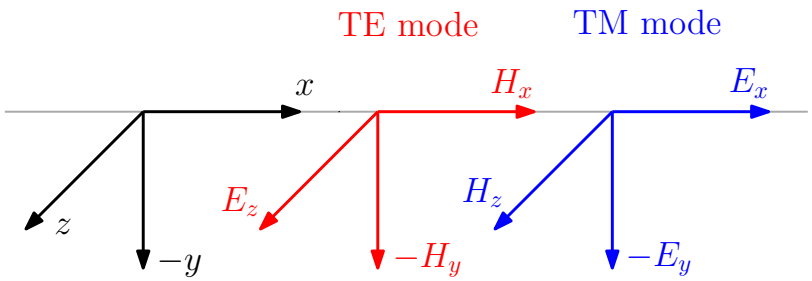

Figure 2.9: *Transverse electric (TE) and transverse magnetic (TM) modes of the magnetotellurics fields for a 2-D conductivity model. The electric field in the TE mode is directed in the strike direction (z) and the magnetic field lies in the xy-plane of the model. Inversely, in the TM mode, the magnetic field points along the strike direction and the electric field has only components in the xy-plane.*

$\Omega \subset \mathbb{R}^2$ with conductivity $\boldsymbol{\sigma}$ (equation 2.84), and external boundary conditions $g(x,y)$. Each equation corresponds to one transverse mode (Figure 2.9), equation (2.102a) as the TE mode and equation (2.102b) as the TM mode. Here, the EM fields are in the spatial domain and the external boundary conditions $g(x,y)$ are a function of space calculated by using analytical solutions for a layered model (Wait, 1953).

Once equations (2.102) have been solved, the other EM field components can be obtained from space derivatives of E_z and H_z using:

$$\boxed{\begin{aligned} \mathbf{E}_t &= -\boldsymbol{\sigma}_2^{-1}\mathbf{R}\nabla H_z && (2.103a)\\ \mathbf{H}_t &= \frac{1}{z}\mathbf{R}\nabla E_z, && (2.103b) \end{aligned}}$$

with $\mathbf{E}_t = \left(E_x, E_y\right)$ and $\mathbf{H}_t = \left(H_x, H_y\right)$.

The equations for an electrically isotropic media are easily obtained from equations (2.102) by imposing $\sigma_{xx} = \sigma_{yy} = \sigma_{zz} = \sigma$ and $\sigma_{xy} = 0$:

$$\boxed{\begin{aligned} -\nabla\cdot\left(\frac{1}{\hat{z}}\nabla E_z\right) + \sigma E_z &= 0 && (2.104a)\\ -\nabla\cdot\left(\frac{1}{\sigma}\nabla H_z\right) + \hat{z}H_z &= 0 \text{ in } \Omega && (2.104b)\\ E_z, H_z &= g(x,y) \text{ on } \partial\Omega, && (2.104c) \end{aligned}}$$

with $\sigma = \sigma(x,y)$, and

$$\boxed{\begin{aligned} \mathbf{E}_t &= -\frac{1}{\sigma}\mathbf{R}\nabla H_z && (2.105a)\\ \mathbf{H}_t &= \frac{1}{z}\mathbf{R}\nabla E_z. && (2.105b) \end{aligned}}$$

2.6.2 Finite elements formulation

To model the MT method with FE, the first step is, as explained before, to derive the weak form of the governing equations. Considering the more general equations for the electrically anisotropic media (2.102) and taking the inner product $L^2(\Omega)$ of two complex valued scalar functions (equation 2.38), with test functions v_1 and v_2, reads:

$$\int_\Omega \bar{v}_1 \left(-\nabla\cdot\left(\frac{1}{\hat{z}}\nabla E_z\right)+\sigma_{zz}E_z\right)d^2r = 0, \tag{2.106a}$$

$$\int_\Omega \bar{v}_2 \left(-\nabla\cdot\left(\mathbf{R}\boldsymbol{\sigma}_2^{-1}\mathbf{R}^T\nabla H_z\right)+\hat{z}H_z\right)d^2r = 0. \tag{2.106b}$$

Using equation (2.42), the integrals can be transformed to:

$$\int_\Omega \left(\nabla\bar{v}_1\cdot\left(\frac{1}{\hat{z}}\nabla E_z\right)+\bar{v}_1\sigma_{zz}E_z\right)d^2r - \oint_{\partial\Omega}\bar{v}_1\frac{1}{\hat{z}}\nabla E_z\cdot\hat{\mathbf{n}}dr = 0, \tag{2.107a}$$

$$\int_\Omega \left(\nabla\bar{v}_2\cdot\left(\mathbf{R}\boldsymbol{\sigma}_2^{-1}\mathbf{R}^T\nabla H_z\right)+\bar{v}_2\hat{z}H_z\right)d^2r - \oint_{\partial\Omega}\bar{v}_2\mathbf{R}\boldsymbol{\sigma}_2^{-1}\mathbf{R}^T\nabla H_z\cdot\hat{\mathbf{n}}dr = 0. \tag{2.107b}$$

Analyzing the boundary integrals, the in-plane field components expressions can be identified using (2.103):

$$-\oint_{\partial\Omega}\bar{v}_1\frac{1}{\hat{z}}\nabla E_z\cdot\hat{\mathbf{n}}dr = \oint_{\partial\Omega}\bar{v}_1\mathbf{R}\mathbf{H}_t\cdot\hat{\mathbf{n}}dr, \tag{2.108a}$$

$$-\oint_{\partial\Omega}\bar{v}_2\mathbf{R}\boldsymbol{\sigma}_2^{-1}\mathbf{R}^T\nabla H_z\cdot\hat{\mathbf{n}}dr = -\oint_{\partial\Omega}\bar{v}_2\mathbf{R}\mathbf{E}_t\cdot\hat{\mathbf{n}}dr. \tag{2.108b}$$

Splitting each of the boundary integrals in an integral for interior boundaries and an integral for exterior boundaries, the integrals for interior boundaries are null per continuity boundary condition of tangential components (natural boundary conditions) and the integrals for the outer boundary vanish, by choosing test functions $v_1, v_2 = 0$ on this boundary (essential boundary conditions), that is $v_1, v_2 \in \mathcal{H}$.

Then, the weak formulation of the MT problem in an electrically anisotropic media $\Omega \subset \mathbb{R}^2$ is:

Find $E_z, H_z \in \mathcal{H}_g$ such that

$$\int_\Omega \left(\nabla\bar{v}_1\cdot\left(\frac{1}{\hat{z}}\nabla E_z\right)+\bar{v}_1\sigma_{zz}E_z\right)d^2r = 0 \tag{2.109a}$$

$$\int_\Omega \left(\nabla\bar{v}_2\cdot\left(\mathbf{R}\boldsymbol{\sigma}_2^{-1}\mathbf{R}^T\nabla H_z\right)+\bar{v}_2\hat{z}H_z\right)d^2r = 0 \tag{2.109b}$$

for all $v_1, v_2 \in \mathcal{H} = [H_0^1(\Omega)]^2$,

where

$$\mathcal{H}_g \equiv \left\{u \in [H^1(\Omega)]^2 : \ u = g \text{ on } \partial\Omega\right\},$$
$$\mathcal{H} \equiv \left\{v \in [H^1(\Omega)]^2 : \ v = 0 \text{ on } \partial\Omega\right\}, \tag{2.110}$$

and $[H^1(\Omega)]^2$ is the space for which the functions and their first order weak derivatives are square integrable in Ω.

The next steps in the FE analysis follow the same scheme as for the CSEM problem explained in the previous section. The space is discretized in a mesh of finite elements, and the problem is projected from an infinite dimensional function space, $\mathcal{H}$, to a finite dimensional one, $\mathcal{H}_h$. The fields E_z and H_z, and the test functions $v_1 = v_2 = v$ are approximated as linear combinations of basis functions $\{\phi_i\}_{i=1}^n \in \mathcal{H}_h$:

$$E_{z,h}(x,y) = \sum_{i=1}^{n} E_i \phi_i(x,y), \tag{2.111a}$$

$$H_{z,h}(x,y) = \sum_{i=1}^{n} H_i \phi_i(x,y), \tag{2.111b}$$

$$v_h(x,y) = \sum_{i=1}^{n} \phi_i(x,y). \tag{2.111c}$$

The discretization of equations (2.109) and the substitution of its variables with the expressions (2.111) leads to:

$$\sum_{i=1}^{n}\sum_{j=1}^{n} \int_\Delta \left(\frac{1}{\hat{z}} \nabla\bar{\phi}_i \cdot \nabla(E_j\phi_j) + \bar{\phi}_i \sigma_{zz} E_j \phi_j\right) d^2r = 0, \tag{2.112a}$$

$$\sum_{i=1}^{n}\sum_{j=1}^{n} \int_\Delta \left(\nabla\bar{\phi}_i \cdot \left(\mathbf{R}\boldsymbol{\sigma}_2^{-1}\mathbf{R}^T \nabla(H_j\phi_j)\right) + \bar{\phi}_i \hat{z} H_j \phi_j\right) d^2r = 0. \tag{2.112b}$$

Equations above are uncoupled and can be expressed in matrix form as two independent systems of linear equations:

$$\mathbf{A}_E \mathbf{U}_E = 0, \tag{2.113a}$$

$$\mathbf{A}_H \mathbf{U}_H = 0, \tag{2.113b}$$

where $\mathbf{A}_E$ and $\mathbf{A}_H$ are $n \times n$ matrices with elements:

$$A_{E,ij} = \int_\Delta \left(\frac{1}{\hat{z}} \nabla\bar{\phi}_i \cdot \nabla\phi_j + \sigma_{zz}\bar{\phi}_i\phi_j\right) d^2r, \tag{2.114a}$$

$$A_{H,ij} = \int_\Delta \left(\nabla\bar{\phi}_i \cdot \left(\mathbf{R}\boldsymbol{\sigma}_2^{-1}\mathbf{R}^T \nabla\phi_j\right) + \hat{z}\bar{\phi}_i\phi_j\right) d^2r, \quad \text{for } i,j = 1,2,\ldots n; \tag{2.114b}$$

respectively, and $\mathbf{U}_E$ and $\mathbf{U}_H$ are unknown vectors of dimension $n \times 1$, where elements

associated to mesh entity j read

$$U_{E,j} = E_j, \tag{2.115a}$$

$$U_{H,j} = H_j, \quad \text{for } j = 1, 2, \dots n. \tag{2.115b}$$

The trial functions are chosen as Lagrange shape functions. Then, the integrals in $\mathbf{A}_E$ and $\mathbf{A}_H$ are elementwise and reduce to the same ones as for the CSEM problem in equation (2.101). Conductivity terms can be moved out of the integrals since they are constant inside each element.

In the linear systems above we have not included the inhomogeneous boundary conditions yet. The vectors $\mathbf{U}_E$ and $\mathbf{U}_H$ contain n_i elements for the interior points in the $\Delta/\partial\Delta$ domain and $n - n_i$ elements for the points in the outer boundary $\partial\Delta$. To correctly apply the Dirichlet conditions we need to split the vector elements into those corresponding to interior points and those corresponding to the outer boundary:

$$\mathbf{U}_E = \mathbf{U}_{E,\Delta/\partial\Delta} + \mathbf{U}_{E,\partial\Delta}, \tag{2.116a}$$

$$\mathbf{U}_H = \mathbf{U}_{H,\Delta/\partial\Delta} + \mathbf{U}_{H,\partial\Delta}, \tag{2.116b}$$

and substitute them in equations (2.113):

$$\mathbf{A}_E \mathbf{U}_{E,\Delta/\partial\Delta} = -\mathbf{A}_E \mathbf{U}_{E,\partial\Delta}, \tag{2.117a}$$

$$\mathbf{A}_H \mathbf{U}_{H,\Delta/\partial\Delta} = -\mathbf{A}_H \mathbf{U}_{H,\partial\Delta}. \tag{2.117b}$$

Finally, the linear systems of equations (2.117) will be solved using direct methods.

References

A. Abubakar, T. Habashy, V. Druskin, L. Knizlnerman, and D. Alumbaugh. 2.5D forward and inverse modeling for interpreting low frequency electromagnetic measurements. *Geophysics*, 73(4):F165–F177, 2008.

D. B. Avdeev. Three-dimensional electromagnetic modelling and inversion from theory to application. *Surveys in Geophysics*, 26:767–799, 2005.

D. B. Avdeev, A. V. Kushinov, O. V. Pankratov, and G. A. Newman. High-performance three-dimensional electromagnetic modelling using modified Newmann series. Wide-band numerical solutions and examples. *Journal of Geomagnetism and Geoelectricity*, 49: 1519–1539, 1997.

I. Babuška and T. Strouboulis. *The finite element method and its reliability*. Oxford University Press, 2001.

E. A. Badea, M. E. Everett, G. A. Newman, and O. Biro. Finite-element analysis of controlled-source electromagnetic induction using Coloumb-gauged potentials. *Geophysics*, 66(3):786–799, 2001.

R.-U. Börner. Numerical modelling in geo-electromagnetics: advances and challenges. *Surveys in Geophysics*, 31:225–245, 2010.

R.-U. Börner, O. G. Ernst, and K. Spitzer. Fast 3-D simulation of transient electromagnetic fields by model reduction in the frequency domain using Krylov subspace projection. *Geophysical Journal International*, 173:766–780, 2008.

S. Constable. Ten years of marine CSEM for hydrocarbon exploration. *Geophysics*, 75(5): 75A67–75A81, 2010.

M. Everett and R. Edwards. Transient marine electromagnetics: The 2.5-D forward problem. *Geophysical Journal International*, 113:545–561, 1992.

C. G. Farquharson and M. P. Miensopust. Three-dimensional finite-element modelling of magnetotelluric data with a divergence correction. *Journal of Applied Geophysics*, 75(4): 699–710, 1993.

J. E. Flaherty. *Course Notes - Finite Element Analysis*. [PDF Document]. Retrieved from Course Notes Online Website. URL `http://www.cs.rpi.edu/~flaherje/`. Last accessed 15th September 2015.

A. Franke, R.-U. Börner, and K. Spitzer. Adaptive unstructured grid finite element simulation of two-dimensional magnetotelluric fields for arbitrary surface and seafloor topography. *Geophysical Journal International*, 171:71–86, 2007.

A. V. Grayver and M. Bürg. Robust and scalable 3-D geo-electromagnetic modelling approach using the finite element method. *Geophysical Journal International*, 198:110–125, 2014.

E. Haber, U. M. Ascher, D. A. Aruliah, and D. W. Oldenburg. Fast simulation of 3D electromagnetic problems using potentials. *Journal of Computational Physics*, 163:150–171, 2000.

G. W. Hohmann. Numerical modeling for electromagnetic methods of geophysics. In M. N. Nabighian, editor, *Electromagnteic methods in applied geophysics*, volume 1, Theory. Society of Exploration Geophysicists, 1988.

F. W. Jones and L. J. Pascoe. The perturbation of alternating geomagnetic fields by three-dimensional conductivity inhomogeneities. *Geophysical Journal of the Royal Astronomical Society*, 27(5):479–485, 1972.

K. Key. 1D inversion of multicomponent, multifrequency marine CSEM data: Methodology and synthetic studies for resolving thin resistive layers. *Geophysics*, 74(2):F9–F20, 2009.

K. Key and J. Ovall. A parallel goal-oriented adaptive finite element method for 2.5-D electromagnetic modelling. *Geophysical Journal International*, 186:137–154, 2011.

F. N. Kong, S. E. Johnstad, T. Rosten, and H. Westerdahl. A 2.5D finite-element-modeling difference method for marine CSEM modeling in stratified anisotropic media. *Geophysics*, 73(1):F9–F19, 2008.

K. H. Lee and H. F. Morrisson. A numerical solution for the electromagnetic scattering by a two-dimensional inhomogeneity. *Geophysics*, 50:466–472, 1985.

M. Leppin. Electromagnetic modeling of 3-D sources over 2-D inhomogeneities in the time domain. *Geophysics*, 57:994–1003, 1992.

X. Li and L. B. Pedersen. Controlled-source tensor magnetotelluric responses of a layered earth with azimuthal anisotropy. *Geophysical Journal International*, 111:91–103, 1992.

Y. Li and S. Dai. Finite element modelling of marine controlled-source electromagnetic responses in two-dimensional dipping anisotropic conductivity structures. *Geophysical Journal International*, 185(2):622–636, 2011.

Y. Li and K. Key. 2D marine controlled-source electromagnetic modelling, Part I - An adaptive finite-element algorithm. *Geophysics*, 72(2):WA51–WA62, 2007.

Y. Li and J. Pek. Adaptive finite element modelling of two-dimensional magnetotelluric fields in general anisotropic media. *Geophysical Journal International*, 175:942–954, 2008.

L. O. Løseth and B. Ursin. Electromagnetic fields in planarly layered anisotropic media. *Geophysical Journal International*, 170:44–80, 2007.

R. L. Mackie, T. R. Madden, and P. E. Wannamaker. Three-dimensional magnetotelluric modeling using difference equations- Theory and comparisons to integral equation solutions. *Geophysics*, 58(2):215–226, 1993.

A. Martí. The role of electrical anisotropy in magnetotelluric responses: from modelling and dimensionality analysis to inversion and interpretation. *Surveys in Geophysics*, 35 (1):179–218, 2014.

Y. Mitsuhata. 2-D electromagnetic modeling by finite-element method with a dipole source and topography. *Geophysics*, 65(2):465–475, 2000.

T. Mogi. Three-dimensional modeling of magnetotelluric data using finite element method. *Journal of Applied Geophysics*, 35:185–189, 1996.

P. Monk. *Finite element methods for Maxwell's equations*. Oxford University Press, 2003.

S. Mukherjee and M. E. Everett. 3D controlled-source electromagnetic edge-based finite element modeling of conductive and permeable heterogeneities. *Geophysics*, 76(4):F215–F226, 2011.

G. A. Newman and D. L. Alumbaugh. Frequency-domain modeling of airbone electromagnetic responses using staggered finite differences. *Geophysical Prospecting*, 43:1021–1042, 1995.

J. Pek and F. A. M. Santos. Magnetotelluric impedances and parametric sensitivities for 1-D anisotropic layered media. *Computer and Geosciences*, 28(8):939–950, 2002.

J. Pek and T. Verner. Finite-difference modelling of magnetotelluric fields in two-dimensional anisotropic media. *Geophysical Journal International*, 128:505–521, 1997.

D. F. Pridmore, G. W. Hohmann, S. H. Ward, and W. R. Sill. An investigation of finite-element modeling for electrical and electromagnetic data in three dimensions. *Geophysics*, 46(7):1009–1024, 1981.

I. K. Reddy and D. Rankin. Magnetotelluric effect of dipping anisotropies. *Geophysical Prospecting*, 19(1):84–97, 1971.

I. K. Reddy and D. Rankin. Magnetotelluric response of laterally inhomogeneous and anisotropic media. *Geophysics*, 40(6):1035–1045, 1975.

Z. Ren, T. Kalscheuer, S. Greenhalgh, and H. Maurer. A goal-oriented adaptive finite-element approach for plane wave 3-D electromagnetic modelling. *Geophysical Journal International*, 194(2):700–718, 2013.

Schwarzbach. *Stability of finite element solutions to Maxwell's equations in frequency domain*. PhD thesis, Technische Universität Bergakademie Freiberg, 2009.

C. Schwarzbach, R.-U. Börner, and K. Spitzer. Three-dimensional adaptive higher order finite element simulation for geo-electromagnetics - a marine CSEM example. *Geophysical Journal International*, 187:63–74, 2011.

P. P. Silvester and R. L. Ferrari. *Finite elements for electrical engineers*. Cambridge University Press, 1996.

J. T. Smith and J. R. Booker. Rapid inversion of two- and three-dimensional magnetotelluric data. *Journal of Geophysical Research*, 96(B3):3905–3922, 1991.

C. H. Stoyer and R. J. Greenfield. Numerical solutions of the response of a two-dimensional Earth to an oscillating magnetic dipole source. *Geophysics*, 41(3):519–530, 1976.

R. Streich. 3D finite-difference frequency-domain modeling of controlled-source electromagnetic data: Direct solution and optimization for high accuracy. *Geophysics*, 74(5): F95–F105, 2009.

R. Streich and M. Becken. Electromagnetic fields generated by finite-length wire sources: Comparison with point dipole solutions. *Geophysical Prospecting*, 59:361–374, 2011.

R. Streich, M. Becken, and O. Ritter. 2.5D controlled-source EM modeling with general 3D source geometries. *Geophysics*, 76(6):F387–F393, 2011.

M. Unsworth, B. Travis, and C. A.D. Electromagnetic induction by finite electric dipole source over a 2-D earth. *Geophysics*, 58(2):198–214, 1993.

J. R. Wait. Propagation of radio waves over a stratified ground. *Geophysics*, 18:416–422, 1953.

P. Wannamaker, G. W. Hohmann, and W. A. SanFilipo. Electromagnetic modeling of three-dimensional bodies in layered earths using integral equations. *Geophysics*, 49:60–74, 1984.

P. E. Wannamaker. Anisotropy versus heterogeneity in continental solid earth electromagnetic studies: Fundamental response characteristics and implications for physicochemical state. *Surveys in Geophysics*, 26:733–765, 2005.

S. H. Ward and G. W. Hohmann. Electromagnetic theory for geophysical applications. In M. N. Nabighian, editor, *Electromagnteic methods in applied geophysics*, volume 1, Theory. Society of Exploration Geophysicists, 1988.

P. Weidelt. Electromagnetic induction in three-dimensional structures. *Journal of Geophysics (Zeitschrift fuer Geophysik)*, 41:85–109, 1975.

P. Weidelt. 3-D conductivity models: implications of electrical anisotropy. In *Three Dimensional Electromagnetics*, pages 119–137. SEG Monograph GD7, Tulsa, USA, 1999.

C. J. Weiss and S. Constable. Mapping thin resistors and hydrocarbons with marine EM methods, Part II – Modeling and analysis in 3D. *Geophysics*, 71(6):G321–G332, 2006.

C. J. Weiss and G. A. Newman. Electromagnetic induction in a fully 3-D anisotropic earth. *Geophysics*, 67(4):1104–1114, 2002.

C. Yin. MMT forward modeling for a layered earth with arbitrary anisotropy. *Geophysics*, 71(3):G115–G128, 2006.

M. S. Zhdanov and S. Fang. Quasi-linear approximation in 3-D electromagnetic modeling. *Geophysics*, 61(3):646–665, 1996.

CHAPTER 3

Implementation of a 2-D adaptive FE modeling program

3.1 Introduction

In this Chapter we present our development of an algorithm to model the frequency-domain CSEM and MT methods on a 2-D conductivity structure using the FE technique. Outstanding features of the program are: 1) the use of the FE method in the modeling of 2.5-D CSEM and 2-D MT in both marine and land environments, and the possibility to model dipping electrical anisotropic structures, 2) the possibility to model 3-D CSEM sources, punctual and finite-length, in any arbitrary orientation and to model inhomogeneities near the source thanks to the modelization of the total field instead of a primary/secondary field approximation, 3) it is possible to use high-order shape functions in the FE method, 4) the FE system matrix is solved using a fast and robust direct solver 5) the meshes can be unstructured, giving the possibility to accommodate complicated geometries and small and large structures in the same grid, 6) an adaptive mesh refinement algorithm is included with the choice of a global or a goal-oriented error estimator.

In recent years, many FE packages, both open source and commercial, have appeared that assemble the governing equations of a given problem and solve the resulting linear system with sophisticated numerical solvers. The emergence of these packages is directly related to the simultaneous appearance of fast and robust numerical solver libraries and high-quality meshing tools. Recent publications make use of these libraries and of the FE packages in their EM application codes. Key and Ovall (2011) uses the open-source constrained and conforming Delaunay triangulation code TRIANGLE (Shewchuk, 1996) for their 2.5-D CSEM FE code. Schwarzbach et al. (2011) use the open-source tetrahedral mesh generator TETGEN (Si, 2007), for the 3-D problem. MUMPS (Amestoy et al., 2006) and PARDISO (Schenk and Gärtner, 2004) direct solvers are used in, e.g., Streich et al. (2011) and Schwarzbach et al. (2011), respectively. Ultimately, open-source FE packages as FEMSTER (Castillo et al., 2005) and deal.II (Bangerth et al., 2007), have also been used for the implementation of the 3-D EM FE modeling problem in Schwarzbach et al. (2011) and Grayver and Bürg (2014), respectively, and the commercial FE package, COMSOL Multihysics (COMSOL, 2015), has been used in e.g. Franke et al. (2007) and Börner (2010).

In the work developed in this thesis we use COMSOL Multihysics FE simulation software together with MATLAB for the implementation of our program. Among the numerous capabilities that COMSOL offers we highlight the sophisticated geometry generator, the high-quality unstructured mesh generator; the possibility to use different shape functions with high-order (higher than quadratic) and the incorporation of several fast and robust numerical solvers, e.g. MUMPS and PARDISO. It also includes an interface to communicate with MATLAB, through which it is possible to program with MATLAB language and using object-oriented programming. Inconveniences are mainly related with the inability to access COMSOL source code.

The basic scheme of our modeling algorithm consists of the discretization of the model geometry in elements (triangles), the assembling of the FE equations we have derived in Chapter 2, the solution of the resulting linear system for a set of wavenumber values, and the inverse Fourier transformation of the solution back to the spatial domain. Additionally, it incorporates an automatic adaptive mesh refinement algorithm. In this Chapter, we describe in detail the strategies we have used in each component of the program.

3.2 Implementation details

The implementation of the 2.5-D CSEM and 2-D MT FE problem derived in Chapter 2 is done using COMSOL Multiphysics (COMSOL, 2015) and MATLAB using the interface that connects them.

A typical FE software framework contains a preprocessing module to define the problem geometry, mesh and data; a processing module to assemble the FE equations and solve the resulting system; and a postprocessing module to output the solution and calculate additional quantities of interest. Lately, a module for the analysis of the FE solution is also added.

The modeling program we have developed in this thesis follows this framework. In Figure 3.1 we present the general flowchart of the program. The necessary inputs are the model and a set of settings mainly related with the experiment setup: frequencies, type of sources, location and orientation of the sources and location of the receivers. The spacing of the wavenumber values at which the fields are computed and the upper and lower limits for the wavenumber spectrum must be specified. The model, the geometry and the electrical conductivity tensor in each region of the geometry, and an initial unstructured triangular mesh, can be generated or imported, following some specific formats, with the COMSOL graphical interface, and saved as a MATLAB file. The geometry of the model is defined as a composition of different domains, and the input conductivity is constant in each domain. In the unstructured grid, the elements are only constrained to be shape regular (triangles) and the element edge length can vary from side to side and element to element.

The program accepts complex geometries and it is possible to include an air layer and a sea layer, and to locate the sources in any position of the model. The sources can be

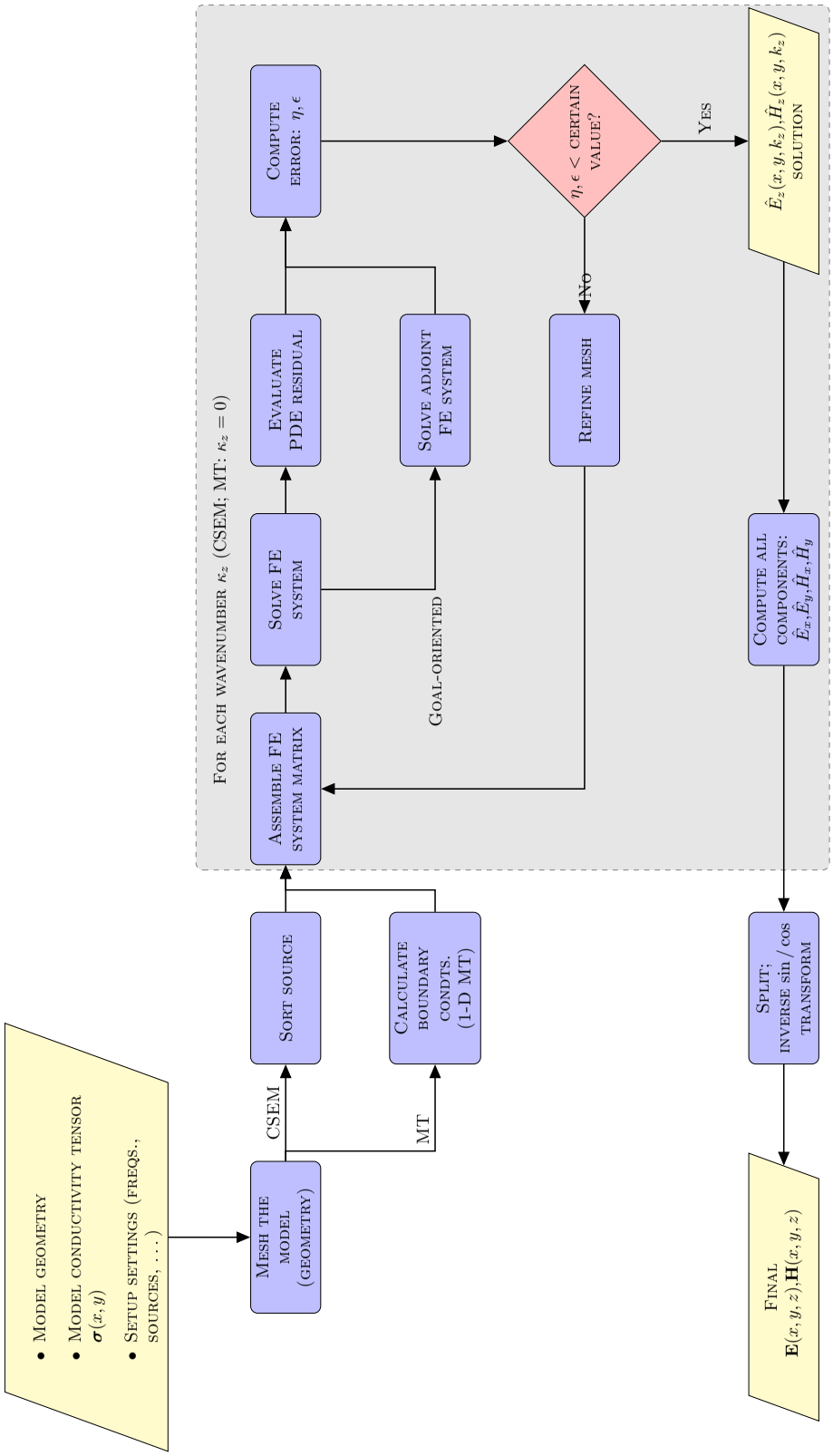

Figure 3.1: *General flowchart of the program for modeling the 2.5-D CSEM and 2-D MT problems.*

electric or magnetic dipoles in arbitrary orientations. The receivers can be also located in any position of the model or in the strike plane. The allowed anisotropy in the model is given by the electrical conductivity tensor in equation (2.84).

The processing and postprocessing modules are programmed in a COMSOL-MATLAB interface and using object-oriented programming. In this environment the inputs are read and sort, and the FE equations derived in Chapter 2 for MT and CSEM are assembled using COMSOL libraries. For CSEM modeling, appropriate source terms are included. Otherwise, for MT modeling, the model is excited by imposing boundary conditions which we calculate analytically as described in Chapter 2.

The resulting linear system of equations is solved using the direct solver MUMPS (Amestoy et al., 2006). Sweeps are performed for different frequencies and sources and over a set of wavenumber values; for each frequency and source, a sweep over wavenumber values is required. The shape functions for the dependent variables, the Fourier transformed strike-directed electric and magnetic fields, are nodal Lagrange functions with order up to $7th$.

We have also implemented an automated *a posteriori* adaptive mesh refinement algorithm adapting a COMSOL library to our problem. The adaptive mesh refinement is an iterative algorithm, which at each iteration selects a subset of elements to refine based on an estimate of their contribution to the solution error. As we will describe later, we use two different criteria to estimate the error: a L^2-norm global error estimation and a goal-oriented error estimation.

As we already mentioned, the system of equations (2.97) is solved for the strike-parallel field components in the wavenumber domain. The other field components, the electric $\hat{E}_x$ and $\hat{E}_y$ and magnetic $\hat{H}_x$ and $\hat{H}_y$, are calculated by differentiating the FE solution fields in the $xy-$ plane (equations 2.88). In the CSEM case, an inverse Fourier transform of all components is necessary to obtain the solution in the spatial domain. The integration is in the strike-parallel wavenumber coordinate and therefore the FE solution must be computed for a set of discrete wavenumber values. Then, we apply a cubic-spline interpolation of the field values for the different wavenumbers, and finally an inverse Fourier transform using the digital filter method is applied.

At last, the required output is calculated if necessary, that is, amplitudes and phases for CSEM or apparent resistivities and phases for MT.

In the following we describe some technical aspects on the methods we use in our program.

3.2.1 Source modeling

Sources used in the CSEM method include magnetic loops and long horizontal wires which are grounded in land-based surveys or deployed on the seafloor or towed through the water in marine surveys (in this thesis we do not consider airborne methods). Vertical electrical sources are also used. The sources most commonly used in present day CSEM applications

are horizontal wires with length of several hundred meters (Streich et al., 2011).

There are distinct strategies used in the literature on how to model the sources. We differentiate between using the primary/secondary fields approximation (e.g. Everett and Edwards, 1992; Unsworth et al., 1993; Li and Key, 2007; Streich et al., 2011) or modeling the total field (e.g. Stoyer and Greenfield, 1976; Mitsuhata, 2000; Key and Ovall, 2011).

In the primary/secondary field approach the source term is eliminated from the equations and the principle of superposition is applied. The EM fields are expressed in terms of a primary field induced by the source in a 1-D layered background model with a primary conductivity and secondary fields which arise in regions where the conductivity differs from the primary one. The reason of this approach is to avoid the modeling of the source term, which is singular and hence it is difficult to represent accurately by a discrete formulation (Unsworth et al., 1993). However, this conventional scheme is not effective for complex structures lacking a simple background model (Mitsuhata, 2000). Moreover, when modeling general 3-D sources, 1-D analytical or semianalytical solutions for the primary field do not exist in the $xy\kappa_z$–domain, and it is necessary to first calculate the primary field in the spatial-domain and then Fourier transform it numerically along the strike direction onto the wavenumber-domain for the 2.5-D problem. These additional calculations increase the computational time and reduces the quality of the solution, since the error in the additional numerical integration is added to the problem.

With the aim of developing a code which can be used in a maximum of geological structure scenarios and to take advantage of the potential of FE methods and unstructured grids in representing complex geometries we model the total field. We include the source terms in the equations and we apply a mesh refinement in the source region.

In Chapter 2 we gave the source term equations for magnetic and electric point dipoles oriented in the three-space directions and we derived their weak form. The point dipole approximation is valid for sufficiently large source-receiver distances (offsets) typical on most common CSEM surveys. However, when the interest is to resolve relatively small structures in an increasingly complex scenario, measurements at short offsets are necessary and the inaccuracy of the dipole approximation is on the order of the target-related anomalies (Streich et al., 2011). For these cases the actual source geometry needs to be considered. We discretize the finite-length wire source into a set of point dipoles and calculate the model responses for each one of them separately. Afterwards, we superpose the solution fields in the receiver locations.

To deal with oriented sources, the program analyzes the input azimuth and dip angles and the type of source and classifies them. If the source is oriented, the program decomposes the orientation in the Cartesian axes and gives appropriate equation source terms in each direction and a parity index, based on the source-receiver configuration, for the calculation of the Fourier inverse transform. As we will describe later on this Chapter, depending on this parity the program uses the sine or cosine filters or both, and only positive wavenumbers or positive and negative wavenumbers for the computation of the inverse Fourier transform.

3.2.2 Direct solver

In Chapter 2, the application of the FE method to model the 2.5-D CSEM and the 2-D MT problems lead to a large and sparse system of linear equations (equation 2.75) of the form:

$$\mathbf{A}\mathbf{x} = \mathbf{b}, \tag{3.1}$$

where $\mathbf{A}$ is the square sparse system matrix, and we changed slightly the notation with respect to equation (2.75) to simplify the following explanations.

To solve the above linear algebraic system we use a direct solver, in particular, the MUMPS package (Amestoy et al., 2006).

Using direct techniques, the solution of (3.1) is found after a finite number of algebraic operations. Direct methods utilize Gaussian elimination, factorizing $\mathbf{A}$ into the product:

$$\mathbf{A} = \mathbf{L}\mathbf{U}, \tag{3.2}$$

known as LU decomposition, where $\mathbf{L}$ is a lower triangular matrix and $\mathbf{U}$ is an upper triangular matrix with unit diagonals. Once $\mathbf{L}$ and $\mathbf{U}$ have been determined it follows:

$$\mathbf{A}\mathbf{x} = \mathbf{L}\mathbf{U}\mathbf{x} = \mathbf{b}, \tag{3.3}$$

and the system is solved by forward and backward elimination steps. In the forward substitution the system:

$$\mathbf{L}\mathbf{y} = \mathbf{b}, \tag{3.4}$$

is solved, and then the backward substitution:

$$\mathbf{U}\mathbf{x} = \mathbf{y}. \tag{3.5}$$

If $\mathbf{A}$ is a symmetric matrix ($\mathbf{A} = \mathbf{A}^T$), as it is for the problem under consideration, the factorization is carried out without the computation of $\mathbf{U}$, but decomposing:

$$\mathbf{A} = \mathbf{L}\mathbf{D}\mathbf{L}^T, \tag{3.6}$$

known as LDL^T factorization, where $\mathbf{L}$ is again a lower triangular matrix, and $\mathbf{D}$ a diagonal matrix. Thus, equation (3.1) reads:

$$\mathbf{A}\mathbf{x} = \mathbf{L}\mathbf{D}\mathbf{L}^T\mathbf{x} = \mathbf{b}, \tag{3.7}$$

and once $\mathbf{L}$ and $\mathbf{D}$ are determined, the system is solved through forward, diagonal and backward substitution steps:

$$\mathbf{L}\mathbf{z} = \mathbf{b}, \quad \mathbf{D}\mathbf{y} = \mathbf{z}, \quad \mathbf{L}^T\mathbf{x} = \mathbf{y}. \tag{3.8}$$

The above procedures ignore sparsity in **A**. For sparse matrices it is sufficient and more memory efficient to store only the non-zero values and their position. This can be done with banded versions of the factorization. There are other techniques that improve the efficiency of the direct solution process, for example, preordering algorithms, which permute the columns and thereby minimize the fill-in. Moreover, numerical stability can be enhanced by pivoting, i.e. allocating the largest absolute values to the diagonal matrix by exchanging columns.

MUMPS incorporates a number of these techniques and computes the direct solution of large sparse systems of linear equations on distributed memory parallel computers using multifrontal Gaussian elimination. It solves a linear system of equations within three phases. In the analysis phase, the matrix structure is analyzed and a suitable ordering and data structures for an efficient factorization are produced. In the subsequent factorization phase, the numerical factorization is performed using the LU decomposition for the unsymmetric case or the LDL^T for the symmetric case. The final solve phase computes the solution of the system by forward and backward substitution using the factors that were just computed (Amestoy et al., 2002). The numerical factorization is the most expensive of these phases and parallelism is exploited.

We have found for our problem that it is more efficient to use a direct solver, like MUMPS, in agreement with recent publications, e.g. Key and Ovall (2011); Streich et al. (2011), instead of an iterative solver. The matrix is symmetric, and multiple transmitter sources result in multiple right-hand side vectors in the linear systems that can be solved using the same factorization of the system matrix **A**. However, it is important to note that to be able to reuse a factorized matrix for multiple sources, the system matrix and accordingly, the FE mesh must be the same for all sources that reuse this factorization. Specific mesh refinement for each source would require a new factorization for every new grid.

3.2.3 Adaptive mesh refinement

As we have advanced in Chapter 2, in the FE method the solution error scales with elements size in the discretized mesh. Solution accuracy can be increased by refining the mesh. However, grid refinement in the overall model can result in a large system, increasing memory and computational time unnecessarily. Hence, an optimal mesh is required with which a minimum number of vertices results in an accurate FE solution. Automated adaptive mesh refinement techniques can solve this problem by iteratively refining the grid and therewith increasing the accuracy. They start with a coarse grid and in each iteration a subset of elements is selected for refinement based on an estimate of their contribution to solution error. Then, the grid is refined by splitting these elements. The process is repeated iteratively until the desired solution accuracy is obtained or computational resources are exhausted.

In Chapter 2 we introduced *a posteriori* methods in the context of analysis of the FE

solution. *A posteriori* methods use the FE solution or the computation of an auxiliary solution to calculate the error estimator. They calculate the error contribution of each mesh element to a certain error function. Adaptive mesh refinement techniques using *a posteriori* error estimation methods seek to reduce the global error in the FE solution or the error of some functional measure which depends on the FE solution, a goal function, by iteratively refining the mesh. *A posteriori* error estimation methods that estimate the global error are called global error estimator methods, and methods that estimate the error of a goal function are referred to goal-oriented error estimator methods.

Automated adaptive mesh refinement algorithms using *a posteriori* error estimators have been included in recent EM geophysical modeling programs (e.g. Franke et al., 2007; Li and Key, 2007; Key and Ovall, 2011; Schwarzbach et al., 2011; Grayver and Bürg, 2014). Most of them use goal-oriented error estimation methods in their adaptive mesh refinement algorithms. The reason is that EM geophysical measurements are made on a few discrete points in the model and therefore the FE solution needs only to be accurate there. The use of global error estimation techniques would not work as efficient as goal-oriented error estimators since several refinement iterations would have little impact on the solution accuracy around the receiver locations (Li and Key, 2007). Moreover, manually refining the mesh in the proximity of the receivers would also not necessarily work since the solution for the elliptic problem depends on data through the entire model (e.g. Babuška and Strouboulis, 2001).

The modeling program we present in this thesis includes an automated adaptive mesh refinement algorithm. The implementation is based on a COMSOL package, and there are two possible methods for the calculation of the error estimator: a global error estimator and a goal-oriented error estimator.

Our program uses the L^2-norm error estimate to estimate the global error. The L^2-norm error estimate relies on an assumption of a strong stability estimate for the PDE problem. From such an assumption, it is possible to show that there is a constant C, such that the L^2-norm of the error, e_l, in the l–th equation satisfies:

$$\|e_l\| \leq C\|h^{q_l}\rho_l\|, \tag{3.9}$$

where ρ_l is the residual in the l–th equation, q_l is the stability estimate derivative order and h is the local mesh element size. The adaptive solver algorithm uses the following L^2–norm error estimator:

$$\left(\int_\Delta \sum_l s_l^{-2} h^{2q_l} |\rho_l|^2 dA\right)^{1/2}, \tag{3.10}$$

with the default value $q_l = 2$, and the scaling factors s_l for the residual with the default value $s_l = 1$. The error indicator for a $k - th$ mesh element is:

$$\eta_k = \sum_l s_l^{-2} h^{2q_l} \alpha_{l,k}^2 A_k, \tag{3.11}$$

where A_k is the area of the $k-th$ mesh element, and $\alpha_{l,k}$ is the absolute value of the l–th equation residual on the $k-th$ mesh element.

The adaptive solver using the global error estimator performs the following iterative algorithm (COMSOL, 2015):

1. Solve the problem on the existing mesh.
2. Evaluate the residual of the PDEs on all mesh elements.
3. Estimate the error in the solution on all mesh elements. The computed error estimate is an error indicator because it involves an unknown constant.
4. Terminate execution if the algorithm has made the requested number of refinements or if it has exceeded the maximum number of elements.
5. Refine a subset of the elements based on the sizes of the local error indicators.
6. Repeat these steps.

The goal-oriented error estimator for adaptive mesh refinement included in the program implements the dual-weighted residual (DWR) method (Becker and Rannacher, 2001). Goal-oriented error estimators compute the error estimate with respect to a given goal functional. They use a sensitivity function to calculate how the errors in several regions of the model influence the error in another particular portion of the model. For this purpose, the DWR method applies a weighting term to the error indicator, where the weight is determined by a dual or adjoint solution of the FE system. The error estimate is calculated as the sum of contributions from individual mesh elements. For each mesh element, the contribution is split over equations and is a product of a residual and dual weights.

Following Becker and Rannacher (2001), let $J(u)$ be a quantity of physical interest derived from the solution u by applying a functional $J(\cdot)$. The goal is to control the error e_k in terms of local residuals $\rho_k(u_h)$ computable on each of the mesh elements τ_k. The effect of the element residual ρ_k on the error $e_{k'}$ at another element $\tau_{k'}$, is governed by the Green function of the continuous problem. In practice it is generally not possible to calculate the complex error interaction analytically, and it has to be computed numerically. Then, the *a posteriori* error estimate reads:

$$|J(u) - J(u_h)| \approx \langle \rho(u_h), \omega_h(z) \rangle, \tag{3.12}$$

where the sensitivity factor $\omega_h(z)$ is obtained by approximately solving an adjoint problem $A^*z = j$, with j a density function associated with $J(\cdot)$. The adjoint solution z may be viewed as a generalized Green's function with respect to the output functional $J(\cdot)$, and accordingly the weight $\omega_h(z)$ describes the effect of local variations of the residual $\rho(u_h)$ on the error quantity $J(u) - J(u_h)$, for instance as a consequence of mesh adaption.

Following again Becker and Rannacher (2001) to derive equation (3.12) in the framework of optimal control, we start with the variational problem:

$$A(u,v) = F(v), \quad \text{for all } v \in V, \tag{3.13}$$

and its discretized form:

$$A(u_h,v_h) = F(v_h), \quad \text{for all } v_h \in V_h, \tag{3.14}$$

where V_h is the finite dimensional space, subspace of V, and $u_h \in V_h$. Then $J(u_h)$ is an approximation of the goal function $J(u)$.

The constraint optimization problem for $u \in V$ is:

$$J(u) = \min!, \quad A(u,v) = F(v), \quad \text{for all } v \in V. \tag{3.15}$$

Introducing the corresponding Lagrangian $\mathcal{L}(u,z) \equiv J(u)+F(z)-A(u,z)$, with the adjoint variable $z \in V$, the minimal solution u is the first component of a stationary point of $\mathcal{L}(u,z)$, which is calculated from the Euler-Lagrange system, consisting of (3.13) and the adjoint problem:

$$A(v,z) = J(v), \quad \text{for all } v \in V. \tag{3.16}$$

By construction, the solution u and z are mutually adjoint to each other in the sense that $J(u) = A(u,z) = F(z)$. Hence, it is equivalent to compute $J(u)$ or $F(z)$.

The Euler-Lagrange system is approximated by the Galerkin method in V_h, resulting in the discrete equations (3.14) for $u_h \in V_h$ and:

$$A(v_h,z_h) = J(v_h), \quad \text{for all } v_h \in V_h, \tag{3.17}$$

and for $z_h \in V_h$. For both errors $e \equiv u-u_h$ and $e^* = z-z_h$ we have the Galerkin orthogonality property $A(e,\cdot) = 0 = A(\cdot,e^*)$ on V_h. Therefore,

$$J(e) = A(e,z) = A(e,e^*) = A(u,e^*) = F(e^*). \tag{3.18}$$

The residuals of u_h and z_h are represented by $\rho(u_h,\cdot) \equiv F(\cdot) - A(u_h,\cdot)$ and $\rho^*(z_h,\cdot) \equiv J(\cdot) - A(\cdot,z_h)$ respectively. Then, applying again the Galerkin orthogonality property:

$$\rho(u_h,z-v_h) = A(e,e^*) = \rho^*(z_h,u-v_h), \tag{3.19}$$

with arbitrary $v_h \in V_h$. Finally the error representation reads:

$$J(e) = \min_{v_h \in V_h} \rho(u_h,z-v_h) = \min_{v_h \in V_h} \rho^*(z_h,u-v_h) = F(e^*). \tag{3.20}$$

Bounds on the error $J(e)$ are:

$$|J(e)| \leq \eta_w(u_h) \equiv \sum_k \rho_k \omega_k, \tag{3.21}$$

where ρ_k are element residuals and ω_k are weights. These quantities are calculated by introducing an extension mapping π_h, from the current FE space to a higher-order FE space:

$$\rho_k = \|\rho(\pi_h, u_h, \cdot)\|_k, \tag{3.22a}$$

$$\omega_k = \|z - \pi_h z\|_k, \tag{3.22b}$$

where the residual is computed assembling the problem for the higher-order FE space. This residual is then used to compute a normalized elementwise norm for each equation. On the other hand, the weight function is estimated using polynomial-preserving recovery technique (Naga and Zhang, 2005) over the dual solution.

Finally, the error estimation function is:

$$|J(e)| = \sum_k \sum_l \rho_{k,l} \omega_{k,l}, \tag{3.23}$$

where the error contribution from each l–th equation is added.

In conclusion, the necessary steps for the iterative adaptive algorithm using the DWR method for the error estimation are:

1. Solve the problem on the existing mesh.
2. Calculate the residual of the PDE on all mesh elements, using a higher order approximation of the shape-functions.
3. Solve the adjoint problem.
4. Calculate the weights.
5. Calculate the error indicator for each mesh element.
6. Terminate execution if the requested number of refinements is reached or if the maximum number of elements is exceeded.
7. Refine a subset of the elements based on the sizes of the local error indicators.
8. Repeat these steps.

The mesh refinement in our program is applied using a fixed mesh fraction technique, that is, refining in each step of the adaptive mesh refinement a fixed fraction of elements with the largest error indicator.

Typical modeling settings of CSEM and MT methods require to compute the solution for different frequencies, transmitter positions and wavenumbers (for CSEM). To apply the adaptive mesh refinement algorithm to each physical parameter value would be computationally very expensive. Instead, our program classifies each of the physical parameters sets of values in groups of near values and combine groups of different physical parameter. Then, in a first stage, the program selects a midvalue of each parameter in each group and applies the adaptive mesh refinement algorithm to these selected values. In a second stage, the resulting mesh for each group is fixed and used to compute the solutions for the rest of parameter values of each group. This strategy has been inspired by the work in Key and Ovall (2011) and will be discussed in more detail in the next Chapter.

3.2.4 From wavenumber domain onto spatial domain

As explained in detail in Chapter 2, for the solution of the CSEM modeling problem using the 2.5-D approach, the EM fields need to be Fourier transformed into the strike-parallel wavenumber domain. However, we seek the solution in the spatial domain and therefore we need to calculate the inverse Fourier transform:

$$\mathcal{F}^{-1}\left[\hat{\mathbf{F}}(x,y,\kappa_z)\right](z) = \mathbf{F}(x,y,z) = \frac{1}{2\pi}\int_{-\infty}^{+\infty}\hat{\mathbf{F}}(x,y,\kappa_z)e^{i\kappa_z z}d\kappa_z. \tag{3.24}$$

To compute it numerically, the EM fields in the κ_z–domain are solved for a set of wavenumber values. In general, it is sufficient to use a few logarithmically spaced wavenumbers since the wavenumber spectra varies smoothly. Around $5-10$ wavenumbers per log_{10} decade, spaced evenly from about 10^{-5} to $10^{-1}m^{-1}$, is sufficient for computations involving the fields in the plane of the transmitter at $z = 0$ (Li and Key, 2007).

For strike-parallel or perpendicular sources, every EM field component is either symmetric or antisymmetric along the strike direction. The integral (3.24) can be separated into its cosine and sine counterparts, and then, depending on the parity of each EM field component, even or odd, the only non-vanishing term is the cosine or sine, respectively:

$$F(x,y,z) = \frac{1}{\pi}\int_0^{\infty}\hat{F}(x,y,k_z)cos(k_z z)dk_z, \tag{3.25a}$$

$$F(x,y,z) = \frac{i}{\pi}\int_0^{\infty}\hat{F}(x,y,k_z)sin(k_z z)dk_z. \tag{3.25b}$$

The integrals above are solved using a digital filter method (Ghosh, 1971) employing available fast algorithms (e.g. Anderson, 1983). The transformed EM fields can be seen as a kernel function $\hat{F}(\kappa_z)$ times an oscillatory function $g(\kappa_z z)$, the cosine or sine:

$$F(z) = \int_0^{\infty}\hat{F}(\kappa_z)g(\kappa_z z)d\kappa_z. \tag{3.26}$$

The kernel function is also an oscillatory function. Due to the oscillatory behavior,

standard quadrature methods can be slow to converge or even fail. The digital filter method and fast Hankel transform, have been proven to be efficient and accurate in numerous geophysical EM applications (e.g. Li and Key, 2007; Streich et al., 2011; Key and Ovall, 2011). Key (2012) investigated if the fast Hankel transform is faster than the quadrature and concluded that it is true when the integral needs to be evaluated at many offsets and the lagged convolution variant of the fast Hankel transform is applied.

Shortly, from Key (2012), the method involves considering the Hankel transform integral:

$$F(z) = \int_0^\infty \hat{F}(\lambda) J_i(\lambda z) d\lambda, \tag{3.27}$$

where J_i is an ith order Bessel function of the first kind.

Employing a coordinate transformation $z = e^x$ and $\lambda = e^{-y}$, the above integral results in:

$$e^x F(e^x) = \int_{-\infty}^\infty \hat{F}(e^{-y}) J_i(e^{x-y}) e^{x-y} dy, \tag{3.28}$$

and applying the integral convolution we obtain

$$I(x) = \int_{-\infty}^\infty \hat{F}(y) h(x-y) dy = \int_{-\infty}^\infty \hat{F}(x-y) h(y) dy. \tag{3.29}$$

The discrete approximation to the convolution is

$$I(j) = \sum_{i=-\infty}^{\infty} \hat{F}(j-i) h(i), \tag{3.30}$$

with indices i and j and the function h as a vector of linear filter coefficients. The idea of the method is to compute optimal filter coefficients for finite length filters and apply it to arbitrary kernel functions $\hat{F}$. Optimal filters coefficients are computed solving (3.30) for a length n filter using known integral transform pairs I and $\hat{F}$. The transform pairs are selected with similar characteristics as the kernels of the original integrals. Once the filters are calculated, the integral (3.26) is solved with:

$$zF(z) \approx \sum_{i=1}^{n} \hat{F}(b_i/z) h_i, \tag{3.31}$$

where the logarithmically spaced filter abscissa are:

$$b_i = z\lambda = e^{ai}, \; i = -l, -l+1, \ldots, l, \tag{3.32}$$

with $l = (n-1)/2$ and a the spacing coefficient.

Commonly, for an arbitrary oriented source, a set of strike-parallel and perpendicular point dipoles is considered. The solution is obtained solving separately the problem for each orientation (in-line and broad-side) and then superposing the resulting fields.

Streich et al. (2011) developed an alternative scheme which demonstrated to be signif-

icantly more efficient for oriented complex 3-D source geometries. This technique is based on splitting each field component into its symmetric and antisymmetric parts:

$$S(x,y,k_z) = \frac{\hat{F}(x,y,k_z) + \hat{F}(x,y,-k_z)}{2}, \tag{3.33a}$$

$$A(x,y,k_z) = \frac{\hat{F}(x,y,k_z) - \hat{F}(x,y,-k_z)}{2}, \tag{3.33b}$$

followed by the calculation of the sine and cosine integrals using a set of positive and negative values of strike-parallel wavenumbers:

$$F(x,y,z) = \frac{1}{\pi}\int_0^\infty S(x,y,k_z)cos(k_z z)dk_z + \frac{i}{\pi}\int_0^\infty A(x,y,k_z)sin(k_z z)dk_z. \tag{3.34}$$

This approximation does not assume any parity of the EM fields and therefore can be used for any orientation of the sources modeling the EM fields at once. At the same time, the integrals can be calculated using the same fast cosine and sine transform filters.

Our program distinguishes the cases when the source is oriented parallel or perpendicular to the strike or when the source is arbitrarily oriented. In the first case, it uses the known parity of the fields and calculates the integrals using only positive wavenumber values. When the source is arbitrarily oriented, the program uses the described alternative scheme and a set of positive and negative wavenumber values.

The sine and cosine integrals are numerically solved using the digital filter method and the 601−point digital filter developed by Key and Ovall (2011). The integrands of the integrals are evaluated by cubic-spline interpolation of the fields computed at the discrete wavenumbers.

When the solution is required in the $z = 0$ plane, the inverse Fourier transform is easily computed using the integral trapezoidal rule.

References

P. Amestoy, A. Guermouche, J.-Y. L'Excellent, and S. Pralet. Hybrid scheduling for the parallel solution of linear systems. *Parallel Computing*, 32:136–156, 2006.

P. R. Amestoy, I. S. Duff, and C. Vömel. Task Scheduling in an Asynchronous Distributed Memory Multifrontal Solver. Technical report, CERFACS, 2002. URL `http://www.cerfacs.fr/algor/reports/2002/TR_PA_02_105.pdf`.

W. L. Anderson. Fourier cosine and sine transforms using lagged convolutions in double-precision (subprograms DLAGF0/DLAGFI): Technical report. Technical report, U. S. Department of the Interior, Geological Survey, 1983. (Open-File Report 83-320).

I. Babuška and T. Strouboulis. *The finite element method and its reliability*. Numerical Mathematics and Scientific Computation. Oxford Science Publications, 2001.

W. Bangerth, R. Hartmann, and G. Kanschat. deal.II – a General Purpose Object Oriented Finite Element Library. *ACM Transactions on Mathematical Software*, 33(4):24/1–24/27, 2007.

R. Becker and R. Rannacher. An optimal control approach to a posteriori error estimation in finite element methods. *Acta Numerica*, 10:1–102, 2001.

R.-U. Börner. Numerical Modelling in Geo-Electromagnetics: Advances and Challenges. *Surveys in Geophysics*, 31:225–245, 2010.

P. Castillo, R. Rieben, and D. White. FEMSTER: an object oriented class library of high-order discrete differential forms. *ACM Transactions on Mathematical Software*, 31(4):425–457, 2005.

COMSOL. Comsol Multiphysics 5.1 User's Guide. *COMSOL, Burlington, MD*, 2015. URL `https://www.comsol.com/`.

M. Everett and R. Edwards. Transient marine electromagnetics: the 2.5-D forward problem. *Geophysical Journal International*, 113:545–561, 1992.

A. Franke, R.-U. Börner, and K. Spitzer. Adaptive unstructured grid finite element simulation of two-dimensional magnetotelluric fields for arbitrary surface and seafloor topography. *Geophysical Journal International*, 171:71–86, 2007.

D. Ghosh. The application of linear filter theory to the direct interpretation of geoelectrical resistivity sounding measurements. *Geophysical Prospecting*, 19:192–217, 1971.

A. V. Grayver and M. Bürg. Robust and scalable 3-D geo-electromagnetic modelling approach using the finite element method. *Geophysical Journal International*, 198:110–125, 2014.

K. Key. Is the fast Hankel transform faster than quadrature? *Geophysics*, 77(3):F21–F30, 2012.

K. Key and J. Ovall. A parallel goal-oriented adaptive finite element method for 2.5-D electromagnetic modelling. *Geophysical Journal International*, 186:137–154, 2011.

Y. Li and K. Key. 2D marine controlled-source electromagnetic modelling, Part I - An adaptive finite-element algorithm. *Geophysics*, 72(2):WA51–WA62, 2007.

Y. Mitsuhata. 2-D electromagnetic modeling by finite-element method with a dipole source and topography. *Geophysics*, 65(2):465–475, 2000.

A. Naga and Z. Zhang. The polynomial-preserving recovery for higher order finite element method in 2D and 3D. *Discrete and Continuous Dynamical Systems - Series B*, 5(30):769–798, 2005.

O. Schenk and K. Gärtner. Solving unsymmetric sparse systems of linear equations with PARDISO. *Future Generation Computer Systems*, 20(3):475–487, 2004.

C. Schwarzbach, R.-U. Börner, and K. Spitzer. Three-dimensional adaptive higher order finite element simulation for geo-electromagnetics – a marine CSEM example. *Geophysical Journal International*, 187:63–74, 2011.

J. R. Shewchuk. Triangle: Engineering a 2D Quality Mesh Generator and Delaunay Triangulator. In M. Lin and D. Manocha, editors, *Applied Computational Geometry: Towards Geometric Engineering*, volume 1148 of *Lecture Notes in Computer Science*, pages 203–222. Springer-Verlag, 1996. From the First ACM Workshop on Applied Computational Geometry.

H. Si. TetGen: a quality tetrahedral mesh generator and 3D Delaunay triangulator. 2007. URL `http://wias-berlin.de/software/tetgen/`.

C. H. Stoyer and R. J. Greenfield. Numerical solutions of the response of a two-dimensional Earth to an oscillating magnetic dipole source. *Geophysics*, 41(3):519–530, 1976.

R. Streich, M. Becken, and O. Ritter. 2.5D controlled-source EM modeling with general 3D source geometries. *Geophysics*, 76(6):F387–F393, 2011.

M. Unsworth, B. Travis, and C. A.D. Electromagnetic induction by a finite electric dipole source over a 2-D earth. *Geophysics*, 58(2):198–214, 1993.

CHAPTER 4

Numerical experiments on modeling

4.1 Introduction

This Chapter analyzes and discusses the performance and accuracy of the developed modeling software described in Chapter 3 as an implementation of the FE formulation derived in Chapter 2. As explained before, the program has been designed with the aim of modeling CSEM and MT data for a broad range of geological and experimental situations. Here, we will illustrate and validate the main characteristics and numerical strategies of the software that give rise to this versatility considering different numerical experiments on 1-D and 2-D synthetic models.

The solution computed with numerical methods is intrinsically influenced by various arbitrary decisions made by the user such as mesh design, polynomial order of the shape functions, location of model boundaries when using Dirichlet boundary conditions and accuracy in the solution of the FE linear system. Additionally for the 2.5-D CSEM problem, the set of wavenumber values are also parameters that must be given *a priori*. In this Chapter we examine the dependency between the accuracy and efficiency of the solution and each one of these parameters. Although these dependencies are well understood and many times the best accuracy is achieved by the finest and largest model, this decreases the time efficiency of the program, thus it is important to find the optimal mesh and size of the model that provides best accuracy with minimum computational time. In this context, we validate our implementation of the adaptive mesh refinement method and of the mesh group strategy presented in Chapter 3, which automatizes some of the user's arbitrary decisions on mesh design by attempting to find an optimal mesh.

On the other hand, increasing the polynomial order of the shape functions can have a similar effect on the accuracy of the solution as making the elements smaller. In general, in the tests in this chapter we use quadratic shape functions. However, we will also investigate the influence of varying the order of the polynomial shape functions on the program accuracy considering linear, quadratic and cubic functions.

Moreover, it is well documented that some physical aspects, i.e. the topography of the model, the dimensions and orientation of the controlled source or the anisotropy of

the electrical model can have a large impact on the measured MT and CSEM responses. However, many modeling programs used today can not simulate some of these features or they can do it with a low order approximation, e.g., modeling the topography with FD by a staggered interface, approximating the source as a point dipole or simplifying the degree of anisotropy. These low order approximations can result in accurate responses for some experimental and geological settings but may not work in many other situations. The numerical experiments in this Chapter are also designed to show the importance of considering a better representation of the physical problem and to validate our program on simulating these features with a higher order approximation, e.g., modeling the topography using FE and triangular unstructured grids, modeling the controlled source length and orientation and including dipping anisotropy in the problem implementation.

To benchmark our program for some of the results we present in this Chapter, we compare our results with solutions obtained with the semi-analytical open-source code DIPOLE1D[1] (Key, 2009) for land and marine CSEM 1-D models, and with the open-source and freely available FE modeling software MARE2DEM[2] (Key and Ovall, 2011) for 2-D models. DIPOLE1D allows to use any electric and magnetic source in an electrically isotropic layered media. The modeling part of MARE2DEM presents similar capabilities to our program; only the possibility to use higher-order polynomial functions for the shape functions and the possibility to consider dipping anisotropy in our program are superior to the features of the available version of MARE2DEM.

Throughout this Chapter we use specific nomenclature for two commonly used source-receiver geometries, in-line and broad-side. The in-line configuration refers to the situation when the source is oriented in the direction of the receiver position profile. In contrast, in the broad-side configuration, the transmitter is oriented perpendicular to the receiver location profile.

4.2 Influence of the model dimensions and the mesh design

Because of the Dirichlet boundary conditions, the model dimensions and the mesh design have a strong influence on the solution accuracy and proper values for these parameters are essential. There are some bounds that can be considered when fixing the size of the model and designing the mesh. These come firstly from the frequencies to model. Imposing Dirichlet boundary conditions to represent the EM fields at infinite distance, requires to place the artificial boundaries as far as possible from the sources to ensure that the fields are sufficiently attenuated. For applications dominated by induction, as the ones that concern us, the distance is usually expressed in terms of the *skin depth*. The *skin depth* is defined as the depth where the amplitude of the fields have fallen to $1/e$ of their value

[1] http://marineemlab.ucsd.edu/Projects/Occam/1DCSEM/; last visited on December, 2015
[2] http://mare2dem.ucsd.edu/; last visited on December, 2015

in the surface and for typical frequencies used in CSEM and MT can be calculated by:

$$\delta = \sqrt{\frac{2}{\omega\mu\sigma}}. \tag{4.1}$$

Then, this parameter is used as an indicator to guarantee the attenuation of the EM fields at the boundaries. Usually, the boundaries are located several skin depth away from the region of interest by increasing the node-spacing gradually. When modeling a range of frequencies in the same experiment, the outer boundaries of the model are fixed considering the lowest frequency which results in the largest skin depth.

The size of the elements in the FE mesh are also defined by the frequency to model. When modeling a range of frequencies, it is the highest frequency which constraints the size of the smallest element because the minimum wavenumber or skin depth needs to be resolved.

Generating smaller elements or augmenting the dimensions of the model increases the size of the problem and consequently the time and memory to solve it. In practice, a trade off is necessary between the gain in time efficiency obtained reducing the dimensions of the model and the loss in accuracy due to increasing the mesh elements size. It is especially useful to consider this balance in the modeling of the air layer. In the air the skin depth is very large and therefore the model should be very big. Accordingly, it is interesting to study how the change in the air layer thickness affects the solution accuracy in a certain model in order to reduce its dimensions to an optimum.

In the 2.5-D modeling of CSEM data the problem is first solved in the wavenumber domain, hence the spacing of the wavenumber values at which the fields are computed and the upper and lower limits of the wavenumber spectra must be specified. We find in the literature that a set of some tens of wavenumber values spaced logarithmically from around 10^{-6} to $10^{-1}m^{-1}$ are sufficient to obtain accurate responses for typical marine (e.g. Everett and Edwards, 1992; Key and Ovall, 2011) and land (e.g. Streich et al., 2011) CSEM model parameters and transmission frequencies.

The wavenumber parameter, κ_z, is related to the mesh element size and this affects the accuracy of the calculated EM fields. Mitsuhata (2000) derives an expression for a rough threshold of κ_z to obtain accurate results, that is: $\kappa_{z,max} < 1/d$, where $\kappa_{z,max}$ is the upper selected wavenumber value and d is the node spacing. This expression proposes the maximum value of κ_z based on the upper limits of κ_x and κ_y which are defined by the spatial discretization d.

The set of numerical experiments in this section is oriented to analyze the influence of the listed parameters in the solution accuracy and to validate our program for different situations. For this purpose, we consider 1-D models for which the numerical solution can be compared with the analytical or semi-analytical ones. Particularly, we concentrate in two models: a land MT model and a marine CSEM model.

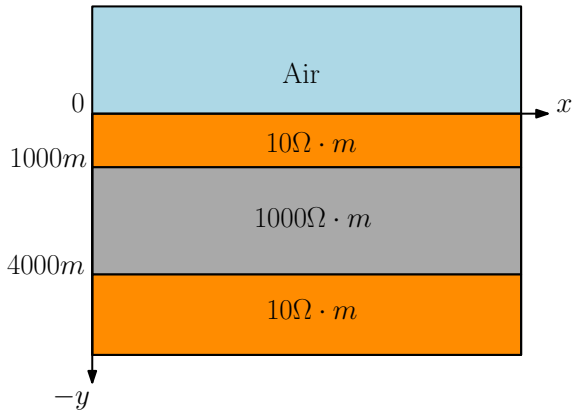

Figure 4.1: *One-dimensional resistivity model used for MT numerical tests. It consists of an air layer and three subsurface layers. The frequencies in the tests using this model are 30 values spaced logarithmically from 10^{-5} to $10^{1}Hz$.*

4.2.1 MT layered model

We simulate the MT responses of the layered model in Figure 4.1 for 30 different values of frequency spaced logarithmically from 10^{-5} to $10^{1}Hz$, a typical range of values used in MT measurements, and for different values of the model dimensions and of the mesh elements size. Then, we analyze the accuracy resulting from the different combinations of parameter values comparing the responses with the analytical solution.

The model in Figure 4.1 consists of an air layer and three subsurface layers with resistivities $10\Omega \cdot m, 1000\Omega \cdot m$ and $10\Omega \cdot m$, and thicknesses $1km$, $3km$ and 'semi-infinite', meaning that extends to the model boundary. The resistivity of the air is taken finite with a value of $10^{9}\Omega \cdot m$ in all the models we examine in this Chapter. The receivers are assumed to lay buried in the first subsurface layer, at $0.1m$ depth. The skin depth for the lowest and for the highest frequency with the resistivity of the receiver's layer is $\delta \approx 5 \times 10^{5} m$ and $\delta \approx 500m$ respectively, and in the air layer is $\delta \approx 5 \times 10^{9} m$ and $\delta \approx 5 \times 10^{6} m$. As mentioned before, the skin depth for the lowest frequency constraints the model dimensions and the skin depth for the highest frequency bounds the mesh elements size.

Taking into account these values we will determine the appropriate parameter values to obtain accurate responses. We consider four model variants with dimensions: $1 \times 10^{5}, 5 \times 10^{5}, 1 \times 10^{6}$ and $5 \times 10^{6} m$, and all with the same fixed mesh elements size of $500m$. Additionally, we study two more models, both with the same model dimensions of $5 \times 10^{6} m$ and with different minimum element sizes: $250m$ and $1000m$, respectively. All the models are square shaped and centered at $x = 0, y = 0$.

The TM mode errors of the apparent resistivity and of the phase between the numerical and the analytical solutions for the different models are shown in Figure 4.2 as a function of frequency. The results are for a receiver located in the center of the model. Accordingly, the distance to the outer boundary is half of the side length value given in the legend, that is $5 \times 10^{4} m, 2.5 \times 10^{5} m, 5 \times 10^{5} m$ and $2.5 \times 10^{6} m$.

Examining the relative errors of the apparent resistivities (Figure 4.2 left), when the

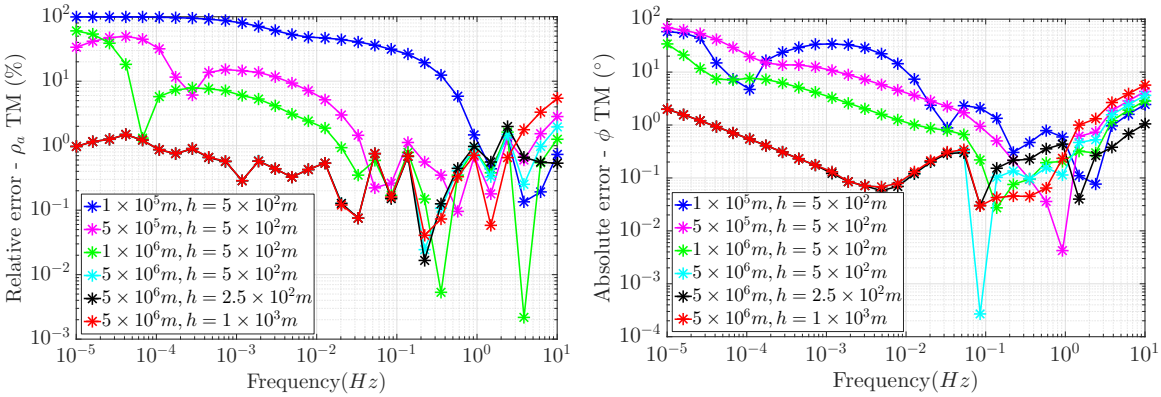

Figure 4.2: *Relative error of the TM apparent resistivity (left) and absolute error of the TM phase (right) as a function of frequency, calculated from the responses of the 1-D MT layered model (Figure 4.1) and the analytical solution, for different model dimensions and mesh element sizes (in colors). All the models are centered in* $(0,0)$*, and the given values in the legend are the side length and the approximate value of the mesh elements edge length,* h*, in the receivers locations.*

distance to the boundary is $5 \times 10^4 m$, a value much smaller than the skin depth for the lowest frequency, the relative error is between 1 and 10% for all the frequencies larger than $1Hz$ and up to values of 100% for lower frequencies. Increasing the model dimensions, decreases the error for a large number of low frequencies, as expected. However, only when the model is $5 \times 10^6 m$ side the relative error is approximately smaller than 1% for all the frequencies. For this model, the boundary is at $2.5 \times 10^6 m$ distance from the receiver, that is a larger value than the skin depth for the lowest frequency in the $10\Omega \cdot m$ layer, but still smaller than the skin depth in the air for the same frequency.

In the same Figure, the effect of reducing the mesh element size to half of its value, $250m$, to the largest model, results in a gain in accuracy for the largest frequencies. The relative error decreases to values smaller than 0.7%. Contrarily, the effect of increasing the element mesh size in the same model to $1000m$, increases the error to a value of approximately 6% at the frequency of $10Hz$. The effects of varying the model dimensions and the mesh elements size in the phase (Figure 4.2 right) are similar to the effects in the amplitude, and the best results, with an absolute error of less than 2° are obtained for the model with $5 \times 10^6 m$ side, and $250m$ element edge length.

Although the best results for the tested cases are, as expected, for the largest model with smallest element size, the results for the largest model with $h = 500m$ are also acceptable for all the frequencies in the range. It is also important to emphasize that if we would not model the complete range of frequencies comprising several orders of magnitude at the same time, we could use a fine mesh with small model dimensions for the largest frequencies and a coarse mesh with large model dimensions for the lower ones.

In Table 4.1 we give information of the number of mesh elements and of the number of DOFs used to compute the solution for each model. The number of DOFs includes both the DOFs of E_z and of H_z using quadratic shape functions. We observe that the number of elements increases largely when augmenting the model dimensions or reducing the mesh

Table 4.1: *Numerical data of tests with the 1-D MT model varying the model dimensions and mesh elements size. Length of the model side, length of the edges of the elements at the receivers locations, number of mesh elements, number of DOFs and run time. The models are square shaped and centered at $x = 0, y = 0$ and the mesh is the same for all frequencies in each case and fixed before the computations (not adaptive). The number of DOFs includes the DOFs for E_z and H_z using quadratic shape functions. The run time values are the time to factorize and solve the system matrix for E_z and H_z, and for the 30 frequencies, using an INTEL i7 4 GHz quad-core processor and 16 GB RAM desktop computer.*

Model size (m)	$h(m)$	**Num. of elements**	**Num. of DOFs**	**Run time** (s) $(30 freq.)$
1×10^5	500	9124	36690	12
5×10^5	500	50018	200314	72
1×10^6	500	97548	390450	141
5×10^6	500	533776	2135402	863
5×10^6	250	1114840	4459690	1895
5×10^6	1000	208622	834758	315

element size. The unstructured mesh can accommodate large elements far from the receivers locations and small elements closed to them, however in these tests we are using a fixed mesh, not adaptive, and the elements in all the layer where the receivers are located are set to a small size, so when the model augments laterally or the elements in this layer are refined, the number of elements increases significantly. In the same Table we provide the run time for each model which includes the time of factorization and solution of the system for both E_z and H_z for the 30 frequencies using an INTEL i7 4 GHz quad-core processor and 16 GB RAM desktop computer. When the model is small, it takes only $12s$ to factorize and solve the system matrix 30 times, however for a larger model and with finer elements it takes $1895s$.

Finally, in Figure 4.3 we show, for both the TE and the TM modes, the apparent resistivities and phases and the corresponding relative and absolute errors, comparing the numerical and analytical solutions, as functions of frequency for the model with $5\times10^6 m$ side and with $250m$ mesh element edge length. The apparent resistivities coincide for both modes and the phases have a difference of 180°. The apparent resistivities at the highest and at the lowest frequencies are asymptotic to $10\Omega\cdot m$, the resistivity of the first and of the third layers. The frequencies in between are about $25\Omega\cdot m$, indicating a resistive layer. The phases at the highest frequency start at 45° and return to this value at lower frequencies. At the frequencies between, they decrease to approximately 20°.

The observed behavior is expected for MT responses in 1-D models, and as shown, the numerically computed responses are very accurate for all the frequencies when compared to the analytical solution, with relative errors in the apparent resistivities of approximately less than 1%, and absolute errors in the phases of generally less than 1°. Only, for the highest and lowest frequencies, the error is slightly larger, but still smaller than 3% in the resistivities, and less than 2° in the phases.

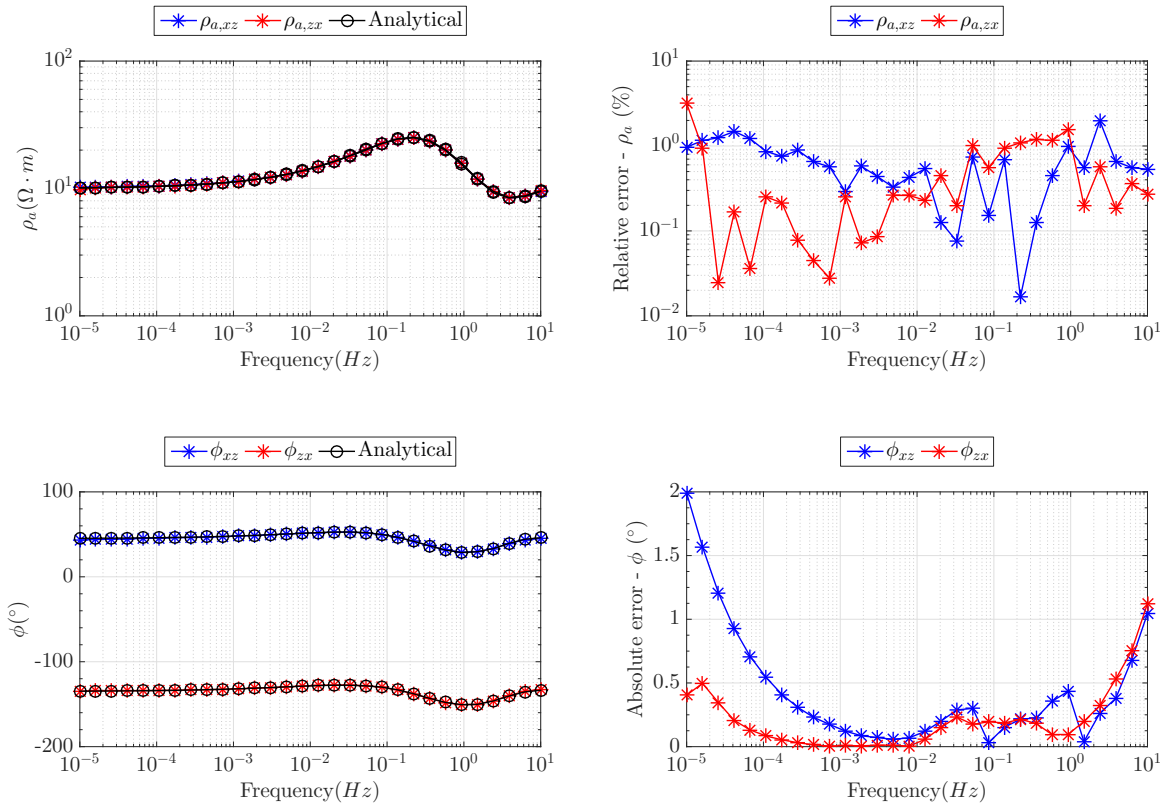

Figure 4.3: *Apparent resistivity (top left), relative error of the apparent resistivity (top right), phase (bottom left) and absolute error of the phase (bottom right) as a function of frequency, for the 1-D MT layered model in Figure 4.1. The error is calculated between the FE numerical solution and the analytical solution. The model used in the numerical calculations has* $5 \times 10^6 m$ *side length and elements edge length* $h = 250m$ *in the receivers locations.*

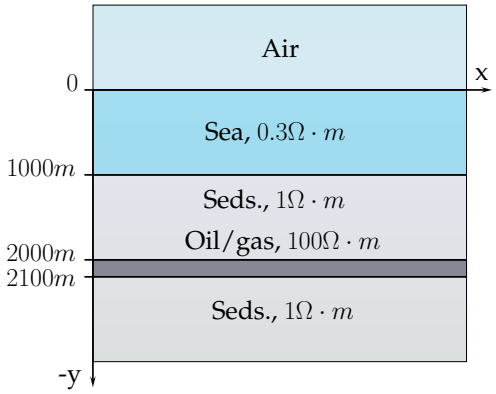

Figure 4.4: *One-dimensional canonical disc resistivity model for marine CSEM proposed by Weiss and Constable (2006). It comprises an air layer, a $1km$ seawater layer and a resistive reservoir of $100\Omega \cdot m$, which could be oil or gas, embedded in a sedimented background of $1\Omega \cdot m$. The reservoir is $100m$ thick and is located at $2km$ depth, $1km$ below the seafloor. The source is located $100m$ above the seafloor and operates at $0.25Hz$ and the receivers are positioned at $0.5m$ above the seafloor, along the x spatial dimension.*

4.2.2 Marine CSEM: one-dimensional canonical model

We conduct numerical experiments to study the influence of the mesh design, the wavenumber parameter, the order of the shape functions and the model dimensions on the solution accuracy for a marine CSEM model.

The model considered for these experiments is the 1-D reservoir canonical model proposed by Weiss and Constable (2006) and displayed in Figure 4.4. The 1-D reservoir canonical model is representative of a large, deepwater oil or gas field. It consists of an air layer, a $1km$ seawater layer with $0.3\Omega \cdot m$ resistivity, a sedimented seafloor with $1\Omega \cdot m$ resistivity, and a $100m$ thick, $100\Omega \cdot m$ reservoir layer at $1km$ depth. The higher resistivity of the reservoir layer is characteristic of the replacement of porewater by resistive hydrocarbons, but could also result from, basaltic sills, carbonates or evaporite layers.

We employ an x–directed horizontal electric point dipole source, transmitting at a frequency of $0.25Hz$ and located at $x = 0, z = 0$, and $100m$ above the seafloor. A linear array of 20 receivers is positioned along the seafloor from -10 to $10km$. The model dimensions are $60km$ wide and $40km$ long, with $20km$ of air layer, except for the experiments studying the influence of the model dimensions on the solution accuracy.

The solution for this model is first computed using three different meshes plotted in Figure 4.5. For these three tests the shape functions are quadratic. The first mesh has an element edge size of around $300m$ in the receivers locations layer. The second and third meshes are a result of uniform refinements of the second and third layers (from top to bottom) of the first mesh with elements edge size of $100m$ and $50m$, respectively. The EM responses in the wavenumber domain are calculated using 28 discrete wavenumber values distributed logarithmically between 10^{-4} and $10^{-1}m^{-1}$.

Figure 4.6 shows the real and imaginary parts of the wavenumber domain in-line electric field, $\hat{E}_x$, as a function of wavenumber κ_z from a receiver located in $x = 1000m$,

$y = -999.5m$, for the three different meshes. We observe that the electric field is constant for κ_z values smaller than $3 \times 10^{-3} m^{-1}$ for all meshes. For higher values of κ_z the fields decay rapidly and at highest values, the fields stop to decay and begin to oscillate. The wavenumber value at which the oscillations occur depends on the mesh used for the calculation of the field. The electric field computed with the mesh with edge element $h \approx 300m$ presents oscillations for $\kappa_z > 1 \times 10^{-2} m^{-1}$. When using the mesh with $h \approx 100m$ the oscillations are for $\kappa_z > 3 \times 10^{-2} m^{-1}$, and when using the third mesh with $h \approx 50m$ the oscillations are for $\kappa_z > 6 \times 10^{-2} m^{-1}$.

Taking into account that the shape functions in this example are quadratic, the node spacing d for each mesh is then $h/2$: $150m, 50m$ and $25m$. If we apply the expression for the maximum effective κ_z given by Mitsuhata (2000), we obtain $\kappa_{z,max} < 6.7 \times 10^{-3}$ for $h \approx 300m$, $\kappa_{z,max} < 2 \times 10^{-2}$ for $h \approx 100m$ and $\kappa_{z,max} < 4 \times 10^{-2}$ for $h \approx 50m$. These values coincide approximately with the beginning of the oscillations and indicate that fields for higher wavenumbers are meaningless and should not be added to the computation of the Fourier inverse transform. Therefore, it is important to check that the relation given by $\kappa_{z,max} < 1/d$ is fulfilled before computing the solution, to decrease the mesh element size or take a smaller value for the upper wavenumber in case it is necessary.

Next, we analyze the results of two experiments changing the polynomial order of the Lagrangian shape functions to linear ($p = 1$) and to cubic ($p = 3$), and we compare them with the results from varying the mesh element size. When augmenting the polynomial order, nodes are added in the midpoints between the nodes of the previous polynomial, thus we expect similar results between decreasing the mesh element size to half of its value and increasing the polynomial order by one. The results for both experiments are plotted in Figure 4.7. The relative error of the amplitude and the absolute error of the phase of the in-line electric field, E_x, are calculated between the numerical and the semi-analytical solutions for the different meshes with different mesh element sizes and for the different cases with different polynomial order of the Lagrangian shape functions. The different meshes used to compute these results are the plotted in Figure 4.5, with mesh elements sizes at the receivers locations of approximately: $h = 300, 100$ and $50m$. In these tests, the polynomial order of the Lagrangian shape functions is set to quadratic. In the two other tests, the polynomial order is changed to linear, $p = 1$, and to cubic, $p = 3$, but the mesh used in each one of them is the same, a mesh with $h = 100m$ at the receiver locations.

Examining the relative errors of the amplitude (Figure 4.7 left), the largest errors are obtained from the model with the largest mesh element size, $h = 300m$ and $p = 2$, and from the model with lower polynomial order, $h = 100m$ and $p = 1$. The model with $h = 300m$ and $p = 2$, has an error around 10% in the amplitudes measured for receivers located at $x = \pm 1km$ and around 1% at the rest of receivers, and the model with $h = 100m$ and $p = 1$ has an error of around 10% for all receivers and around 1% for receivers closer to the source. Decreasing the mesh element size at the receivers locations from $h = 300m$ to $h = 100m$ and $50m$ decreases the relative error to values of less than 0.3% in all receivers. The error is slightly smaller for $h = 100m$ than for $h = 50m$, contrarily of what we would expect,

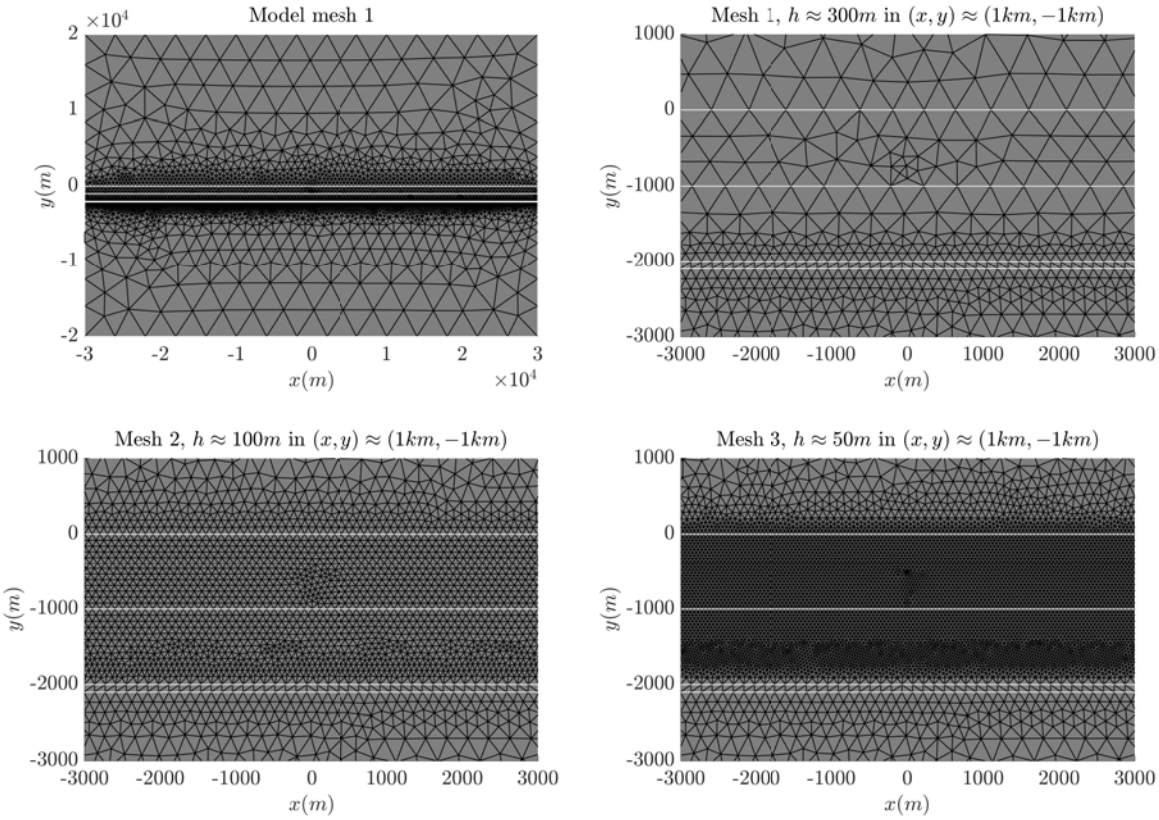

Figure 4.5: *Three different unstructured triangular meshes used in the FE computations of the wavenumber experiments for the 1-D CSEM canonical model.* ***Top left****: whole model mesh, with edge element size* $\approx 300m$ *in* $x \approx 1000m, y \approx -1000m$*, nearby a receiver location.* ***Top right****: zoom of the top left mesh.* ***Bottom left****: zoom of a second mesh with edge element size* $\approx 100m$ *in* $x \approx 1000m, y \approx -1000m$*, nearby a receiver location. The whole mesh is the same as in the top left, only in the second and third layers (from top to bottom) the triangular elements are smaller.* ***Bottom right****: zoom of a third mesh with edge element size* $\approx 50m$ *in* $x \approx 1000m, y \approx -1000m$*, nearby a receiver location. The whole mesh is the same as in the top left, only in the second and third layers (from top to bottom) the triangular elements are smaller.*

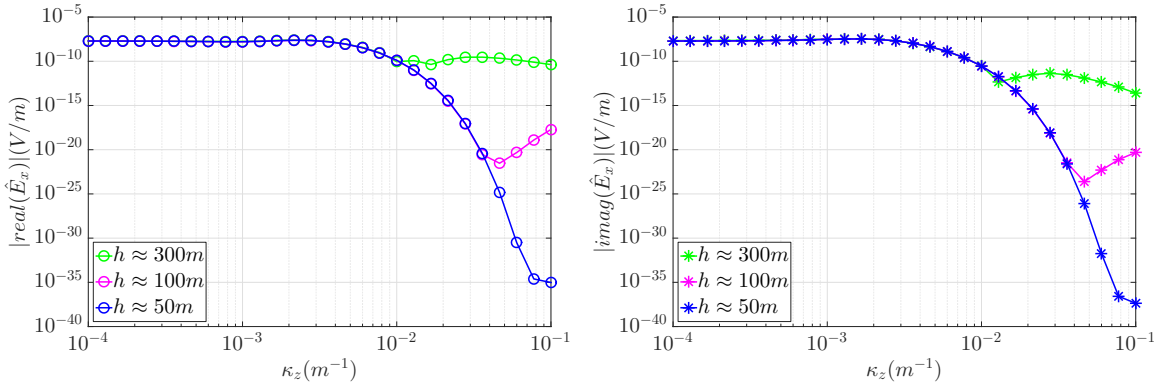

Figure 4.6: *Real (left) and imaginary (right) parts of the wavenumber domain electric field* $\hat{E}_x$ *in* $(x, y) = (1000, -999.5)m$ *as a function of wavenumber* κ_z*, computed using three different unstructured triangular meshes with edge element size* $h = 300, 100$ *and* $50m$ *in this position.*

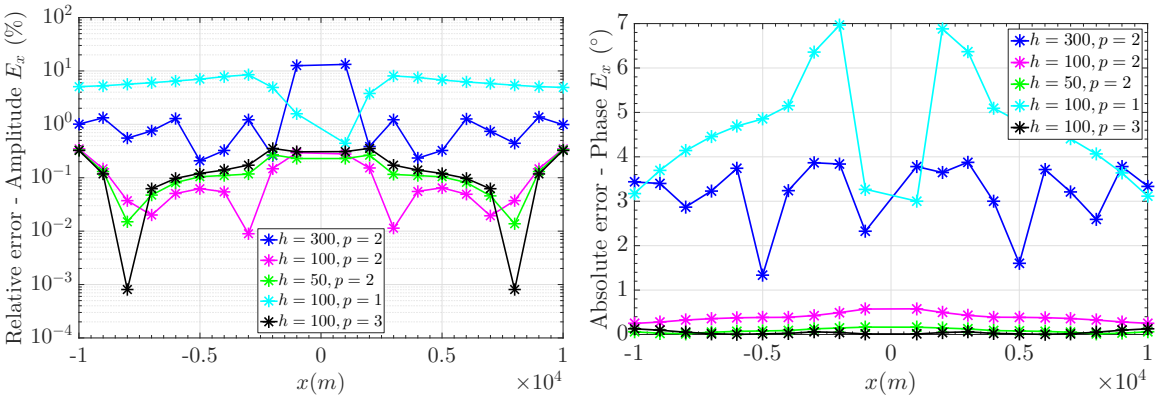

Figure 4.7: *Relative error of the amplitude of the in-line electrical field E_x (left) and absolute error of its phase (right) as a function of the x coordinate receivers locations, calculated from the responses of the 1-D CSEM canonical model and the analytical solution, for different tests varying the mesh elements size (h, edge length in m) and varying the order of the Lagrangian polynomial shape functions (p).*

and only for receivers located at $\pm 1km$, the model with $h = 50m$ has a smaller error value. We associate these small differences to oscillations of the error when it is already small enough to become independent of the mesh element size and starts to be dominated by perturbation errors (e.g., integration errors, boundary approximation errors). The rise in the polynomial order from quadratic to cubic do not diminish the amplitude relative error, the values are similar and even slightly larger than for the quadratic case with $h = 100m$ and with $h = 50m$.

Observing the absolute error of the phases (Figure 4.7 right), again the largest errors are for the models with $h = 300m$ and $p = 2$ and with $h = 100m$ and $p = 1$, with an error of less than 4° for the first model and between 3° and 7° for the second one. Decreasing the mesh element size from $h = 300m$ to $h = 100m$ and $50m$ decreases the absolute error to less than 0.6° with slightly smaller values for the model with $h = 50m$. When increasing the polynomial order to $p = 3$ we observe a small decay in the absolute error of the phases compared with the same model with $p = 2$, contrarily to the observed behavior of the amplitude relative error.

From these results we can conclude that the relative error reduces when decreasing the mesh element size or increasing the polynomial order, as expected, and that the reduction of the mesh elements size has more effect for receivers closer to the source. However, when the mesh element size is $h = 100m$ and the polynomial order is quadratic, the amplitude relative error and the phases absolute error do not change significantly if we reduce the size of the elements or increase the order of the polynomial, and the improvement in the accuracy is only observed in the phases. The reason could be that for a mesh with elements of this size, the error is not related anymore to the FE approximation, but to the perturbation error. For a frequency of $0.25Hz$, the skin depth, δ, in the sea water is about $550m$ and in the sediments is about $1000m$, so the mesh with element size $100m$ is already $(1/5)\delta$. On the other hand, reducing the polynomial order to linear for the same mesh with elements

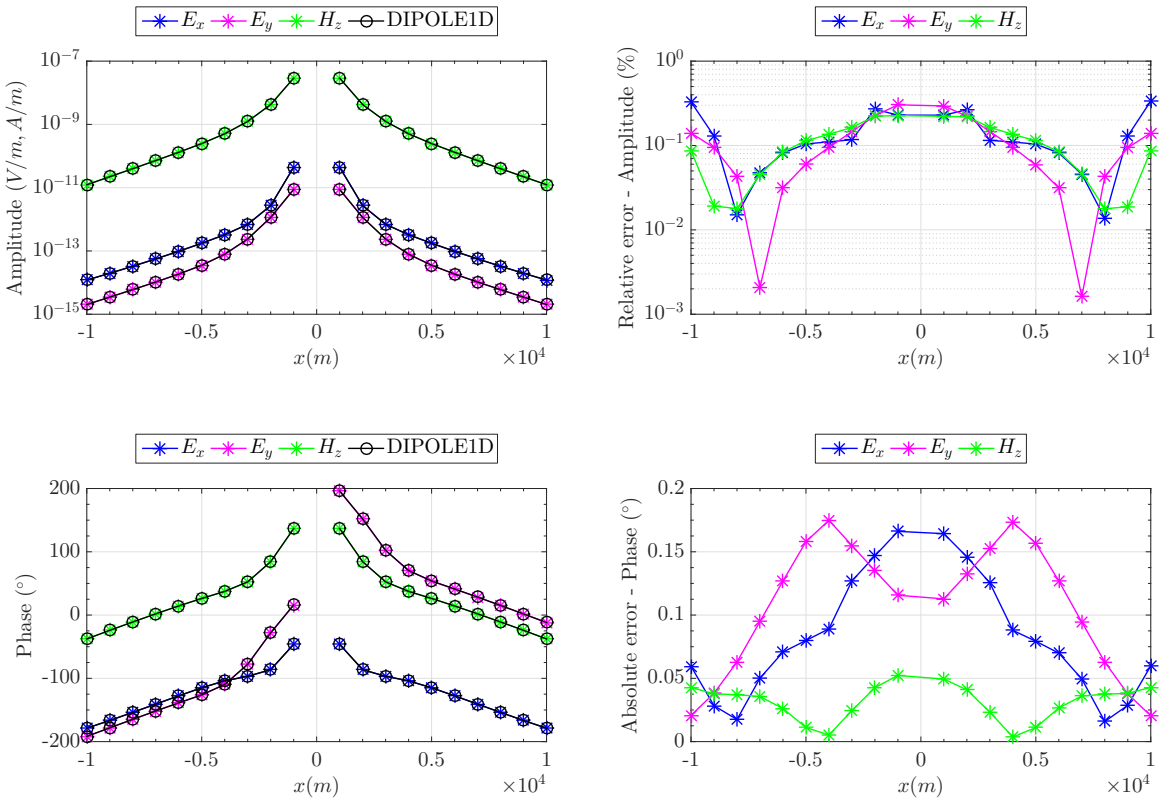

Figure 4.8: *Amplitude, phase, amplitude relative error and phase absolute error of the electric field components E_x, E_y and of the magnetic field component H_z as a function of the $x-$coordinate receivers position for the 1-D canonical model computed with mesh 3 in Figure 4.5.* ***Top left:*** *Amplitude of E_x, E_y and H_z as a function of the $x-$coordinate receivers computed with FE (in colors) and with the semi-analytical code DIPOLE1D (in black).* ***Top right:*** *E_x, E_y and H_z amplitude relative error between the FE solution and the semi-analytical solution obtained from DIPOLE1D.* ***Bottom left:*** *Phase of E_x, E_y and H_z as a function of the $x-$coordinate receivers computed with FE (in colors) and with the semi-analytical code DIPOLE1D (in black).* ***Bottom right:*** *Absolute error of the E_x, E_y and H_z phase, between the FE solution and the semi-analytical solution obtained from DIPOLE1D.*

size $100m$, increases the error and supports our conclusion.

The amplitude and phase of all the non-zero field components, E_x, E_y and H_z, computed numerically using the finest mesh in Figure 4.5 ($h \approx 50m$ at the receivers locations) are shown in Figure 4.8 as a function of the x receivers position, together with the semi-analytical solution computed with DIPOLE1D (Key, 2009). The relative errors in the amplitudes and absolute errors in the phases, between the numerical and the semi-analytical solutions, are also plotted and show the results are accurate with amplitude relative errors smaller or equal to 0.3% and phase absolute errors smaller than 0.2 degrees.

In the last experiments with this model, we study the accuracy of the solution when reducing the model dimensions. The skin depth at $0.25Hz$ is: in the air with resistivity $10^9 \Omega \cdot m$, $\delta \approx 3 \times 10^7 m$, in the seawater with resistivity $0.3\Omega \cdot m$, $\delta \approx 550m$, and in the first layer with resistivity $1\Omega \cdot m$, $\delta \approx 1000m$. The seawater layer, where the source and receivers are located, strongly attenuate the EM fields, so for a marine model the overall model dimensions can be reduced compared to a land model. In the tests above we already used appropriate model dimensions, a $60km \times 40km$ model. In the next experiments, the

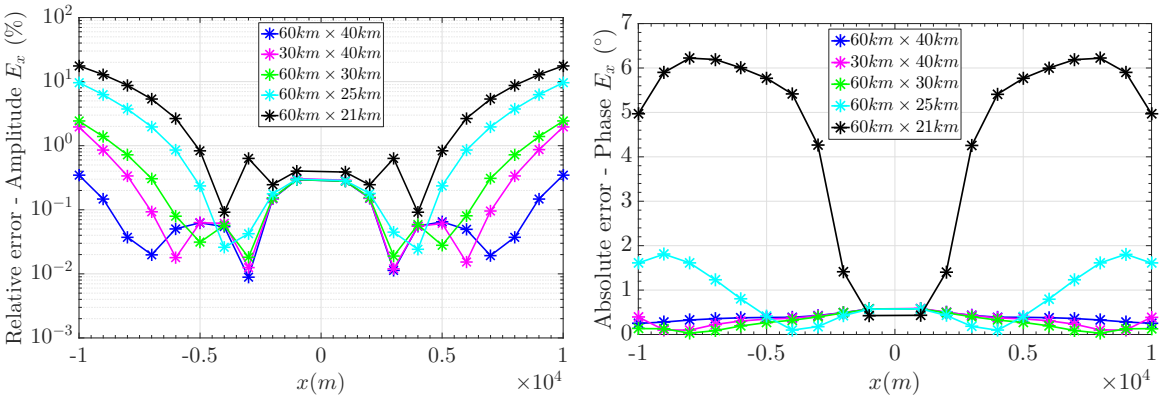

Figure 4.9: *Relative error of the amplitude of the in-line electric field component E_x (left) and absolute error of its phase (right) as a function of the x coordinate receivers locations, calculated from the FE responses of the 1-D CSEM canonical model and the semi-analytical solution, for different model dimensions (in colors). All the models are centered in 0 in the horizontal coordinate. The models with $40km$ height have $20km$ of air layer, the one with $30km$ height has $10km$ of air layer, the one with $25km$ height has $5km$ of air layer and the model with $21km$ has $1km$ of air layer. The semi-analytical solution is calculated using DIPOLE1D.*

purpose is to study if these dimensions can be reduced without affecting significantly the solution accuracy. We execute five tests with model dimensions: $60km$×$40km$, $30km$×$40km$, $60km \times 30km$, $60km \times 25km$ and $60km \times 21km$.

Figure 4.9 displays the relative error of the in-line electric field (E_x) and the absolute error of its phase between the numerical and the semi-analytical solutions, as a function of receiver locations for the different models. All the models are centered at $x = 0$, and they differ in the air layer: $20km$ (for the models with $40km$ height), $10km$ (for the models with $30km$ height), $5km$ (for the models with $25km$ height) and $1km$ (for the models with $21km$ height), and in the horizontal dimension: $60km$ and $30km$. All the results are computed with a similar mesh (only changing because of the dimensions of the model), with mesh element edge length $100m$ at the receiver locations, that is $(1/5)\delta$ in the seawater, and with quadratic Lagrangian shape functions.

The relative error in the amplitude is 0.3% and 0.2% in the cases for receivers located at $1km$ ($x = \pm 1km$) and $2km$ ($x = \pm 2km$) to the source, respectively, indicating the independence of the model dimensions. The error at the rest of receivers positions and for all the model dimensions cases increases with the distance to the source (located at $x = 0$). The largest error, up to 11%, occurs for the model with $1km$ air layer. Although the attenuation in the water is very high, the $1km$ air layer is not enough to avoid boundary effects on the responses. When the air layer is $5km$ ($25km$ height) the error is already less than 10%. The model with $10km$ air layer ($60km \times 30km$) and the model with $30km$ horizontal length ($30km \times 40km$) have a very similar error, with smaller values than 3% and could be acceptable if computation time is a concern. The best accuracy is achieved for the model with $60km \times 40km$ sides, with $20km$ air layer and lateral boundaries at $30km$ to the source. The relative error is, in this case, smaller than 0.3%.

The absolute error in the phase presents a similar behavior as for the amplitude when

Table 4.2: *Numerical data of tests with the 1-D CSEM canonical model varying the model dimensions, the mesh elements size and the shape function order. Model dimensions, edge element size (h), shape function order (p), number of mesh elements, number of DOFs and run time data. The meshes are plotted in Figure 4.5 and the edge element size information refers to a region around the receivers locations. The solution time data is the time employed to assemble the FE equations and to solve the resulting linear system for 29 wavenumber, κ_z, values, using an INTEL i7 4 GHz quad-core processor and 16 GB RAM desktop computer.*

Model size (km^2)	$h(m)$	p	**Num. of elements**	**Num. of DOFs**	**Run time** (s) $(29\kappa_z)$
60×40	300	2	11512	46230	19
60×40	100	2	46622	186742	71
60×40	50	2	143326	573650	258
60×40	100	1	46622	46750	17
60×40	100	3	46622	419978	188
30×40	100	2	23080	92570	40
60×30	100	2	45787	183404	68
60×25	100	2	45411	181928	71
60×21	100	2	43731	175412	68

varying the model dimensions, with the largest error of up to 6.2° for the $60\times21km$ model, and errors smaller than 0.5° for the three models with $10km$ and $20km$ air layer.

For completeness, in Table 4.2 we give some numerical data from the computations of the experiments above. It contains, for each experiment, the model dimensions, the edge element size, the shape function order, the number of mesh elements, the number of DOFs and the run time data for 29 κ_z wavenumber values. The number of DOFs includes the DOFs for both $\hat{E}_z$ and $\hat{H}_z$. The solution time is the time employed in the assemble of the FE equations and the solution of the resulting linear system for 29 values of κ_z, that is, the time spent in solving the problem 29 times, using an INTEL i7 4 GHz quad-core processor and 16 GB RAM desktop computer.

4.3 Adaptive mesh refinement

As we have shown above, the mesh design influences the solution accuracy and the time efficiency of the program. In the experiments above, the different frequency and wavenumber constraints and the possibility to benchmark the 1-D solution, helped us to find the mesh resulting in the best accuracy by trial and error. However, generally for 2-D models, the semi-analytical solution do not exist and we need another way to control and reduce the error. As discussed in Chapter 2 and Chapter 3, automated adaptive mesh refinement techniques provide a measure of FE approximation errors and use it to iteratively refine, globally or locally, the FE grid to enhance the solution accuracy.

Our FE program includes an adaptive mesh refinement algorithm as described in Chapter 3. It is based on *a posteriori* error estimate, utilizing a computed FE solution to estimate quantitatively the discretization error. Further, it is possible to use two different error es-

timators: a residual error estimator, using a L^2-norm error estimate, and a goal-oriented error estimator based on a dual-weighted residual method. With the residual error estimator the aim is to reduce the global error based on the residual of the system of equations and mesh refinement is applied for elements with estimated largest errors. On the other hand, the goal-oriented error estimator aims to reduce the error of a functional measure, in our case: $(\nabla\hat{E}_z + \nabla\hat{H}_z)|_{x_r,y_r}$, where x_r, y_r are the receiver locations. Here, the mesh is refined only on regions of the model that affect more strongly the error of the functional measure.

As discussed previously, the PDEs we are solving when modeling CSEM and MT data depend, for a certain conductivity model, on the operating frequency, the strike-directed wavenumber κ_z and on the source setup parameters. In the previous section we have shown that different values of these parameters require different mesh designs for a proper solution quality. Computing the optimal mesh for each configuration of parameters is computationally very expensive. Instead, we split the different parameters in groups of nearby values and calculate the suitable mesh applying the adaptive mesh refinement to representative values of the parameters in each one of these groups. Then, the resulting optimal mesh is used for the computation of the other parameter values of the group. We refer to 'mesh group' to the group of configurations of parameters that share the same mesh.

In this section, we validate the performance of the adaptive mesh refinement method on CSEM and MT models, on marine and land environments. Besides, we also study the accuracy of the solution when using the adaptive mesh refinement method and varying the order of the shape functions (p-refinement) from quadratic ($p = 2$) to linear ($p = 1$) and cubic ($p = 3$).

4.3.1 Validation and robustness

To validate the performance of our adaptive mesh refinement algorithm and to demonstrate its robustness, we compare our solution to the semi-analytical solution of a 1-D model.

Again, we consider the 1-D CSEM canonical model introduced in the previous section (Figure 4.4) with an in-line horizontal electric point dipole operating at a frequency of $0.25Hz$, and located in the center of the model, $100m$ above the seafloor, $(x, y) = (0, -900)m$. The set of wavenumber values to compute the solution are again 28 values distributed logarithmically from 10^{-4} to $10^{-1}m^{-1}$ and 0. We group the wavenumber values with 9 members for the adaptive mesh refinement, with $\kappa_z = 0$ and $\kappa_z = 1\times10^{-1}m^{-1}$ as individual groups, giving a total of 5 mesh groups. The representative value of the parameter κ_z in each group is the midvalue of the group, that is for each of the 5 groups: $0, 2.7826\times10^{-4}, 2.7826\times10^{-3}, 2.7826\times10^{-2}$ and $1\times10^{-1}m^{-1}$. Since we only compute the solution for one source position and for one frequency, the total number of mesh groups equals the number of κ_z groups, that is 5.

In the first test we use quadratic order Lagrangian shape functions and we apply the

goal-oriented adaptive mesh refinement algorithm with 5 iterations. The process to compute the solution with the adaptive mesh refinement mainly consists on two phases, as described in Chapter 3. In the first stage, the program computes, for the representative values of the parameters of each group, the solution of the system of equations (primal solution), the residual and the dual solution using the given goal function and calculates an elementwise error indicator. These computations are repeated iteratively until the stopping criteria is reached, refining in each iteration a fraction of elements with the worst error indicator value. For this test we set this fraction to 20%. Then, in the second stage, the obtained mesh for each group is used to calculate the solution for the remaining group members.

To illustrate this computational process, Figures 4.10 and 4.11 display from top to bottom, the solution (in the κ_z domain), the dual solution, the residual and the error indicator for $\hat{E}_z$ and $\hat{H}_z$ respectively, after a first refinement step and for the mesh group 2 with $\kappa_z = 2.8 \times 10^{-4} m^{-1}$. Examining the dual solution of $\hat{E}_z$ in Figure 4.10, the largest values are localized in the receivers positions. In a different way, the residual is larger in a region around the source that extends some kilometers laterally and in depth. As a result, the elementwise error indicator in the same Figure is largest at the receiver locations and at the source position.

The results are similar for $\hat{H}_z$ (Figure 4.11), with the largest values of the dual solution localized at the receiver positions and the largest values of the residual located around the source, but more confined to the source position than the residual of $\hat{E}_z$. The resulting error indicator is, as expected a combination of the dual solution and the residual, with larger values in the receiver positions.

Figures 4.12-4.15 illustrate the elementwise error indicator associated with $\hat{E}_z$ and the corresponding mesh, for the initial mesh and in different refinement levels. The results in each Figure correspond to a mesh group and we have excluded the figure of mesh group 1 since when $\kappa_z = 0$, $\hat{E}_z$ is 0 for the source-receiver configuration under consideration. Similarly, Figures 4.16-4.20 display the elementwise error indicator with the associated mesh at different refinement steps and for the different mesh groups, but for the dependent variable $\hat{H}_z$.

Comparing first, the elementwise error indicator associated with the variable $\hat{E}_z$ between the different mesh groups with different values of κ_z in Figures 4.12-4.15, the regions with larger error and consequently more refinement, vary depending on the magnitude of κ_z.

The elementwise error indicator for mesh group 2 with $\kappa_z^{g_2} = 2.8 \times 10^{-4} m^{-1}$ (Figure 4.12) is larger in the receiver and source locations and in the central region of the model below the resistive layer, approximately from $2km$ depth to $10km$ depth, in the initial mesh. As the adaptive mesh refinement proceeds, the mesh is mainly refined in these regions, and consequently the elementwise error indicator decreases. After the third refinement step, the elementwise error indicator has already decreased in the region below the resistive layer and the refinement continues principally in the source and receiver locations, as it

can be observed in the plot corresponding to the 5^{th} iteration (bottom panel). For mesh group 3 with $\kappa_z^{g_2} = 2.8 \times 10^{-3} m^{-1}$ (Figure 4.13), the largest error indicator is much more concentrated at the source and receiver locations, and the mesh adaption acts in this region. We also observe that, as the iterations proceed, the error decreases in the receivers locations, and the mesh adaption concentrates in the source location and in the receiver locations closer to the source. The result after the 5^{th} iteration is a finer mesh in the source location and a coarser mesh in the other regions compared to the mesh for the same iteration number of group 2 (Figure 4.12 bottom panel). This behavior is even more accentuated for mesh group 4 and 5, with $\kappa_z^{g_4} = 2.8 \times 10^{-2} m^{-1}$ and $\kappa_z^{g_5} = 1 \times 10^{-1} m^{-1}$ (Figures 4.14 and 4.15). Note that, for these figures we only show the results until the third iteration, since the error decreases faster than for mesh group 2 and 3.

The error indicator of $\hat{H}_z$ evolves similarly to $\hat{E}_z$ with the iterations of the goal-oriented adaptive mesh refinement algorithm and for the different mesh groups (Figures 4.16-4.20). The error indicator for mesh group 1 in Figure 4.16 is larger at the receiver locations and in a central region below the resistive layer. When the adaption evolves, these regions are refined and the elementwise error indicator decreases as it can be observed for iterations: 1, 3 and 5. The error indicator for mesh group 2, in Figure 4.17, is similar to the error for mesh group 1 and the adaptive mesh refinement proceeds also in a similar way, with the only difference of a large error also in the air layer some kilometers above the source, where consequently the mesh is refined too. For mesh group 3 (Figure 4.18) the error indicator is large around the source and receiver locations, as in the $\hat{E}_z$ case. Finally, the error indicator for the largest κ_z values of mesh groups 4 and 5 (Figures 4.19 and 4.20) is, for the initial mesh, large at the source and receiver locations and in the air layer, some kilometers above the receivers positions. In the first iteration of the adaptive mesh refinement, the mesh is refined in these regions and the error decreases fast in the air layer and in the most distant receivers relative to the source. In the next iterations (second and third), the largest errors are concentrated around the source location and its closest receivers, and the mesh refinement occurs in this region.

To study the evolution of the solution accuracy during the adaptive mesh refinement process, Figure 4.21 displays the relative error of the amplitude and the absolute error of the phase of the in-line electric field component compared to the semi-analytical solution for 5 mesh refinement steps of the goal-oriented adaptive mesh refinement algorithm. The error is based on the comparison of our numerical solution result to a semi-analytical result calculated using DIPOLE1D (Key, 2009). Examining the relative error of the amplitude (Figure 4.21 left), it decays mostly during the first three iterations. Initially the error is between 1% and 10%, and after the first adaptive mesh refinement iteration it decreases at all the receivers to values smaller than 1%, except at the receivers closest to the source, where the error is still larger than 5%. After a second mesh refinement step, the reduction of the error is small, and after the third mesh refinement step, the error at the receivers closest to the source decreases to values smaller than 1%, too. In the last two iterations, the 4^{th} and 5^{th} mesh refinement steps, the variations are small.

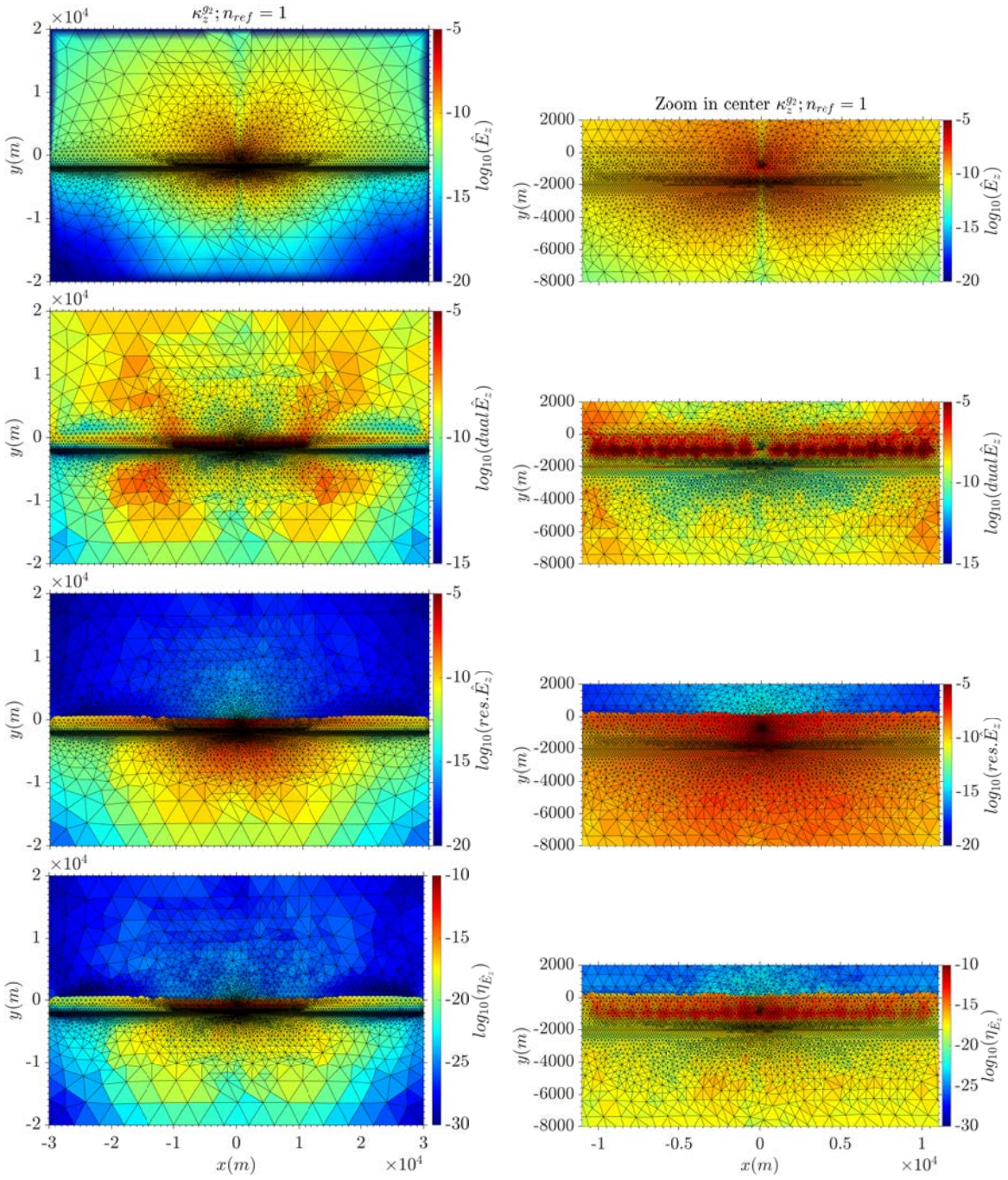

Figure 4.10: *From top to bottom: $\hat{E}_z$, dual of $\hat{E}_z$, residual and error indicator with corresponding mesh, for the parameter value $\kappa_z^{g_2} = 2.8 \times 10^{-4} m^{-1}$ after the first iteration of the goal-oriented adaptive mesh refinement algorithm for the 1-D CSEM canonical model. Plots on the right side zoom into the center where the source and receivers are located.*

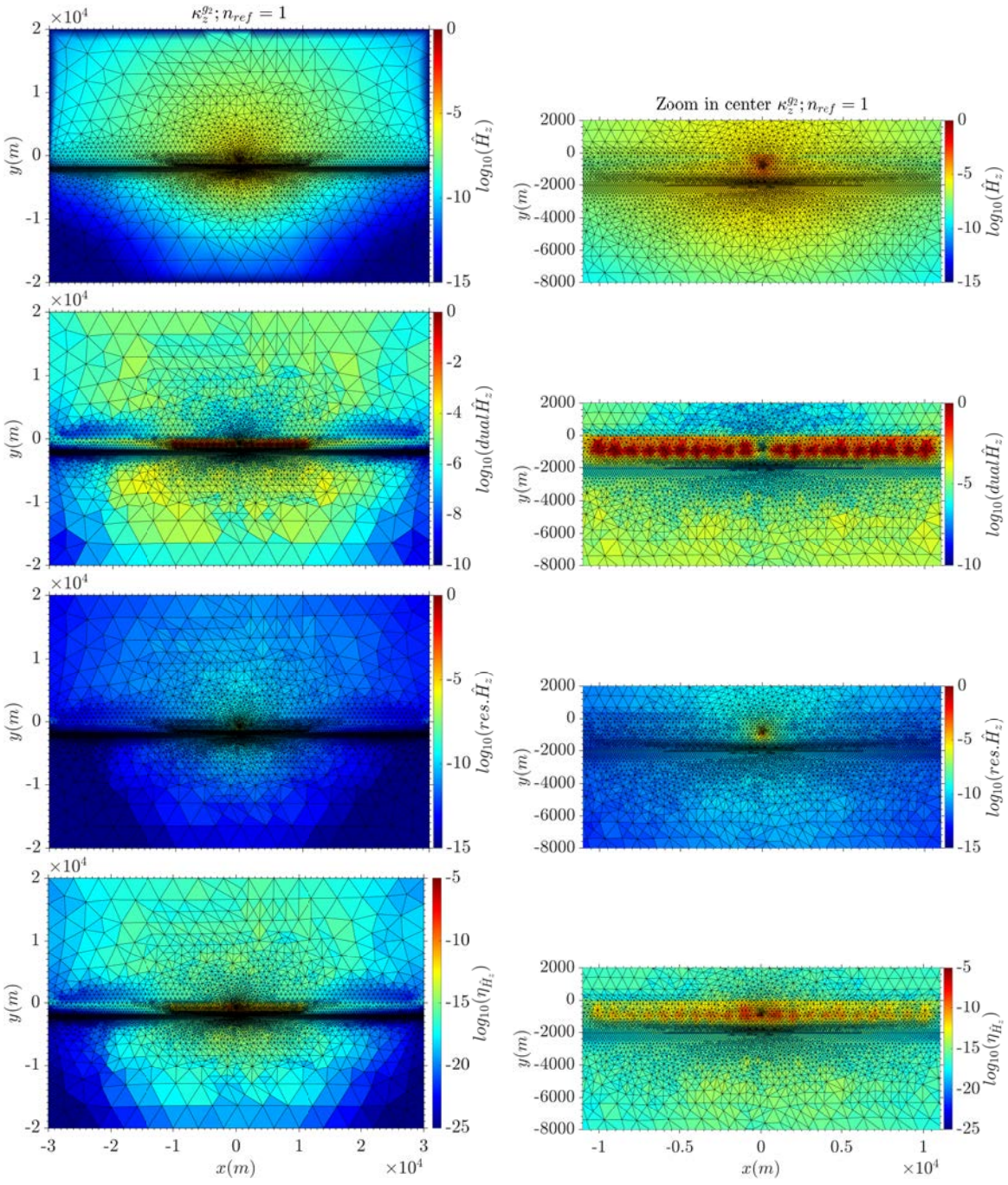

Figure 4.11: *From top to bottom: $\hat{H}_z$, dual of $\hat{H}_z$, residual and error indicator with corresponding mesh, for the parameter value $\kappa_z^{g_2} = 2.8 \times 10^{-4} m^{-1}$ after the first iteration of the goal-oriented adaptive mesh refinement algorithm for the 1-D CSEM canonical model. Plots on the right side zoom into the center where the source and receivers are located.*

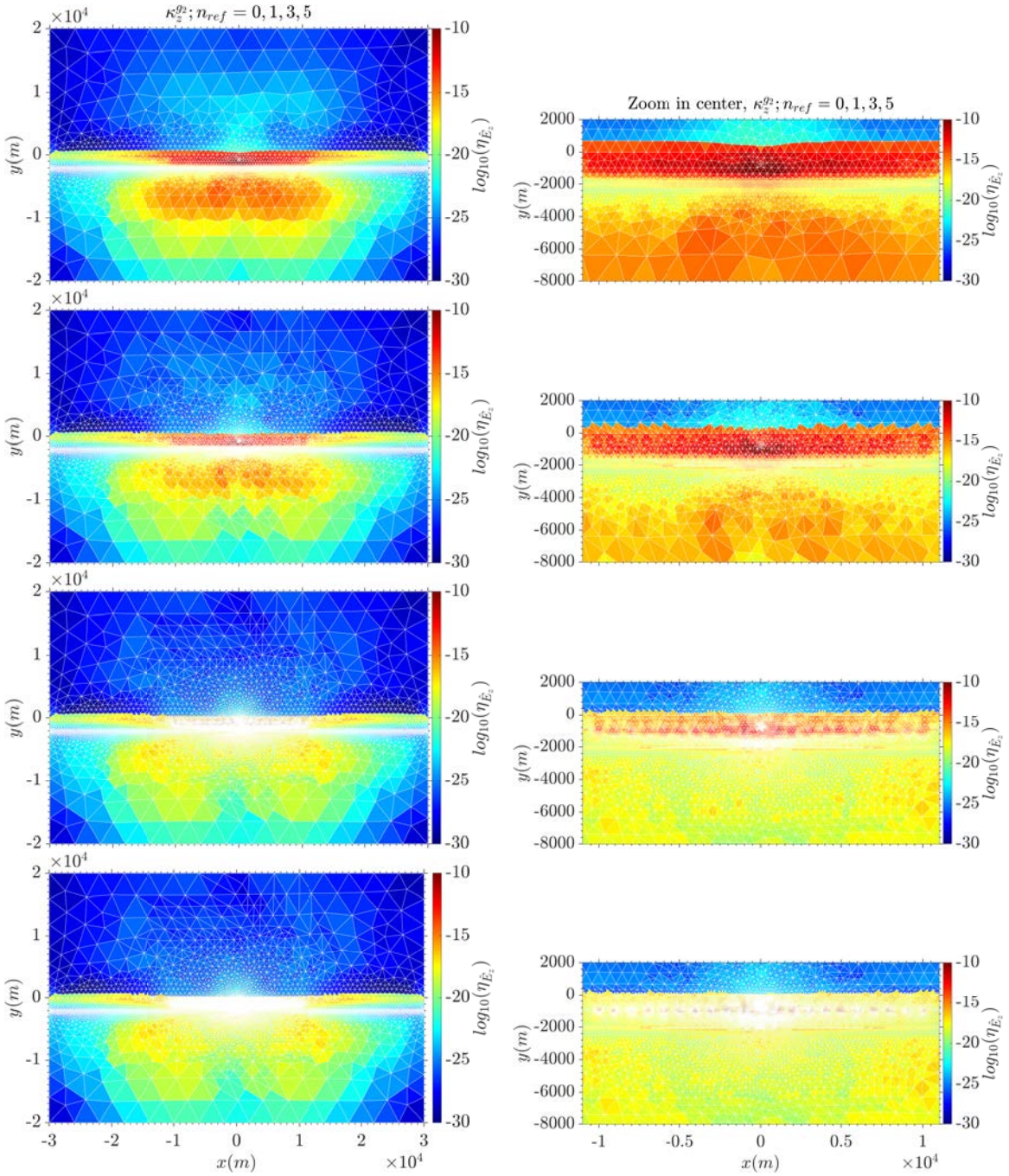

Figure 4.12: *Elementwise error indicator of the dependent variable $\hat{E}_z$ for the parameter value $\kappa_z^{g_2} = 2.8 \times 10^{-4} m^{-1}$, in different steps of the goal-oriented adaptive mesh refinement algorithm, for the 1-D CSEM canonical model and corresponding adaptive mesh. From top to bottom, error for the initial mesh and for three goal-oriented adaptive mesh refinement steps:* 1, 3 *and* 5. *Plots on the right side zoom into the center where the source and receivers are located.*

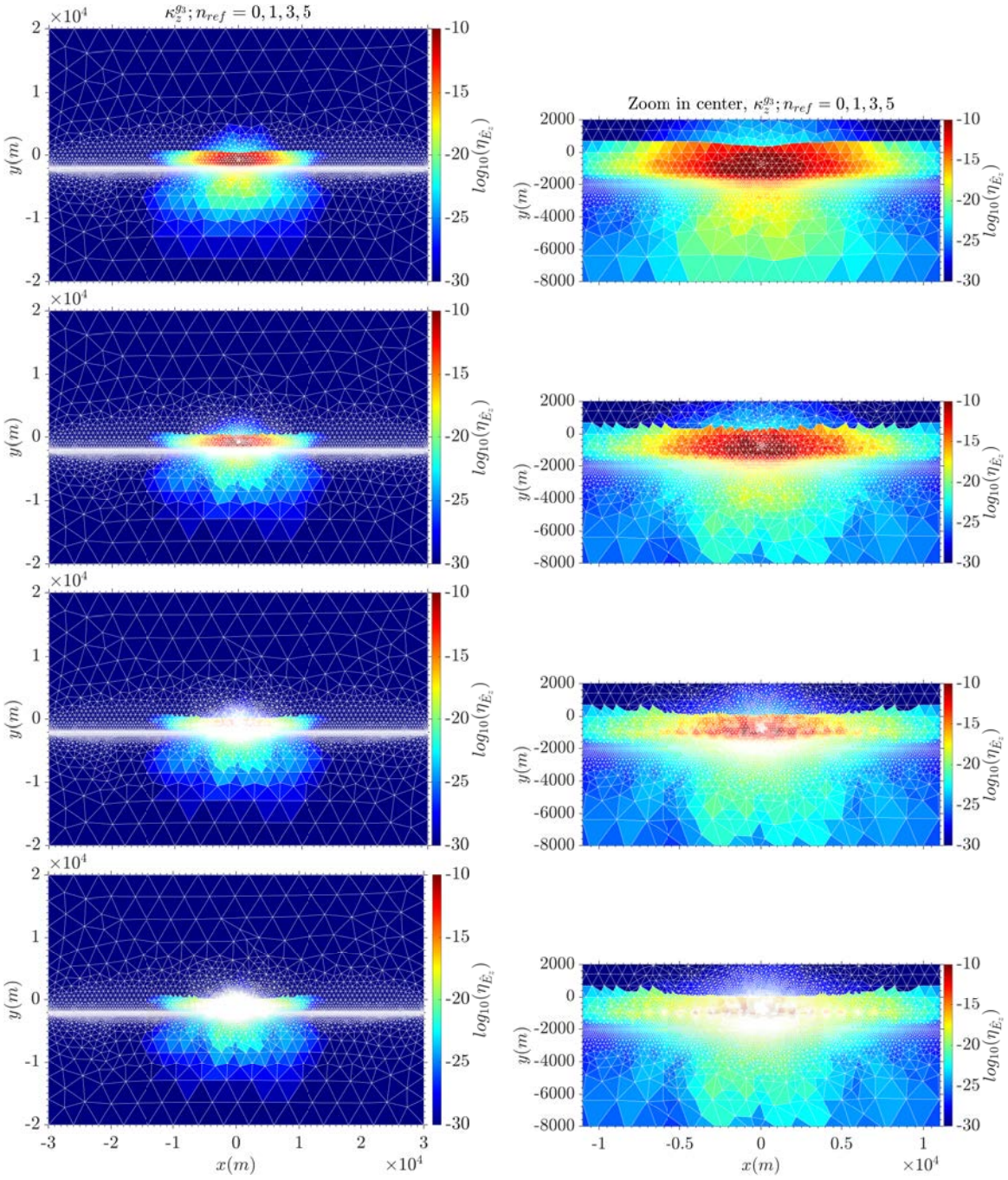

Figure 4.13: *Elementwise error indicator of the dependent variable $\hat{E}_z$ for the parameter value $\kappa_z^{g_3} = 2.8 \times 10^{-3} m^{-1}$, in different steps of the goal-oriented adaptive mesh refinement algorithm, for the 1-D CSEM canonical model and corresponding adaptive mesh. From top to bottom, error for the initial mesh and for three goal-oriented adaptive mesh refinement steps:* 1, 3 *and* 5. *Plots on the right side zoom into the center where the source and receivers are located.*

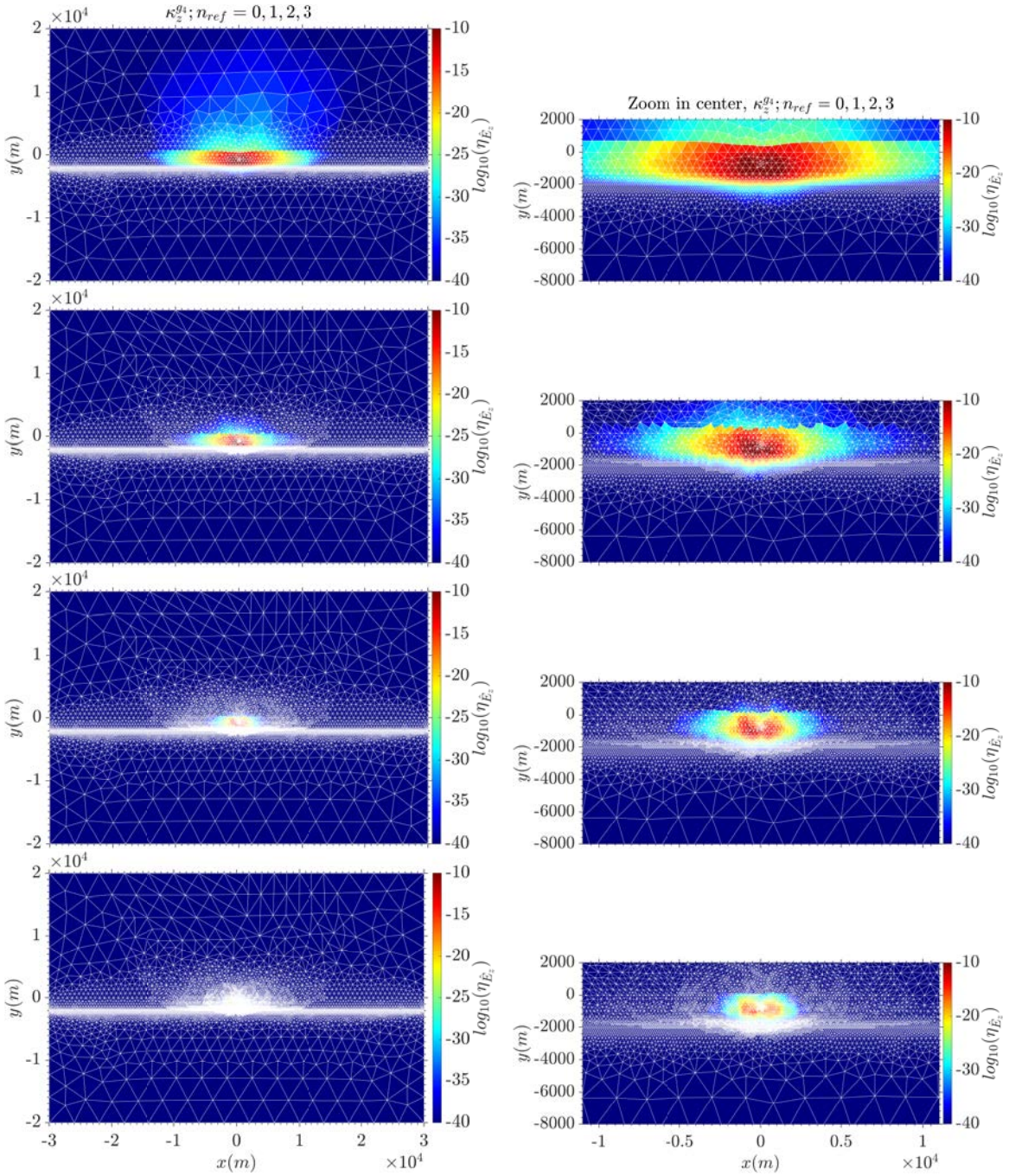

Figure 4.14: *Elementwise error indicator of the dependent variable $\hat{E}_z$ for the parameter value $\kappa_z^{g4} = 2.8 \times 10^{-2} m^{-1}$, in different steps of the goal-oriented adaptive mesh refinement algorithm, for the 1-D CSEM canonical model and corresponding adaptive mesh. From top to bottom, error for the initial mesh and for three goal-oriented adaptive mesh refinement steps: 1, 2 and 3. Plots on the right side zoom into the center where the source and receivers are located.*

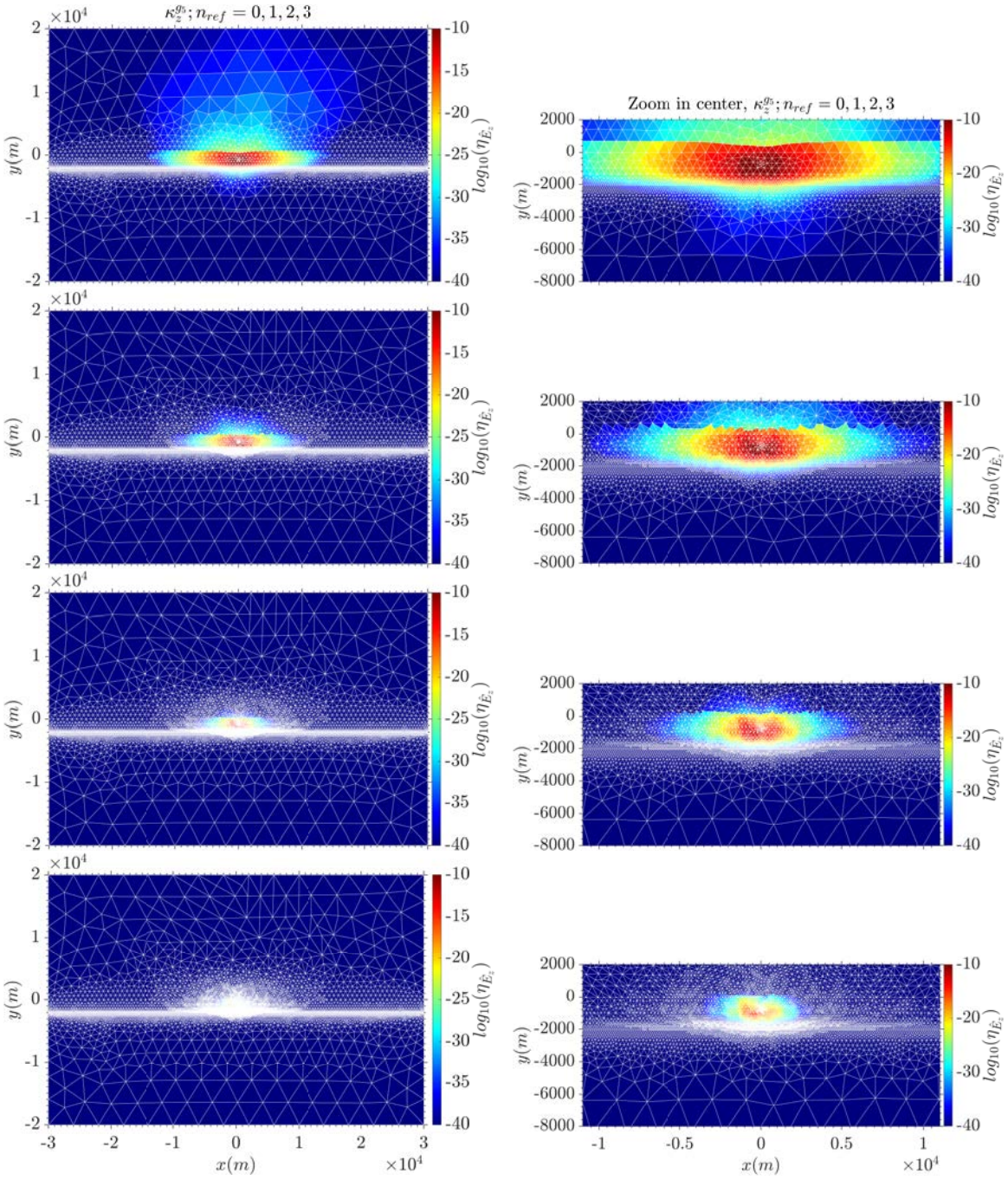

Figure 4.15: *Elementwise error indicator of the dependent variable $\hat{E}_z$ for the parameter value $\kappa_z^{g_5} = 1 \times 10^{-1} m^{-1}$, in different steps of the goal-oriented adaptive mesh refinement algorithm, for the 1-D CSEM canonical model and corresponding adaptive mesh. From top to bottom, error for the initial mesh and for three goal-oriented adaptive mesh refinement steps: 1, 2 and 3. Plots on the right side zoom into the center where the source and receivers are located.*

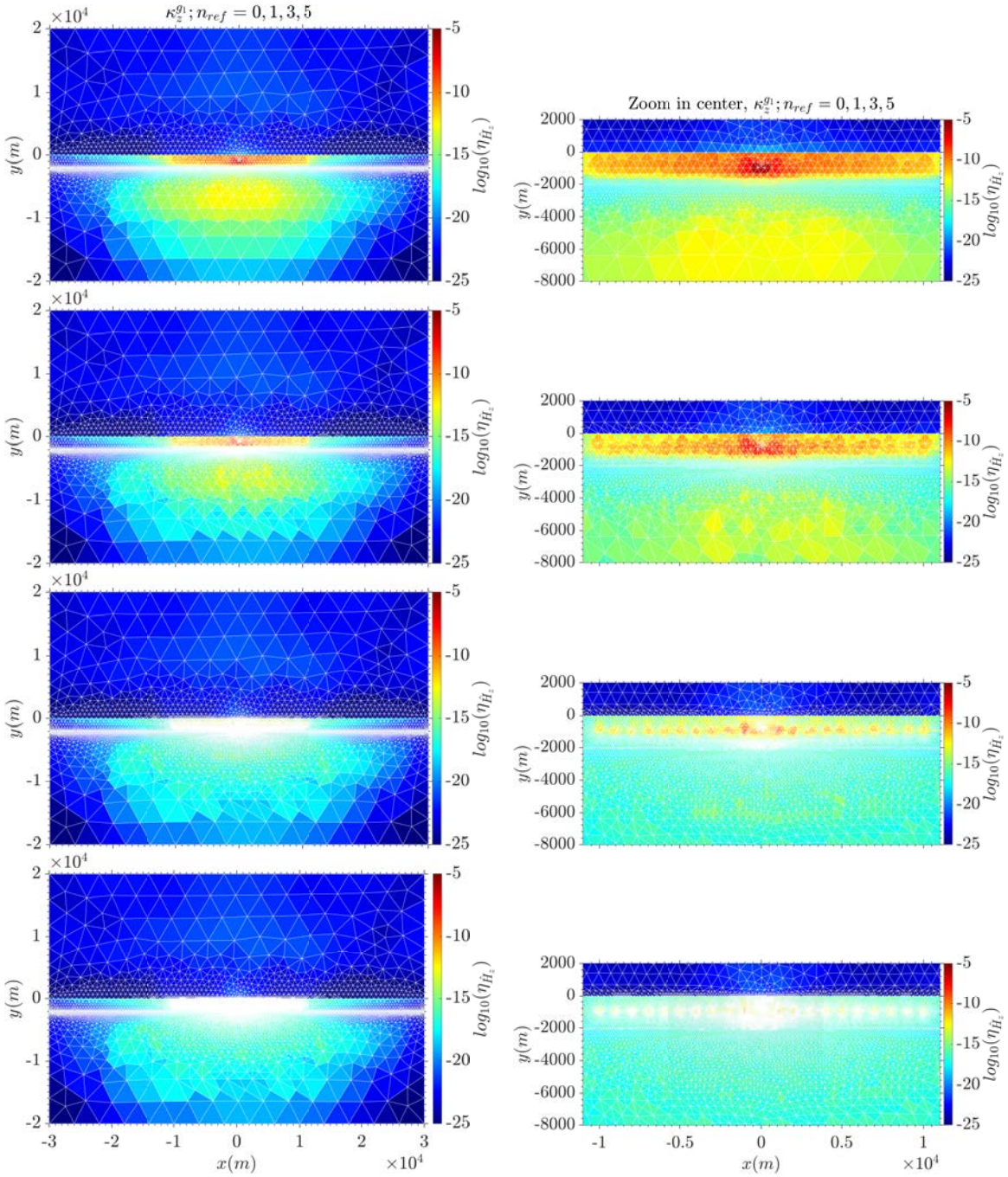

Figure 4.16: *Elementwise error indicator of the dependent variable $\hat{H}_z$ for the parameter value $\kappa_z^{g_1} = 0$, in different steps of the goal-oriented adaptive mesh refinement algorithm, for the 1-D CSEM canonical model and corresponding adaptive mesh. From top to bottom, error for the initial mesh and for three goal-oriented adaptive mesh refinement steps: 1, 3 and 5. Plots on the right side zoom into the center where the source and receivers are located.*

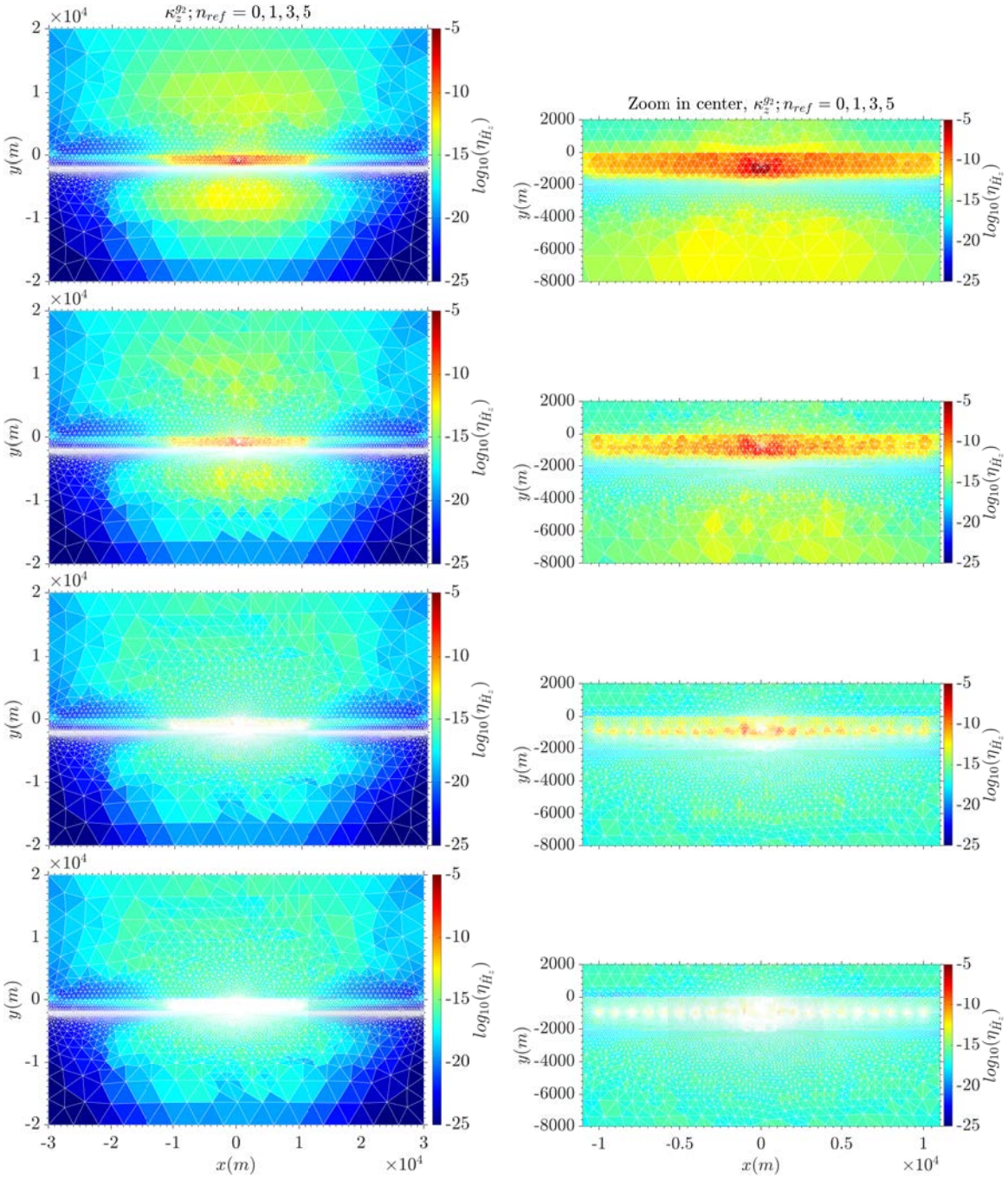

Figure 4.17: *Elementwise error indicator of the dependent variable $\hat{H}_z$ for the parameter value $\kappa_z^{g_2} = 2.8 \times 10^{-4} m^{-1}$, in different steps of the goal-oriented adaptive mesh refinement algorithm, for the 1-D CSEM canonical model and corresponding adaptive mesh. From top to bottom, error for the initial mesh and for three goal-oriented adaptive mesh refinement steps:* 1, 3 *and* 5. *Plots on the right side zoom into the center where the source and receivers are located.*

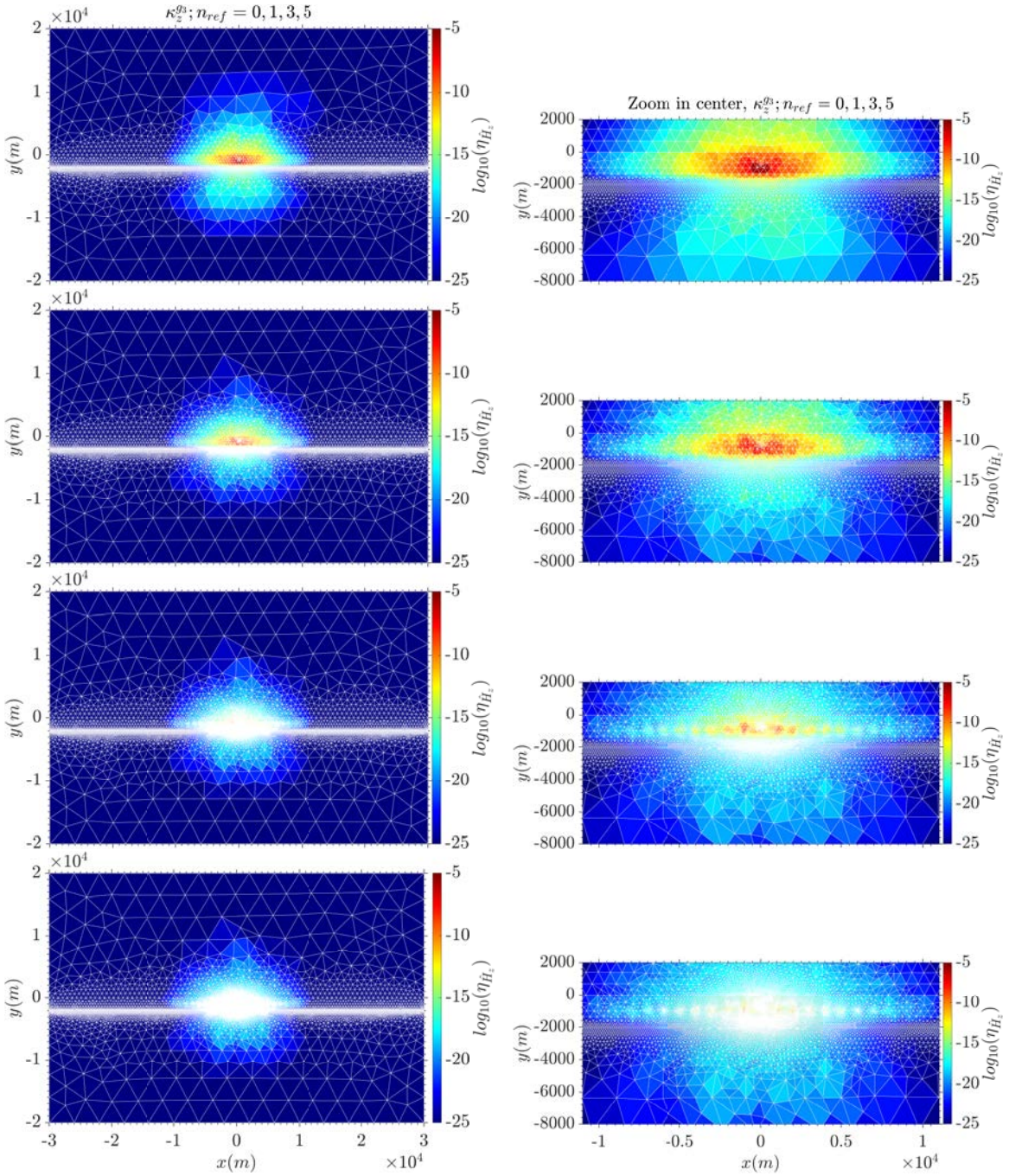

Figure 4.18: *Elementwise error indicator of the dependent variable $\hat{H}_z$ for the parameter value $\kappa_z^{g_3} = 2.8 \times 10^{-3} m^{-1}$, in different steps of the goal-oriented adaptive mesh refinement algorithm, for the 1-D CSEM canonical model and corresponding adaptive mesh. From top to bottom, error for the initial mesh and for three goal-oriented adaptive mesh refinement steps: 1, 3 and 5. Plots on the right side zoom into the center where the source and receivers are located.*

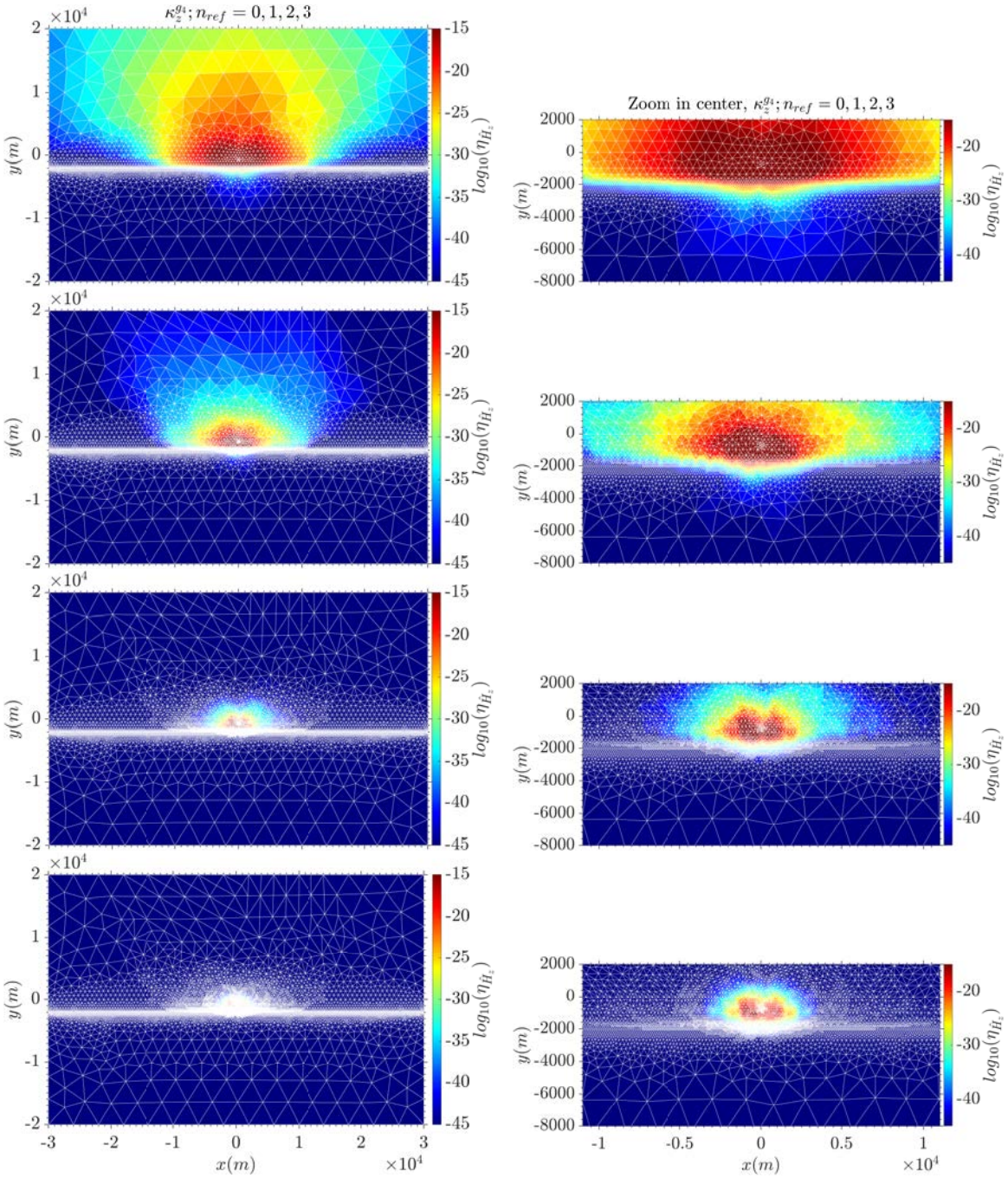

Figure 4.19: *Elementwise error indicator of the dependent variable $\hat{H}_z$ for the parameter value $\kappa_z^{g_4} = 2.8 \times 10^{-2} m^{-1}$, in different steps of the goal-oriented adaptive mesh refinement algorithm, for the 1-D CSEM canonical model and corresponding adaptive mesh. From top to bottom, error for the initial mesh and for three goal-oriented adaptive mesh refinement steps: 1, 2 and 3. Plots on the right side zoom into the center where the source and receivers are located.*

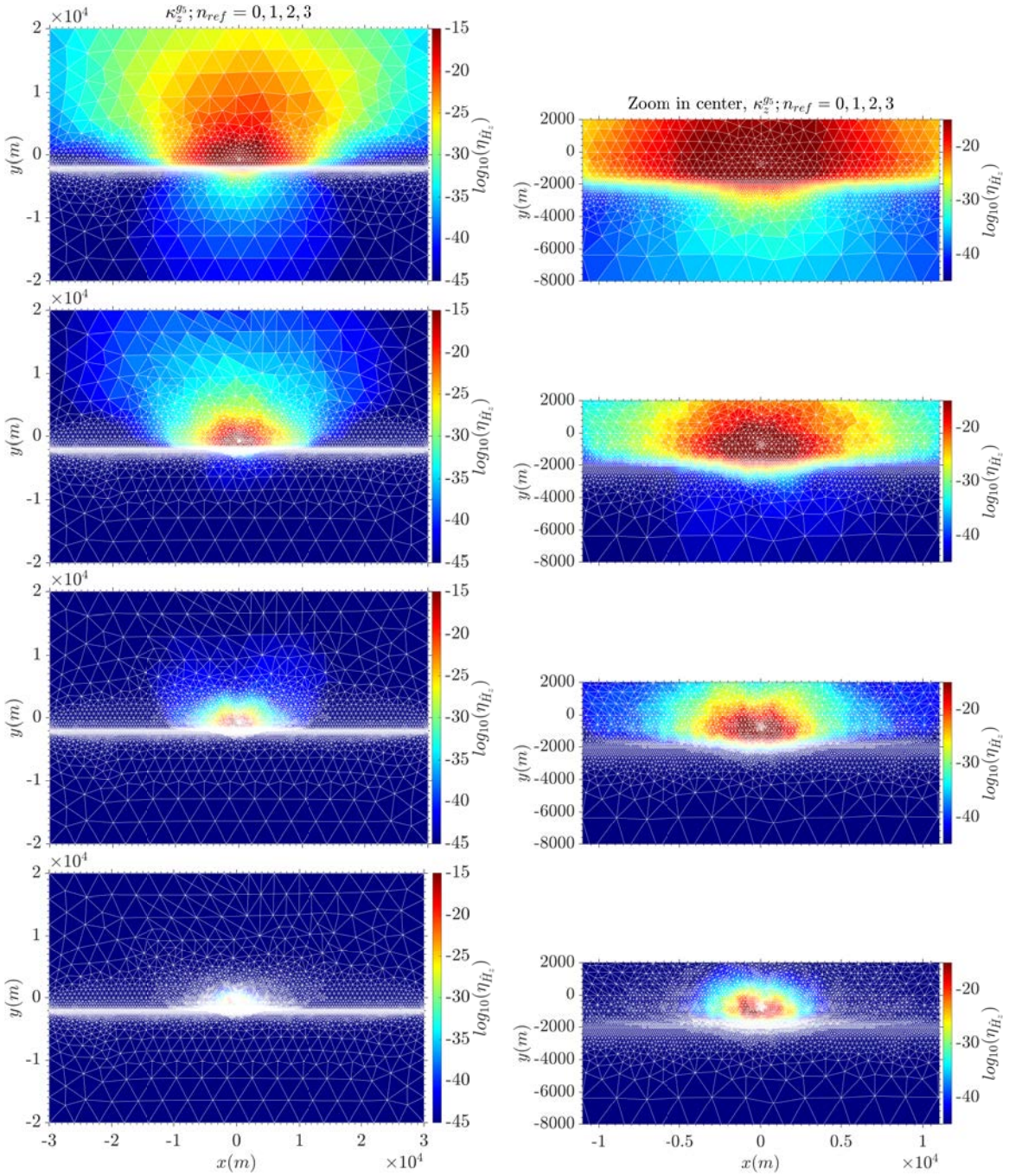

Figure 4.20: *Elementwise error indicator of the dependent variable $\hat{H}_z$ for the parameter value $\kappa_z^{g5} = 1 \times 10^{-1} m^{-1}$, in different steps of the goal-oriented adaptive mesh refinement algorithm, for the 1-D CSEM canonical model and corresponding adaptive mesh. From top to bottom, error for the initial mesh and for three goal-oriented adaptive mesh refinement steps: 1, 2 and 3. Plots on the right side zoom into the center where the source and receivers are located.*

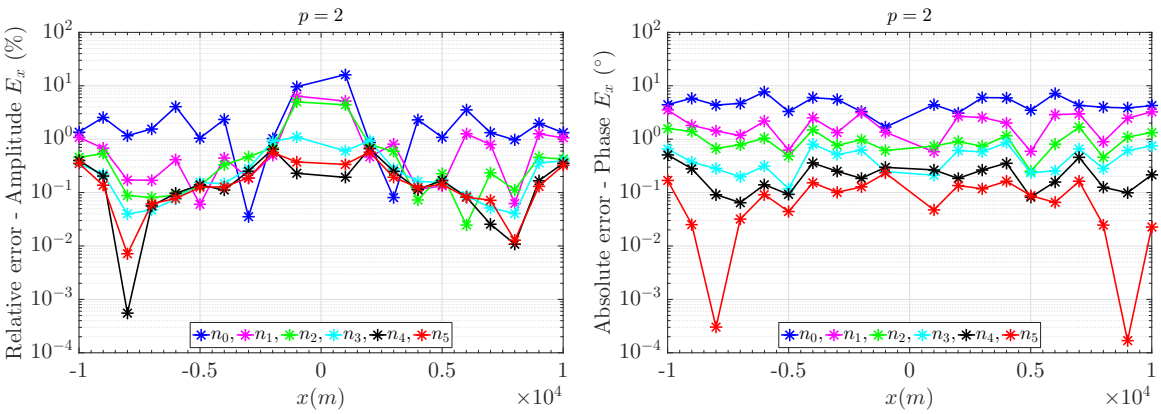

Figure 4.21: *Relative error of the amplitude (left) and absolute error of the phase (right) of the in-line electric field, E_x, compared with the semi-analytical solution for several goal-oriented adaptive mesh refinements steps using quadratic order polynomial shape functions for the 1-D CSEM canonical model.*

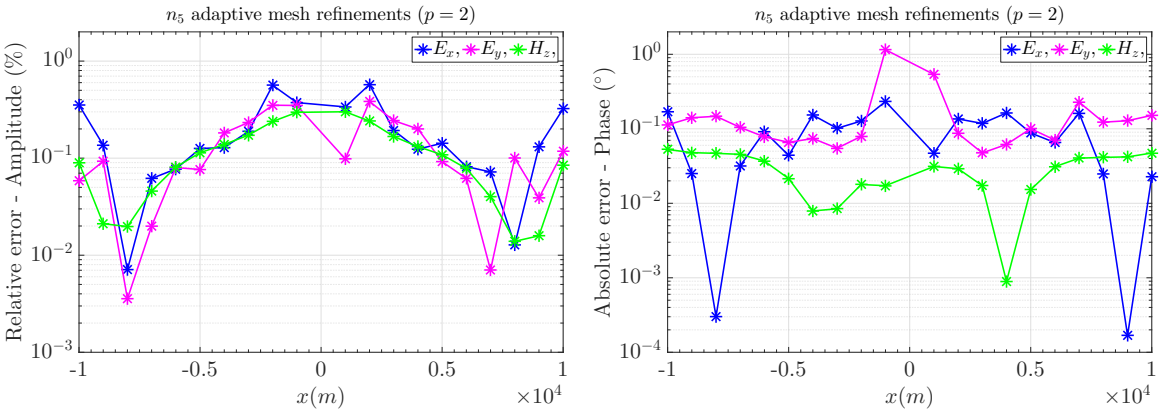

Figure 4.22: *Relative error of the amplitude (left) and absolute error of the phase (right) of the E_x, E_y and H_z components, compared with the semi-analytical solutions for the 1-D CSEM canonical model, after 5 steps of the goal-oriented adaptive mesh refinement algorithm and using 5 groups of mesh refinement and quadratic order of shape functions.*

Observing the absolute error in the phases (Figure 4.21 right), it is possible to appreciate an approximately constant diminution after each mesh refinement step, changing from an initial error of 10° to a final error of 0.1° after the fifth mesh refinement step.

For completeness, Figure 4.22 illustrates the relative error of the amplitude and the absolute error of the phase for the rest of the non-zero EM field components of this experiment, E_x, E_y and H_z. The relative error in the amplitude is for all the receivers and for all the EM field components, smaller than 1% and the absolute error of the phase is smaller than 1°. Note that the relative error in the amplitude and the absolute error in the phase are slightly smaller for the H_z component in some of the receivers. This is expected since we solve the system of equations for $\hat{H}_z$ and $\hat{E}_z$, and the other components, $\hat{E}_x$ and $\hat{E}_y$, are obtained as mixture of spatial derivatives of the strike-directed fields, increasing their error.

Next, we analyze the run time of the computations above using the adaptive mesh refinement algorithm to solve for the 1-D CSEM model. In Figure 4.23 we plot the time as

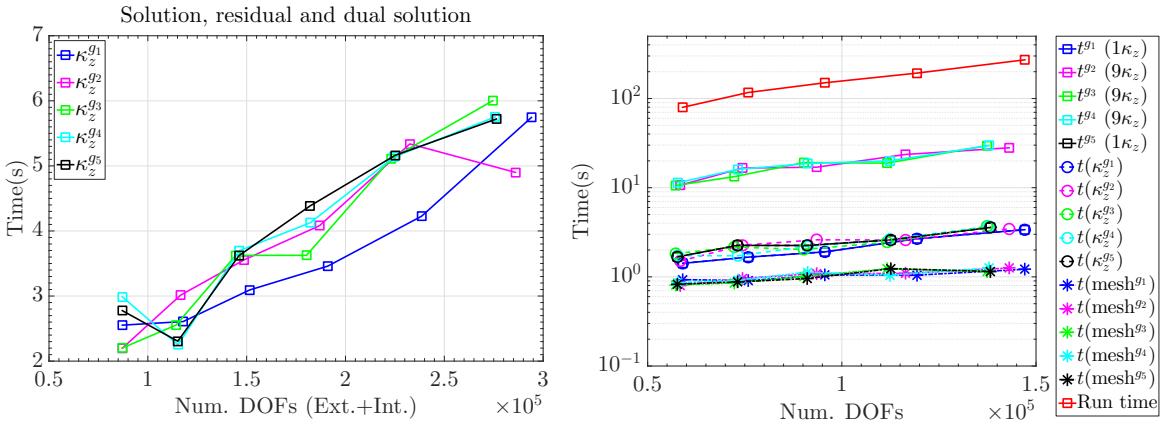

Figure 4.23: *Time versus number of DOFs in the modeling of the 1-D CSEM canonical model. The computer used in the test is a desktop computer with an INTEL i7 4GHz quad-core processor and 16GB RAM. Left: In the goal-oriented adaptive mesh refinement process, time for factorization and solution of the system matrices, calculation of the residual and computation of the dual solution as a function of the number of DOFs (external, the ones associated to $\hat{E}_z$ and $\hat{H}_z$, plus internal, from the dual solution of $\hat{E}_z$ and $\hat{H}_z$ and the error estimation) for the different κ_z values representative of each mesh group (in colors). Right: Time versus number of DOFs of the primal solution for: factorization and solution of the system matrices for all the parameter values of each of the mesh groups (squares and colors); factorization and solution of the system of matrices for the κ_z values representative of each mesh group (circles and colors); selection of elements to refine and mesh refinement (asterisks and colors) and total run time (squares in red).*

a function of the number of DOFs for this experiment, categorized for different stages of the adaptive mesh refinement process. The computer used in the experiments is a desktop computer with an INTEL i7 4 GHz quad-core processor and 16 GB RAM.

As we previously explained, the first phase of the goal-oriented adaptive mesh refinement technique calculates an elementwise error indicator to decide which elements to refine, it computes the solution of the assembled system of equations, the residual of this system and the dual solution using the given goal function. This requires the factorization and solution of the primal system of matrices, the calculation of the residual using higher order polynomial shape functions and the solution of the dual variables using the factorized matrix from the solution of the primal variables. Summarizing, the program performs in this phase two factorizations of the system matrix and solves three systems of matrices. The total number of DOFs is now the sum of DOFs of the primal solution and DOFs of the dual solution. This first phase is executed for each one of the mesh groups independently, using the representative values of the parameters of each group, in this case κ_z.

On the LHS in Figure 4.23, we compare the required time in the first stage for each of the 5 mesh groups and as a function of the total number of DOFs (from the primal and the dual solution), corresponding to the initial mesh and to each one of the 5 adaptive mesh refinement steps. The computation time using the initial mesh (with 87093 DOFs) and in the mesh resulting from the first refinement step (with about 1.1×10^5 DOFs) are between 2 and 3s for all groups and increases linearly with the number of DOFs, up to a time between 5 and 6s in the fifth iteration, for a number of DOFs between 2.7×10^5 and 2.9×10^5.

In the second phase of the adaptive mesh refinement process, the resulting grids from

the first phase are used to compute the solution for the rest of wavenumber values of each mesh group. On the RHS in Figure 4.23, we compare the time spent on these calculations (squares in blue, magenta, green and cyan) as a function of the number of DOFs. Each data point corresponds to a mesh refinement step up to 5 for the different mesh groups, including also the data for the initial mesh. The number of DOFs refers only to the ones of the primal solution, since there are no calculations of the error in this phase. Further, the Figure includes the necessary time for the factorization of the system matrix and solution for only one of the parameter values of each group (discontinuous line with circles and in colors), and the time used to select the elements to refine and to refine them (discontinuous line with asterisks in colors).

The total time of factorization and solution for each of the 9 values of κ_z for mesh groups 2, 3 and 4 is $10s$ for the initial mesh and grows slowly up to $30s$ for the resulting mesh after 5 adaptive mesh refinement steps. For mesh groups 1 and 5 the time is much smaller since they only contain one value in each group, and coincides with the time data of the factorization and solution for only one value of κ_z for each group (discontinuous line with circles and in colors). These values are about $2s$ for the initial mesh and $3s$ for the final mesh, after 5 adaptive mesh refinement steps.

The time to select the elements to refine and to refine the mesh (circles in colors and dashed line) is about $1s$ for all groups and does not increase notable with the number of DOFs.

Finally, the total run time (squares in red) is $80s$ for the initial mesh, and increases up to $300s$ for the final mesh, after 5 adaptive mesh refinement steps, with an increase of about 2×10^5 number of DOFs from the initial value. This total run time in the last refinement step includes the goal-oriented adaptive mesh refinement process time for 5 iterations and 5 mesh groups (summing up all values of the left plot: $5 \times 3s + 5 \times 3s + 5 \times 3.5s + 5 \times 4s + 5 \times 5s + 5 \times 6s = 122.5s$), the time for the computation of the solution for each of the parameter values of each group (3 groups $\times 30s$ + 2 groups $\times 3s$, for $n_{ref} = 5$) and the time for mesh refinement in each iteration for each group (5 iterations $\times 5$ groups $\times 1s$, for $n_{ref} = 5$), which sums up to approximately $243.5s$. The remaining time until $300s$ includes among other things the loading of all input (e.g. the model geometry and the initial mesh), the generation of mesh groups, the data transfer in several parts between the COMSOL structure and MATLAB, and the calculation of the Fourier inverse transform.

The time efficiency of the program could be improved, in a first attempt, by parallelizing the computations of the mesh groups since they run independently, which would already reduce the $\approx 244s$ by a factor of approximately 3 (because there are 5 groups but 2 have only one member requiring already a very short time) in the test under consideration.

4.3.2 Influence of the shape function order and of the error estimator method

In the second set of numerical experiments in this section we model again the 1-D CSEM canonical model (Figure 4.4), but varying the order of the polynomial shape functions. In

the previous tests we used a quadratic order and now we study the effect in the solution accuracy of changing it to linear ($p = 1$) and cubic ($p = 3$), when using the adaptive mesh refinement method, and we compare the results to the ones resulting from the quadratic case.

In Table 4.3 we provide information of the initial and final (after 5 adaptive mesh refinement steps) number of DOFs and number of elements involved in the tests for the different cases of shape function order: $p = 1, 2$ and 3, and for each mesh group. The mesh groups used in the adaptive mesh refinement are the same as in the tests above, with the representative parameter κ_z given in the table ($\kappa_z^{g_i}$). The number of DOFs given in the table corresponds only to the primal solution, and the number of DOFs per element varies depending on the shape function order as explained in Chapter 2. The table also includes information about the variation of the global error estimate between the initial and the final mesh ($\eta_\omega^{5,g_i}/\eta_\omega^{0,g_i}$), for each state characterized by the order of the shape functions and by the mesh group. Later in this Chapter, we will discuss this index in more detail.

For all cases the initial mesh is the same, with 10864 elements, and the initial number of DOFs changes depending on the shape function order, with the minimum number of DOFs for case $p = 1$ and the maximum for $p = 3$, by construction, and the same numbers

Table 4.3: *Numerical data of tests with the 1-D CSEM canonical model using the goal-oriented adaptive mesh refinement algorithm, with 5 mesh groups of κ_z and for three cases with order of shape functions: linear, quadratic and cubic. The data is: mesh group index, representative value of κ_z in each group, order of the shape functions (p), number of elements in the initial mesh, number of mesh elements after the 5^{th} adaptive mesh refinement iteration, number of DOFs (of $\hat{E}_z$ and $\hat{H}_z$) in the initial mesh, number of DOFs after the 5^{th} adaptive mesh refinement step, normalized error estimate.*

Mesh group i	$\kappa_z^{g_i}(m^{-1})$	p	**Num. of elements** n_0	**Num. of elements** n_5	**Num. of DOFs** n_0	**Num. of DOFs** n_5	$\eta_\omega^{5,g_i}/\eta_\omega^{0,g_i}$
1	0	1	10864	37324	10954	37414	2.89×10^{-2}
		2	10864	36736	43634	147122	3.98×10^{-4}
		3	10864	38830	98042	349736	1.06×10^{-5}
2	2.8×10^{-4}	1	10864	35700	10954	35790	2.86×10^{-2}
		2	10864	35730	43634	143098	3.88×10^{-4}
		3	10864	37774	98042	340268	1.05×10^{-5}
3	2.8×10^{-3}	1	10864	34202	10954	34292	1.48×10^{-2}
		2	10864	34300	43634	137378	1.87×10^{-4}
		3	10864	35670	98042	321296	6.50×10^{-6}
4	2.8×10^{-2}	1	10864	34777	10954	34870	1.06×10^{-9}
		2	10864	34437	43634	137932	8.15×10^{-11}
		3	10864	34806	98042	313538	8.42×10^{-11}
5	1×10^{-1}	1	10864	34691	10954	34782	3.72×10^{-15}
		2	10864	34523	43634	138272	2.90×10^{-20}
		3	10864	34951	98042	314834	1.94×10^{-23}

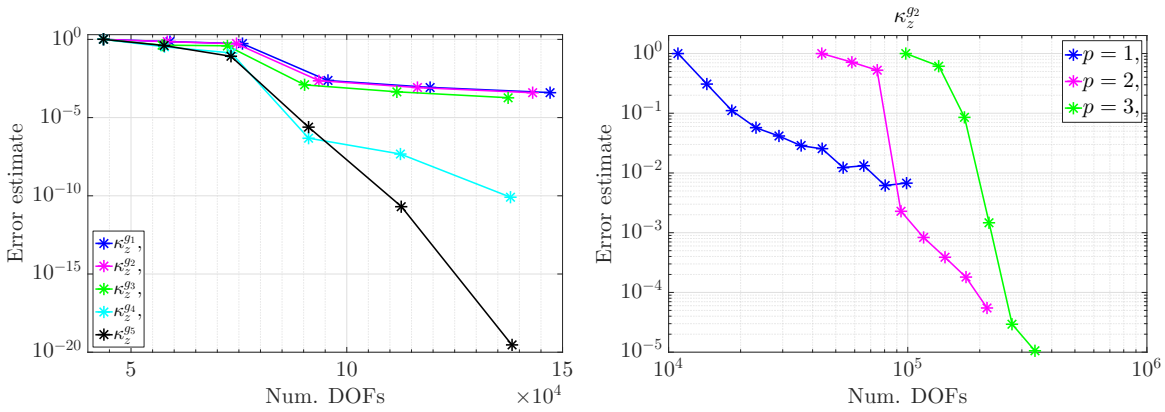

Figure 4.24: *Error estimate as a function of number of DOFs for the 1-D CSEM canonical model. Left: Error estimate versus number of DOFs for the 5 different mesh groups (in color) used in the adaptive mesh refinement. Right: Error estimate versus number of DOFs using different order in the polynomial shape functions: linear, quadratic and cubic (colors) for mesh group 2 (using κ_z^{g2}). The error estimate values are normalized to the value in the initial mesh for each case of mesh group and of p.*

for all groups. After the fifth mesh refinement step of the goal-oriented adaptive mesh refinement algorithm, the number of DOFs and the number of elements has increased to about 3.5 times its initial value for all mesh groups.

To discuss the variation of the global error estimate, also included in Table 4.3, let us draw your attention to Figure 4.24, where the normalized error estimate value is displayed as a function of the number of DOFs for the different mesh groups and for a different order of the polynomial shape functions.

On the LHS of Figure 4.24, the shape function order is quadratic and each data point corresponds to one mesh refinement step, starting with the data from the initial mesh. The error estimate values are normalized to the error value in the initial mesh. We observe that the decrease of the error in the first and second refinement steps is very small ($\approx 10^{-1}$) and that it is after the third step, when the model has about ≈ 92000 DOFs, two times the initial value, that the decrease is significant. Also note the different behavior after the third refinement step between the mesh groups 1, 2 and 3, and the mesh groups 4 and 5 with the highest values of κ_z. For mesh groups 1, 2 and 3, the error after the third mesh refinement step decays to a value between 2×10^{-3} and 1×10^{-3}, and remains approximately between 1×10^{-3} and 1×10^{-4} in the next refinement steps, even though the number of DOFs increases. Contrarily, the error of mesh groups 4 and 5 decays after the third refinement level to a smaller value than mesh groups 1, 2 and 3, to 4.8×10^{-7} and to 2.5×10^{-6}, respectively, and the decay continues steeply as the mesh refinement steps advance and the number of DOFs increases. This decrease is more sharp for κ_z^{g5} ($1\times10^{-1}m^{-1}$) than for κ_z^{g4} ($2.8\times10^{-2}m^{-1}$). The reason is that after mesh refinement step 3, the size of the elements at the receiver locations are sufficiently small for the high wavenumbers to fulfill the relation we discussed in the previous section ($\kappa_{z,max} < 1/d$) and the error decreases. However the EM field values for κ_z^{g4} and κ_z^{g5} are very small (as shown in Figure 4.6) and it takes longer for them to converge, so the variations between iterations are large.

On the RHS panel of Figure 4.24, the error estimate is plotted as a function of number of DOFs for the three cases of varying the polynomial order of the shape functions to $p = 1, 2$ and 3. The data in this plot corresponds to mesh group 2 with $\kappa_z^{g_2} = 2.8 \times 10^{-4} m^{-1}$ and the error estimate values are normalized for each case to its value for the initial mesh. Each data point corresponds to a mesh refinement step, including the initial mesh, and in each refinement step, 20% of the elements with worst error have been refined. The main differences are between the decay error curves of $p = 1$ and $p = 2, 3$. The model with $p = 1$ starts with very few DOFs (10954), and the error estimate value diminishes slowly as the number of DOFs increases. When the number of DOFs reaches the value of $\approx 1 \times 10^5$, after 10 adaptive mesh refinement steps, the error estimate value has decreased to 6.8×10^{-3} times its initial value. Models using $p = 2$ and $p = 3$ start with a higher number of DOFs than $p = 1$, 43634 and 98042, respectively, and their decay after a few iterations is much more abrupt than the one for $p = 1$. The error for $p = 2$, falls after the third refinement step to 2.3×10^{-3} with 93562 number of DOFs, and then continues to reduce constantly in each refinement step. For $p = 3$, the decay is more notable already in the first and second refinements, falling down to 0.6 and 8.5×10^{-2}. After the third iteration, the normalized error is 1.5×10^{-3}, a similar value to the error in the same iteration for $p = 2$, but here the number of DOFs is larger: 218930. The error continues to decrease for larger number of DOFs and more abruptly than for $p = 2$.

To analyze how the error between the solution obtained with the goal-oriented adaptive mesh refinement method and the semi-analytical solution changes with the number of DOFs, when varying the shape functions order p, in Figure 4.25 we display the relative error of the amplitude (left) and the absolute error of the phase (right) of the in-line electric field component, E_x, for $p = 1, 2$ and 3 and for different receivers locations $x = 1, 5$ and $9km$ (from top to bottom). The number of DOFs in the plots are the ones corresponding to mesh group 2 using $\kappa_z^{g_2} = 2.8 \times 10^{-4} m^{-1}$.

The same Figure also contains data from a third experiment (in black) and data discussed in the previous section (cyan). Firstly, this third experiment employs quadratic shape functions and a residual error estimator in the adaptive mesh refinement process, in contrast to the weighted residual used in the experiments above. The global error estimator is a L^2-norm of the residual (equation 3.10). In this case, as explained in Chapter 3, the goal is to reduce the global error in the model and not the error of the goal function, using the residual to estimate the error. The purpose of this experiment is to compare the performance of this method with the goal-oriented method, analyzing the error (compared to the semi-analytical solution) when increasing the number of DOFs (refining the mesh). Secondly, the data from the previous section corresponds to the tests we used to study the influence of the element size in the receivers locations to the error of the solution. In each of these tests the meshes were fixed, and the element sizes were approximately the same for all elements in the receiver locations domain. We considered three cases with element sizes $h = 300, 100$ and $50m$ (Figure 4.5) with a corresponding number of DOFs: 46230, 186742 and 573650. The action of reducing the size of the elements in the entire receiver domain

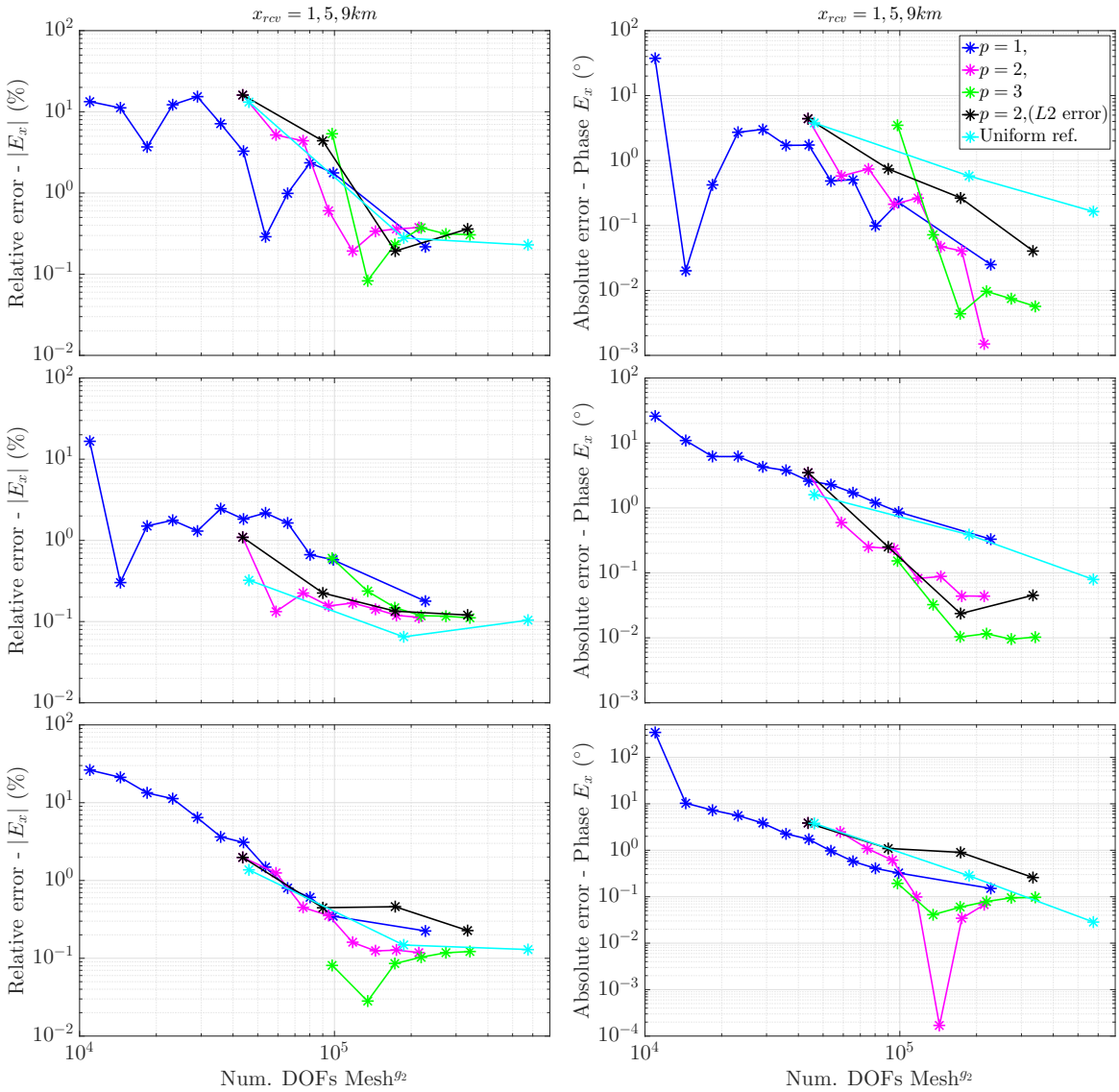

Figure 4.25: *Relative error of the amplitude (left) and absolute error of the phase (right) of the in-line electric field component, E_x, as a function of the number of DOFs in different receiver locations, ($x = 1, 3, 9km$ from top to bottom), obtained using: the goal-oriented (weighted residual) adaptive mesh refinement algorithm with different order of the shape functions ($p = 1, 2, 3$; blue, magenta, green); the residual L^2-norm error estimator for the adaptive mesh refinement (black) and a uniform refinement of the region where the receivers are located (cyan). The number of DOFs for adaptive mesh refinement methods are the ones corresponding to mesh group 2 using $\kappa_z^{g_2} = 2.8 \times 10^{-4} m^{-1}$.*

can be seen as a uniform refinement of the mesh domain, since all elements are refined. Therefore, we will also compare this refinement method with the adaptive refinement.

We start examining the relative error of the amplitude as a function of the number of DOFs for a receiver located at $1km$ offset ($x = 1km$) in Figure 4.25 top left. Concentrating only on the errors of the solutions obtained using the goal-oriented adaptive mesh refinement method: $p = 1, 2$ and 3, we observe a similar behavior to the error estimate values in Figure 4.24 right.

For $p = 1$ the error in the initial mesh, with 10954 DOFs, is about 13%. When the adaptive mesh refinement iterations advance and the number of DOFs increases, the error for $p = 1$ decreases slowly while oscillating. After the sixth refinement step, with 43902 number of DOFs the error is still larger than 3%, and although it reaches a minimum of 0.3% in the seventh refinement step, with 53664 DOFs, the error increases again to a value of about 2% when the number of DOFs is 80322. For $p = 2$ the error in the initial mesh, with 43634 DOFs, is also about 16%, however the decay of the error with the increment of the number of DOFs is more abrupt than for $p = 1$, and after the fourth refinement step, with 116362 number of DOFs, the error reaches to a minimum of 0.2%, that stabilizes to a value of about 0.4% when the number of DOFs is 143098, in the next step. The initial error for $p = 3$, with 98042 DOFs, is about 5%, a smaller value than for $p = 1$ and $p = 2$, and it decays faster than for any of the other cases, with an error of 0.08% after the first refinement step, with 134912 DOFs. In the following iterations the error stabilizes to a value of about 0.3%.

In the same plot, the relative error calculated with the solution using the adaptive mesh refinement with a global error estimator and quadratic shape functions presents a similar behavior with the number of DOFs to the goal-oriented case with $p = 2$. However, the slope of the line is smoother, and when the DOFs are about 90000, the error is 4%, a larger value than the 0.6% error for the goal-oriented case for a similar number of DOFs.

The performance of the error using a uniform refinement and quadratic shape functions is also similar to the other two cases with $p = 2$. The observed differences are a larger increment of the number of DOFs between refinement steps, it passes from 46230 to 186742 after the first refinement level and to 573650 in the second refinement level, with a smaller decay of the error compared to the other methods; it decays from 13% to 0.3% and to 0.2%. Thus, the error-number of DOFs line corresponding to the uniform refinement presents a smaller slope than the ones corresponding to the adaptive mesh refinement methods.

The absolute error of the phase at $x = 1km$ is very similar to the described relative error of the amplitude (Figure 4.25 top right and top left). The slopes are similar for data obtained using goal-oriented methods with $p = 1, 2$ and 3, but smoother for data obtained using a global error estimator method and a uniform refinement method. The initial error for $p = 1$ is 37°, a larger value than for all $p = 2$ cases, about 4°, and $p = 3$, 3.5°. When the number of DOFs is about 175000, the error is 0.6° for the uniform refinement method, 0.3° for the L^2-norm error estimator method, 0.04° for the goal-oriented method with $p = 2$,

and 0.004° with $p = 3$. Thus, the error for large number of DOFs corresponding to the uniform refinement method and to the adaptive method with the global error estimator is higher than the error corresponding to the adaptive method with the goal-oriented mesh refinement.

Interpreting the results at $x = 1km$, the goal-oriented method with $p = 1$ starts with a few number of DOFs and needs many mesh refinement steps to increase them and therefore, to be able to accommodate the strong variations of the EM fields closed to the source. The goal-oriented method with $p = 2$ starts with more DOFs than $p = 1$. In the first iterations the error is larger than the one for $p = 1$ for the same number of DOFs. However, since for $p = 2$ each element has more DOFs, the goal-oriented method refines the appropriate elements and in a few iterations the error decays to a lower value than for $p = 1$ and for the same total number of DOFs. Then, the solution converges and although performing more mesh refinement steps, the error does not decrease. A similar interpretation is valid for $p = 3$, but in competition with $p = 2$, it needs more number of DOFs to converge, since it has more DOFs per element. Within the adaptive mesh refinement cases, comparing the global error estimator with the goal-oriented method, the differences in the amplitude error are not very notable at this receiver location, but the slightly better performance of the goal-oriented method could indicate that there are some elements that are not located where the residual is higher, that are affecting the solution in the receiver location, as we have seen before, which are refined by the goal-oriented method but not by the global error estimator. These results, also show that the differences between both methods are larger for the phases which might indicate that this effect is more notable on phases than on amplitudes. On the other hand, the uniform mesh refinement increases faster the number of DOFs, because in each refinement step it refines all the elements (in the domain), instead of only the elements with higher estimated error. At the same time, it only refines elements in this domain and does not take into account elements from other domains that could be affecting the error in the receiver locations, which could explain the phase behavior associated to this method.

For receivers at $x = 5km$ and $x = 9km$ the performance of the error for the different cases is similar to the described one at $x = 1km$. For a receiver at $x = 5km$ (middle panels) some differences are a lower initial error for $p = 2$ and $p = 3$ than at $x = 1km$. It is 1% for adaptive mesh refinement methods with $p = 2$, 0.3% for the uniform mesh refinement method ($p = 2$) and 0.6% for the adaptive mesh refinement method with $p = 3$. Another difference, compared to the error for $x = 1km$, is that for $p = 1$ the error in the firsts iterations decreases faster. With only 18406 DOFs the error is already at 2%. However, to decrease this value to an error of less than 1%, the necessary number of DOFs is similar to the previous example, 80322. We also observe that the error corresponding to the case of the goal-oriented refinement method with $p = 2$, stabilizes after the first refinement step with 58378 DOFs, much faster than at $x = 1km$, and that the slope of $p = 3$ is smoother. The absolute error in the phase in this case, starts approximately at the same values as before, only the initial error for $p = 3$ is significantly smaller, 0.15°, and in general all the curves

corresponding to the goal-oriented method have a smaller slope than at $x = 1km$, and more similar to the two other mesh refinement methods.

The interpretation of the smoother curves at this location ($x = 5km$) is that the EM fields do not vary as strong as at $1km$ from the source, and the same error values can be reached with less number of DOFs. As described above, the error for $p = 1$ and $p = 2$ reduces faster (with less number of DOFs, and refinements) and by using $p = 2$ and $p = 3$ the initial error is smaller than at $x = 1km$, with $p = 2$ decreasing the error faster. The explanation of the phase error could be the same one as at $x = 1km$.

Finally, at $9km$ distance to the source (Figure 4.25 bottom), the initial error for $p = 1$ and $p = 2$ is similar to $x = 5km$ and lower than at $x = 1km$, and the initial error for $p = 3$ is smaller, 0.08%. The error for $p = 1$ decreases more smoothly than at $x = 5km$. The error corresponding to the goal-oriented adaptive mesh refinement method with $p = 2$ needs more DOFs, 116362, to converge to a value of 0.15° and the error using the global error estimator would need much more DOFs to reach a similar value than at $x = 5km$. The absolute error in the phase does not show large changes comparing it with the error in the phase at $x = 5km$. The most significant difference is that the error for large number of DOFs and adaptive methods is larger than at $x = 1$ and $5km$. The error from data computed using the goal-oriented method stabilizes to 0.1° compared to a value around 0.01° at $x = 1,5km$, and the error from data computed using the adaptive method with the L^2-norm remains at a value larger than 0.1° for large number of DOFs, 333428.

The interpretation of the changes in the curves at $x = 9km$ regarding the curves at $x = 1,5km$ are that the goal-oriented method, although it is refining elements in this location, refines more elements at $x = 5km$ which is closer to the source, for this reason some more refinement steps are necessary at this location for $p = 1$ and $p = 2$ than at $x = 5km$ to reach the same error values. It is possible that another goal function in the adaptive mesh refinement method, which could better weight the receivers locations, could improve these results.

The different behavior of the adaptive method using the global error estimator has also a similar cause but much more accentuated than the goal-oriented method, since the larger residual is at the source location and this method is not weighted. To illustrate how differently these methods are refining the mesh, in Figure 4.26 we plot the initial mesh for all these tests, a mesh corresponding to the goal-oriented adaptive mesh refinement method and a mesh corresponding to the residual adaptive mesh refinement method for similar number of DOFs. As commented, the goal-oriented method refines elements at all receivers locations, where the error indicator has large values, and the global error estimator method refines elements around the source, where the residual is larger.

From these tests we find an outperformance of the goal-oriented adaptive mesh refinement method with $p = 2$ compared to the same method with $p = 1$ and $p = 3$, and in comparison to the uniform refinement method or the adaptive mesh refinement method with a global error estimator.

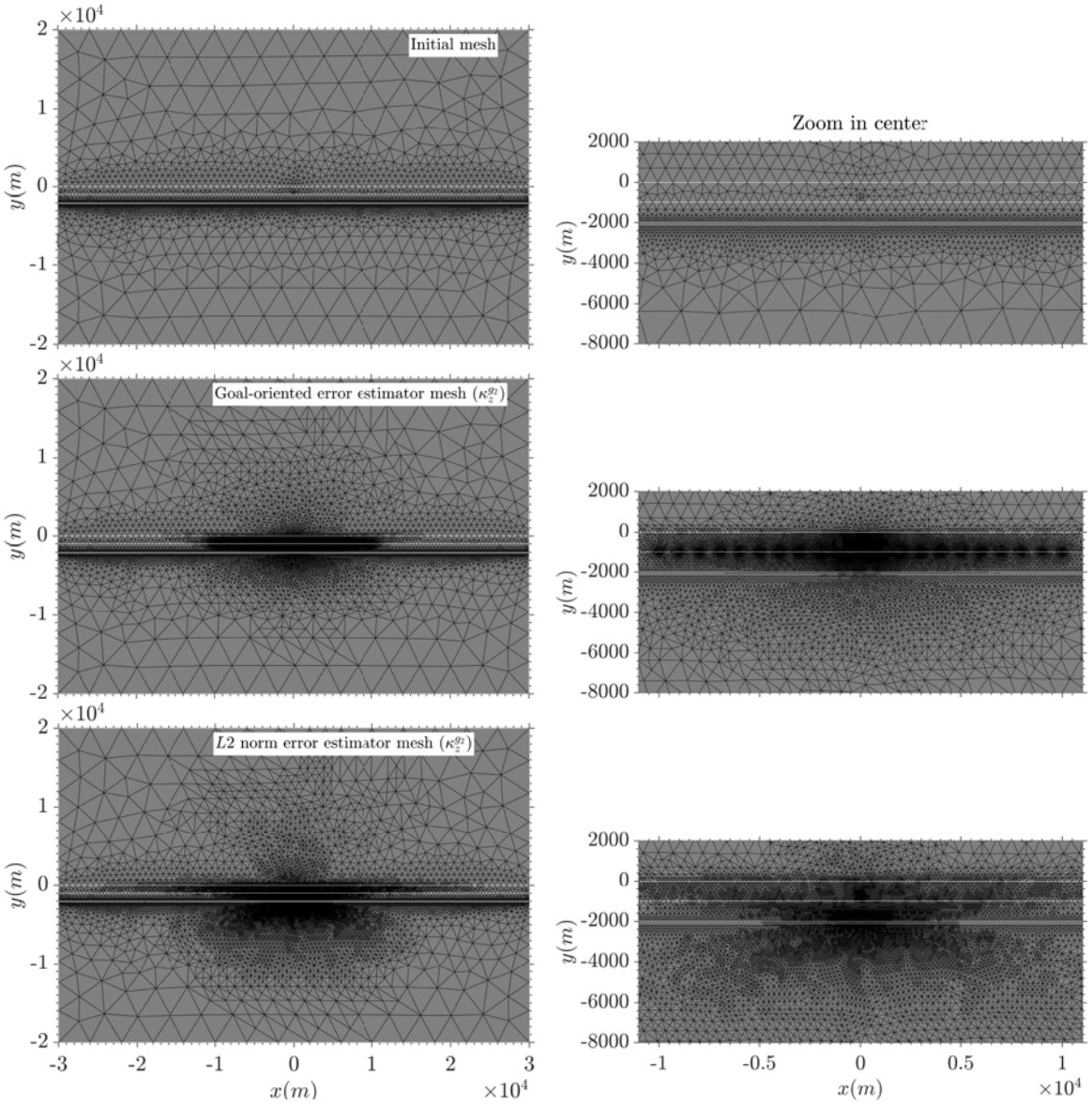

Figure 4.26: *Different meshes obtained from modeling the 1-D CSEM canonical model using different error estimator strategies in the adaptive mesh refinement: a goal-oriented or weighted residual error estimator and a residual error estimator (L^2-norm). From top to bottom: Initial mesh, mesh obtained using the goal-oriented error estimator and mesh obtained using the L^2-norm error estimator. The plots in the right are a zoom in center of the plots in the left, zooming the source and receivers locations. The initial number of DOFs are* 43634*, and the plotted meshes resulting from the different adaptive mesh refinement strategies have a very similar number of DOFs:* 175098*, for the goal-oriented error estimator and* 173152*, for the L^2-norm residual error estimator. The grids are for the mesh group* 2 *with* $\kappa_z^{g_2} = 2.8 \times 10^{-4} m^{-1}$.

4.4 Modeling complex geometries

In this section we validate the performance of our program on modeling complex geometries, such as an undulating seafloor topography or a graben-like structure embedded in thin and thick sedimented layers. Additionally, we study the distortion effects caused by the bathymetry on a CSEM model.

4.4.1 Two-dimensional CSEM model with undulating seafloor topography

Marine CSEM data are strongly affected by bathymetry because of the conductivity contrast between seawater and the crust below the seafloor. The bathymetry influences all electric and magnetic components to different extents (Li and Constable, 2007). The effects depend on several experimental settings and on the interface conductivity contrast and geometry. In particular, the bathymetry effects are determined by the transmission frequency, the seabed conductivity, the seawater depth, the transmitter-receiver geometry, and the roughness of the seafloor topography (Li and Constable, 2007). In order to avoid misinterpretation of marine CSEM data sets it is necessary to take bathymetry into account.

The topography also affects MT data (e.g. Wannamaker et al., 1986). On land, the topographic distortion influences principally the TM mode where the electric field is perpendicular to the geological strike, and in a marine environment both, the TM and the orthogonal TE modes are distorted (Schwalenberg and Edwards, 2004).

There are two possible approximations to take topography into account, it can be included directly into the model or its effects can be estimated and the data corrected prior to inversion (Schwalenberg and Edwards, 2004). The incorporation of the topography in the model using FE or FD numerical methods is straightforward, with the FE method being superior over the FD method. Using the FD method the topography is handled using the 'stair-case' method, whereby rectangular conductivity cells approximate the sloping seafloor as sequences of stair steps with variable height and width. Contrarily, the FE method allows a more precise representation of the topography, accommodating any arbitrary surface using small and large elements where required.

In this section, we will show the flexibility of our program to accommodate the topography using unstructured grids which permits both decreasing the element size towards the interface and retaining well-shaped elements, and the efficiency of the goal-oriented adaptive mesh refinement technique to refine only the required regions of the model for accurate responses on the receivers locations. We will also examine the changes in the efficiency of the adaptive mesh refinement method when varying the polynomial order to $p = 1, 2$ and 3. Finally, we will use this model to study the distortion caused by the bathymetry, restricting the analysis to the in-line electric field component (E_x).

As first model we consider a 2-D canonical model with a flat seafloor (Figure 4.27). It comprises, as in the 1-D case, an air layer and a $1km$ sea layer, and the $100\Omega \cdot m$ reservoir

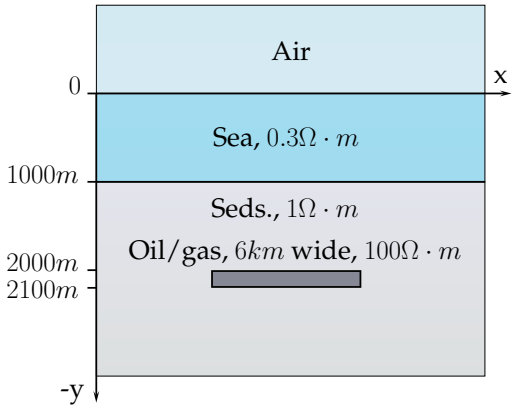

Figure 4.27: *Two-dimensional canonical disc resistivity model for marine CSEM proposed by Weiss and Constable (2006). It comprises an air layer, a $1km$ seawater layer and a resistive reservoir of $100\Omega \cdot m$, which could be oil or gas, embedded in a sediments background of $1\Omega \cdot m$. The reservoir is a $6km$ wide block, $100m$ thick and is located at $2km$ depth, $1km$ below the seafloor. The source is located $100m$ above the seafloor and operates at $0.25Hz$ and the receivers are located at $0.5m$ above the seafloor, along the x spatial dimension.*

layer is substituted, in this case, by a rectangular block, $100m$ thick, $6km$ wide at the same depth ($2km$) and centered at $x = 0$. The source is again an in-line horizontal electric dipole located $100m$ above the seafloor and operating at a frequency of $0.25Hz$, and the receivers are distributed along the x–direction, every $1km$ from $-10km$ to $10km$, at $0.5m$ above the seafloor.

We also examine a second model, variant of the 2-D canonical model, with the only difference of an inclusion of an undulating seafloor topography (Figure 4.28). The shape of the harmonic interface can be expressed as:

$$y(x) = Y \cos(\frac{2\pi}{\lambda}x), \tag{4.2}$$

with amplitude $Y = 100m$ and wave length $\lambda = 4000m$, and with maximums at $y = -1000m$ and minimums at $y = -1200m$ (Figure 4.28 right). The receivers are located in the same horizontal positions as for the flat model, and at $0.5m$ above the seafloor, following the topography. Thus, the ones situated over a ridge are at $-999.5m$ depth, and the ones over the depression are at $-1199.5m$ depth.

The sinusoidal interface topography of this second model, although not very realistic, has been previously used to study topography effects on MT applications (e.g. Franke et al., 2007), and Schwalenberg and Edwards (2004) derived a MT analytical solution for this interface on land and marine scenarios. Li and Constable (2007) also considered it in a variant form to study bathymetry effects on CSEM data using a FE modeling program.

To begin with, we compute the EM field solution for the flat and bathymerty 2-D canonical models for different order of the polynomial shape functions, using $p = 1, 2$ and 3. We use the same set of wavenumber parameter values as for the 1-D canonical model, comprised of 28 values distributed logarithmically from 10^{-4} to $10^{-1}m^{-1}$ and $\kappa_z = 0$. Also as

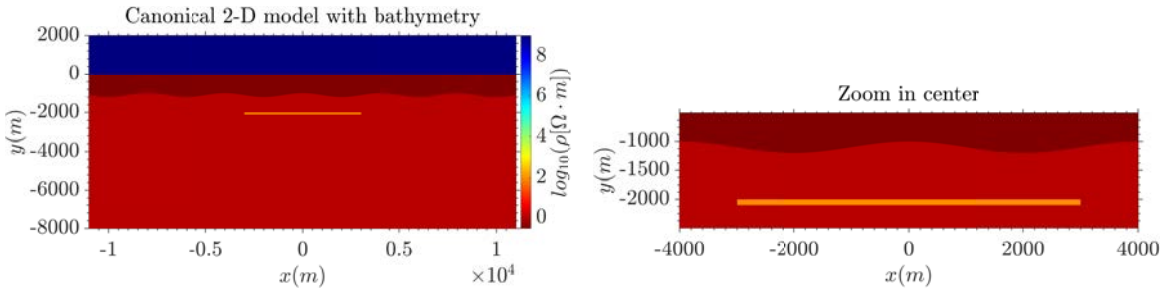

Figure 4.28: *Left: 2-D CSEM canonical model with undulating seafloor topography. Right: zoom in center of the 2-D canonical model with the sinusoidal interface between the sea and the crust. The maximum and minimum of the oscillations are at $-1000m$ and at $-1200m$ respectively, and the wavelength is $4km$. The receivers are located every $1km$ from $-10km$ to $10km$, at $0.5m$ above the seafloor.*

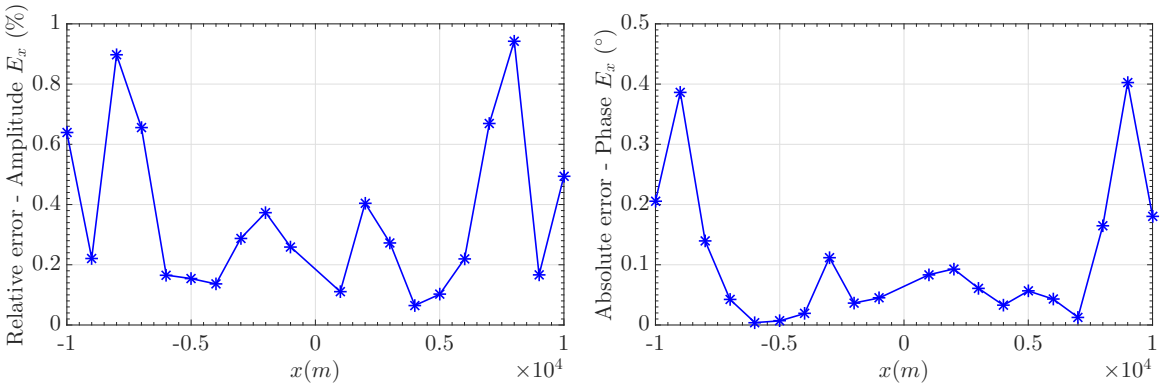

Figure 4.29: *Comparison of the responses of the 2-D canonical model with the ones of a flat seafloor, computed with our program and with MARE2DEM (Key and Ovall, 2011). Left: Relative error of the in-line electric field component E_x. Right: Absolute error of the phases of E_x.*

for the 1-D case, we set 5 mesh groups of κ_z parameter values, and we apply the goal-oriented adaptive mesh refinement technique to representative parameter values of each group, the ones listed in Table 4.3, separately. As a stopping criteria for the adaptive mesh refinement we set to decrease the error estimate to at least a fraction of 10^{-3} of its initial value ($\eta_w^{r,g^i}/\eta_w^{0,g^i} \approx 10^{-3}$). The choice of this value for the normalized error estimate is only justified by our experience after running several tests.

In Figure 4.29 we compare, for the flat model, the in-line electric field responses obtained with our program with the responses computed using MARE2DEM (Key and Ovall, 2011). We plot the relative error of the amplitude and the absolute error of the phase of E_x as a function of the receiver positions with the transmitter at $x = 0$. The errors are very small, with amplitude errors below 1% and phase errors of less than 0.5°.

In Table 4.4 we list the initial and final number of elements and of DOFs for the flat and for the bathymetry model, and for different order of the polynomial shape functions. For both the flat and bathymetry models the final number of elements and number of DOFs is larger for lower p, and the initial number of DOFs is larger for larger p by construction of the FE. The differences in the initial and final number of elements and number of DOFs between the flat and the bathymetry models for each p are small, and in general slightly

Table 4.4: *Initial and final number of elements and number of DOFs of mesh group 2, when modeling the 2-D canonical model with flat seafloor and with $\lambda = 4km$ undulating bathymetry, for different order of the polynomial shape functions, $p = 1, 2$ and 3, using the goal-oriented adaptive mesh refinement algorithm. The final mesh is obtained after the error estimate has decreased at least 10^{-3} its initial value: $\frac{\eta_\omega^{r,g2}}{\eta_\omega^{0,g2}} \approx 10^{-3}$.*

Model	p	Num. of elements n_0	Num. of elements $\frac{\eta_\omega^{r,g2}}{\eta_\omega^{0,g2}} \approx 10^{-3}$	Num. of DOFs n_0	Num. of DOFs $\frac{\eta_\omega^{r,g2}}{\eta_\omega^{0,g2}} \approx 10^{-3}$
Flat	1	4564	888390	4630	888456
	2	4564	46842	18386	187498
	3	4564	9974	41270	89960
Bathymetry	1	4809	765097	4880	765168
	2	4793	49551	19312	198344
	3	4761	10521	43058	94898

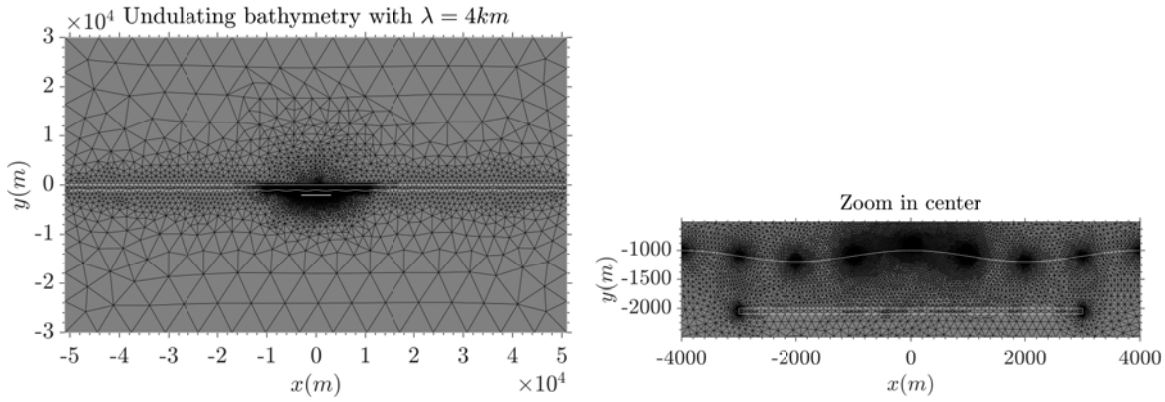

Figure 4.30: *Final mesh of the canonical 2-D model with $\lambda = 4km$ undulating bathymetry for mesh group 2 using κ_z^{g2} and $p = 2$, obtained after applying the goal-oriented adaptive mesh refinement algorithm, with stopping criteria a decrease in the error estimate of at least 10^{-3} of its initial value. In the right, a zoom of the center of the unstructured triangular mesh showing the fine meshing around the receiver locations and along the bathymetry.*

larger for the bathymetry model, since some extra elements are required to accommodate the smooth topography (Figure 4.30). This illustrates the flexibility of the FE method using triangular unstructured grids to accommodate the topography while maintaining the size of the elements in the rest of the mesh. We also note some slight variability on the initial number of elements of the bathymetry model for different number of p, although the selected parameters for generating the initial mesh were the same. We attribute these differences to an error of the geometry generator to build a sinusoidal curve of $1 \times 10^5 m$, which produce a slightly different shape for different runs of the program, which translates to a slightly different mesh.

The differences of number of elements and number of DOFs between the different mesh groups on the different mesh refinement steps are similar to the ones showed for the 1-D case, as it can be observed in Figure 4.31 left. We can observe that the normalized error

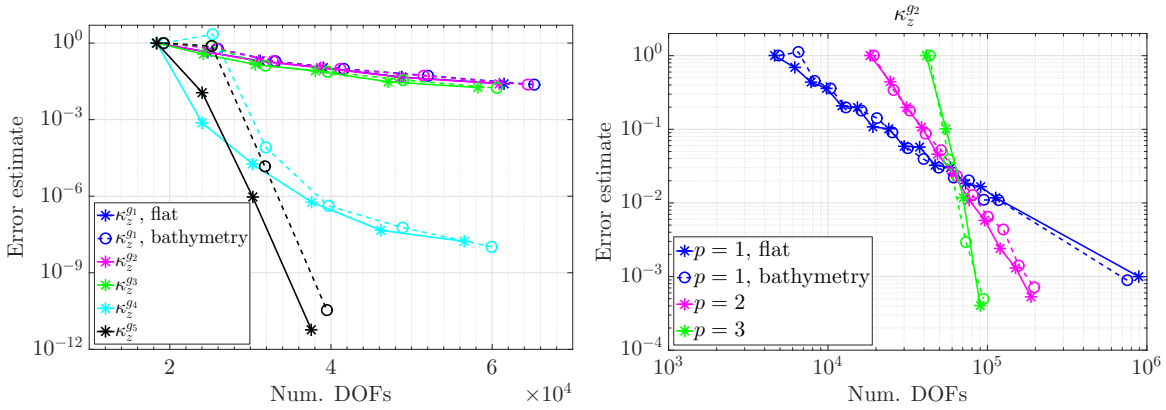

Figure 4.31: *Error estimate as a function of number of DOFs for the 2-D CSEM canonical model with a flat seafloor and an undulated topography seafloor. The error estimate values are normalized to the value in the initial mesh for each case of mesh group and of p. Left: Error estimate versus number of DOFs for the 5 different mesh groups (in color) used in the adaptive mesh refinement and for the model with flat seafloor (solid line) and bathymetry (dashed line). Right: Error estimate versus number of DOFs using different order in the polynomial shape functions: linear ($p = 1$), quadratic ($p = 2$) and cubic ($p = 3$), and for the model with flat seafloor (solid line) and for the one with bathymetry (dashed line). The number of DOFs corresponds to mesh group 2 (using κ_z^{g2}).*

estimate decreases much faster for mesh groups 4 and 5, with the largest wavenumber values, when increasing the number of DOFs (refinement steps proceed), and that is similar for mesh groups 1, 2 and 3.

In Figure 4.31 right, we plot the normalized error estimate as a function of number of DOFs for the flat and bathymetry models, and for different order of the polynomial shape functions, p. The curves behavior is again similar to the 1-D case, with steeper slope for larger p. We also note that $p = 1$ is the least appropriate, since it needs about 8×10^5 DOFs to decrease the error a fraction of 10^{-3}, compared to $p = 2$ and $p = 3$ which need much less DOFs, about 2×10^5 and 1×10^5 respectively. As we already commented, the difference between the curves corresponding to the flat and to the bathymetry models, are small.

In Figures 4.32 and 4.33 we plot the $\hat{E}_z$ and $\hat{H}_z$ elementwise error indicator, respectively, for the bathymetry model and for the initial mesh and for different mesh refinement steps of the adaptive mesh refinement process for mesh group 2 ($\kappa_z^{g2} = 2.8 \times 10^{-4}$). The results correspond to quadratic shape functions, and the number of elements of the initial and final (level 10) grids are listed in Table 4.4. Observing Figure 4.32, the initial error is largest in the receiver locations, in the reservoir and in the region below the reservoir. As the adaptive mesh refinement progresses, these regions are refined and the error decreases. The error distribution for $\hat{H}_z$ in Figure 4.33 is similar to the one of $\hat{E}_z$, and the main difference is that the error is also large in the air in a region above the source. Accordingly this region is also refined in the adaptive mesh refinement process. After the 10^{th} refinement step, we observe a very fine mesh in the receiver locations, and following the bathymetry, and a fine mesh in the reservoir region and in the air, in a region above the source.

As a complementary information, in Figures 4.34 and 4.35, we plot for $\hat{E}_z$ and $\hat{H}_z$, respectively, the field component solution, the dual solution, the residual and the error

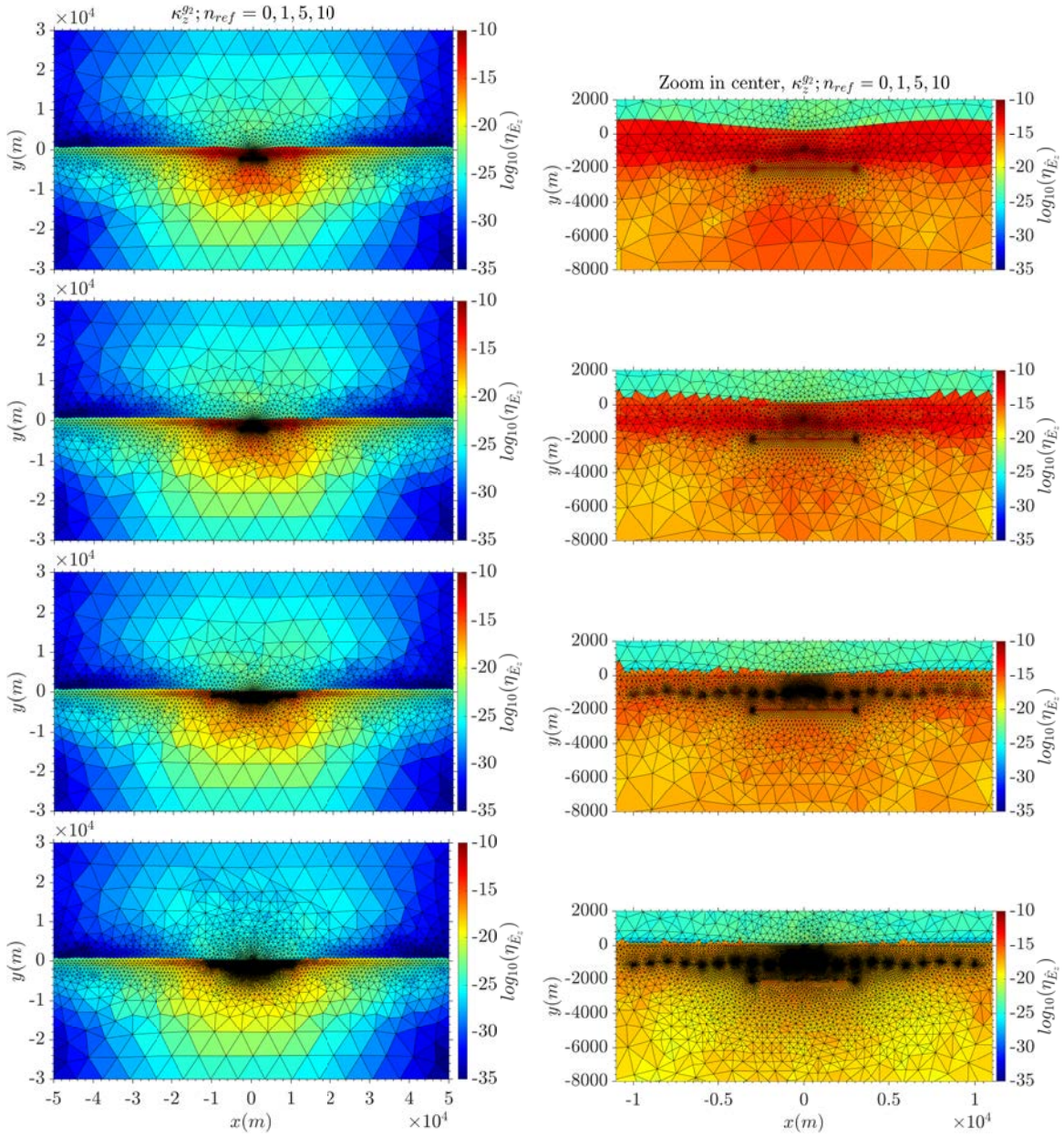

Figure 4.32: *Elementwise error indicator of the dependent variable $\hat{E}_z$ for the parameter value $\kappa_z^{g_2} = 2.8 \times 10^{-4} m^{-1}$ in different steps of the goal-oriented adaptive mesh refinement algorithm, for the 2-D CSEM canonical model with $\lambda = 4km$ undulating bathymetry and corresponding adaptive mesh. The results correspond to quadratic shape functions. From top to bottom, error for the initial mesh and for three goal-oriented adaptive mesh refinement steps: $1st, 5th$ and $10th$. The plots on the right side are a zoom in center of plots in the left, zooming the source and receivers regions of the model.*

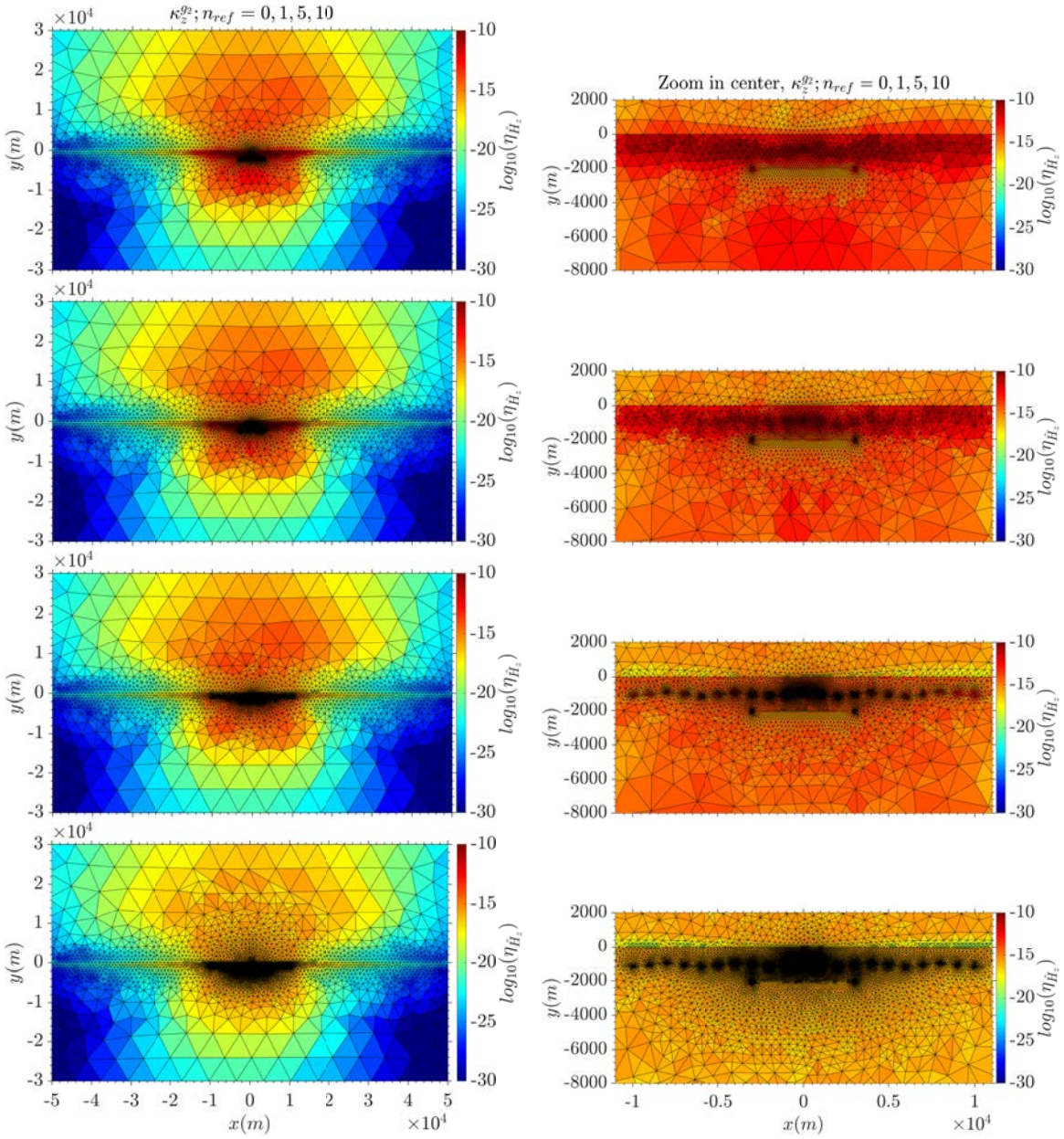

Figure 4.33: *Elementwise error indicator of the dependent variable $\hat{H}_z$ for the parameter value $\kappa_z^{g2} = 2.8 \times 10^{-4} m^{-1}$ in different steps of the goal-oriented adaptive mesh refinement algorithm, for the 2-D CSEM canonical model with $\lambda = 4km$ bathymetry and corresponding adaptive mesh. The results correspond to quadratic shape functions. From top to bottom, error for the initial mesh and for three goal-oriented adaptive mesh refinement steps: $1st, 5th$ and $10th$. The plots on the right side are a zoom in center of plots in the left, zooming the regions of the source and receivers locations.*

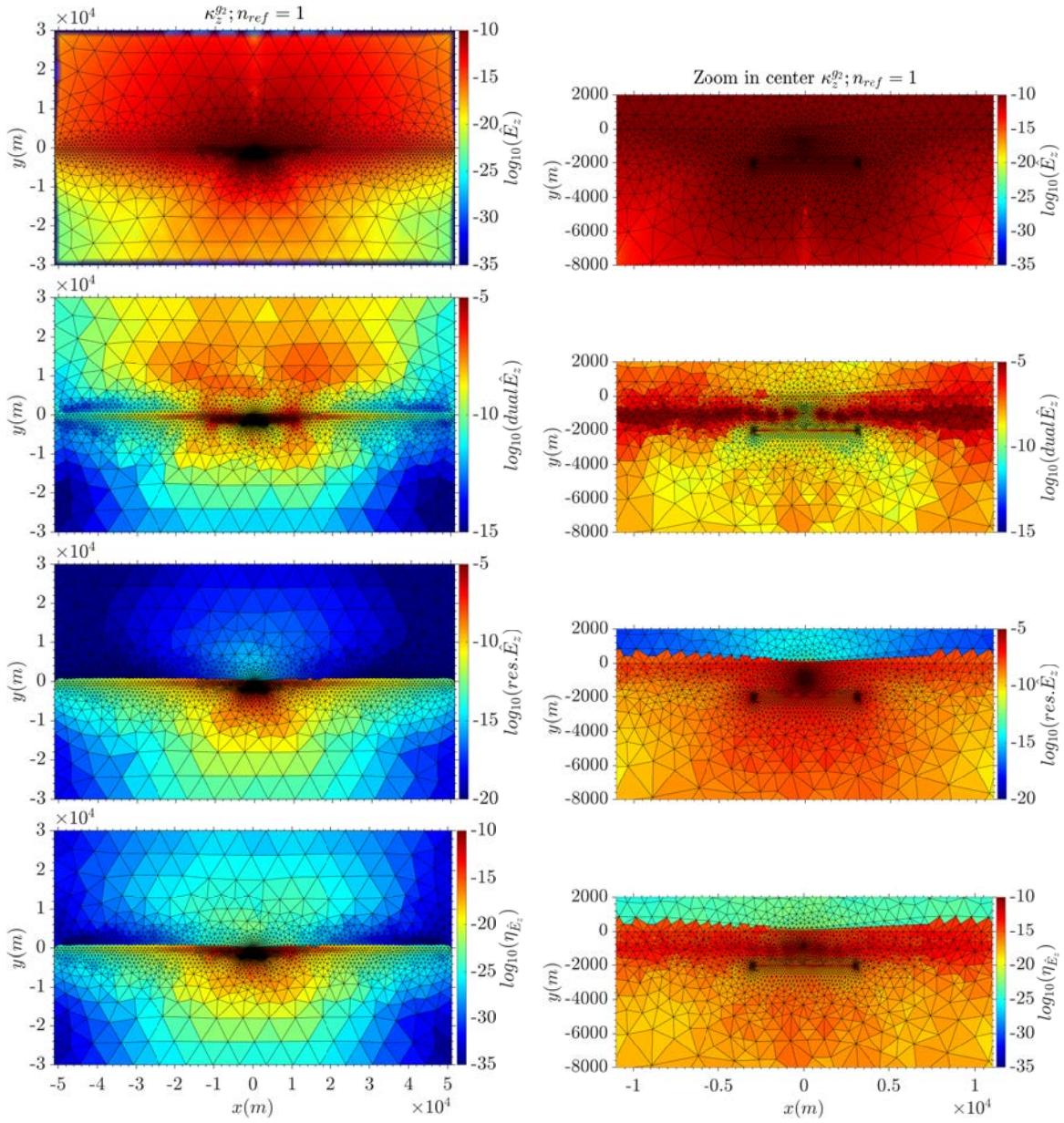

Figure 4.34: *From top to bottom: $\hat{E}_z$, dual of $\hat{E}_z$, residual and error indicator with corresponding mesh, for the parameter value $\kappa_z^{g_2} = 2.8 \times 10^{-4} m^{-1}$ and quadratic shape functions, after the first step of the goal-oriented adaptive mesh refinement algorithm for the 2-D CSEM canonical model with $\lambda = 4km$ undulating bathymetry. Plots on the right side zoom into the center where the source and receivers are located.*

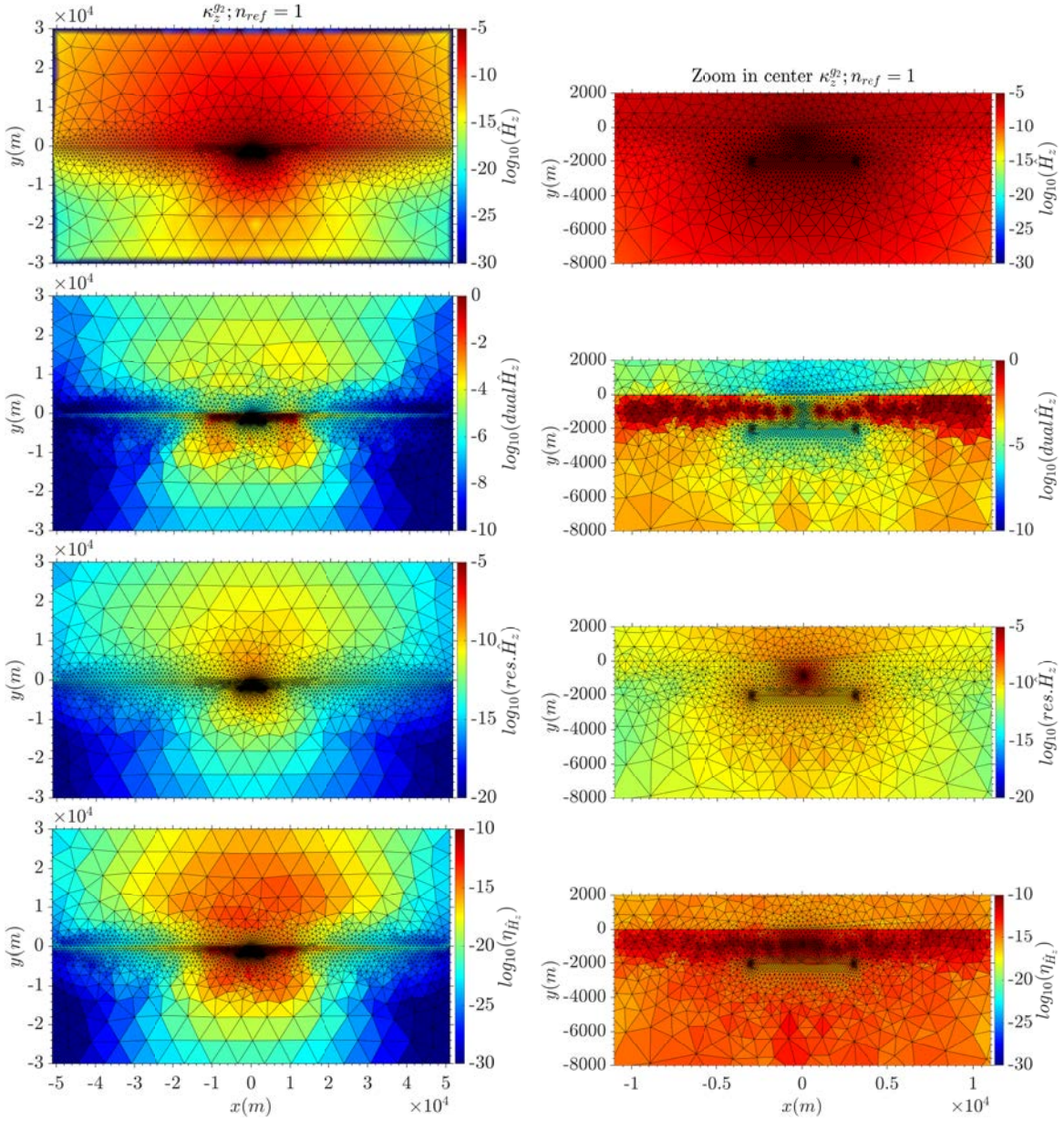

Figure 4.35: *From top to bottom: $\hat{H}_z$, dual of $\hat{H}_z$, residual and error indicator with corresponding mesh, for the parameter value $\kappa_z^{g_2} = 2.8 \times 10^{-4} m^{-1}$ after the first step of the goal-oriented adaptive mesh refinement algorithm for the 2-D CSEM canonical model with $\lambda = 4km$ undulating bathymetry. Plots on the right side zoom into the center where the source and receivers are located.*

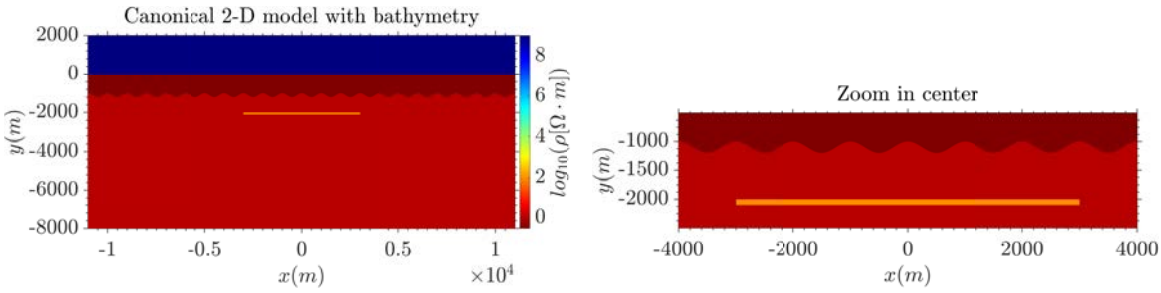

Figure 4.36: *Left: 2-D CSEM canonical model with $\lambda = 1km$ undulating seafloor topography. Right: zoom in center of the 2-D canonical model with the sinusoidal interface between the sea and the crust. The maximum and minimum of the oscillations are at $-1000m$ and at $-1200m$ respectively, and the wavelength is $1km$. The receivers are located every $1km$ from $-10km$ to $10km$, at $-999.5m$.*

indicator, resulting from the product of the dual solution and the residual. All these surface plots are for mesh group 2, obtained using quadratic shape functions and correspond to data after the first mesh refinement step. In both cases, $\hat{E}_z$ and $\hat{H}_z$, the largest values of the dual solution are on the receivers locations. In contrast, the largest values of the residual are around the source and around the reservoir regions. The spatial distribution of the error indicator for both $\hat{E}_z$ and $\hat{H}_z$ is then a combination of the distributions for the dual solution and the residual. The error indicator for $\hat{E}_z$ is larger at the receivers locations and around the source and reservoir regions, and the error indicator for $\hat{H}_z$ has its largest values also in these regions and additionally in an air region above the source.

Finally, we use the computed solutions using quadratic shape functions to study the distortion of the in-line electric field component by the undulating seafloor topography on the 2-D canonical model. Additionally to the original 2-D canonical model with flat seafloor and $1km$ sea layer (Figure 4.27), and the variant with undulating bathymetry of wavelength $\lambda = 4km$ (Figure 4.28), we consider three other models, also variants of the 2-D canonical model. The first one is the 2-D canonical model with a flat seafloor and a thicker sea layer of $1.2km$. A second model is the 2-D canonical model with bathymetry, but changing the wavelength of the harmonic interface to $\lambda = 1km$ (Figure 4.36). In Figure 4.37 we show the mesh for this last model after some steps of the goal-oriented adaptive mesh refinement algorithm, where again it can be observed the fine meshing around the receivers locations and along the sea-crust interface. We note that the meshing along all the interface is finer than for the model with $\lambda = 4km$ bathymetry (Figure 4.30), since it needs to accommodate a more abrupt topography. The third model is simply the original 2-D canonical model without the reservoir, thus, a homogeneous model with an air layer and a $1km$ sea layer.

For all the models the source is located at $100m$ above the seafloor and the operating frequency is $0.25Hz$. The receivers are located along the $x-$direction every $1km$, from $-10km$ to $10km$, and at $0.5m$ above the seafloor. That means that in the flat models, 2-D canonical and homogeneous, with a sea layer of $1km$, the receivers are located at $-999.5m$ depth and that in the flat canonical 2-D model with $1.2km$ sea layer, the receivers are at $-1199.5m$ depth. In the model with $\lambda = 4km$ undulating bathymetry, the receivers follow

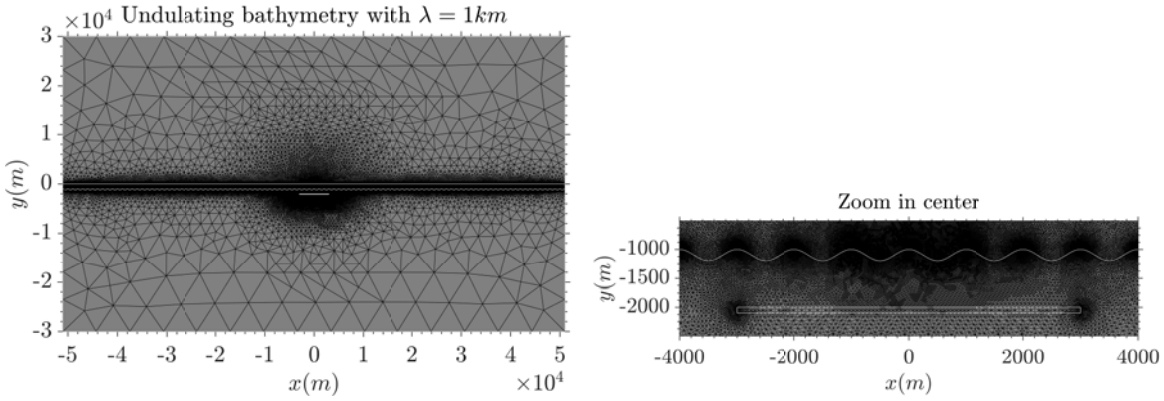

Figure 4.37: *Model mesh of the canonical 2-D model with $\lambda = 1km$ bathymetry for mesh group 2 using $\kappa_z^{g_2}$ and $p = 2$, obtained after 4 steps of the goal-oriented adaptive mesh refinement algorithm. On the right, a zoom of the center of the unstructured triangular mesh showing the fine meshing around the receiver locations and along the bathymetry.*

the slope and are located at $-999.5m$ above the ridge, at $-1199.5m$ above the depression and at $-1099.5m$ in between. Finally, in the model with $\lambda = 1km$ undulating bathymetry, all the receivers are situated above a ridge, at $-999.5m$ depth, since they are horizontally distributed every $1km$ along a profile.

In Figure 4.38 we plot the amplitude and phase of the in-line electric field component, E_x, as a function of the receiver locations for these 5 models, and the relative error of the amplitude and the absolute error of the phase between the responses from: the bathymetry model with $\lambda = 4km$ and the flat model with $1km$ sea layer, the bathymetry model with $\lambda = 4km$ and the flat model with $1.2km$ sea layer, the bathymetry model with $\lambda = 1km$ and the flat model with $1km$ sea layer, the flat model with $1km$ sea layer and the homogeneous model. The error curves corresponding to differences between models with bathymetry and flat models give information of the distortion caused by the bathymetry, and the error curve corresponding to the differences between the flat model and the homogeneous model shows the distortion caused by the reservoir.

Concentrating first on the distortion caused by the reservoir (Figure 4.38) , it is for most of the receivers larger than the anomaly distortion caused by the bathymetry. The relative error of the amplitude is about 1% at $x = \pm 1km$, and grows with the distance to the source to 100% at $x = \pm 3km$, coinciding with the lateral boundaries of the reservoir. For receivers located at further distances than $x = \pm 3km$ the error remains at 100% and about $x > \pm 7km$ decays again to a value of 1%. A similar behavior can be observed for the absolute error of the phase, with the largest distortion, of about $50-60°$, registered at $x = \pm 3,4,5km$, and an error of about 20° registered at receivers located at $x = \pm 6,7,8km$.

The distortion caused by the bathymetry of $\lambda = 4km$ is also significant. The amplitude relative error between the responses of the $\lambda = 4km$ bathymetry model and the flat model with $1km$ sea layer oscillates from $2-3\%$ to about 10%. We note a correspondence between the location of the maximums and minimums of the error in the amplitude with the ridge and valley topography. We differentiate two opposite relations of this correspondence. The

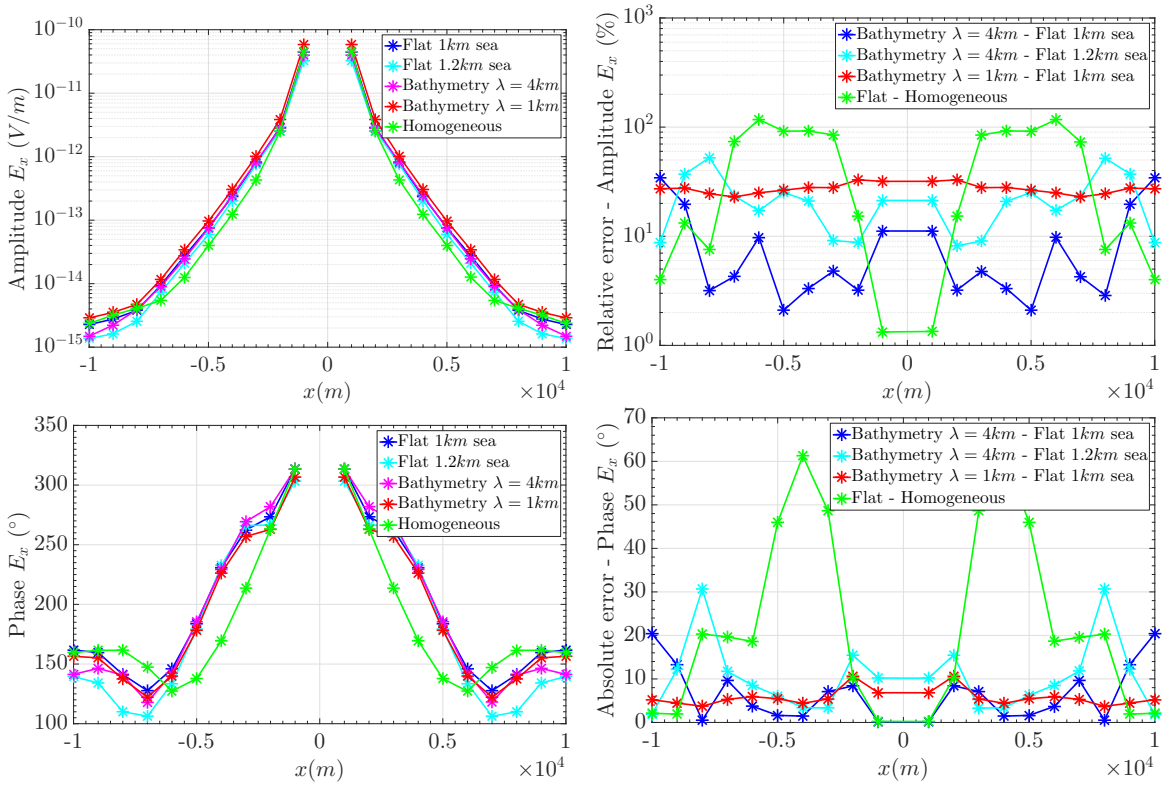

Figure 4.38: *Left, from top to bottom: Amplitude and phase of the in-line electric field component for five different models (colors): 2-D canonical model with a flat seafloor, 2-D canonical model with a flat seafloor and a $1.2km$ sea layer, 2-D canonical model with $\lambda = 4km$ undulating bathymetry, 2-D canonical model with $\lambda = 1km$ undulating bathymetry and homogeneous model (with air and sea layers). Right, from top to bottom: relative error of the amplitude and absolute error of the phase between: the $\lambda = 4km$ bathymetry model and the flat model with $1km$ sea layer, the $\lambda = 4km$ bathymetry model and the flat model with $1.2km$ sea layer, the $\lambda = 1km$ bathymetry model and the flat model with $1km$ sea layer and between the flat model and the homogeneous model. The error curves for the three first cases (blue, cyan,red) gives information of the distortion caused by topography and the last one (green) gives information on the distortion caused by the reservoir. These results for the different models are obtained using quadratic Lagrangian shape functions and after applying the goal-oriented adaptive mesh refinement algorithm.*

first relation is for the receivers closest to the source $|x| < 5km$, and shows that the error is minimum for receivers located in the valley, $x = \pm 2km$, and maximum for locations between the ridge and the valley, $x = \pm 1,3km$. The second relation is for receivers located at more than $5km$, and then, the maximum of the error corresponds to a valley in the topography, $x = \pm 6,10$, and the minimum of the error to a ridge in the topography, $x = \pm 8km$. We interpret the distortion behavior as caused principally from a combined inductive and galvanic effects for the receivers closest to the source, and by the geometry for receivers at longer distance. A geometry effect means that we are comparing the responses from the bathymetry model with receivers at different depths, with a flat model where all receivers are at the same depth, $-999.5m$. Then, the error is minimum for receivers above the ridge because they are also located at $-999.5m$, and maximum at the valley because the difference of the depth locations of the receivers between the bathymetry model and the reference model is maximum. On the other hand, the absolute error of the phase seems to be mainly affected by a geometry effect, since the maximums, at about 10°, coincide with the locations of the depressions, and the minimums at about 1° coincides with the locations of the ridges.

To verify this interpretation, we also plot the error between the same $\lambda = 4km$ bathymetry model and the flat model with $1.2km$ sea layer. Then, the receivers in the valley are at the same depth as the receivers in the reference model, and have the same water column above them. We observe that when compared with this reference model, all the receivers present a larger error than in the previous case, with values oscillating between 10% to $20 - 50\%$. The variations of the error with the receivers location follow approximately the expected behavior from the explanation above. Responses for the receivers with smaller offsets have maximum errors in positions between the ridge and the valley, $x = \pm 1,3km$, and minimums in positions coinciding with the topographic valleys, $x = \pm 2km$. Responses for the receivers with the largest offset present a minimum error in the topographic depressions, $x = 6,10km$, and a maximum in the topographic ridges, $x = 8km$. However, it is difficult to identify these minimums for large offsets, since the error curve presents an upward shift for receivers $|x| > 3km$, coinciding with the lateral boundary of the reservoir.

Comparing the phase error of the $\lambda = 4km$ undulating bathymetry model to error of the flat model with $1.2km$ sea layer, we also observe a different behavior between the responses for receivers near the source and over the reservoir, and the responses for more distant receivers. The responses for receivers near the source have a maximum error, about 16°, at the topographic valleys $x = \pm 2km$, and a minimum error, 4°, above the ridges $x = \pm 4km$. The responses from receivers at larger offsets have minimum error, of 8° and 2°, at positions above the valleys, at $x = 6$ and $10km$, respectively, and a maximum error, of 30°, above the ridge, at $x = 8km$. Hence, it seems the error is dominated for larger offsets by the geometry effect.

Finally, we analyze the error between the $\lambda = 1km$ bathymetry model and the flat model with $1km$ sea layer. In this case, the receivers in the bathymetry model are all located above a topographic ridge, at the same depth of the receivers in the flat model, $-999.5m$.

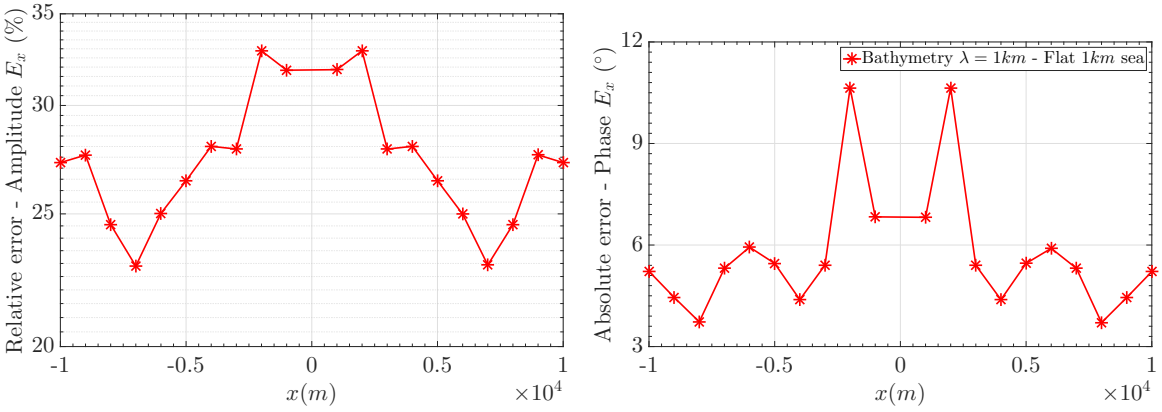

Figure 4.39: *Relative error of the amplitude (left) and absolute error of the phase (right) of the in-line electric field component, between responses of the 2-D canonical model with $\lambda = 1km$ undulating bathymetry and responses of the same model with a flat interface.*

The relative error of the amplitude is, in this case, larger than for the $\lambda = 4km$ bathymetry model, with values between 22 and 33%, approximately, and the absolute error of the phase is between 3° and 10°.

To examine the error variations more conveniently, in Figure 4.39 we plot the relative error of the amplitude and the absolute error of the phase for this case solely. We observe a maximum of the error of the amplitude of about 30%, for the receivers located closest to the source and another one above the reservoir, at $x = \pm 1,2km$. At $x = \pm 3,4km$ the error has decayed to approximately 27%, and this decay continues until it reaches the value of 22% at $x = \pm 7km$. For receivers at further distance, the error increases to a maximum of 26% at $x = \pm 9,10km$.

Examining the absolute error of the phase in this last case, there is a maximum of about 10° at $x = \pm 2km$ and at $x \pm 3,4km$ the error has decayed to 4°. For receivers with larger offsets the oscillations continue but with lower amplitude, with maximums at $x = 6$ and $10km$ of about 6° and a minimum at $x = 8km$ of about 3°.

We explain the large error at all positions because of an inductive-galvanic effect, larger than in the $\lambda = 4km$ undulating bathymetry model, due to a more rough bathymetry in this last test. On the other hand, we explain the larger error close to the source and above the reservoir because of an interaction between the bathymetry distortion and the reservoir distortion.

4.4.2 Two-dimensional MT graben-like model

To validate our program on a 2-D MT model with a complex geometry, we consider the graben-like model introduced in the COMMEMI project (Zhdanov et al., 1997) and referred as the COMMEMI model 2D-4. The COMMEMI model 2D-4 (Figure 4.40) consists of an air layer and three layers with resistivities $25\Omega \cdot m$, $1000\Omega \cdot m$ and $5\Omega \cdot m$ with a graben-like structure embedded between the first and the second layer. The first layer is $0.5km$ thick. The graben-like structure has a resistivity of $2.5\Omega \cdot m$ and diminishes to the right-

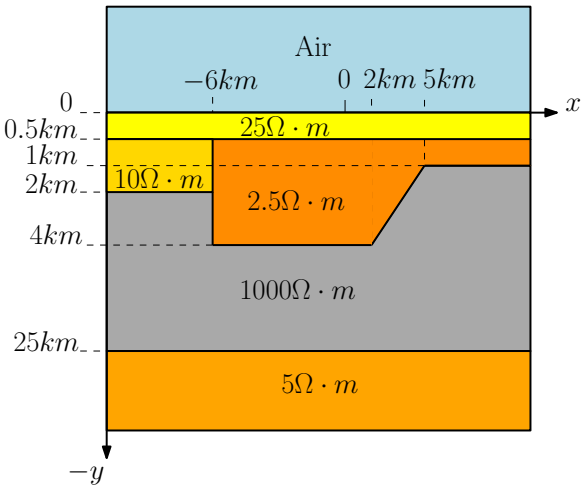

Figure 4.40: *Scheme of the COMMEMI model 2D-4 by Zhdanov et al. (1997). It comprises an air layer and three layers with resistivities* $25\Omega \cdot m, 1000\Omega \cdot m$ *and* $5\Omega \cdot m$ *with a graben-like structure embedded between the first and the second layers. The first layer is* $0.5km$ *thick. The graben-like structure has a resistivity of* $2.5\Omega \cdot m$ *and diminishes to the right-hand model boundary. The thicker part is* $3.5km$ *and the thiner part is* $1km$ *thick. On the left-hand model boundary the stratification is different because of a semi-infinite layer with* $10\Omega \cdot m$ *resistivity and with* $1.5km$ *thickness. Frequencies used in the tests for this model are* $0.01, 1/9$ *and* $1Hz$.

hand side model boundary. The thicker part is $3.5km$ and the thinner part is $1km$ thick. On the left-hand side model boundary the stratification is different because of a semi-infinite layer with $10\Omega \cdot m$ resistivity and with $1.5km$ thickness. The receivers are located in the subsurface at $-0.1m$ depth, distributed along the x–axis, at: $-20, -10, -7, -6, -5, 0, 2.5, 8$ and $16km$. The model is studied using three frequencies: $0.01, 1/9$ and $1Hz$. The lowest frequency forces large model dimensions of $2000km \times 2000km$.

We solve for E_z and H_z in this model, applying the goal-oriented adaptive mesh refinement to each frequency separately, with three mesh groups each one with only one frequency, and using quadratic shape functions. The goal function is again a gradient of the dependent variables E_z and H_z. We set to refine in each iteration of the adaptive mesh refinement algorithm, a fraction of 10% of the elements with larger error.

In Figures 4.41 and 4.42 we plot the elementwise error indicator for the initial mesh, for the first refinement step and for the last one (5^{th} level), for E_z and H_z, respectively. The data correspond to mesh group 2 with frequency $1/9Hz$ which we found representative of the results for all other frequencies. We observe that although the mesh is coarse in the top and bottom of the model, in the middle the mesh is very fine in order to accommodate the 0.5 and $1-2km$ layers. For both E_z and H_z, the initial error is larger in the air layer, in the receiver locations, in the corners of the embedded graben-like structure and in the top of the bottom layer, at around $y = -25km$. As the adaptive mesh refinement algorithm progress, these regions are refined, and after the 5^{th} iteration, the error indicator has decreased in these regions to more than 10^{-5} of its initial value.

Figures 4.43 and 4.44 show the spatial distribution of the dual solution, the residual and the error indicator for the same frequency of $1/9Hz$, for the first refinement step and

for E_z and H_z, respectively. We observe that for E_z (Figure 4.43), the dual solution is largest in the receivers locations but it is also large in both the center of the model and in the air layer. On the other hand, the residual is largest in the thin layers, in the graben-structure and in the air layer. Consequently, the elementwise error indicator is distributed as described above.

The dual solution for H_z in Figure 4.44 shows smaller values in the air layer compared to E_z. The largest values are in the receivers locations, in the first thin layers, in the graben-structure and in the top of the more bottom layer. The residual shows also a different spatial distribution compared to E_z. The air layer has the largest values, and the residual in the center of the model is more than 10^5 orders of magnitude smaller, with only significant larger values in the corners of the graben-structure. The error indicator can be easily seen as the product of these two quantities, resulting in a similar distribution as for E_z, as described above.

We associate the larger error values in the air compared to the rest of the model, because of large EM fields values in this region. As described in Chapter 2, in MT we excite the model by giving boundary conditions on the EM fields in the top of the model. In the air the EM fields have a similar value as in the top of the model and the diffusion is significant when penetrating the Earth. Thus, the largest values in the air give a largest residual. The largest values of the dual solution in the air could be explained partly for the same reason but also because of the strong variation of the conductivity values in the air-Earth interface, affecting the accuracy of the solution in the receivers locations.

As a consequence of the large error in the air, the mesh refinement concentrates in this region, augmenting largely the number of elements before decreasing the error in the receiver locations. However, for the first model we examined in this Chapter (Figure 4.1), for which we did not apply the adaptive mesh refinement algorithm, a coarse mesh in the air was resulting in accurate results at the receivers. Therefore, we think the adaptive mesh refinement algorithm should be improved to apply it in MT examining other error estimators.

In Table 4.5 we provide the initial and final (after 5 mesh refinement steps) number of elements and number of DOFs used to calculate the solutions for the three frequencies. The same table lists the time used to assemble and solve the solution, the residual and the dual solution in the 5^{th} iteration of the adaptive mesh refinement algorithm, and the time to solve the system of equations on the mesh resulting after the 5^{th} mesh refinement iteration. All quantities are given for the three frequencies and correspond to the solution of both E_z and H_z together. We find that there are not significant variations of the number of elements, and consequently number of DOFs or solution time, between frequencies. The initial number of elements is large since the model dimensions are large ($2000km \times 2000km$) and the mesh needs to accommodate the shallow thin layers of the model. Consequently, the number of DOFs is also large and larger than the number of elements since we are solving for both E_z and H_z and using quadratic shape functions. The increase of these quantities after the 5^{th} mesh refinement step is significant, the number of elements is al-

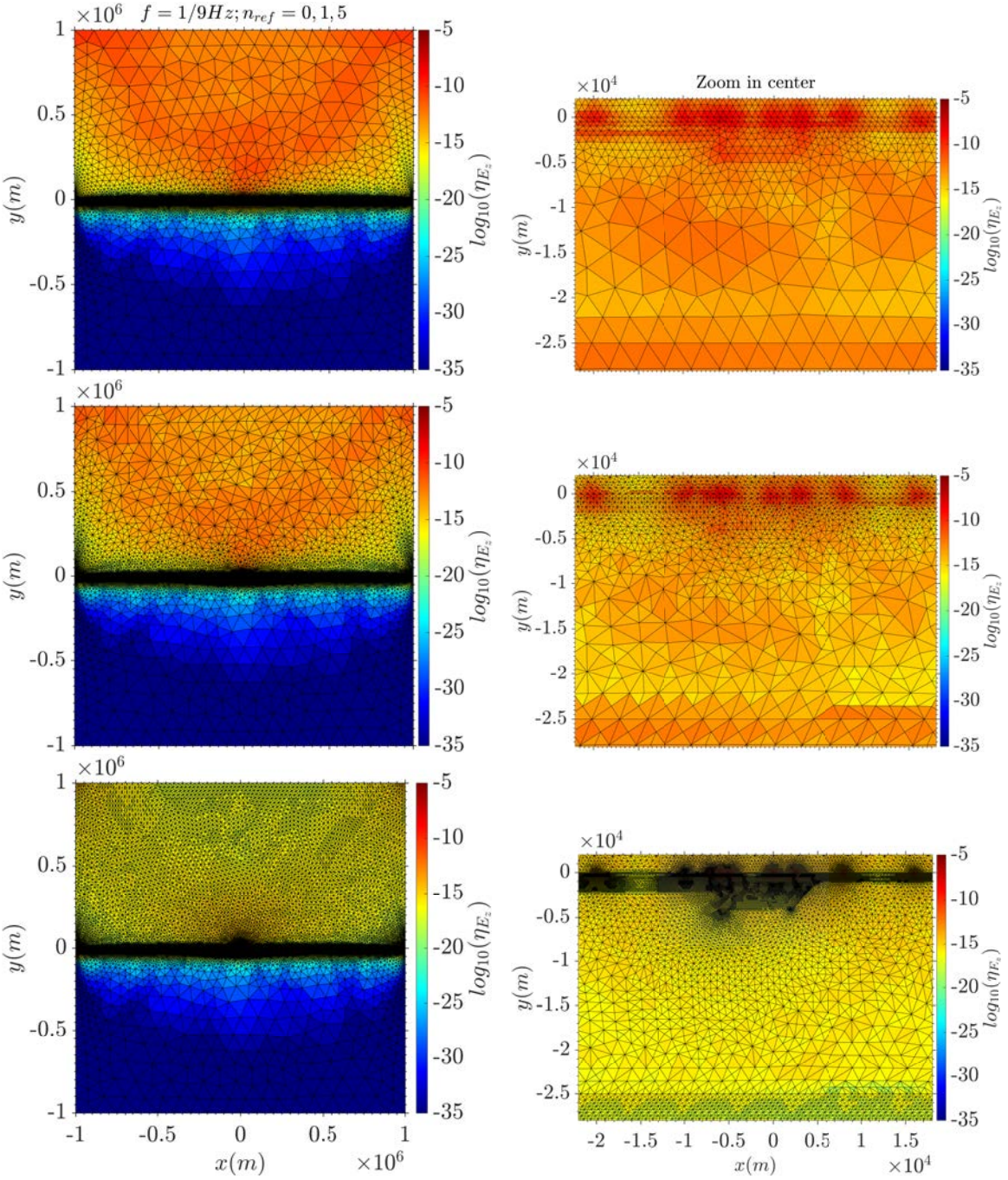

Figure 4.41: *Elementwise error indicator of the dependent variable E_z at $1/9Hz$ frequency in different steps of the goal-oriented adaptive mesh refinement algorithm, for the MT COMMEMI model 2D-4 and corresponding adaptive mesh. The results correspond to quadratic shape functions. From top to bottom, error for the initial mesh and for two goal-oriented adaptive mesh refinement steps: $1st$ and $5th$. Plots on the right side zoom into the center where the embedded graben-structure and the receivers are located.*

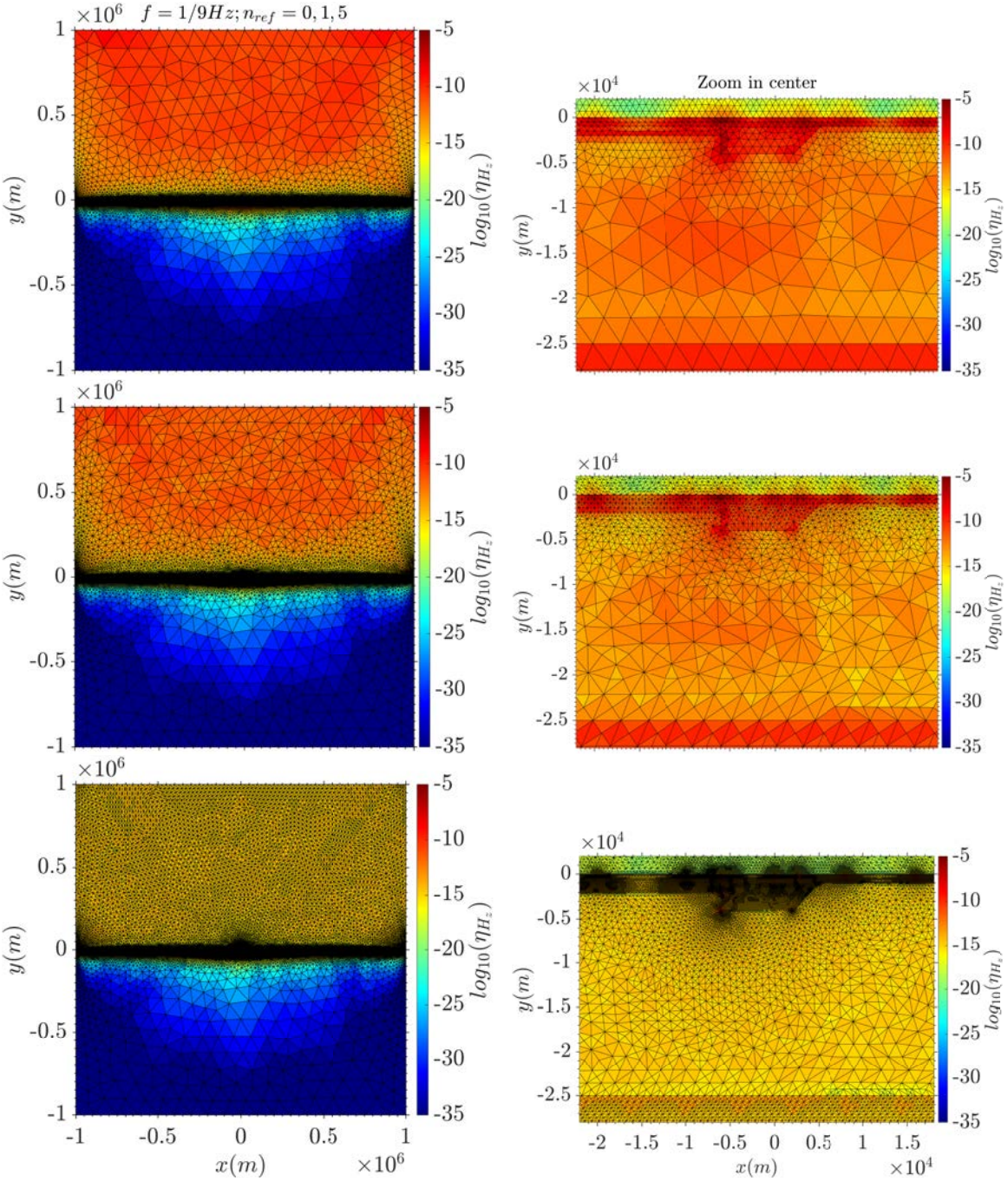

Figure 4.42: *Elementwise error indicator of the dependent variable H_z at $1/9Hz$ frequency in different steps of the goal-oriented adaptive mesh refinement algorithm, for the MT COMMEMI model 2D-4 and corresponding adaptive mesh. The results correspond to quadratic shape functions. From top to bottom, error for the initial mesh and for two goal-oriented adaptive mesh refinement steps: $1st$ and $5th$. Plots on the right side zoom into the center where the embedded graben-structure and the receivers are located.*

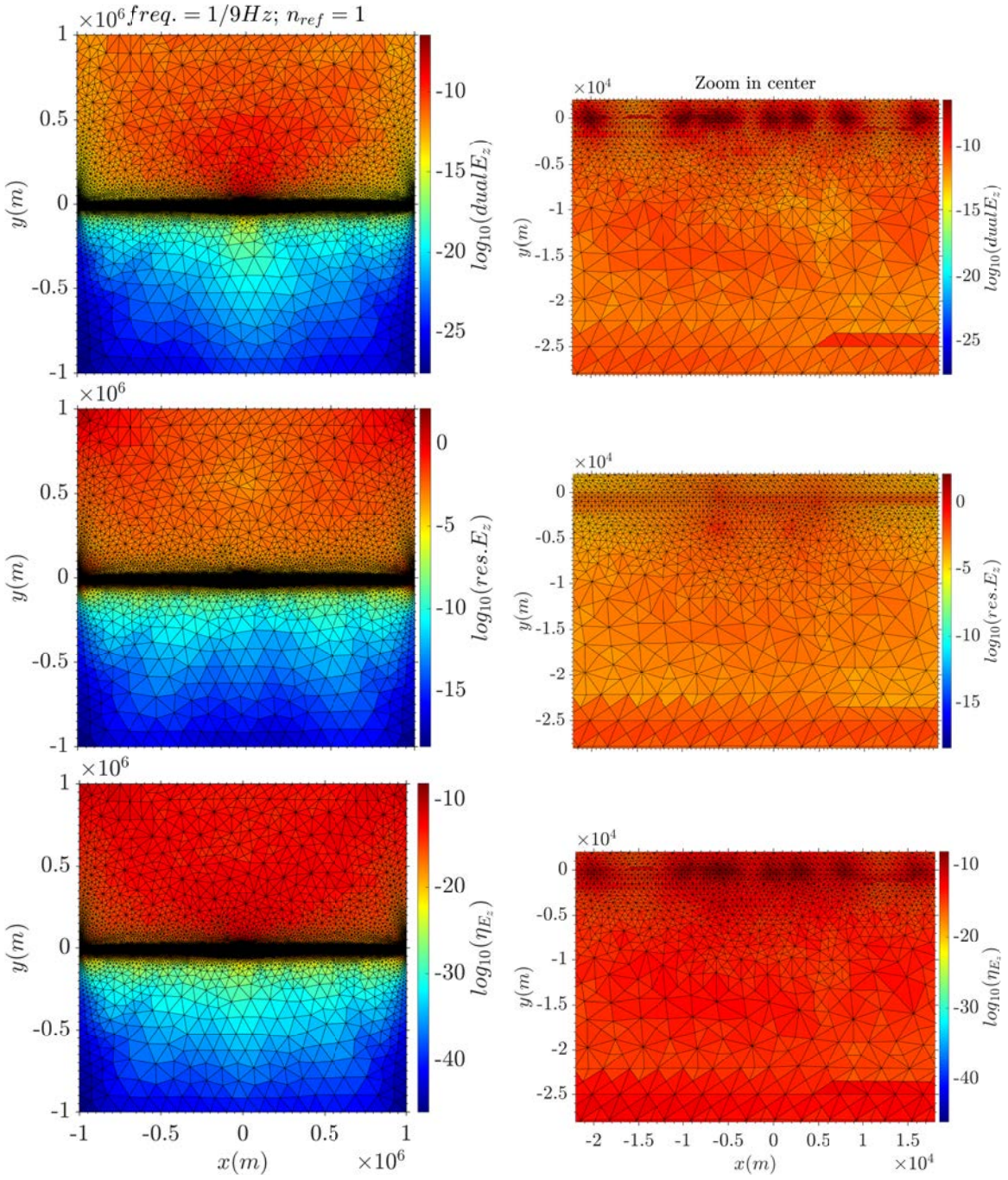

Figure 4.43: *From top to bottom: E_z, dual of E_z, residual and error indicator with corresponding mesh, at $1/9Hz$ frequency and using quadratic shape functions, after the first step of the goal-oriented adaptive mesh refinement algorithm for the MT COMMEMI model 2D-4. Plots on the right side zoom into the center where the embedded graben-structure and the receivers are located.*

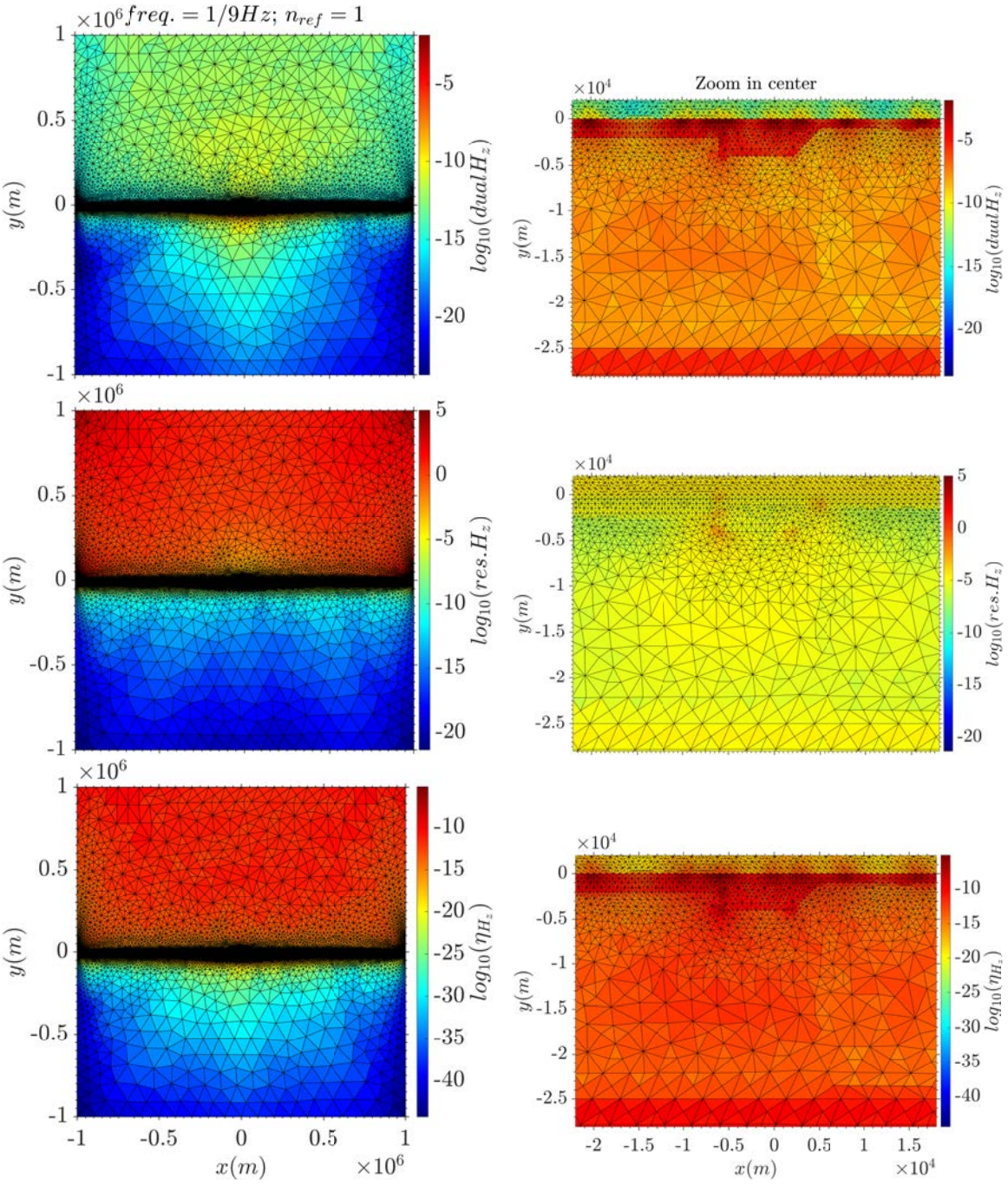

Figure 4.44: *From top to bottom: H_z, dual of H_z, residual and error indicator with corresponding mesh, at $1/9Hz$ frequency and using quadratic shape functions, after the first step of the goal-oriented adaptive mesh refinement algorithm for the MT COMMEMI model 2D-4. Plots on the right side zoom into the center where the embedded graben-structure and the receivers are located.*

Table 4.5: *Frequency, initial and 5^{th} mesh refinement step number of elements and number of DOFs, time for calculation of the solution, the residual and the dual solution and time for calculation of the solution in the resulting mesh, after the 5^{th} mesh refinement step, when modeling the MT COMMEMI model 2D-4. The computer used in the tests is an INTEL i7 4 GHz quad-core processor and 16 GB RAM desktop computer.*

Frequency (Hz)	Num. of elements n_0	Num. of elements n_5	Num. of DOFs n_0	Num. of DOFs n_5	Time n_5: Sol., Res., Dual (s)	Sol. Time n_5 (s)
0.01	103575	187601	414804	751208	25.01	12.49
1/9	103575	187276	414804	749874	27.88	13.36
1	103575	185428	414804	742534	26.59	13.08

most twice the initial value. As discussed above the error estimator function we are using in the adaptive mesh refinement seems not to be adequate in this form to be applied to MT models, and other functions or methods should be investigated.

The time that needs the solver to assemble and solve the system of equations is also large since the number of DOFs is large. It needs about $13s$ using an INTEL i7 4 GHz quad-core processor and 16 GB RAM desktop computer. If additionally we calculate the dual solution and the residual it takes about twice this time.

In Figure 4.45 we also show the variation of the global error estimate with the number of DOFs for the three different frequencies. We observe that after the 5^{th} mesh refinement step, with about 7.5×10^5 DOFs, the error for the lower frequencies, 0.01 and $1/9Hz$, is smaller than 10^{-1} the initial value and, in contrast, the error for the highest frequency of $1Hz$ has not reached this threshold. The reason is that the skin depth is larger for lower frequencies, thus, the mesh is fine enough for the lowest frequencies but not for the highest ones, which need a finer mesh for the same accuracy. When the number of DOFs are almost twice its value in the 5^{th} mesh refinement step, 13×10^5, the error for the $0.01Hz$ frequency has not decreased, it is 3×10^{-2} its initial value. For the same number of DOFs, at a frequency of $1/9Hz$, the error has decreased slightly, from 5×10^{-2} to 1.5×10^{-2}, and for the highest frequency of $1Hz$ it has reached the 10^{-1} threshold, arriving to a value of 3.5×10^{-2} its initial value. This shows that after the 5^{th} mesh refinement step the error for the lowest frequency of $0.01Hz$, is not sensitive anymore to the refinement, contrarily to the error for 1/9 and $1Hz$, which could still be reduced. This shows again that the performance of the adaptive mesh refinement is not optimal for this problem.

Finally, we compare our results with the responses computed with MARE2DEM (Key and Ovall, 2011) and with the corresponding solutions published in Zhdanov et al. (1997) from the COMMEMI project, an international project on the comparison of modeling methods for electromagnetic induction. To compute the solutions using the MARE2DEM program we used the default FE parameters in the free-available code, and for the comparison with solutions obtained from the COMMEMI project we took the corrected mean values (with index 1). The quantities to benchmark the solution are the apparent resisiv-

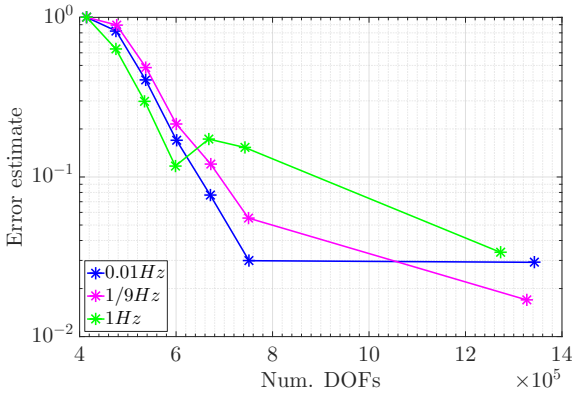

Figure 4.45: *Normalized error estimate as a function of the number of DOFs for three different frequencies:* $0.01, 1/9$ *and* $1Hz$ *(in colors), when modeling the MT COMMEMI model 2D-4 using the goal-oriented adaptive mesh refinement algorithm. The normalization is realized dividing the error estimate values by the initial value for each frequency case.*

ities and phases for both the TE and TM modes calculated from the EM fields solution. The comparison with the COMMEMI data is done only for the apparent resistivities at the slightly different receivers locations that are available, these are at: $-10, -7, -6, -5, 2, 3.5$ and $5km$.

Figure 4.46 shows the apparent resistivities for the two EM modes as a function of receiver locations calculated using our program, together with the results calculated using MARE2DEM and the ones from the COMMEMI project. The COMMEMI results are plotted with the standard deviation given in Zhdanov et al. (1997) as an error bar. The same figure illustrates the relative error of the apparent resistivities for the two polarization modes as a function of the receivers positions and for the three frequencies, calculated between our solution and the MARE2DEM solution, and between our solution and the COMMEMI results.

In Figure 4.47 the phases and absolute errors of the phases are plotted for both modes and for the three different frequencies, from the results obtained with our program and from the results obtained using MARE2DEM. The absolute errors are also plotted, calculated between the solutions computed with our program and the solutions of MARE2DEM.

Describing qualitatively the apparent resistivity curves (Figure 4.46), at $0.01Hz$ the TM mode shows stronger variations with the resistivity than the TE mode. The TM mode apparent resistivity is about $70\Omega \cdot m$ at receivers $-20, -10$ and $-7km$ as a result of the resistive, $1000\Omega \cdot m$, layer at $2km$ depth. It starts to decay at $-6km$, where the more conductive graben-structure is located, to a minimum value of $3\Omega \cdot m$ at $0km$, approximately in the center of the $2.5\Omega \cdot m$ structure. Then, the resistivity grows steeply along the inclined plane until a value of about $35\Omega \cdot m$ at the $5km$ position, where the inclined plane finishes and becomes a thin layer, $1km$ thick. The curve is then flat, with a resistivity of about $50\Omega \cdot m$ at 8 and $16km$ positions, a smaller value than the one on the LHS of the graben-structure. The TE apparent resistivity curve shows a smoother shape than the TM mode, however it is affected by the resistivity variations in a larger range of positions. It is about $50\Omega \cdot m$ at

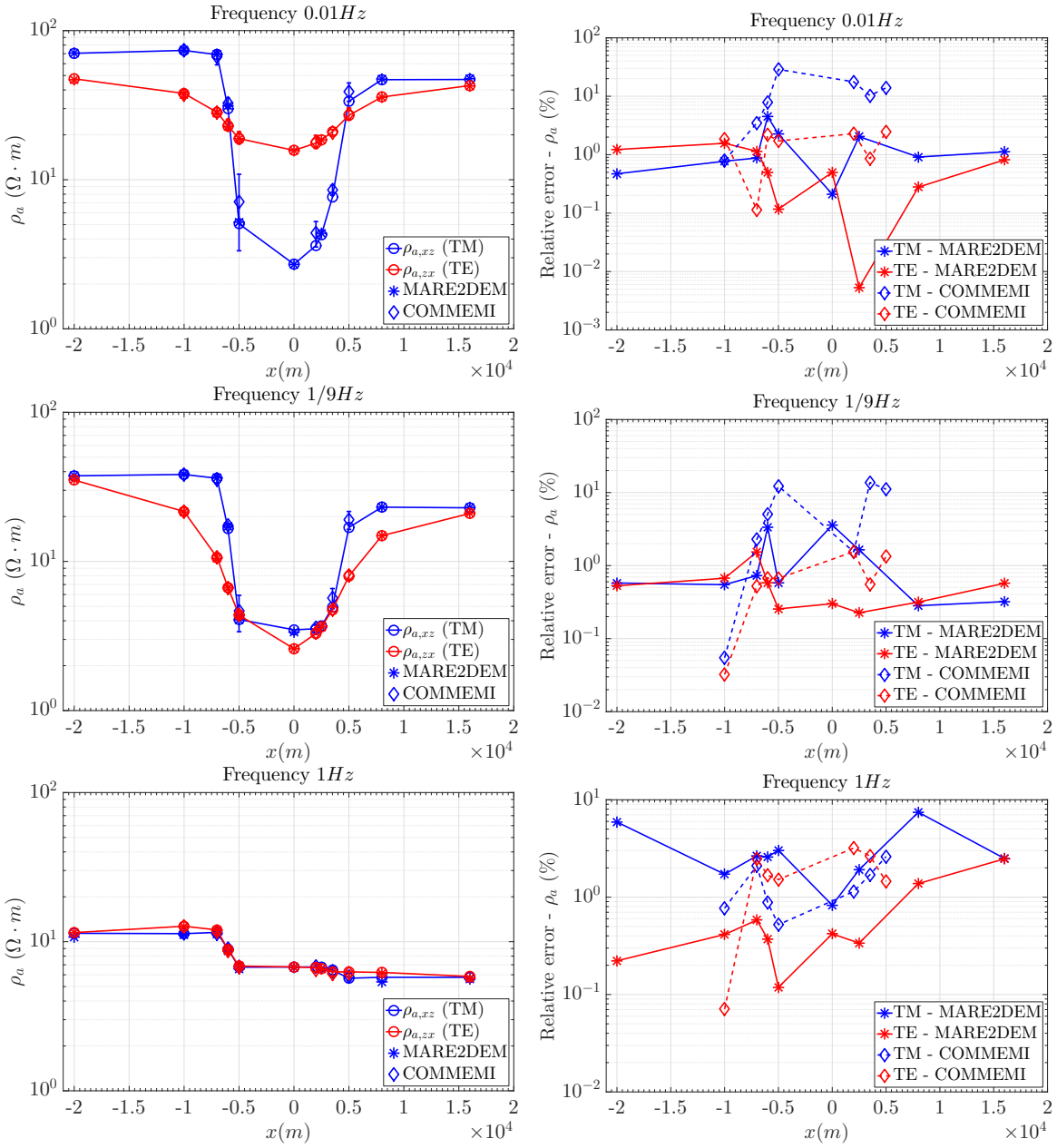

Figure 4.46: *Computed TM (blue) and TE (red) modes apparent resistivities (left) and relative error of the apparent resistivities (right) as a function of the receivers locations, for three different frequencies (from top to bottom):* $0.01, 1/9$ *and* $1Hz$*, for the MT COMMEMI model 2D-4. The apparent resistivity plots also include data calculated with the MARE2DEM program (Key and Ovall, 2011) and data from the COMMEMI project (Zhdanov et al., 1997), corrected mean values (with index 1) with standard deviation. The relative error is calculated between our results and the results obtained using MARE2DEM (solid line), and between our results and the results from the COMMEMI project (dashed line). The apparent resistivity values calculated using MARE2DEM and the ones from the COMMEMI project are not all at the same receivers locations, since the published COMMEMI data is given at different receiver locations compared to the original model. The receivers locations for the MARE2DEM results are:* $-20, -10, -7, -6, -5, 0, 2.5, 8$ *and* $16km$*, and for the COMMEMI results are:* $-10, -7, -6, -5, 2, 3.5$ *and* $5km$*.*

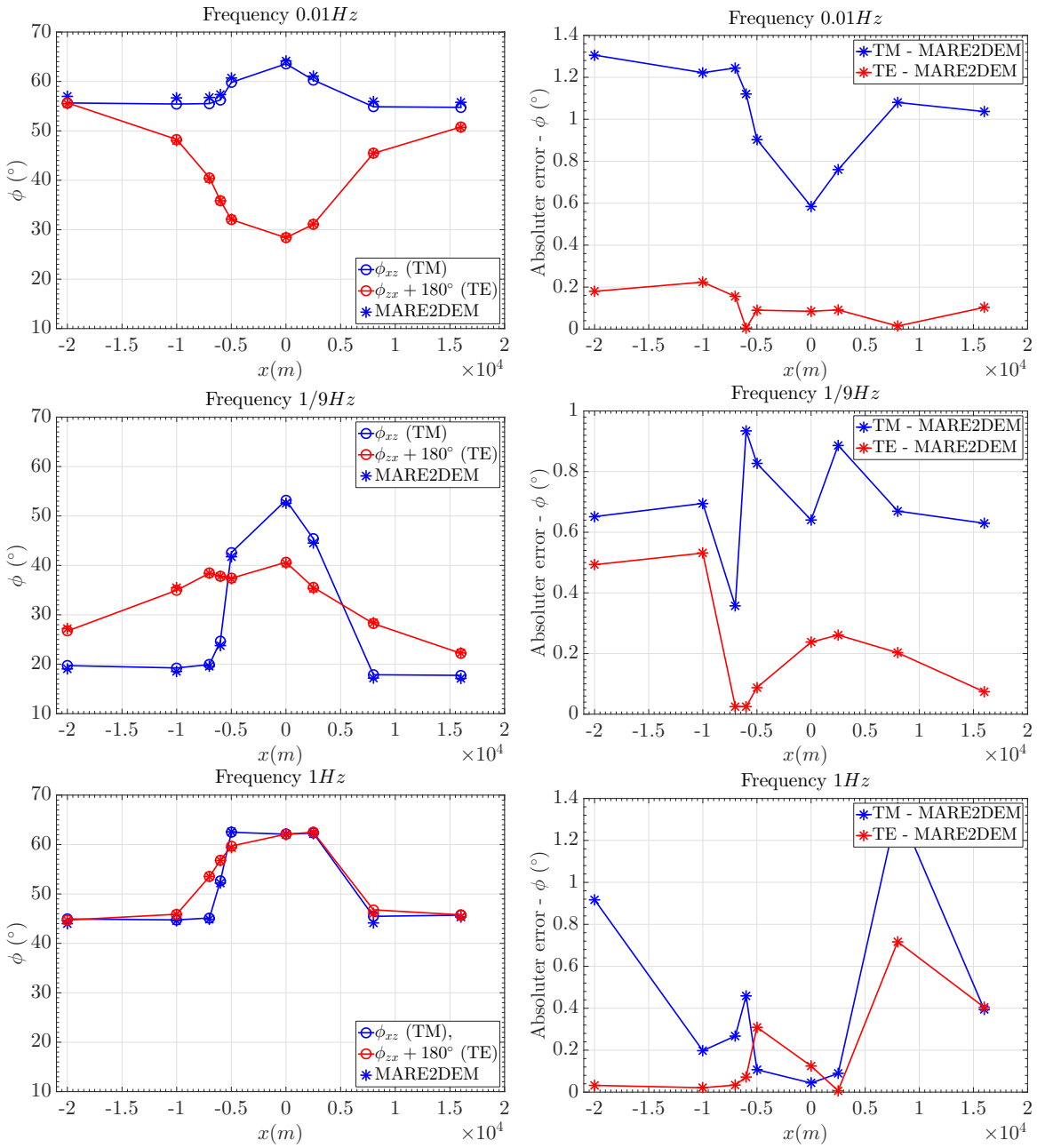

Figure 4.47: *Computed TM (blue) and TE (red) modes phases (left) and absolute error of the phases (right) as a function of the receivers locations, for three different frequencies (from top to bottom):* $0.01, 1/9$ *and* $1Hz$*, for the MT COMMEMI model 2D-4. The phases plots also include data calculated with the MARE2DEM program (Key and Ovall, 2011). We add* $180°$ *to the TE mode phase for a better visualization of the results. The relative error is calculated between the results obtained with our program and the results obtained using MARE2DEM.*

$-20km$, and in the next receiver position, at $-10km$, the value has decayed to $40\Omega \cdot m$. If we continue moving to the right, the decay continues smoothly to a minimum of more than $15\Omega \cdot m$ at $x = 0$. After this position to the right, the resistivity curve starts to grow also smoothly, with a maximum of about $40\Omega \cdot m$ at the last receiver location, at $16km$.

The relative error at this frequency, comparing our results to the ones of MARE2DEM, is less than 2% at most of receivers for both the TE and TM modes, and only slightly higher, 4%, for the TM mode at $-6km$ position in which the resistivity curve changes abruptly. The relative error compared to the COMMEMI results is below 3% for TE resistivities and larger for the TM resistivities at most of the receivers, with values up to 30% at $-5km$. However, we want to note that the COMMEMI results are mean values with error bars, and that all the solutions with our code fall inside the error bars.

In the same Figure, at $1/9Hz$ frequency, the apparent resistivity is not so much affected by the $1000\Omega \cdot m$ resistive layer at $2km$ depth compared to the result at $0.001Hz$, it is about $35\Omega \cdot m$ at $-20km$. As for the lowest frequency, we observe the decay of the TM mode apparent resistivity at $-6km$, coinciding with the LHS lateral boundary of the embedded graben-structure, and of the TE mode, at $-10km$ further away of the graben-structure. The minimum value is at $x = 0$ for both modes, with $2.5\Omega \cdot m$ for the TE and $3\Omega \cdot m$ for the TM modes. When moving to the right of the graph, the TM mode apparent resistivity grows more steep than the TE mode, as observed for the $0.01Hz$ frequency. The slope changes for the TM curve at $5km$ with about $20\Omega \cdot m$ and continues growing smoothly until it reaches the $25\Omega \cdot m$ at $8km$. The value is the same, $25\Omega \cdot m$, at $16km$, and also approximately the same that reaches the TE mode in a smoother way.

At the same frequency, the relative error compared with the MARE2DEM solution is less than 2% for the TE mode, with the largest value at $-7km$, and less than 4% for the TM mode with the largest values at $-6km$ and 0 positions, coinciding with the start of the decay of the apparent resistivity curve and with its minimum. The relative error compared to the COMMEMI results also shows larger values for the TM mode than for the TE mode. It is about 10% for the TM mode and less than 2% for the TE mode. The largest discrepancies of the TM mode apparent resistivity coincide approximately with the abrupt decay of the resistivity on the LHS of the graben-structure, and with receivers over the inclined plane, at 3.5 and $5km$, where the apparent resistivity grows steeply. However, all the resistivity values calculated with our program fall inside the error bars of the COMMEMI results.

At the highest frequency of $1Hz$ (Figure 4.46 bottom) the resistivity variations are very smooth compared to the ones at lower frequencies, and very similar for both TE and TM modes. At the RHS of the graben-structure, the resistivity is about $10\Omega \cdot m$ for both EM modes, influenced by the shallower layers. Continuing to the right, at $-6km$ the resistivity decreases slightly and at $-5km$, the receiver is above the graben-structure and the apparent resistivity is about $6.5\Omega \cdot m$. This indicates that the graben-structure influences the apparent resistivity, but since the apparent resistivity value is larger than for the other lower frequencies at the same location, we interpret that this frequency is more sensitive to the shallower resistive layer which has a larger resistivity value of $25\Omega \cdot m$. The apparent re-

sistivity remains constant for all the other receivers above the graben for both EM modes. After the horizontal position of $2km$, the apparent resistivity for the TM mode starts to fall down smoothly to a value of about $5.5\Omega \cdot m$ at $5km$, coinciding with the position where the inclined plane finishes and the graben-structure becomes a thin layer. Moving more to the right of the model, the resistivity variations are very smooth for the TM mode, and at $16km$, the apparent resistivity is about $6\Omega \cdot m$. The decay for the TE mode from $2km$ to $16km$ positions is slightly smoother than for the TM mode, and at $16km$ the apparent resistivity is also $6\Omega \cdot m$.

For the same frequency, the relative error compared to the MARE2DEM solution is larger for the TM mode than for the TE mode. The relative error for the TM mode is between 1 and 8% with the largest values at -20 and $8km$, and the relative error for the TE mode is between 0.1% and 2.5%, with the largest value at $16km$. The relative error compared to the COMMEMI results is similar for both modes with values of less than 4%.

Examining the phases in Figure 4.47 we observe that at $0.01Hz$ the phases are between 30° and 65° (after the addition of 180° to the TE mode), and that the more conductive graben-structure produces a maximum in the TM mode and a minimum in the TE mode. The apparent resistivities at the same frequency, show changes in the TM mode which are more abrupt than for the TE mode and coincide more precisely with the positions of the change of the resistivity. Contrarily, the jump in the phase due to the graben-structure is larger for the TE mode than for the TM mode, passing from 55° to 30° in the first one, and from 55° to 64° in the second one. The absolute error of the phases at this frequency is between 0.6 and 1.4° for the TM mode, and below 0.3° for the TE mode.

In the same Figure, at $1/9Hz$, the effect of the graben-structure in the phases is a maximum for both modes, more pronounced for the TM mode. The jump for the TE mode is from 27° to 40°, and the jump for the TM mode is from 20° to 53°. We observe, as for the $0.01Hz$ frequency, that the changes in the phase of the TM mode coincide precisely with the changes in the resistivity structures, and that the TM mode is affected by these variations in a larger spatial range than the TE mode. The absolute error of the phases is between 0.4 and 1° for the TM mode and below 0.4° for the TE mode.

Finally, the spatial variation of the phases at the highest frequency of $1Hz$ (Figure 4.47 bottom) is very similar for both modes as observed in the apparent resistivities at this frequency. The conductive graben-structure effect in the phases is again a maximum for receivers above it, passing from 45° to 62°, and again to 45° when moving to the right of the conductive structure. Also, as for the lower frequencies, the variations of the TM mode phase coincide precisely with the variations of the resistivity, and the variations of the TE mode are affected by the resistivity changes in a larger rank of receiver positions. The absolute errors of the phase are small, below 1.4° for the TM mode and 0.8° for the TE mode.

From these tests, we can conclude that our numerical results are accurate when compared to COMMEMI and MARE2DEM results, although we have detected that the performance of the adaptive mesh refinement algorithm for MT is not efficient and we should

investigate a more appropriate error estimator. The program models accurately the abrupt changes in the apparent resistivities and phases which coincide with jumps in the resistivity due to the geological structure, and also the apparent resistivities and phases corresponding to the inclined plane forming the graben-structure. The thin layers at the upper part of the subsurface model are also well resolved by the highest frequencies. We also observed a better accuracy of the TE mode with respect the TM mode. This result is also contained in the COMMEMI results. The COMMEMI TM mode error bars are also larger than the TE mode ones, indicating more variability in the TM mode results between different programs. The explanation is that the TM mode is more sensitive to the air layer, and consequently the solution is less stable.

4.5 Oriented and finite-length 3-D sources

Usually, in 2-D modeling codes and in the previous models we used in this Chapter for numerical experiments, the CSEM sources are approximated as point dipoles. However, typical CSEM sources used in land and marine environments are horizontal wires with length of several hundred meters, that generate 3-D EM fields, sensitive to both, resistive and conductive, and relatively deep targets. When the source-receiver distance is sufficiently large, the point dipole is a good approximation. However, when the goal of the CSEM survey is to resolve small structures, it is necessary to reduce the offset, and then the inaccuracy of the dipole approximation can be on the order of the target anomalies, thus, it is necessary to consider the actual source geometry (Streich and Becken, 2011).

In Chapter 3, we described the capability of our program to model the orientation and length of the sources and give some details on the implementation. In this section, we benchmark this component of the program, modeling different orientation and geometry of the CSEM source and at the same time, we discuss the importance of considering a more realistic approximation of the CSEM source on certain model situations.

For this purpose, we start considering a land CSEM model grossly simulating the geology at the carbon sequestration site in Ketzin, Germany. This model was examined by Streich et al. (2011) and by Streich and Becken (2011) for similar source studies in the framework of a 1-D solution and of a 2.5-D numerical solution using a primary/secondary field approach and FD. In Figure 4.48 we illustrate a 1-D and a 2-D approximations of the model.

The 1-D model (Figure 4.48 left) is composed of an air layer and three subsurface layers. The resistivity in the first layer is $3\Omega \cdot m$ and the thickness $635m$. The second layer represents the storage layer with resistivity $10\Omega \cdot m$ and thickness $15m$ and the third layer is $1\Omega \cdot m$.

In the 2-D model (Figure 4.48 right), the storage layer is substituted by two blocks embedded between the $3\Omega \cdot m$ and the $1\Omega \cdot m$ layers. One of the blocks has a $5\Omega \cdot m$ resistivity and is $30m$ thick, $1.3km$ wide and its top side is located at $635m$ depth. The other one, has a $10\Omega \cdot m$ resistivity, is $76m$ thick and $1.5km$ wide and its top side is located at $612m$ depth.

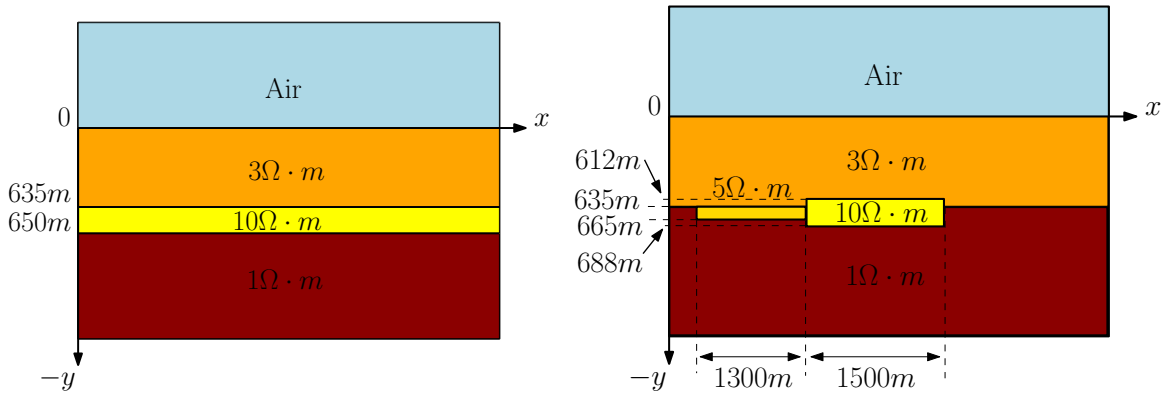

Figure 4.48: *One-dimensional (left) and two-dimensional (right) resistivity models, grossly simulating the geology at the carbon sequestration site in Ketzin Germany proposed by Streich et al. (2011). The model includes an air layer and a first layer of* $3\Omega \cdot m$ *resistivity and* $635m$ *thick. The storage cavity is represented with a* $15m$ *thick,* $10\Omega \cdot m$ *layer in the 1-D model over a* $1\Omega \cdot m$ *resistivity layer. In the 2-D model, the storage layer is substituted by two blocks embedded between the* $3\Omega \cdot m$ *and the* $1\Omega \cdot m$ *layers. One of the blocks has a* $5\Omega \cdot m$ *resistivity and is* $30m$ *thick,* $1.3km$ *wide and its top side is located at* $635m$ *depth. The other one, has a* $10\Omega \cdot m$ *resistivity, is* $76m$ *thickness and* $1.5km$ *wide and its top side is located at* $612m$ *depth. The source is buried* $0.1m$ *in the subsurface and is located at* $x = 0$ *and the receivers are buried at* $0.15m$ *depth and distributed along the positive* $x-$*coordinate.*

On land, the dipole sources need to be particularly long to achieve strong EM fields and surface obstacles may force the practitioner to orient the source in a certain manner. We simulate the CSEM source on the Ketzin model in four different situations: a) an in-line (90° azimuth) horizontal electric point dipole, b) a 120° azimuth oriented horizontal electric point dipole, c) an in-line straight $1km$ length grounded wire, and d) a 120° azimuth oriented grounded wire, $1km$ length. The source is located at $0.1m$ depth and centered in $(x,z) = (0,0)$ and operates at $0.1Hz$ in all cases. The receivers are at $0.15m$ depth and distributed every $500m$ along the x-direction, from $-10km$ to $10km$.

As explained in Chapter 3, we model an oriented source all-at-once, computing its response for positive and negative wavenumber values, and the long grounded wire is simulated by superposing the EM fields computed separately for different point dipole sources situated in certain positions along its length. The wavenumber data set is again composed of 28 values distributed logarithmically from 10^{-4} to $10^{-1}m^{-1}$ and $\kappa_z = 0$. For oriented sources 28 negative values of κ_z, distributed between -1×10^{-1} and $-1\times10^{-4}m^{-1}m^{-1}$, are added to the data set. The $1km$ length dipole is modeled using 10 point dipoles. For the computation of the EM fields solution we have applied the goal-oriented adaptive mesh refinement strategy to different mesh groups of wavenumber values. We used 5 groups when modeling an in-line dipole, and 9 groups when modeling an oriented source.

First, we examine the 1-D case (Figure 4.48 left). This model is costly to solve, because the $15m$ thin layer forces a very fine mesh that extends with the layer to the lateral outer boundaries, resulting in a large number of DOFs. As an example, for the in-line horizontal electric point dipole (HEPD), the initial number of DOFs of the primal solution is 292710, and the final number of DOFs, after two mesh refinement iterations and for mesh group

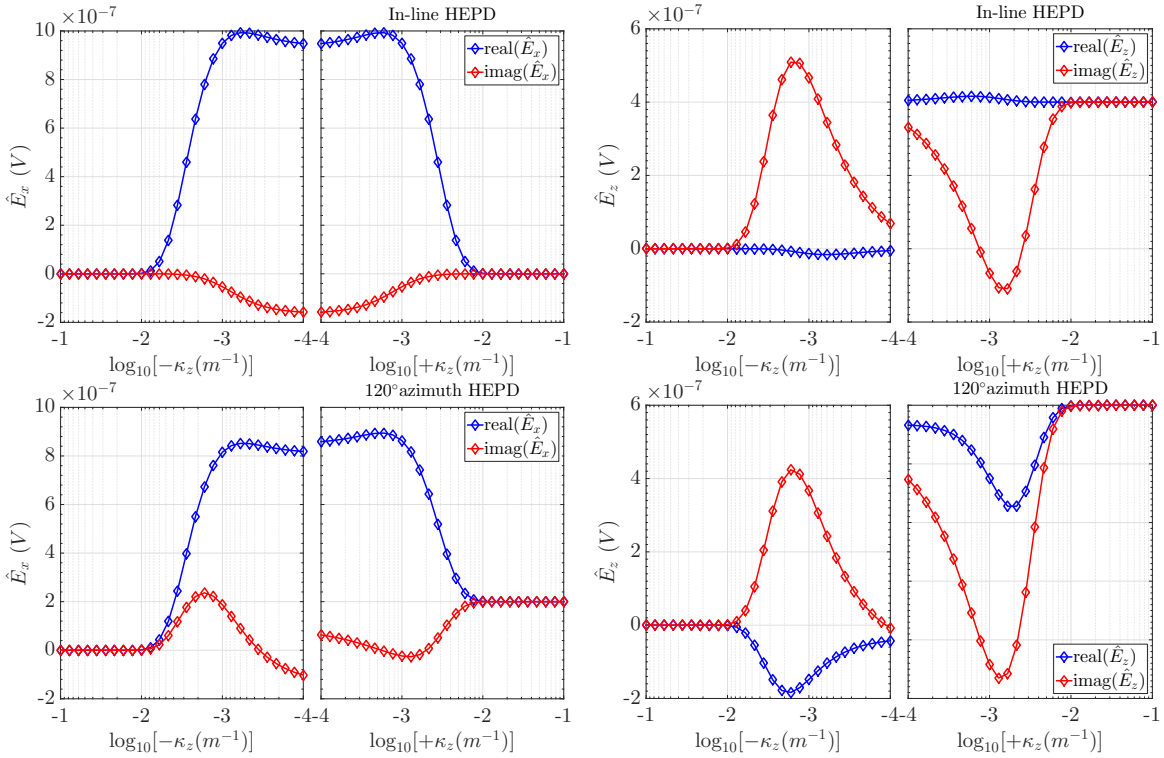

Figure 4.49: *In-line (left) and broad-side (right) electric field component in the κ_z-domain as a function of negative and positive wavenumber (κ_z) values ($\log_{10}$) resulting from an in-line horizontal electric point dipole (top) and from an oriented 120° azimuth horizontal electric point dipole (bottom) on the 1-D Ketzin model.*

2, with $\kappa_z = 2.78 \times 10^{-4} m^{-1}$, is 385348. However, we found that two iterations of the goal-oriented adaptive mesh refinement algorithm are sufficient to obtain accurate results.

Figure 4.49 shows an intermediate result. The in-line and the broad-side electric field components in the κ_z-domain, $\hat{E}_x$ and $\hat{E}_z$, respectively, are plotted as functions of $\log_{10}(\kappa_z)$, for negative and positive values, and for two different orientations of the HEPD source: in-line (90° azimuth) and oriented 120° azimuth. For the in-line HEPD (Figure 4.49 top), the in-line electric field component $\hat{E}_x$ is an even function to the $\kappa_z = 0$ axis and the broad-side component $\hat{E}_z$ is an odd function to the same axis. From these plots and the explanation in Chapter 3, it is easy to see that with this source orientation, the inverse Fourier transform for the in-line electric field component can be calculated with only positive wavenumber values multiplying the integral kernel by two and using digital filters for the cosine and sine functions, and that for the broad-side component the same integral will be null.

When the HEPD is oriented 120° azimuth (Figure 4.49 bottom), the symmetry of the in-line and broad-side electric field components is not even nor odd to the $\kappa_z = 0$ axis. To calculate the inverse Fourier transform using the digital filters for the cosine and sine functions, it is necessary to either decompose the source in an in-line and broad-side sources for which the EM field components symmetry is even or odd, then, compute the solution for each case and superpose them, or compute the solution for negative and positive wavenumber values, and decompose each field component in its even and odd parts. Both

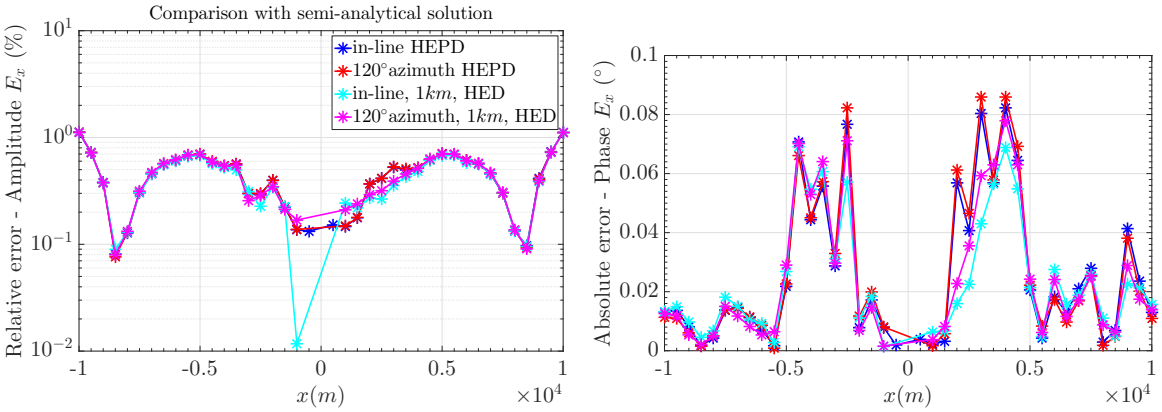

Figure 4.50: *Relative error of the amplitude (left) and absolute error of the phase (right) of the in-line electric field component, E_x, as a function of receivers locations, for the 1-D Ketzin model with different orientation and geometry of the CSEM source (in colors), when compared with semi-analytical responses calculated using DIPOLE1D (Key, 2009). The frequency of operation is $0.1Hz$ and the different source cases are: in-line (90° azimuth) horizontal electric point dipole (blue), 120° azimuth oriented horizontal electric point dipole (red), in-line horizontal electric dipole (grounded wire) $1km$ length (cyan) and 120° azimuth oriented horizontal electric dipole of $1km$ length (magenta).*

approximations are equivalent and require approximately the same run time when modeling the total field, since with the first one it is necessary to compute the solution two times, and with the second one it is necessary to compute the solution for double the number of wavenumber values. In our program we use the second one for sources with an orientation different from the axis.

We compute the solution for the 1-D model in Figure 4.48 left for all source cases using the appropriate strategy depending on the source orientation. In Figure 4.50 the in-line electric field component, E_x, is compared for the different cases to the semi-analytical solution calculated with DIPOLE1D (Key, 2009), which allows oriented sources and length sources on 1-D models. The solution is in all cases accurate with errors in the amplitude between 0.1 and 1%, approximately, and errors in the phase of less than 0.1°.

In Figure 4.51 we plot the amplitude and phase of the in-line electric field component for the same model and for four different source cases, and for the same model with the in-line electric point dipole, but without the reservoir layer. In the same Figure we also show the relative error in the amplitude and the absolute error in the phase calculated between the electric field for the in-line HEPD in the Ketzin model and the electric field for: a) the same source in a model without the reservoir layer, b) a 120° azimuth oriented HEPD, c) an in-line $1km$ length HED and d) a 120° azimuth oriented, $1km$ length HED.

Observing the error in the amplitude, the reservoir layer at this frequency ($0.1Hz$) is more notable at about $3km$ from the source, with an error of 10% when compared to the same model without the storage layer, and the error is about 1% for receivers located at $6km$ or larger offsets. This indicates that small offsets, between 1 and $5km$ will be necessary to measure the effect of the very thin target layer on the electric field. The difference between modeling the orientation of the point dipole (120° azimuth) or approximating it

as an in-line directed point dipole gives a relative error in the amplitude of about 10% at all receivers locations, thus of the same order of magnitude as the error caused by the storage layer. The largest errors are caused by the differences between modeling the longitude ($1km$ length) of the grounded wire or approximating it as a point dipole, with values larger than 10% for offsets smaller than $3km$. Finally, the differences between modeling the source with its longitude ($1km$) and orientation (120° azimuth) or modeling it as an in-line point dipole, results in errors of 10% in the amplitude, with smaller values in receivers located at offsets smaller than $3km$.

The phases (Figure 4.51 bottom) are less sensitive to the source approximation and to the storage layer, with error values smaller than 1.4° for all cases and about 0 for the 120° azimuth oriented point dipole. Also the error curve for the in-line $1km$ length electric dipole is slightly different from the rest, with values of about 1° in small offsets (smaller than $3km$), where for the rest of cases, the errors are less than 0.2°.

According to these results, in this model it is necessary to simulate both the orientation and geometry of the source since the errors caused in the amplitudes and phases by a simpler approach are similar or even larger than the anomaly caused by the target layer.

We extend the study of the modeling of the sources to the Ketzin 2-D case (Figure 4.48 right), described at the beginning of this section.

We model again the same four source variants: a) an in-line HEPD, b) a 120° azimuth HEPD, c) a $1km$ grounded wire oriented in the in-line direction, and d) a $1km$ grounded wire with 120° azimuth orientation. The source is located as in the 1-D case at $0.1m$ depth and centered at $(x,z) = (0,0)$, and the receivers are at $0.15m$ depth and every $500m$ along the x-direction. We simulate all these source cases for 3 different frequencies: $0.01, 0.1$ and $1Hz$.

The solution is computed in each case using the goal-oriented adaptive mesh refinement algorithm. We apply it to 5 and 9 groups of κ_z values, for the in-line and for the 120° azimuth oriented source, respectively, and to each frequency separately, resulting in 15 and 27 mesh groups, respectively. The long grounded wire is calculated using 10 point dipoles, all modeled using the same mesh. The FE with the adaptive mesh refinement methods are more efficient for this model than for the 1-D Ketzin model, since now the storage structure is not a thin layer but two small blocks, and the FE mesh can be very fine in the reservoir location without the need to extend this fine mesh region to all the model. The initial number of DOFs is 46346, a considerable smaller value compared to the 292710 of the 1-D case.

The differences on the in-line electric field component between modeling the orientation and geometry of the CSEM source or modeling it as an in-line point dipole approximation in the 2-D Ketzin model are given in Figure 4.52, for the different frequencies, through the relative error of the amplitude and the absolute error of the phase. The errors are calculated between the responses for each source case under study and the responses for the in-line electric point dipole source. The error between the responses of the model with the blocks and the same model without them is also plotted (in blue). The error in the

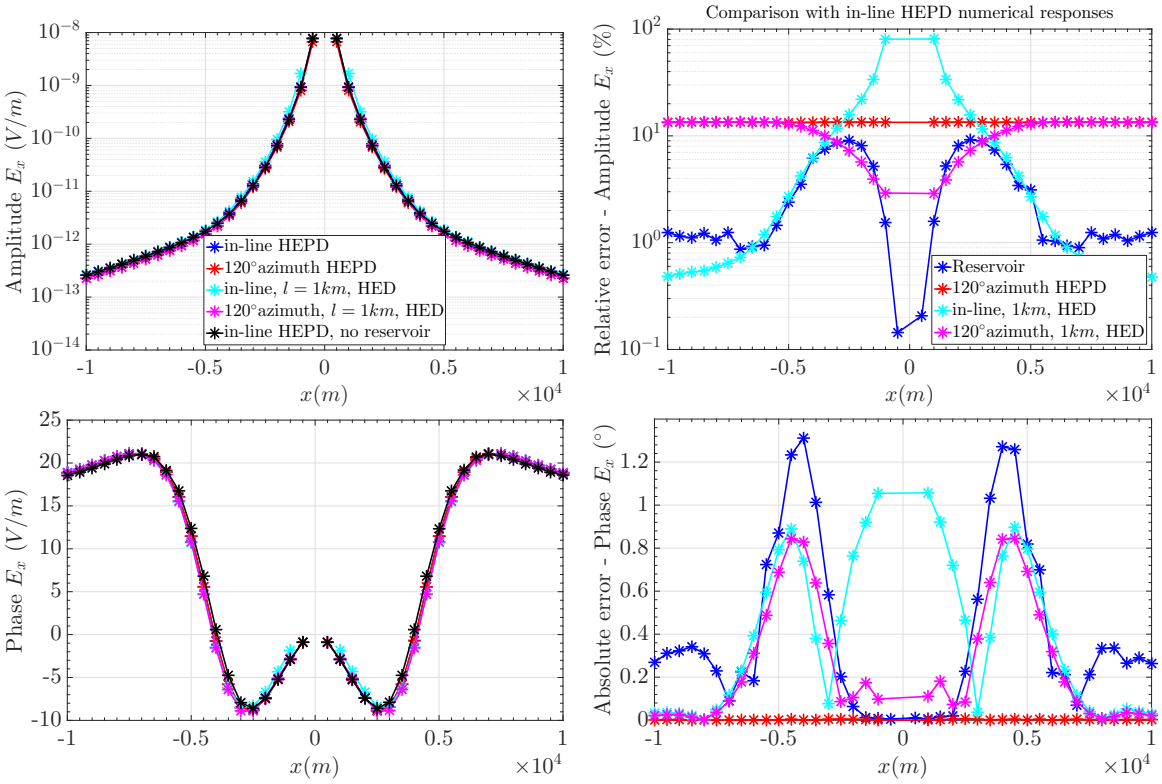

Figure 4.51: *Differences on the in-line electric field component when modeling the orientation and geometry of the CSEM source in the 1-D Ketzin model. Amplitude and phase (left, from top to bottom) and relative error of the amplitude and absolute error of the phase (right, from top to bottom) of the in-line electric field component as a function of receivers locations for different orientation and geometry of the CSEM sources. The frequency of operation is* $0.1Hz$ *and the different source cases are: in-line (*$90°$ *azimuth) horizontal electric point dipole (blue),* $120°$ *azimuth oriented horizontal electric point dipole (red), in-line horizontal electric dipole (grounded wire)* $1km$ *length (cyan) and* $120°$ *azimuth oriented horizontal electric dipole of* $1km$ *length (magenta). The electric field for an in-line horizontal electric point dipole on the same model, but without the reservoir layer is also plotted (black). The errors are calculated between the responses of the model without reservoir and the model with it using an in-line HEPD (blue), and between the responses for each of the described sources and the response of the in-line HEPD for the 1-D Ketzin model.*

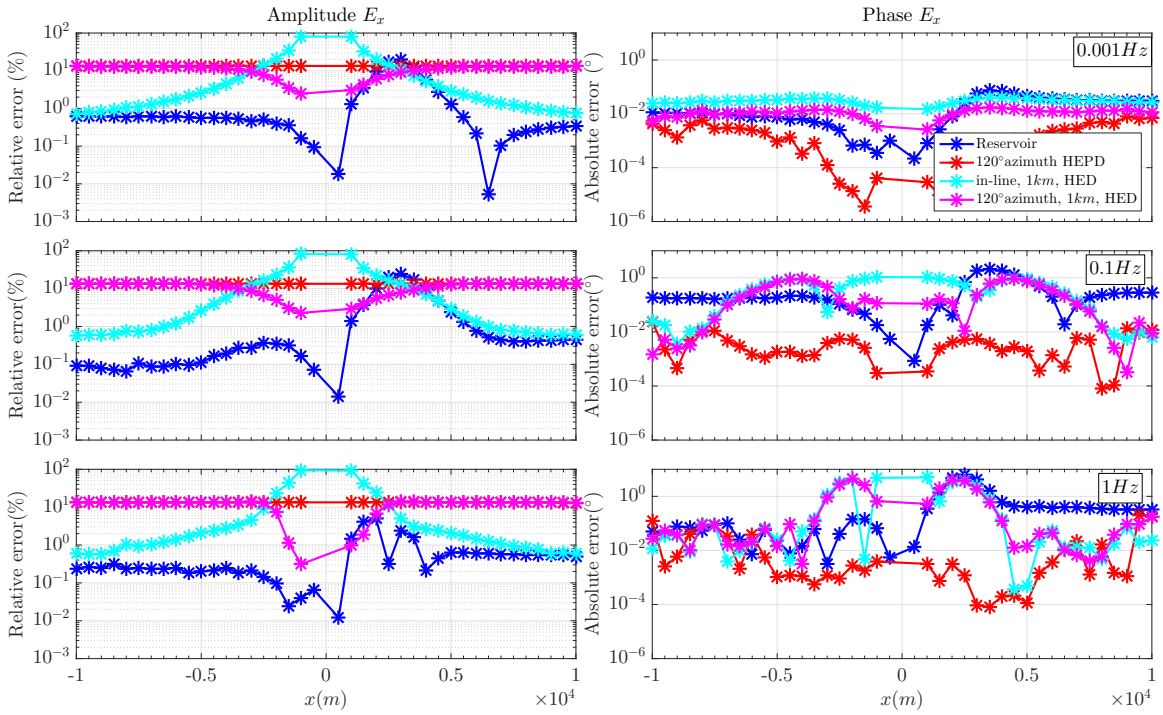

Figure 4.52: *Relative error of the amplitude (left) and absolute error of the phase (right) of the in-line electric field component, E_x, as a function of receivers locations, calculated between the responses using different orientation and geometry approximations of the CSEM sources and the responses from an in-line horizontal electric point dipole source in the 2-D Ketzin model, for three different frequencies (from top to bottom): $0.001, 0.1$ and $1Hz$. The error of the electric field between the 2-D Ketzin model responses and the responses of the same model, but without the storage blocks, using an in-line horizontal electric point dipole source in both models, is also plotted (blue). The different source cases are: $120°$ azimuth oriented horizontal electric point dipole (red), in-line horizontal electric dipole (grounded wire) $1km$ length (cyan) and $120°$ azimuth oriented horizontal electric dipole of $1km$ length (magenta).*

amplitude caused by the different sources is similar between different frequencies and also similar to the 1-D case. The error associated to the 120° azimuth oriented HEPD is 10% at all receivers, and the error associated to the point approximation of the in-line electric dipole is the largest for small offsets of less than $3km$, with values between 100 and 10%, and it decays to smaller values at larger offsets. When the source has finite-length and is oriented with 120° azimuth, the error in comparison to the in-line HEPD is mostly dominated by the orientation, showing a similar curve to the 120° azimuth oriented electric point dipole, with 10% error at all receivers, except at small offsets, where the error is between 1 and 10%. The reservoir block causes an error of similar magnitude to the error associated with the source approximation, about 10% at 0.001 and $0.1Hz$ and smaller at $1Hz$, but more localized to its actual position, with a maximum at $3km$.

The error in the phases (Figure 4.52 right) is smaller than 0.1° for all cases at $0.001Hz$, and below 2% at 0.1 and $1Hz$, with the largest errors caused by the longitude of the source and with similar values to the ones caused by the reservoir blocks.

From these synthetic experiments we observe again the necessity to model the correct orientation and longitude of the source for this model, where the small target requires small offsets for detection and produces anomalies in the in-line electric field of similar magnitude to the ones caused by the source approximation.

Finally, we examine a marine CSEM experiment. We consider the 1-D canonical model (Figure 4.4) and four different sources approximations: a) an in-line HEPD, b) an in-line $100m$ HED, c) a 120° azimuth oriented HEPD, and d) a 120° azimuth oriented HEPD with orientation also in the vertical direction, with 20° dip angle. A $100m$ floating wire is a typical marine CSEM source used in marine CSEM surveys for commercial hydrocarbon exploration. As the source is much shorter than in the land experiment, we expect in this case, smaller discrepancies with the point dipole approximation. On the other hand, the oriented source with an azimuth and dip angles is a practical problem in marine surveys, where the water currents distort the source shape and orientation, thus, it is important to study the effect of this factor on the model responses.

In the tests, the source operates at $0.25Hz$ and it is located $100m$ above the seafloor and centered at $(x,z) = (0,0)$. To benchmark the solution also along the broad-side direction ($z \neq 0$), the receivers are on the seafloor, at $-999.5m$, distributed every $100m$ from $x = -5km$ to $x = 5km$, and from $z = -5km$ to $z = 5km$, forming a mesh of receivers.

To compute the solution we used again the same set of wavenumber values as for the land model, and we applied the goal-oriented adaptive mesh refinement algorithm with a tolerance error criteria of 10^{-3}, which result in about 10 iterations for most of the mesh groups. To simulate the source with length, we used 10 point dipoles and the same mesh to compute the solution for each one of them.

In Figure 4.53 we present the results from these tests. We show a set of xz surface plots (horizontal plane, at $y = -999.5m$) for each source case. We plot: a) the amplitude of the in-line electric field component, b) the relative error of the amplitude of the in-line electric field component when comparing it to the semi-analytical solution and c) the error of the

amplitude of the in-line electric field component calculated between the responses from different tests with different source cases. Thereby, we benchmark the solution for each source case and we compare the effect of the source geometry and orientation. To calculate the semi-analytical solution we use again DIPOLE1D (Key, 2009).

The first row of plots in Figure 4.53 corresponds to the responses of the in-line HEPD, and the error plot on the right (Figure 4.53 c) corresponds to the comparison of the response of this source and the response of the same source but for the 1-D canonical model without the reservoir layer. The second row of plots are for the responses of an in-line $100m$ wire (HED), and the plot on the right (Figure 4.53 f) compares the responses of this source case with the responses of the in-line HEPD in the same model. On the third row, the source is a 120° azimuth oriented HEPD, and the error on the right plot (Figure 4.53 i) is calculated between the responses of this source and the responses of an in-line HEPD. Finally, the fourth row of plots corresponds to a 3-D oriented HEPD, with a 120° azimuth angle and a 20° dip angle. The plot on the right (Figure 4.53 l) compares the amplitude for this source with the amplitude for a horizontal source oriented an angle of 120° azimuth.

The errors when comparing the responses to the semi-analytical solutions are for all source cases very small, with values of about 0.001% for receivers between $z = -2km$ and $z = 2km$, and with slightly larger errors, of about 0.1%, for receivers closer to the source in the x-direction. The errors for all source cases, at receivers between $z = -4km$ and $z = -5km$ and between $z = 4km$ and $z = 5km$, are about 0.1%, with larger values, of about 10%, for receivers closer to the source in the $x-$direction.

In the same Figure, examining the plots on the right column, in the upper plot, we observe that the reservoir layer is appreciable at almost all the receivers positions, with anomalies between 10 and 100%. In the plot below (Figure 4.53 f), the error between considering the length of the source ($100m$) or approximating it as a point dipole is very small, less than 1% at most receivers, indicating that for this model a point dipole is a good approximation. Contrarily, the error between the amplitude for the 120° azimuth oriented HEPD and the amplitude for the in-line HEPD (Figure 4.53 i) is significant, about some decades for most receivers. Finally, in Figure 4.53 l), we observe that modeling the dip angle or considering the source horizontally oriented differs significantly. The error is about 10% and it is larger on the RHS of the plot, for this inclination of the source (dip angle).

From these results we conclude that a point dipole approximation is accurate in a marine scenario with a realistic source of $100m$ length and with the target reservoir at a large distance to the source compared to the region influenced by the dipole geometry. However, we confirm that for the same scenarios, a slightly different orientation of the source modifies significantly the electric field responses. This influence of the orientation extends several kilometers from the source location and can be of the same order of magnitude as the electric field distortion caused by the target reservoir.

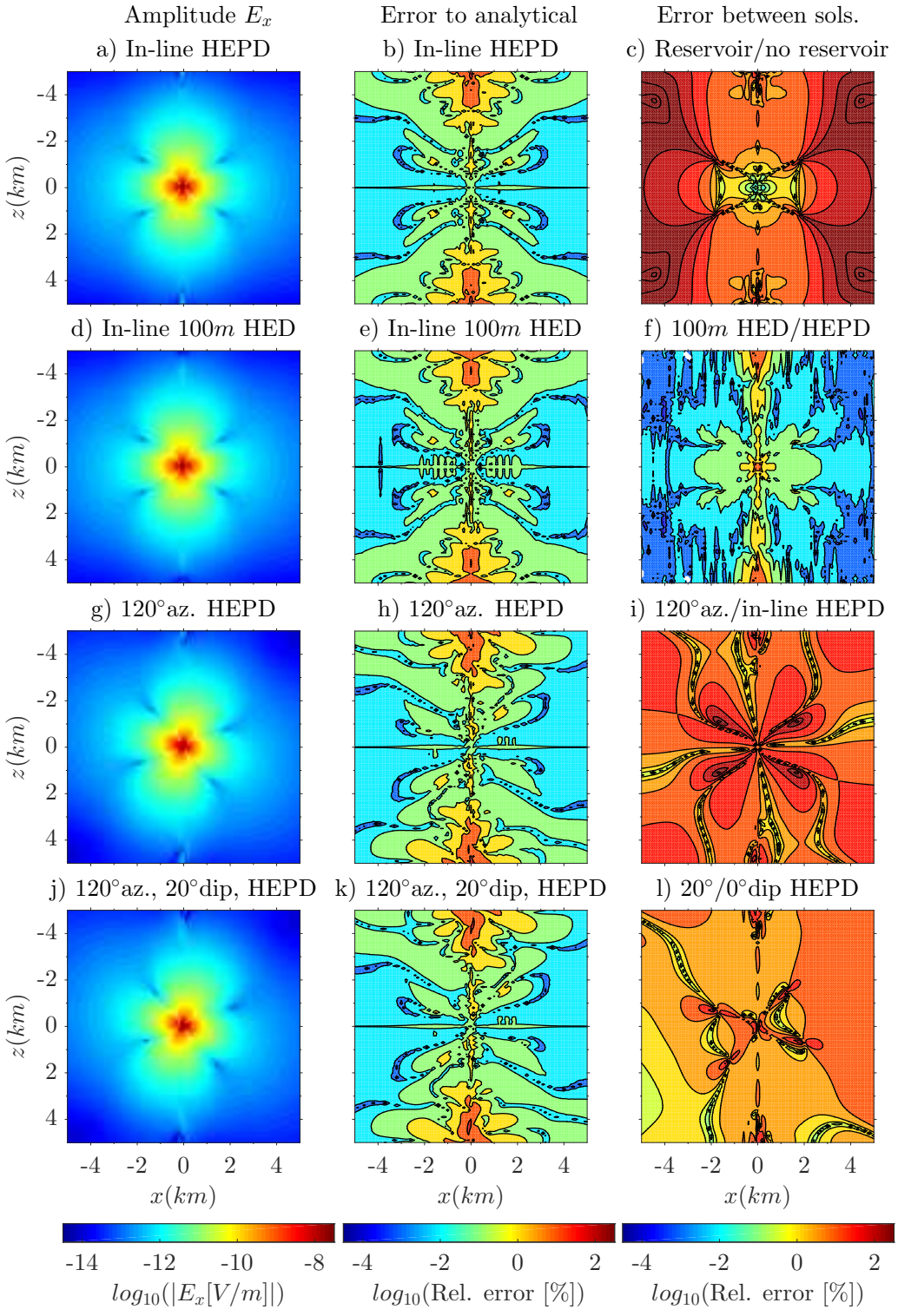

Figure 4.53: *Amplitude, relative error compared to the semi-analytical solution and relative error calculated between in-line electric field component responses for different source cases on the 1-D canonical model, with receivers in the horizontal plane xz and at $y = -999.5m$. a) Amplitude and b) relative error for an in-line HEPD. c) Relative error between the amplitude for an in-line HEPD in the 1-D canonical model with and without the reservoir layer. d) Amplitude and e) relative error for an in-line $100m$ HED, and f) relative error between this response and the one for an in-line HEPD. g) Amplitude and h) relative error for a $120°$ azimuth HEPD and i) relative error between this amplitude and the one for an in-line HEPD. j) Amplitude and k) relative error for a $120°$ azimuth, $20°$ dip HEPD. l) Relative error between the amplitude for the $120°$ azimuth, $20°$ dip HEPD and the amplitude for a $120°$ azimuth ($0°$ dip) HEPD.*

4.6 Anisotropy

4.6.1 Introduction

Electrical anisotropy can have a profound effect on both CSEM and MT measurements. To avoid a misinterpretation of the results it is necessary to incorporate such effects into the imaging processes.

In this thesis we have implemented both the CSEM and MT dipping anisotropic problems in the developed FE program. However, in this section we will only examine the CSEM anisotropic case, since it is less studied compared to MT.

Electrical anisotropic effects observed in CSEM data can be originated in a microscopic scale (e.g. preferred orientations within crystals) or in a macroscopic scale when the method can not resolve oriented structures smaller than the averaged volume. In geologic basins in which CSEM is employed for hydrocarbon exploration, horizontally layered sedimentary sequences are often encountered that can exhibit transverse anisotropy on a macroscopic scale - a scale much larger than individual sedimentary layers (e.g. Newman et al., 2010).

For vertical anisotropy or transverse isotropy with a vertical axis of symmetry (TIV) the resistivity (or conductivity) tensor is uniaxial, that is, a diagonal tensor with one of the components with different resistivity from the other two, and can be described by independent vertical and horizontal resistivities, ρ_v and ρ_h. On the other hand, another case of anisotropy with a uniaxial resistivity tensor is the transverse isotropy with a horizontal axis of symmetry (TIH), also described by ρ_v and ρ_h, but with a perpendicular axis of symmetry to the TIV case. The effects of a horizontally anisotropic seafloor excited by an HED transmitter are analyzed by Everett and Constable (1999) in the framework of deep crustal studies.

In the case of horizontal strata, the anisotropy is vertical and $\rho_v > \rho_h$. The degree of vertical electrical anisotropy is variable and is defined by the anisotropy coefficient $\lambda = \sqrt{\rho_v/\rho_h}$. For horizontally layered sedimentary sequences λ ranges between one and three (Tompkins, 2005).

Anisotropy effects on CSEM measurements depend strongly on source-receiver configuration (Newman et al., 2010) and field amplitudes increase dramatically with increasing subsurface anisotropy (Tompkins, 2005). Ramananjaona et al. (2011), among others, showed that the TM mode (in-line electric field data) is sensitive to the vertical resistivity and to the anisotropic ratio and that the TE mode (broad-side electric field data) is more sensitive to the horizontal resistivity. On the other hand, Tompkins (2005) and Li and Dai (2011) observed that electrical anisotropy in the overburden has a much larger effect on the measurements than reservoir anisotropy. Furthermore, Tompkins (2005) showed that if data recorded over a vertically anisotropic earth are interpreted assuming isotropic earth models, reservoir properties, such as depth, resistivity or lateral extent will be erroneously estimated, with errors depending on the excess of anisotropy. Abubakar (2010) studied

the ability to resolve transverse electric anisotropy of the reservoir in a 2-D model using in-line data with either electric or magnetic transmitters and with either electric or magnetic receivers respectively, and concluded that it is necessary electric and magnetic data and both transmitters to discriminate horizontal and vertical resistivity.

The described anisotropy effects are based on studies of transverse isotropic, horizontal, TIH, and vertical, TIV, resistivity models. In the same manner, most of marine CSEM modeling and data interpretation state-of-the-art algorithms which account for anisotropy are also restricted to transverse isotropy. Li and Dai (2011) and Davydycheva and Frenkel (2013) overcome this limitation on their 2-D FE and 3-D FD modeling programs, respectively, and incorporate the possibility to model transverse isotropy with a tilted axis of symmetry (TTI), which can be found on geologic structures typical for accumulation of hydrocarbons, as synclines or anticlines. Li and Dai (2011) study the impact on CSEM data of dipping anisotropy overburden on an underlying target in a 2-D model and Davydycheva and Frenkel (2013) simulate the effect of 3-D TTI on more complex models, with a reservoir embedded on syncline and anticline structures. They both find that ignoring the TTI effect, if it is present, might lead to incorrect assessment of the dimensions and location of the target reservoir.

In the dipping anisotropic case (TTI) the resistivity tensor $\boldsymbol{\rho}$ is not uniaxial (equation 2.84 with $\boldsymbol{\rho} = \boldsymbol{\sigma}^{-1}$). It can be expressed in terms of the principal resistivities ρ_x, ρ_y and ρ_z, in the principal axes x', y' and z', applying a 3-D rotation of dip angle α_d, to the principal resistivity tensor $\boldsymbol{\rho'} = diag(\rho_x, \rho_y, \rho_z)$, around the z–axis (strike direction) (Figure 2.8):

$$\boldsymbol{\rho} = \boldsymbol{R}^T diag(\rho_x, \rho_y, \rho_z)\boldsymbol{R} = \begin{pmatrix} \rho_x \cos^2\alpha_d + \rho_y \sin^2\alpha_d & (\rho_y - \rho_x)\sin\alpha_d \cos\alpha_d & 0 \\ (\rho_y - \rho_x)\sin\alpha_d \cos\alpha_d & \rho_x \sin^2\alpha_d + \rho_y \cos^2\alpha_d & 0 \\ 0 & 0 & \rho_z \end{pmatrix}, \tag{4.3}$$

where $\boldsymbol{R}$ is a rotational matrix, which for the coordinate system in this thesis is:

$$\boldsymbol{R} = \begin{pmatrix} \cos\alpha_d & -\sin\alpha_d & 0 \\ \sin\alpha_d & \cos\alpha_d & 0 \\ 0 & 0 & 1 \end{pmatrix}, \tag{4.4}$$

for a rotation angle in the clockwise direction.

In this section we validate our FE implementation of the anisotropic CSEM problem. We simulate the responses of models with vertical anisotropy (TIV) and dipping anisotropy (TTI), using an anticline structure model proposed in Davydycheva and Frenkel (2013) for this second case, and we analyze and compare the results.

4.6.2 Marine CSEM experiments with vertical and dipping anisotropy

In this section we conduct numerical experiments modeling marine CSEM on anisotropic electrical resistivity models. The set of models used in the experiments are a 1-D model

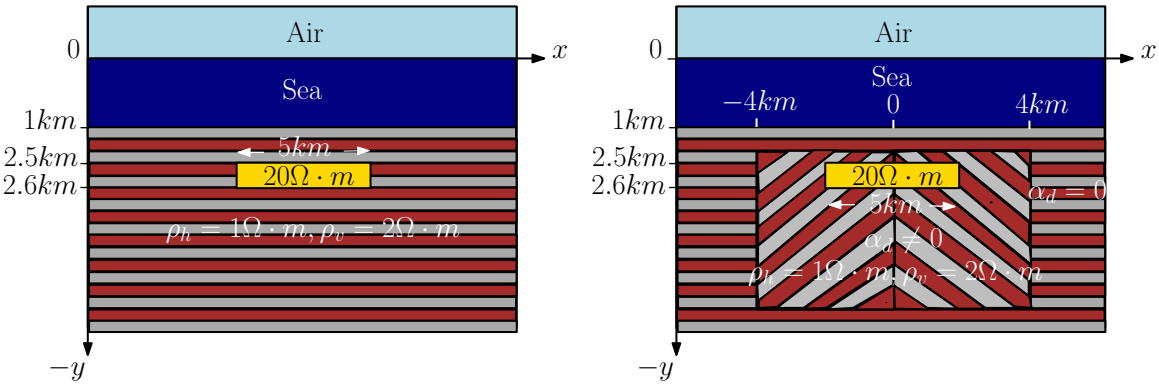

Figure 4.54: *Anisotropic resistivity models schemes. Left: Two-dimensional marine model with a $1km$ thick, $0.3\Omega{\cdot}m$ resistivity sea layer and with an isotropic $20\Omega{\cdot}m$ reservoir, $5km$ wide, $100m$ thick, embedded at $2.5km$ depth in horizontal strata simulated as a TIV half-space with vertical resistivity $\rho_v = 2\Omega{\cdot}m$ and horizontal resistivity $\rho_h = 1\Omega{\cdot}m$. Right: Model in the left with an additional anticline structure simulated as two TTI resistivity blocks, $4km$ wide, centered at $x = -2km$ and $x = 2km$, respectively, and with their top at $1.6km$ depth. The TTI resistivity of the blocks is $\rho_v = 2\Omega \cdot m$ and $\rho_h = 1\Omega \cdot m$, with a dip angle α_d in the right block and $-\alpha_d$ in the left block.*

with a sea layer and a TIV resistivity half-space and two 2-D models, one with a sea layer and a reservoir embedded in TIV resistivity sediments (Figure 4.54 left), and another one also with the sea layer and the TIV resistivity sedimented subsurface, but with the reservoir embedded in an additional anticline structure simulated as two bulk-tilted anisotropic (TTI) structures (Figure 4.54 right).

The transmitter is, in all the experiments, an horizontal electric point dipole located at $50m$ above the seafloor, and we consider it at different locations, $x = 0, 2, 4$ and $6km$, and for the in-line and broad-side configurations. The operating frequencies are $0.05, 0.25$ and $1Hz$, and the receivers are located at $-999.5m$ depth, every $1km$ from $x = -15km$ to $x = 15km$. Model dimensions are in all cases: $100km \times 60km$, and the model is centered at $x = 0, y = 0$, with an air layer of $30km$, and with a $1km$ depth sea layer. The set of wavenumber, κ_z, values used in the experiments are 37 values spaced logarithmically from 10^{-5} to $10^{-1}m^{-1}$.

First, we examine the 1-D model. The vertical anisotropy in the subsurface has resistivities: $\rho_v = 2\Omega{\cdot}m$ and $\rho_h = 1\Omega{\cdot}m$. We simulate the EM fields for this model and we compare them with two additional models with the same layered structure but with isotropic subsurface resistivity of $1\Omega \cdot m$ and $2\Omega \cdot m$, respectively. The CSEM responses of a layered model with TIV resistivity is well studied and let us benchmark our algorithm.

The responses for the three layered models are computed with the FE program applying the adaptive mesh refinement algorithm to 15 mesh groups, 3 groups of frequencies times 5 groups of wavenumbers. The transmitter is considered only at $x = 0$, with two perpendicular orientations: in-line and broad-side, and both orientation cases are included in the same mesh group for adaptive mesh refinement. The stopping criteria is a decrease of 10^{-3} of the global error, or a maximum number of iterations of 10, refining 30% of elements in each iteration.

In Figure 4.55 we show the results. The field amplitude is plotted as a function of the receiver position for each model and for all non-zero field components of the in-line (Figure 4.55 left): E_x, E_y and H_z, and of the broad-side configurations (Figure 4.55 right): E_z, H_x and H_y and for the three frequencies: $0.05, 0.25$ and $1Hz$ (in rows).

For in-line configuration fields, the responses of the anisotropic model are almost identical to the responses of the $2\Omega \cdot m$ isotropic model at all frequencies and for all offsets. The differences between the E_x and H_z fields on these models and on the $1\Omega \cdot m$ isotropic model are more pronounced for offsets smaller than $10km$, being negligible for larger offsets. Differently, the differences for E_y increase with the distance to the source.

Contrarily, for the broad-side configuration, the fields from the anisotropic model are almost identical to the ones from the $1\Omega \cdot m$ isotropic model. Only the H_x horizontal component presents some variations to the $1\Omega \cdot m$ isotropic model because it is affected by the interaction of the airwave with the seafloor.

The explanation of this behavior is that the in-line configuration electric fields are in the model plane and propagate in the seafloor with a significant vertical component, thus in the vertical anisotropic model they are more sensitive to the vertical resistivity component of $2\Omega \cdot m$, and the responses approach to the ones of an isotropic model with this resistivity. On the other hand, in the broad-side configuration the electric fields are purely azimuthal and largely horizontal, thus in the vertical anisotropic model they are more sensitive to the horizontal component of the resistivity of $1\Omega \cdot m$, and the responses approach the ones of an isotropic model with this resistivity.

The obtained modeling results of the EM fields for a TIV 1-D model are consistent with the expected responses behavior and validate our implementation. Additionally, in Figure 4.56, the accuracy of the numerically computed field responses for the isotropic $1\Omega \cdot m$ and $2\Omega \cdot m$ 1-D models are shown, comparing them with the semi-analytical solution calculated with DIPOLE1D. The plots show the relative error of the amplitude of each field component, for each transmitter/receivers configuration (in-line and broad-side) and for each frequency, as a function of the receiver locations, with the transmitter positioned at $x = 0$. The errors for the in-line configuration are below 3%, with the largest errors at the largest offsets. At $1Hz$, the in-line configuration vertical field component, E_y, presents large errors of several orders of magnitude, up to 10^4% for the $1\Omega \cdot m$ model, for offsets larger than approximately $10km$. We have tried different refined meshes to decrease this error without success, however this does not change neither the analysis above nor the validity of the anisotropy implementation. For the broad-side configuration the amplitude errors are below 1% at all frequencies and at all receiver locations, thus smaller than for the in-line configuration. These plots show a good accuracy of all field components at all frequencies for both broad-side and in-line configuration, except for the vertical electrical field component, E_y, at large offsets (approximately larger than $10km$).

Next, we simulate the responses of a 2-D model with an isotropic reservoir embedded in vertical anisotropic sediments (Figure 4.54 left). It consists of an air layer, a $1km$ sea layer and a $5km$ wide, $100m$ thick and $20\Omega \cdot m$ isotropic resistivity block, simulating a

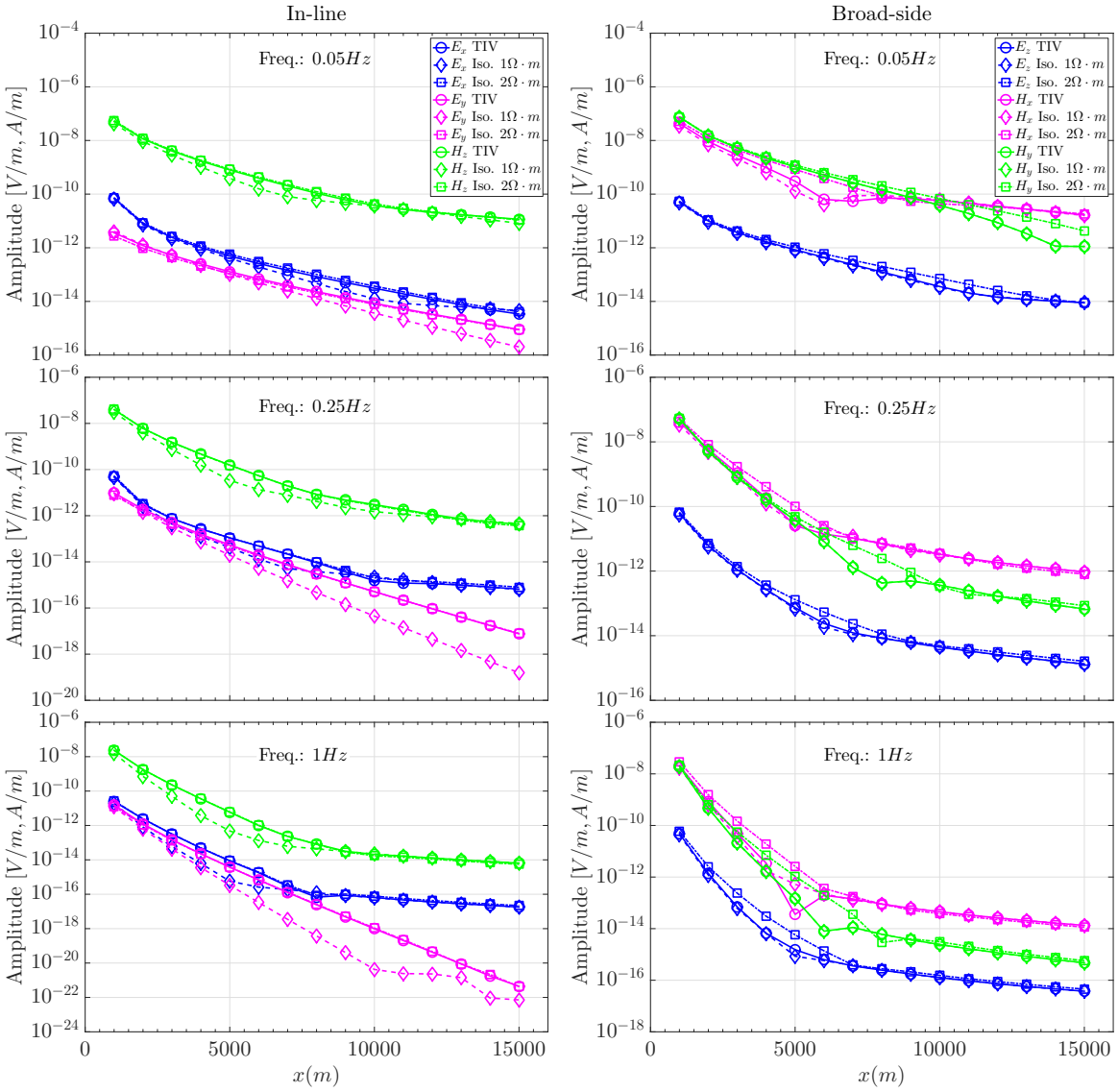

Figure 4.55: *Comparison between responses of a vertical anisotropic 1-D model and of isotropic 1-D models. Amplitude of the in-line (left) and broad-side (right) configuration field components, E_x,E_y and H_z and E_z,H_x and H_y, respectively, as a function of the receiver locations (with the transmitter at $x = 0$), for three different 1-D models: a TIV sedimented seafloor model (circles) and a $1\Omega \cdot m$ (diamonds) and a $2\Omega \cdot m$ (squares) isotropic seafloor models; and for three different frequencies (from top to bottom): $0.05, 0.25$ and $1Hz$.*

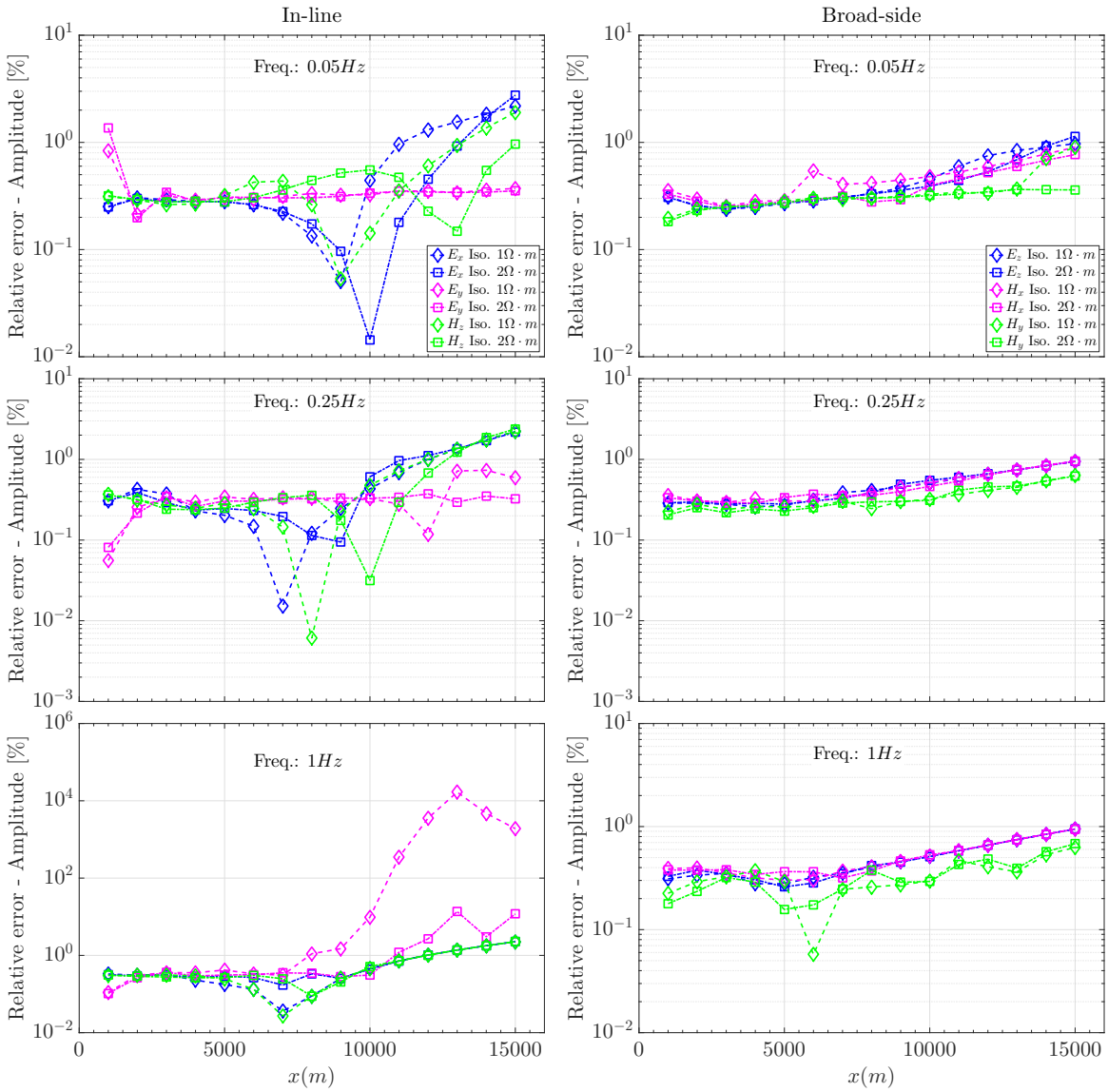

Figure 4.56: *Comparison of the numerically computed responses of two 1-D isotropic models with $1\Omega \cdot m$ and $2\Omega \cdot m$ resistivities, respectively, with the corresponding semi-analytical solutions calculated with DIPOLE1D. Relative error between the numerical and the semi-analytical amplitudes of the in-line (left) and broad-side (right) configuration field components, E_x, E_y and H_z and E_z, H_x and H_y, respectively, as a function of the receiver locations (with the transmitter at $x = 0$), for the $1\Omega \cdot m$ (diamonds) and for the $2\Omega \cdot m$ (squares) isotropic seafloor models; and for three different frequencies (from top to bottom):* $0.05, 0.25$ *and* $1Hz$.

reservoir, embedded in vertical anisotropic sediments of $\rho_v = 2\Omega \cdot m$ and $\rho_h = 1\Omega \cdot m$. The reservoir is at $1.5km$ depth below the seafloor and centered at $x = 0$.

The solution is computed for 4 transmitter positions, $x = 0, 2, 4$ and $6km$ and for two transmitter orientations (in-line and broad-side) in each position, and at three frequencies: $0.05, 0.25$ and $1Hz$. We apply the adaptive mesh refinement algorithm to 20 mesh groups prior to the computation of the solution for all parameters values. These mesh groups are a combination of 4 groups for the source locations, 1 group for the frequencies, and 5 groups for the wavenumber values. The stopping criteria is again a decrease of 10^{-3} of the global error, or a maximum number of iterations of 10, refining 30% of elements in each iteration.

In Figure 4.57 we show the results of the in-line configuration horizontal electric field for this model. The first two rows of plots are the amplitudes and phases of E_x, respectively, as a function of the receivers locations, for the three different frequencies of $0.05, 0.25$ and $1Hz$ and for different transmitter locations, $x = 0, 2, 4$ and $6km$. The third row of plots is the amplitude normalized by the Ex amplitude response of the TIV 1-D model examined above (a sea layer and a TIV half-space), and shows the effect of the reservoir. The plots are again the responses for the different frequencies and transmitter locations. In the last row, we plot the amplitude of E_x normalized by the amplitude response of the same reservoir 2-D model but with an isotropic seafloor of $1\Omega \cdot m$, for different frequencies and transmitter positions. Normalizing by the responses of the same model structure but with isotropic sediments shows the effect of the vertical anisotropic sediments.

Observing the effect of the reservoir (Figure 4.57 third row of plots), when the source is positioned above the center of the reservoir ($x = 0$), the normalized amplitude shows two maximums, increments of the field amplitude due to the reservoir, on each site of the source, approximately between $x \pm 4$ and $x = \pm 10km$ depending on the frequency, at shorter offsets for larger frequencies. The reservoir is centered at $x = 0$, is $5km$ wide and is positioned at $1.5km$ depth, and each frequency shows a maximum of sensitivity at different offsets. The values of the increment are similar for frequencies of $0.25Hz$ and $1Hz$, about 1.1, but the changes are more abrupt for the highest frequency. At $0.05Hz$ there is also an increment of the amplitude, it changes to 1.05, but it is smoother than for higher frequencies. As the source moves to the right and away of the reservoir, until $x = 6km$, the augment of the amplitude for the different frequencies is observed at the left side of the source, indicating the presence of the reservoir. In these situations, the increase of the amplitude is larger than when the source is positioned above the center of the reservoir, since now the offset distance for which the sensitivity is larger coincides approximately with the distance to the reservoir, for all frequencies. Thus, the largest values are observed when the transmitter is located at $x = 4km$, at $1.5km$ from the right boundary of the reservoir, and for this case, the maximums of the normalized amplitude are approximately 1.7 at $1Hz$ and located at $x = -3km$, 1.5 at $0.25Hz$ and located at $x = -5km$, and 1.2 at $0.05Hz$ and located at $x = -8km$.

Observing the effect of the vertical anisotropy on the bottom row of plots of Figure 4.57, there is an increment of the normalized amplitude and it is much larger than the increase

due to the reservoir at all frequencies and for all transmitter positions. The increment at each frequency has two maximums, one at each side of the source, of approximately 12−14 at $5km$ offset and at $1Hz$ frequency, of 4 at $7km$ offset and at $0.25Hz$ frequency, and of 2 at $10km$ offset and at $0.05Hz$ frequency. The offset locations of these maximums and their magnitude are approximately constant when varying the source position, as expected since we are observing the effect of the TIV resistivity in the sediment.

From these results we observe that some data with vertical anisotropy can not be treated as isotropic since the anisotropy effect is large and could mask the reservoir or indicate its position in a different location, with different dimensions and resistivity value.

In Figure 4.58 we show the same plots for the broad-side configuration. First, we analyze the plots of the normalized amplitude by the TIV half-space responses, which show the effect of the reservoir. The results are similar to the ones described for the in-line configuration, but smaller. For the transmitter at $x = 0$ there are two maximums on both sides of the source, of about 1.05 for both the 0.25 and $1Hz$ frequencies and smaller for the $0.05Hz$ frequency. The maximum increment of the amplitude can be observed, at all frequencies, for the transmitter located above the reservoir, at $x = 2km$, at $500m$ of the reservoir right lateral boundary, with values of about 1.14 for the $1Hz$ frequency at $x = 5km$, 1.1 for the $0.25Hz$ frequency at $x = 6km$, and 1.05 for the lowest frequency of $0.05Hz$ at $x = 10km$. The smaller effect of the reservoir is explained because of the lower sensitivity of the broad-side configuration.

The vertical anisotropic effect for this source/receivers configuration (Figure 4.58 bottom) is also smaller than for the in-line configuration. The curves show an increase of the amplitude for the receivers with smallest offset at all frequencies and two peaks at 5 and $6km$ offset, of 1.8 and 1.25, at 0.25 and $1Hz$ frequencies, respectively. At $0.05Hz$ the increase of the amplitude due to the anisotropy is approximately constant to 1.1 value from $1km$ to $12km$ offset.

From these results, we conclude that the vertical anisotropy effect can be observed in both in-line and broad-side configurations, but the effect is larger for the in-line disposition. This can be explained because in the plots, the isotropic sediments of the 2-D model we used for the normalization are $1\Omega \cdot m$, the same resistivity value of the horizontal component, ρ_h, in the anisotropic case, and as we observed in the experiments before with a 1-D TIV model, the broad-side configuration is more sensitive to the horizontal component of the resistivity and the in-line configuration to the vertical one.

In Figure 4.59 we show the accuracy of the discussed results for the TIV 2-D model, comparing them to the responses computed using MARE2DEM (Key and Ovall, 2011) FE program. The relative error of the amplitude and absolute error of the phase of the horizontal electric field are plotted for the in-line and broad-side configurations of source and receivers and for the three different frequencies: $0.05, 0.25$ and $1Hz$, as a function of the receivers locations, with the transmitter located at $x = 0$. The same errors are also plotted in the same Figure for the responses of the isotropic 2-D model, with seafloor resistivity $1\Omega \cdot m$. The relative errors of the amplitudes are below 1% for all analyzed cases and in

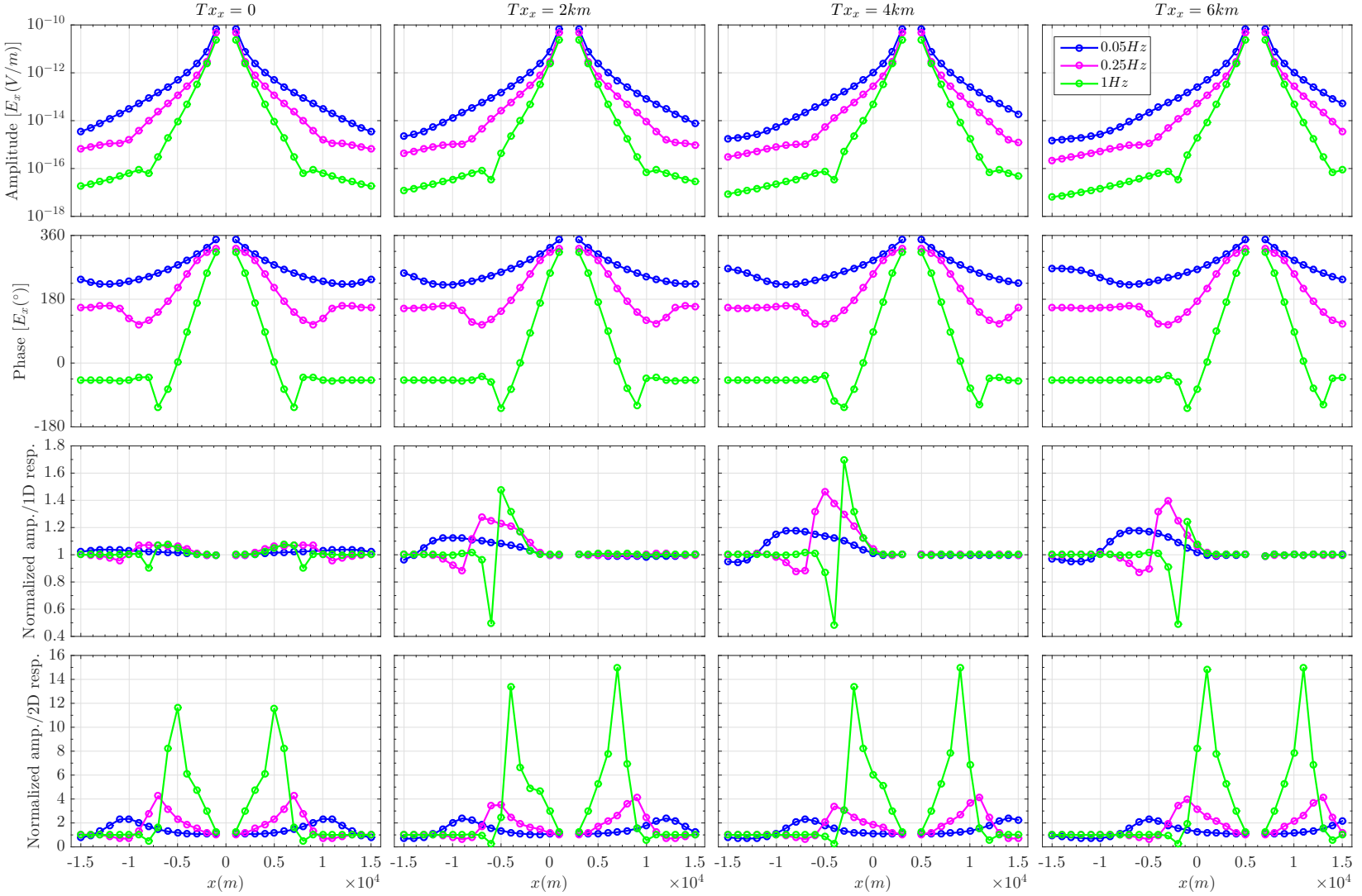

Figure 4.57: *In-line configuration electric field responses of a 2-D marine model with an isotropic reservoir and vertical anisotropic (TIV) sediments. From top to bottom: E_x amplitude, phase, amplitude normalized by homogeneous 1-D TIV model response and amplitude normalized by 2-D reservoir isotropic model response, for three frequencies: $0.05, 0.25$ and $1Hz$ (in colors), and for transmitter locations, $x = 0, 2, 4$ and $6km$ (from left to right).*

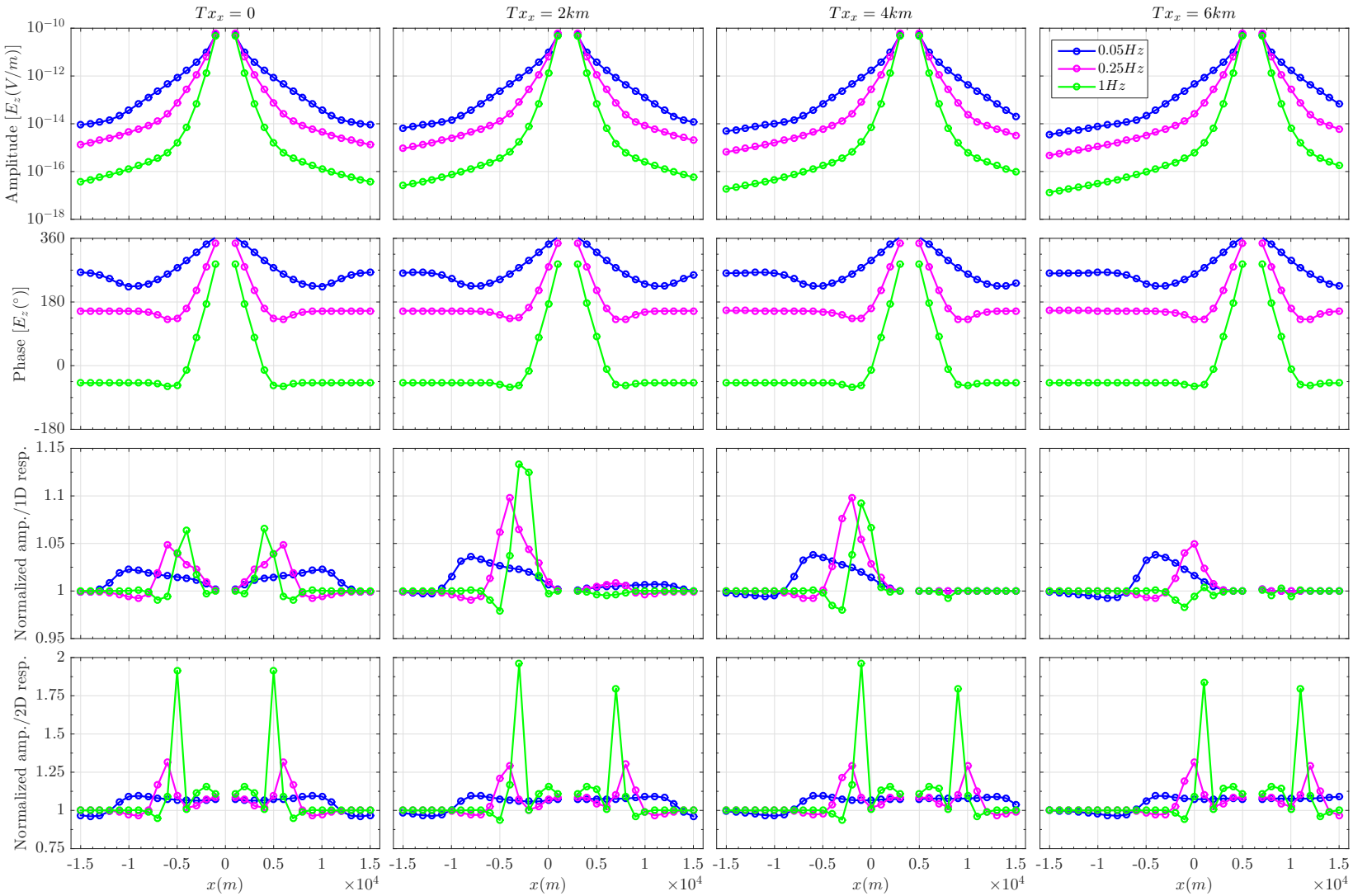

Figure 4.58: *Broad-side configuration electric field responses of a 2-D marine model with an isotropic reservoir and vertical anisotropic (TIV) sediments. From top to bottom: E_z amplitude, phase, amplitude normalized by homogeneous 1-D TIV model response and amplitude normalized by 2-D reservoir isotropic model response, for three frequencies: $0.05, 0.25$ and $1Hz$ (in colors), and for transmitter locations, $x = 0, 2, 4$ and $6km$ (from left to right).*

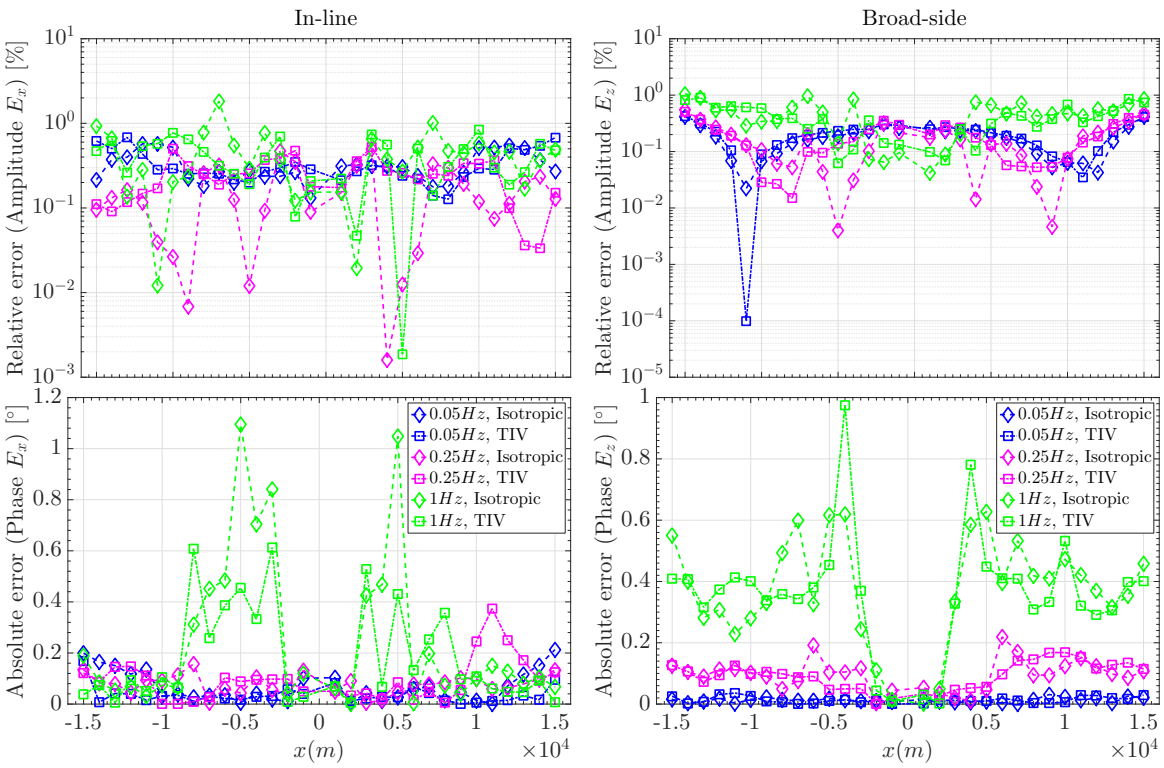

Figure 4.59: *Comparison of the computed responses for the 2-D reservoir model with TIV seafloor and for the 2-D reservoir model with isotropic seafloor with the responses calculated using the FE program MARE2DEM. Relative error of the horizontal electric field amplitude (top) and absolute error of the phase (bottom) for the in-line (left) and broad-side (right) source/receivers configurations, and for different frequencies:* $0.05, 0.25$ *and* $1Hz$ *(in colors), as a function of the receivers locations, with the transmitter at* $x = 0$.

both in-line and broad-side configurations, and the absolute errors of the phases are below 1.2° in all cases, indicating a good agreement between both FE programs solutions.

Finally, we examine a 2-D model where the resistive reservoir is embedded in an anticline structure surrounded by vertical anisotropic sediments (Figure 4.54 right). The anticline structure is simulated with two $4km$ wide blocks, centered at $x = -2km$ and $x = 2km$, respectively, and located at $1.6km$ depth, $600m$ below the seafloor, with anisotropic resistivities of TTI type. The TTI resistivities of these blocks are $\rho_h = 1\Omega \cdot m$ and $\rho_v = 2\Omega \cdot m$, and we consider two different cases, one with a dip angle of $\alpha_d = 20°$, in the right block, and $\alpha_d = -20°$, in the left block, and another one with a dip angle of $\alpha_d = 40°$, in the right block, and $\alpha_d = -40°$, in the left block. The sediments surrounding these blocks are assumed with TIV resistivity, with the same $\rho_h = 1\Omega \cdot m$ and $\rho_v = 2\Omega \cdot m$. The computational parameters used to solve for the responses of these models are the same as specified for the model above, with a reservoir embedded in TIV sediments.

In Figure 4.60 we plot the results for the in-line configuration. The Figure shows the horizontal electric field amplitude, phase, amplitude normalized by the response of the same model without the anticline and amplitude normalized by the response of the same model but without the anticline and with $1\Omega \cdot m$ isotropic sediments. These results are plotted for the three frequencies, for the two models with different dip angle and for different

horizontal position of the transmitter: $x = 0, 2, 4$ and $6km$.

Observing the amplitudes and the phases, it is easy to distinguish between the curves for the different frequencies, with a faster decay of the fields for the larger frequencies. However, it is difficult to appreciate the differences between the two models with different resistivity dip angle. In the same Figure, the plots of the normalized amplitude highlight the effects of the dipping anisotropic structure.

First we examine the amplitude normalized by the responses of a 2-D reservoir model embedded in vertical anisotropic sediments. These plots show the effects of the anticline on the model responses. When the transmitter is positioned at $x = 0$, we observe a decay of the amplitude, between $1km$ and $4km$ offset, coinciding with the position of the anticline structure, to values smaller than one, symmetric to the source position. This decay is larger for higher frequencies, and larger also for the model with dip angles $\pm 40°$. Thus, the smallest values of the normalized amplitude are for the model with dip angle $40°$ and at $1Hz$, with values of 0.6. At offsets larger than approximately $4km$, the normalized amplitude increases until it reaches the value of one, at approximately $10km$. When the transmitter is moved to the right, the drop of the normalized amplitude occurs in the left side, where the anticline structure is positioned, and it reaches smaller values than when the transmitter was above the center of the structure, about 0.4 for dip $40°$ and at $1Hz$. The minimum is followed by a maximum of the normalized amplitude, to values larger than one, and its location and magnitude depends for each case on the frequency. The largest values and more abrupt maximums are for the frequency of $1Hz$ and are about 2.8 for the model with dip angle $40°$.

In the bottom row of Figure 4.60, the amplitude of the horizontal in-line electric field is normalized by the response of a 1-D model with an air and a sea layers and a TIV half-space with the same ρ_v and ρ_h resistivities as in the model under study, highlighting the effect of the anticline and the reservoir together. The normalized amplitude curves are very similar to the ones above, and the main differences are that the maximums and the minimums values are slightly smaller in this case. The effect of the reservoir should be an augment of the amplitude, however, as it can be observed, the anticline structure dominates the responses and the effect of the reservoir is almost masked.

In Figure 4.61 we show the same plots as in Figure 4.60 for the broad-side configuration. The amplitude normalized by the responses of a 2-D model with vertical anisotropic seafloor shows a very similar behavior as observed in the in-line configuration, with a drop of the amplitude, larger for larger dip angle and for higher frequencies, but with slightly smaller magnitude than in the in-line configuration. To highlight the effect of both the anticline structure and the reservoir we normalize the amplitude by the responses of a 1-D TIV model (Figure 4.61 bottom). The results in this case present differences with the in-line configuration. When the source is located at $x = 0$, the normalized amplitudes at $1Hz$ show a small decay of the amplitude above the anticline structure, followed by an abrupt change to a maximum of about 1.05 at $x = 4km$ and to a minimum at $x = 5km$, coinciding with the boundaries of the structure. These maximums and minimums of the

normalized amplitude are small, and the minimums are more abrupt for the model with larger dip angle. For frequencies of 0.25 and $1Hz$, the normalized amplitude above the anticline presents a small increase. When moving the transmitter to the right, at $x = 2km$ and $x = 4km$, the effect is similar in the left side, above the anticline, with a combined effect of the anticline and the reservoir with a decrease and increase of the amplitude at $1Hz$ and only an increase at $0.25Hz$, showing more sensitivity to the reservoir than to the anticline.

Thus, in the broad-side configuration, both the effects of the anticline and the combined effect of the anticline with the reservoir, are smaller than for the in-line configuration. The combined effect of the anticline with the reservoir is a drop or a maximum of the amplitude depending on which factor, the anticline or the reservoir, is more important for a certain frequency and receiver offset.

Next, we analyze the distribution of the in-line geometry electric fields for the studied anisotropic models compared to the distribution for the 2-D isotropic reservoir model. Figure 4.62 shows surface plots in the $xy-$plane of the in-line electric field for the isotropic case, the vertical anisotropic case and the dipping anisotropic case considering two positions of the transmitter: $x = 0$ and $x = 2km$. The colors in the plots are the amplitude of the electric field in the in-line geometry ($\boldsymbol{E} = (E_x, E_y)$) in a logarithmic scale and the arrows show the direction of the real part of the in-line geometry electric field. Examining the model with the reservoir embedded in vertical anisotropic sediments, it can be observed that the electric field decay is slower compared to the isotropic case. This effect is caused by the larger resistivity in the vertical direction compared to the horizontal and causes the observed augment of the amplitude when the receivers are located on the seafloor. Analyzing the electric field distribution for the model with the anticline, when the transmitter is at $x = 0$ it is possible to notice slightly a slower decay of the field inside the anticline structure. When the transmitter is at $x = 2km$, above the center of the positive tilted structure (a block $4km$ wide, with resistivity dip angle +40°), the electric field is asymmetric with the source location and decays slower along the dipping direction.

The observed TIV seafloor anomalies of a large increment of the amplitude which mask the reservoir anomaly are in agreement with the results by Li and Dai (2011) and Davydycheva and Frenkel (2013). On the other hand, the anticline anomaly consisting in a drop of the amplitude which masks the effect of the reservoir is also observed by Davydycheva and Frenkel (2013).

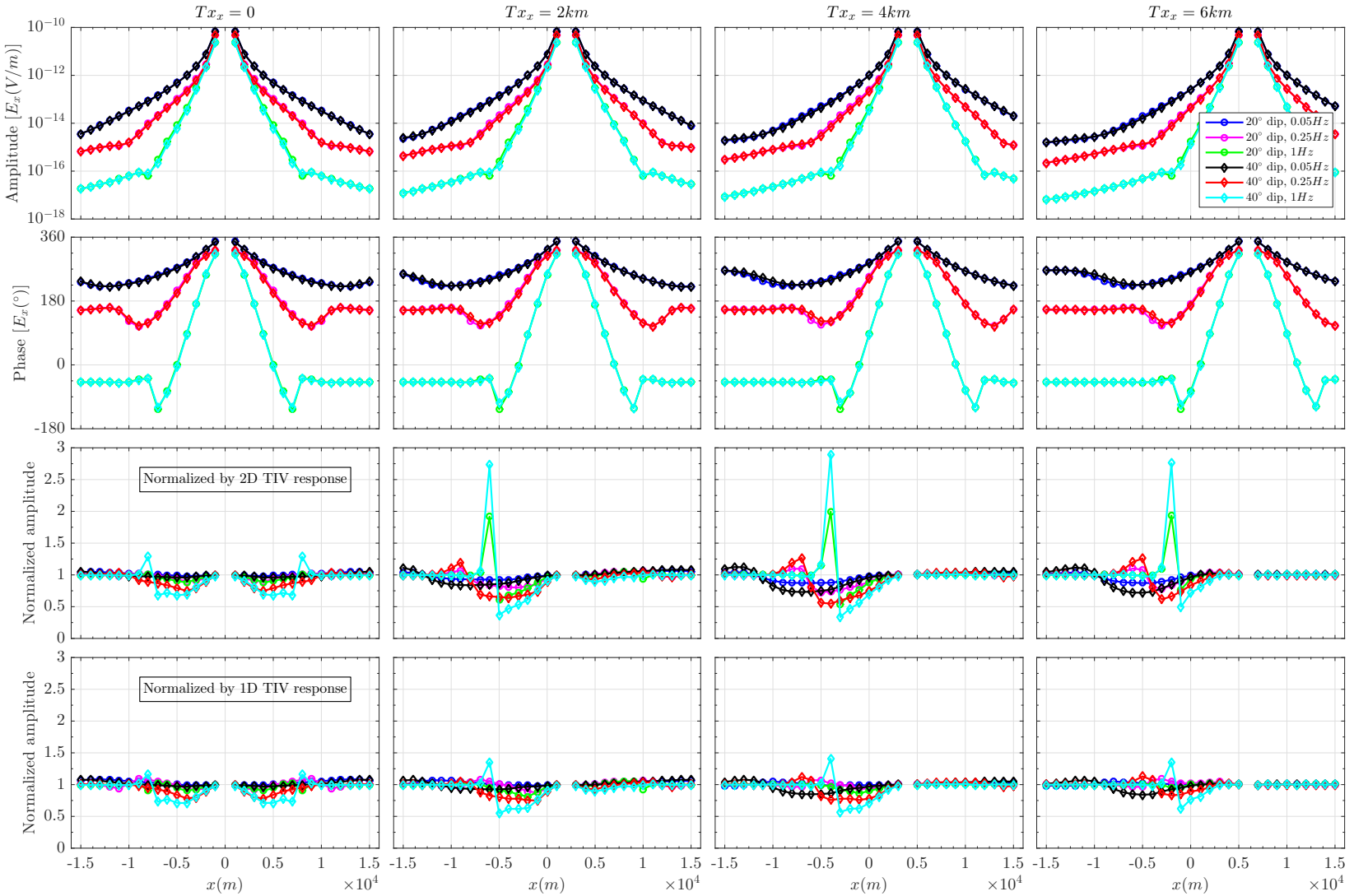

Figure 4.60: *In-line configuration electric field responses of a 2-D marine model composed of an isotropic reservoir embedded in an anticline structure (TTI resistivity) surrounded by vertical anisotropic (TIV) sediments. From top to bottom: E_x amplitude, phase, amplitude normalized by 2-D TIV model response and amplitude normalized by 1-D TIV model response, for three frequencies: $0.05, 0.25$ and $1Hz$ (in colors), for two models with resistivity dip angle: $\alpha_d = 20$ and $40°$, respectively, and for transmitter locations: $x = 0, 2, 4$ and $6km$ (from left to right).*

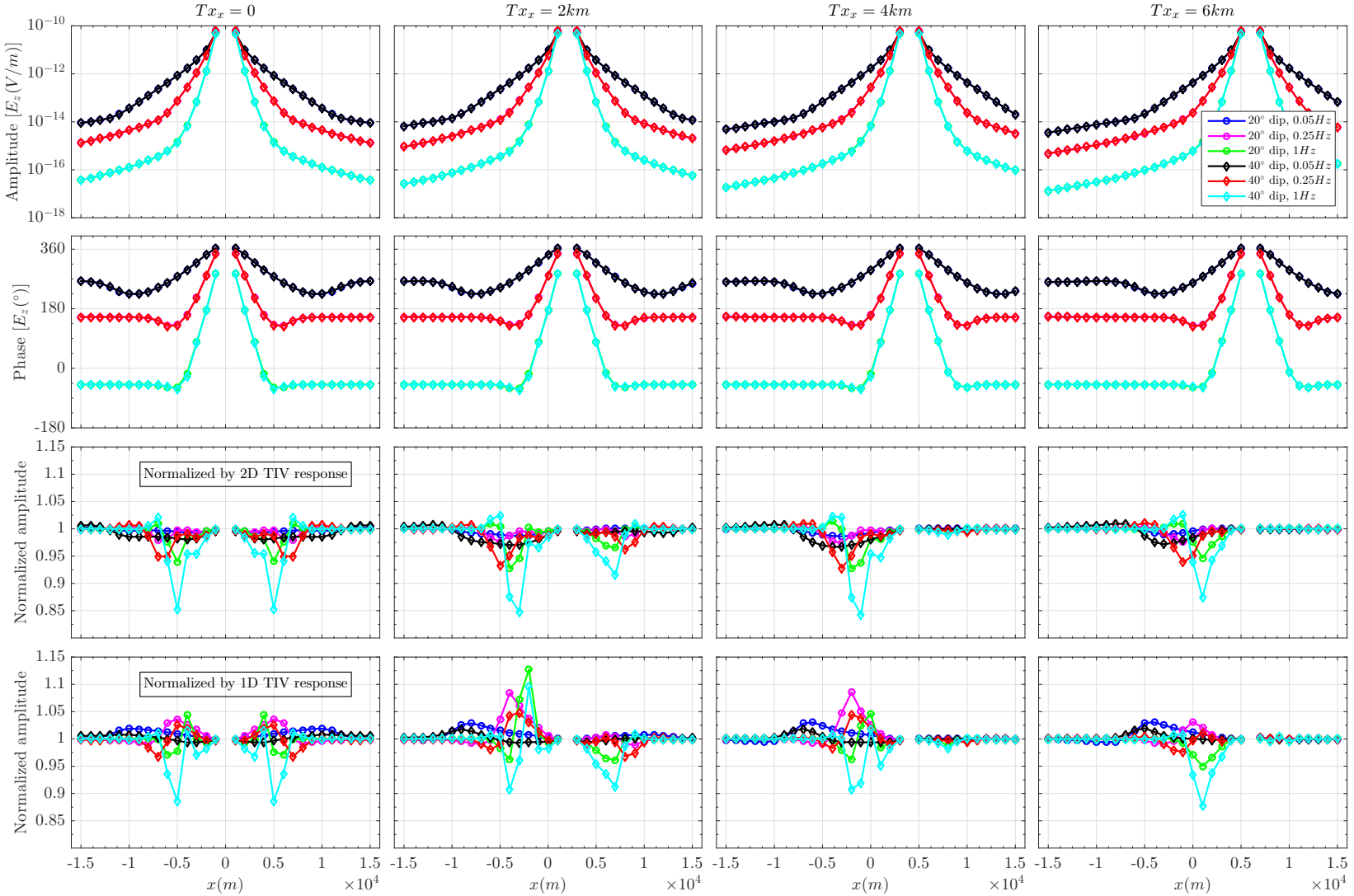

Figure 4.61: *Broad-side configuration electric field responses of a 2-D marine model composed of an isotropic reservoir embedded in an anticline structure (TTI resistivity) surrounded by vertical anisotropic (TIV) sediments. From top to bottom: E_z amplitude, phase, amplitude normalized by 2-D TIV model response and amplitude normalized by 1-D TIV model response, for three frequencies: $0.05, 0.25$ and $1Hz$ (in colors), for two models with resistivity dip angle: $\alpha_d = 20$ and $40°$, respectively, and for transmitter locations: $x = 0, 2, 4$ and $6km$ (from left to right).*

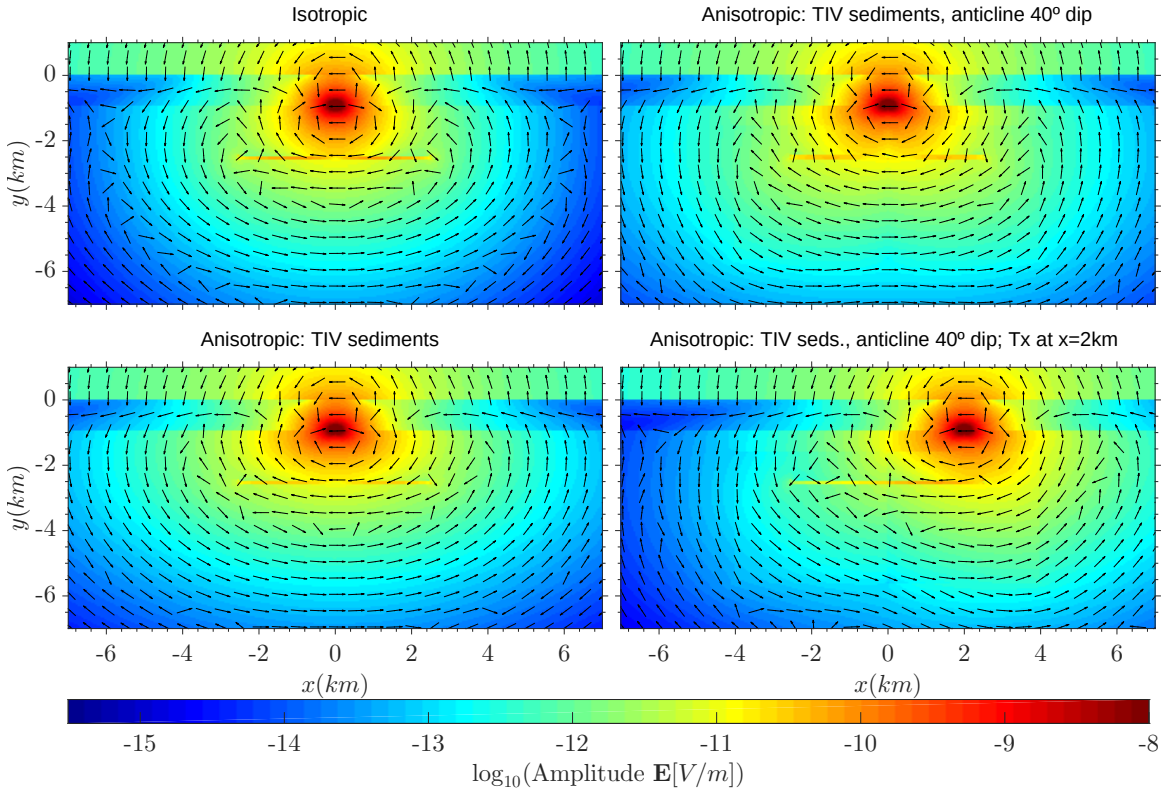

Figure 4.62: *In-line electric field surface plots of the $xy-$plane for three variant models of the 2-D marine reservoir model: a model with the isotropic reservoir embedded in isotropic sediments of $1\Omega \cdot m$ (top left); a model with the isotropic reservoir embedded in vertical anisotropic sediments (TIV) with resistivities $\rho_h = 1\Omega \cdot m$ and $\rho_v = 2\Omega \cdot m$ (bottom left); a model with the isotropic reservoir embedded in an anticline structure (TTI) with dip angle $40°$, and surrounded by vertical anisotropic sediments (top and bottom right). The anisotropic models schemes are represented in Figure 4.54. The transmitter is located above the center of the reservoir at $x = 0$ in the isotropic and vertical anisotropic plots, and at $x = 0$ and $x = 2km$ in the dipping anisotropic plots. The colors in the plots are the amplitude of the electric field in the in-line geometry ($\boldsymbol{E} = (E_x, E_y)$) in a logarithmic scale and the arrows show the direction of the real part of the in-line geometry electric field.*

References

A. Abubakar. Sensitivity study of multi-sources receivers CSEM data for TI-anisotropy medium using 2.5D forward and inversion algorithm. In *72nd Annual Conference and Exhibition, EAGE*, 2010.

S. Davydycheva and M. Frenkel. The impact of 3D tilted resistivity anisotropy on marine CSEM measurements. *The Leading Edge*, 32(11):1374–1381, 2013.

M. Everett and R. Edwards. Transient marine electromagnetics: the 2.5-D forward problem. *Geophysical Journal International*, 113:545–561, 1992.

M. E. Everett and S. Constable. Electric dipole fields over an anisotropic seafloor: theory and application to the structure of 40 ma pacific ocean litosphere. *Geophysical Journal International*, 136:41–56, 1999.

A. Franke, R.-U. Börner, and K. Spitzer. Adaptive unstructured grid finite element simulation of two-dimensional magnetotelluric fields for arbitrary surface and seafloor topography. *Geophysical Journal International*, 171:71–86, 2007.

K. Key. 1D inversion of multicomponent, multifrequency marine CSEM data: Methodology and synthetic studies for resolving thin resistive layers. *Geophysics*, 74(2):F9–F20, 2009.

K. Key and J. Ovall. A parallel goal-oriented adaptive finite element method for 2.5-D electromagnetic modelling. *Geophysical Journal International*, 186:137–154, 2011.

Y. Li and S. Constable. Special Section – Marine Control-Source Electromagnetic Methods. 2D marine controlled-source electromagnetic modeling: Part 2 – The effect of bathymetry. *Geophysics*, 72(2):WA63–WA71, 2007.

Y. Li and S. Dai. Finite element modelling of marine controlled-source electromagnetic responses in two-dimensional dipping anisotropic conductivity structures. *Geophysical Journal International*, 185(2):622–636, 2011.

Y. Mitsuhata. 2-D electromagnetic modeling by finite-element method with a dipole source and topography. *Geophysics*, 65(2):465–475, 2000.

G. A. Newman, M. Commer, and J. J. Carazzone. Imaging CSEM data in the presence of electrical anisotropy. *Geophysics*, 75(2):F51–F61, 2010.

C. Ramananjaona, L. MacGregor, and D. Andréis. Sensitivity and inversion of marine electromagnetic data in a vertically anisotropic stratified earth. *Geophysical Prospecting*, 59:341–360, 2011.

K. Schwalenberg and R. N. Edwards. The effect of seafloor topography on magnetotelluric fields: an analytical formulation confirmed with numerical results. *Geophysical Journal International*, 159:607–621, 2004.

R. Streich and M. Becken. Electromagnetic fields generated by finite-length wire sources: comparison with point dipole solutions. *Geophysical Prospecting*, 59:361–374, 2011.

R. Streich, M. Becken, and O. Ritter. 2.5D controlled-source EM modeling with general 3D source geometries. *Geophysics*, 76(6):F387–F393, 2011.

M. Tompkins. The role of vertical anisotropy in interpreting marine controlled-source electromagnetic data. *75th Annual International Meeting, SEG, Expanded Abstracts*, pages 514–517, 2005.

P. E. Wannamaker, J. A. Stodt, and L. Rijo. Two-dimensional topographic responses in magnetotellurics modeled using finite elements. *Geophysics*, 51(11):2131–2144, 1986.

C. J. Weiss and S. Constable. Mapping thin resistors and hydrocarbons with marine EM methods, Part II – Modeling and analysis in 3D. *Geophysics*, 71(6):G321–G332, 2006.

M. S. Zhdanov, I. M. Varenstov, J. T. Weaver, N. G. Golubev, and V. A. Krylov. Methods for modelling electromagnetic fields. Results from COMMEMI - the international project on the comparison of modelling methods for electromagnetic induction. *Journal of Applied Geophysics*, 37:133–271, 1997.

CHAPTER 5

Controlled-source electromagnetic inversion: a PDE-constrained optimization in full-space

5.1 Introduction

Electromagnetic data measured by the CSEM (or MT) method can not be interpreted directly. To infer about the spatial distribution of the Earth's conductivity it is necessary to solve an inverse problem, that is, to find the mathematical representation of the Earth's conductivity model for which the predicted responses best match the actual observations. The inverse problem can therefore be described as an optimization problem in which the misfit between predicted and actual observations is systematically minimized by varying the unknown conductivity parameters, subject to the constraint that the prediction satisfies the CSEM (or MT) governing PDEs.

In a more general framework, inverse problems are known as parameter estimation, a particular case of PDE constrained optimization. In this context, the governing PDEs are named state equations and the dependent variables, state variables. These problems are also found in a vast number of other investigation areas, e.g. aerodynamics or biomedical imaging, and are still the focus of active research.

Inversion of EM geophysical data is a specially challenging and computationally intense task. The EM inverse problem is nonlinear which means that the relation between the parameter to estimate and the state variable is nonlinear, and undetermined, if any solution can be found, there are infinite number of other acceptable solutions. Moreover, the solutions are unstable, which means that very large changes to the model result in only small or even no change in the fit to the data. These features make the inverse problem ill-posed. Furthermore, the problem is also large-scale; usually with thousands of data points to be inverted in the tens of thousands of model parameters (Avdeev, 2005).

To deal with the non-uniqueness and instability of the problem, a common strategy is to apply a penalty to the model, usually, some variation on first-order derivative smoothness. Then, the inverse problem is generally solved numerically minimizing a functional which penalizes both misfit to the data and model roughness, using derivative-based optimization methods, such as non-linear conjugate gradients (e.g. Newman and Alumbaugh, 2000;

Rodi and Mackie, 2001; Commer and Newman, 2008), quasi-Newton (e.g. Haber, 2005; Avdeev and Avdeeva, 2009) or Gauss-Newton (e.g. Mackie and Madden, 1993; Siripunvaraporn et al., 2004).

The non-linear conjugate gradients (NLCG) method minimizes the objective (or penalty) function prescribed for the non-linear inverse problem by direct optimization. It calculates the gradient of the objective function with respect to the model parameters and uses it to define a search direction in the model space. The objective function is then minimized along this direction using a line search which requires at most a few evaluations of the forward operator, and the model parameter is updated. The whole process is repeated iteratively until the stopping criteria is reached.

Differently, Gauss-Newton (GN) is based on a linearization of the forward function approximating it with a first-order Taylor expansion about some reference model. The objective function is also approximated to a second-order in a Taylor expansion around a current estimate of the model solution. The Newton step for the model update is derived from this expansion. Then, the gradient and the Hessian of the objective function in the Newton step are approximated for the linearized forward function, where second-order derivatives are discarded, resulting in the system of normal equations. This system contains the forward function and the Jacobian. The Jacobian, or sensitivity matrix, is the derivative of the forward function with respect to the model parameters and relates changes in the model to corresponding changes in predicted data. In the minimization process, the system of normal equations is solved and the solution is then taken as a new reference model. The process is repeated recomputing the Jacobian for the updated model parameters. Occam's inversion (Constable et al., 1987; deGroot Hedlin and Constable, 1990), very popular in the EM community, is a variant of GN.

Finally, the quasi-Newton method applies directly the Newton method to minimize the objective functional and approximates the inverse of the Hessian through a recursive update process.

For further details of the application of these optimizations methods to solve EM inverse problems we refer to the reviews of Avdeev (2005) and Siripunvaraporn (2012).

All these optimization strategies show different benefits and drawbacks when applied to the EM inverse problem, but in all of them the computation of the forward solution typically constitute the most expensive part (e.g. Siripunvaraporn, 2012; Egbert and Kelbert, 2012). A key component in the GN scheme is the Jacobian. Computing the full Jacobian required for any direct GN algorithm is a very demanding computational task for multidimensional EM problems (e.g. Siripunvaraporn, 2012; Egbert and Kelbert, 2012). This has motivated various algorithmic approximations for the Jacobian based on EM fields computed for homogeneous or 1-D Earth models (Smith and Booker, 1991; Farquharson and Oldenburg, 1996) or approximate the solutions of the normal equations with a memory efficient Krylov-space solver such as conjugate-gradients (CG) (e.g. Mackie and Madden, 1993). This last approximation only needs the computation of matrix-vector products with the Jacobian, which can be accomplished without forming or storing the whole matrix, at

the cost of two forward solutions (e.g. Egbert and Kelbert, 2012). In contrast, NLCG or quasi-Newton methods avoids explicitly forming and storing the coefficient matrix of the normal equations. However, the GN approach exhibits convergence rates with order lower than quadratic, but significantly higher than linear, in comparison to NLCG and limited memory quasi-Newton methods which exhibit linear convergence (Nocedal and Wright, 1999).

Recent advances have focused on two directions, on one hand, Grayver et al. (2013) have shown that an efficient 3-D inverse algorithm using a GN optimization approach with explicit formation of the Jacobian is affordable using a direct solver for the forward solution, and is even likely to require less memory than combination of direct solvers and implicit Jacobian usage for many moderate-scale CSEM surveys. This inversion scheme takes advantage of minimizing the number of model updates using a method with high convergence rate such as GN, and of using a direct solver for the forward solution, which allows multiple solutions reusing the same matrix factorization by forward and backward substitutions. This last point enables the explicit computation of the Jacobian.

On the other hand, new inversion algorithms have been developed formulating and discretizing the forward and inverse problems in a FE framework (Key, 2012; Schwarzbach and Haber, 2013; Grayver, 2015). Most of the inversion codes to date were built around FD techniques on orthogonal meshes or based on the IE method, while many state-of-the-art forward programs are based on FE. Schwarzbach and Haber (2013) presents a 3-D FE based inversion program using a GN with CG optimization approach and rigorously derive two regularization functions for the inversion scheme: a smoothing function using a primal-dual mixed FE formulation which generalizes the standard Laplacian operator for a piecewise constant conductivity model on unstructured meshes, and a total variation regularization function for the same models. Moreover, Grayver (2015) has developed an inversion algorithm based on a 3-D FE forward program with the possibility to use different meshes for forward and inverse problems. The use of different meshes to compute the state variables and the model parameters avoids overparametrization of the model variable or underparametrization of the state variables, and has already showed its benefits on FD based inversion programs (Sasaki, 2001; Commer and Newman, 2008). The novel approach in Grayver (2015) is to additionally calculate the optimal mesh for each case. The mesh to calculate state variables and sensitivities (adjoint variables) have to provide accurate EM responses, whereas the mesh to calculate the model parameter variables should adequately represent imaged subsurface structure. They use an adaptive mesh refinement method to calculate the optimal state and adjoint mesh, applying it independently to different frequencies, and an automatic approach for efficient initial model parameter mesh design based on the linearized model resolution matrix.

All the inversion schemes we have mentioned above share a common initial approximation which consists of eliminating the PDE constraint from the optimization problem, by substituting it using equality constraints in the predicted variable of the objective function misfit term. Then, the only variable in the optimization is the model parameter.

Methods using this approach are *reduced-space* methods, because they reduce the space of optimization variables, and are also sometimes referred to as *black-box* methods (Herzog and Kunisch, 2010), since they treat the state equation as a black-box, embedding it into an optimization loop. By contrast, there is a developed mathematical theory in the full-space, in which the PDE-constrained optimization problem is addressed directly (e.g. Nocedal and Wright, 1999; Biros and Ghattas, 2005; Huber, 2013), treating the state and model parameters variables as independent optimization variables, which are coupled through the PDE constraint. These methods are sometimes called *all-at-once* methods (e.g. Haber et al., 2004; Bangerth, 2008; Herzog and Kunisch, 2010) or *one-shot* methods, because they solve the forward problem and the inverse problem simultaneously in one iterative process.

The main advantage of *all-at-once* methods over black-box methods is that while black-box approaches require the repeated costly solution of the (nonlinear) state equation for each evaluation of the objective function and of the adjoint equation to evaluate the sensitivities and the gradients, *all-at-once* methods avoid these calculations and they only need to solve exactly the state equation at the very end of the optimization process. This advantage comes at the cost of many more optimization variables and of the presence of equality constraints.

All-at-once inversion schemes have already been applied to solve EM inverse problems in a FD framework (Haber et al., 2000, 2004; Wilhelms et al., 2013). In Haber et al. (2004), they applied this method to invert time- and frequency-domain 3-D EM data, concluding that this procedure has potential for a solution to be reached faster than in traditional unconstrained optimization approaches.

When formulating the PDE-constrained optimization problem directly, there are two possibilities: first discretize the optimization problem and then solve a discrete optimization problem or first optimize the continuous problem and obtain a set of equations to discretize. The first approach is referred as *discretize-optimize* and the second one *optimize-discretize* (Haber, 2007). In most cases, and in Haber et al. (2000, 2004); Wilhelms et al. (2013) the *discretize-optimize* strategy is preferred because with the *optimize-discretize* approach one can obtain inconsistent gradients (Haber, 2007). On the other hand, using the *discretize-optimize* approach, discretizations cannot be changed by adapting the mesh between nonlinear iterations, and the potential to significantly reduce the numerical cost by taking into account the spatial structure of solutions is lost (Bangerth, 2008). Changing the mesh between nonlinear iterations in the *discretize-optimize* approach, changes the size of the finite dimensional problem making the norms in different inversion steps not comparable.

Furthermore, recent research has formulated algorithms using *all-at-once* methods in a FE framework and using a continuous function space setting to allow for discretizations that are adaptively refined as nonlinear iterations proceed (Bangerth, 2008; Herzog and Kunisch, 2010; Günther, 2010). In these optimizations schemes, the commonly used Newton steps or line search are first formulated on continuous function spaces and then discretized. The advantage is that then, the finite dimensional norms are independent

of the mesh size and individual steps of the algorithm are comparable even if they used differently refined meshes. This can reduce significantly the numerical effort to solve the inverse problem and at the same time the possibility to use an adaptive mesh coarser where we lack information or where a fine mesh is not required which makes the inverse problem better posed (Bangerth, 2008).

In this thesis we have investigated the applicability of a PDE-constrained full-space optimization scheme to the solution of the 2.5-D CSEM inverse problem. Our objective is to formulate a framework for our problem based on this approach, using the FE method for numerical discretization. The advantages of such a formulation is on one hand, to include all the benefits the FE method offers on modeling, and that we have shown in the previous chapters of this thesis, and on the other hand, for the inversion to take advantage of techniques with convergence rates higher than linear and that at the same time avoid the cumbersome task of solving the exact forward problem in every iteration. Another interest of using the FE method in combination with a PDE-constrained full-space optimization strategy, is that if formulated using an *optimize-discretize* approach, it can naturally include the possibility to use optimal meshes for both state and control variables for each updated model in the inversion process. Moreover, it makes it possible to incorporate equality/inequality and linear/non-linear constraints in the inversion.

Particularly, in this Chapter, we derive a formulation of a PDE-constrained full-space optimization scheme for the solution of the isotropic 2.5-D CSEM inverse problem. We derive it first, using a *discretize-optimize* strategy and we implement the problem in the COMSOL-MATLAB structure using a general-purpose optimization algorithm for its solution. Then, we apply the program to two synthetic inversion examples and we show the results. Finally, we derive a formulation for the same problem using an *optimize-discretize* scheme, as a first step towards an inversion program with adaptive FE meshes.

5.2 The inverse problem as a PDE-constrained optimization

The inverse problem of estimating the subsurface conductivity model, m, compatible with the EM observations at discrete surface locations, d^{obs}, can be formulated as an optimization problem in which all the physical quantities are governed by a set of PDEs. Thus, the PDE-constrained optimization problem can be expressed as:

$$\begin{aligned} &\min_{u,m} F(u,m) = \frac{1}{2}\|Qu - d^{obs}\|^2 + \frac{\beta}{2}\|R(m - m_{ref})\|^2 \\ &\text{subject to} \quad e(u,m) = 0, \end{aligned} \tag{5.1}$$

with $e(u,m)$ the set of governing PDEs or state equations, and u the state variables or the EM fields solution of the PDEs. The function F is referred to as the objective or penalty function and in equation (5.1) it is a Tikhonov functional (Tikhonov and Arsenin, 1977). The first term in the function is a L^2 norm misfit term between observed and predicted

data with Q a measurement operator which transforms and projects the fields onto the observables in the measurement locations and the second term is a regularization functional to stabilize the minimization, with β the regularization parameter that balances the effect of data misfit and model regularization during minimization. As discussed in the section above, the inverse problem is ill-posed, thus it is common to regularize the problem with a penalty term which restricts the set of acceptable solutions to those that meet some a priori constraints on model structure, commonly, smoothness constraints.

In geophysical EM applications, it is a standard approach to eliminate the field u in the objective function using equality constraints, obtaining an unconstrained optimization problem of the form (Haber et al., 2000):

$$\min_m F(m) = \frac{1}{2}\|Q\mathcal{S}(m) - d^{obs}\|^2 + \frac{\beta}{2}\|R(m - m_{ref})\|^2, \tag{5.2}$$

where $\mathcal{S}$ is a solution operator, $u = \mathcal{S}(m)$, which solves $e(\mathcal{S}(m), m) = 0$. This approach is possible because the state variable u can be uniquely (or at least locally uniquely) determined from the PDE: $e(u, m) = 0$ (e.g. Herzog, 2010). In the resulting problem there is only one optimization variable, the model parameter m, and the minimization problem is commonly solved using gradient-based optimization methods as described in the introduction of this chapter.

In contrast, in this thesis we address the PDE-constrained optimization problem (5.1) directly in the full-space, solving for both the fields and the model parameter at the same time with an *all-at-once* approach.

Under appropriate conditions (see e.g. Nocedal and Wright, 1999; Tröltzsch, 2010), solutions of the PDE-constrained optimization problem (5.1) with the PDE as an explicit side constraint, are stationary points of an associated Lagrangian defined as:

$$\mathcal{L} = F(u, m) + (e(u, m), \lambda), \tag{5.3}$$

which couples the penalty function F (in equation 5.1) with the state equation constraints through Lagrange multipliers λ. Then, the first-order necessary conditions for optimality are given in abstract form by (see e.g. Nocedal and Wright, 1999; Tröltzsch, 2010):

$$\nabla_x \mathcal{L}(x)(\tilde{x}) = 0, \tag{5.4}$$

where $x = \{u, m, \lambda\}$ are the optimal solutions and $\tilde{x}$ are the perturbation directions $\tilde{x} = \{\tilde{u}, \tilde{m}, \tilde{\lambda}\}$. The derivatives in (5.4) are formally Gâteaux derivatives, and in our problem are particularly Fréchet derivatives (see e.g. Tröltzsch, 2010) which are ultimately determined as directional derivatives.

In the Lagrangian (5.3) we only consider PDE equality constraints and assume, for ease of exposition, that inequality constraints such as bounds in the model parameter, $m_l \leq m \leq m_u$, are non-existent or inactive at the solution. In the more general case, they can be included in the Lagrangian, and then the first-order necessary conditions are typically

known as the Karush-Kuhn-Tucker (KKT) conditions (e.g. Nocedal and Wright, 1999).

To solve the inverse problem (5.1), the first-order necessary conditions (5.4) need to be solved, but due to their nonlinearity, a direct solution of (5.4) is not possible. There are a large variety of methods to solve the KKT system (see e.g. Nocedal and Wright, 1999; Haber et al., 2000; Biros and Ghattas, 2005; Hinze et al., 2009), but all fast converging optimization methods use the idea of Newton's method in some sense (Hinze et al., 2009).

Newton's method generates a sequence of iterates $x_k = \{u_k, m_k, \lambda_k\}$ hopefully converging to the exact solution $x = \{u, m, \lambda\}$ of (5.4) as $k \to \infty$. In each iteration, it computes a search direction δx_k to update the current x_k and get x_{k+1}, by using a local approximation of (5.4). This approximation is a second-order Taylor expansion of $\mathcal{L}$ that takes the direction to the stationary point of the approximation as next search direction. Thus, the Newton step for the Lagrangian functional is:

$$\nabla_x^2 \mathcal{L}(x_k)(\delta x_k, \tilde{x}) = -\nabla_x \mathcal{L}(x_k)(\tilde{x}). \tag{5.5}$$

Formulating the inverse problem in this way has several advantages (e.g. Huber, 2013). First, the linear systems arising from this formulation, the constraints Jacobian's and the Lagrangian's Hessian, are sparse and can be evaluated exactly and stored explicitly, thus avoiding additional approximation errors. Second, inexact solutions of the PDEs are acceptable. The state variables are not assumed to satisfy all the constraints in each iteration, they are not forced to be feasible, thus the algorithm can visit infeasible points and feasibility and optimality can be simultaneously gained through the optimization iterations. Finally, the evaluation of the objective function for every new updated model is very cheap since it is not necessary to reassemble, refactorize and solve the PDEs as is the case using reduced-space methods.

On the other hand, the systems of equations arising from (5.5) are usually indefinite, i.e. they have negative and positive eigenvalues, and are very large. Therefore, it is in this point that the different strategies emerge to approximate the Hessian of the Lagrangian and to guarantee that the reduced Hessian is positive definite. For solving these large scaled optimization problems inexact Newton methods, Sequential Quadratic Programming (SQP) methods or Interior Point (IP) methods have been developed and implemented. For an overview of these techniques we refer to Nocedal and Wright (1999).

In this thesis we consider a state-of-the-art SQP algorithm (Gill et al., 2002, 2005, 2015) with a limited-memory quasi-Newton approximation to the Hessian. SQP methods are equivalent to Newton's method applied to the KKT conditions (5.5) and are sometimes referred as Lagrange-Newton methods. They solve in every iteration a Quadratic Programming (QP) problem to generate a new search direction. The QP problem is built from a quadratic approximation of the Lagrangian and by linearizing the equality and inequality constraints.

5.3 Measurements and state variables for isotropic 2.5-D CSEM

In CSEM we measure the EM fields or a relation between them in certain positions on the surface of the model we want to characterize, and for different frequencies and different transmitter locations. Accordingly,

$$d^{obs} = d^{obs}(\boldsymbol{r}_i^{src}, \boldsymbol{r}_j^{rcv}, \omega_k), \quad i = 1,\ldots,n_s, \quad j = 1,\ldots,n_r, \quad k = 1,\ldots,n_f, \tag{5.6}$$

where $\boldsymbol{r}_i^{src}, \boldsymbol{r}_j^{rcv}$ and ω_k are the ith source position vector, the jth receiver position vector and the kth operating frequency (angular frequency), respectively. Then, the objective function for the multi-experiment is:

$$F(u,m) = \left(\sum_{k=1}^{n_f} \eta_k \sum_{i=1}^{n_s} \sum_{j=1}^{n_r} \frac{1}{2} \left\| W_{ijk}^d \left(d_{ijk}^{syn} - d_{ijk}^{obs} \right) \right\|^2 \right) + \frac{\beta}{2} \|R(m - m_{ref})\|^2, \tag{5.7}$$

with a frequency weighting:

$$\eta_k = \frac{\omega_k^{-2}}{\sum_{s=1}^{n_f} \omega_s^{-2}}, \tag{5.8}$$

and a data weighting:

$$W_{ijk}^d = \frac{1}{|d_{ijk}^{obs}| \epsilon_{ijk}}, \tag{5.9}$$

with ϵ_{ijk} the estimated relative error of the ijk-datum. The frequency weighting function is discussed by Abubakar et al. (2008), and balances each frequency data component.

As explained in detail in Chapter 2, when modeling CSEM data with a 2.5-D approximation, the EM fields are not solved directly, but for the κ_z-domain transformed along-strike directed EM field components, $\hat{E}_z$ and $\hat{H}_z$. Thus, to obtain the EM fields in the spatial domain we need to solve the governing PDEs of these transformed fields for a set of κ_z values (see Chapter 2). Since we want to use a PDE-constrained optimization strategy with the PDEs as explicit side constraints, we need to include the overall set of PDEs for all the κ_z values in the optimization process.

To simplify the following derivations and in the remainder of this thesis, we assume that the transmitter is a x–directed horizontal electric dipole, that we model as a point dipole, located at $z = 0$, in the model plane. Additionally, we take the amplitude and phase of the in-line electric field component, E_x, as observables d^a and d^p, respectively.

Applying these assumptions and splitting the operator Q, that relates:

$$\boldsymbol{d}_{ijk}^{syn} = \{ d_{ijk}^{syn,a}, d_{ijk}^{syn,p} \}, \tag{5.10}$$

with:

$$\boldsymbol{u}_{ik} = \left\{ \boldsymbol{u}_{ik}^l \right\} = \left\{ \hat{E}_{z,ik}^l \left(x, y, \kappa_z^l \right), \hat{H}_{z,ik}^l \left(x, y, \kappa_z^l \right) \right\}, \quad \text{with} \quad l = 1,\ldots,n_{\kappa_z}, \tag{5.11}$$

into two operators $Q = PO$, results in:

$$\boldsymbol{d}^{syn}_{ijk} = (Q(\boldsymbol{u}_{ik}))_{ijk} = (PO(\boldsymbol{u}_{ik}))_{ijk}. \tag{5.12}$$

Then, we define the operator $P = \{P^a, P^p\}$, as the operator that calculates the amplitudes and phases of $E_{x,ik}(x,y,z)$ and projects them onto the receivers locations (x_j, y_j, z_j):

$$\begin{aligned} d^{syn,a}_{ijk} &= P^a E_{x,ik}(x,y,z) = |E_{x,ik}(x_j,y_j,z_j)| = \\ &\left(Re\left(E_{x,ik}\left(x_j,y_j,z_j\right)\right)^2 + Im\left(E_{x,ik}\left(x_j,y_j,z_j\right)\right)^2\right)^{1/2}, \end{aligned} \tag{5.13a}$$

$$d^{syn,p}_{ijk} = P^p E_{x,ik}(x,y,z) = \varphi_{E_x,ik}(x_j,y_j,z_j) = \arctan\left(\frac{Im\left(E_{x,ik}\left(x_j,y_j,z_j\right)\right)}{Re\left(E_{x,ik}\left(x_j,y_j,z_j\right)\right)}\right), \tag{5.13b}$$

and the operator O, as the operator that relates the field $E_{x,ik}(x,y,z)$ with the state variables $\boldsymbol{u}_{ik}$:

$$E_{x,ik}(x,y,z) = O\boldsymbol{u}_{ik}(x,y,\kappa_z) = \int_{-\infty}^{\infty} \hat{E}_{x,ik}(x,y,\kappa_z) e^{-i\kappa_z z} d\kappa_z \Big|_{z=0} \approx \sum_{l=1}^{n_{\kappa_z}} \nu^l \hat{E}^l_{x,ik}(x,y,\kappa^l_z), \tag{5.14}$$

where the integral is numerically approximated for $z = 0$, and ν^l denote weight functions of the numerical integration, and $\hat{E}^l_{x,ik}$ is related to $\hat{E}^l_{z,ik}$ and $\hat{H}^l_{z,ik}$, through:

$$\hat{E}^l_{x,ik} = (\kappa^l_{e,k})^{-2}\left(-i\kappa^l_z \partial_x \hat{E}^l_{z,ik} + \hat{z}_k \partial y \hat{H}^l_{z,ik} - \hat{z}_k \hat{J}^s_{x,i}\right). \tag{5.15}$$

In this last expression equation (2.27) applies for $\hat{E}^l_{x,ik}$ considering the isotropic problem, and $\hat{E}^l_{z,ik}, \hat{H}^l_{z,ik}, (\kappa^l_{e,k})^{-2}$ and $\hat{z}_k$ are:

$$\hat{E}^l_{z,ik} = \hat{E}^l_{z,ik}(x,y,\kappa^l_z), \tag{5.16a}$$

$$\hat{H}^l_{z,ik} = \hat{H}^l_{z,ik}(x,y,\kappa^l_z), \tag{5.16b}$$

$$(\kappa^l_{e,k})^{-2} = \left((\kappa^l_z)^2 + \hat{z}_k \sigma\right)^{-1}, \tag{5.16c}$$

$$\hat{z}_k = i\mu_0 \omega_k. \tag{5.16d}$$

The relation between $\hat{E}^l_{x,ik}$ and $\hat{E}^l_{z,ik}, \hat{H}^l_{z,ik}$, in equation (5.15), can be also written in a more compact form as:

$$\begin{aligned} \hat{E}^l_{x,ik} &= (\kappa^l_{e,k})^{-2}\left[\begin{pmatrix}\partial_x & \partial_y\end{pmatrix}\begin{pmatrix}-i\kappa^l_z & 0\\ 0 & \hat{z}_k\end{pmatrix}\begin{pmatrix}\hat{E}^l_{z,ik}\\ \hat{H}^l_{z,ik}\end{pmatrix} - \hat{z}_k \hat{J}^s_{x,i}\right] \\ &= (\kappa^l_{e,k})^{-2}\left[\nabla \boldsymbol{c}^l_k \boldsymbol{u}^l_{ik} - \hat{z}_k \hat{J}^s_{x,i}\right], \end{aligned} \tag{5.17}$$

where $\boldsymbol{c}^l_k$ is defined as:

$$\boldsymbol{c}^l_k = \begin{pmatrix}-i\kappa^l_z & 0\\ 0 & \hat{z}_k\end{pmatrix}. \tag{5.18}$$

Taking into account the relation between measurements and state variables, the inverse problem for the 2.5-D CSEM PDEs reads:

$$\begin{aligned} &\text{minimize} \quad \left(\sum_{k=1}^{n_f} \eta_k \sum_{i=1}^{n_s} \sum_{j=1}^{n_r} \frac{1}{2} \left\| W_{ijk}^d \left(\boldsymbol{d}_{ijk}^{syn} - \boldsymbol{d}_{ijk}^{obs} \right) \right\|^2 \right) + \frac{\beta}{2} \| R(m - m_{ref}) \|^2, \\ &\text{subject to} \quad e_{ik}^l (\hat{E}_{z,ik}^l, \hat{H}_{z,ik}^l, m) = 0, \quad \text{for } i = 1, \ldots, n_s;\ k = 1, \ldots, n_f;\ l = 1, \ldots, n_{\kappa_z}. \end{aligned} \tag{5.19}$$

The Lagrangian function (5.3) for our particular problem is then,

$$\begin{aligned} \mathcal{L} = &\left(\sum_{k=1}^{n_f} \eta_k \sum_{i=1}^{n_s} \sum_{j=1}^{n_r} \frac{1}{2} \left\| W_{ijk}^d \left(\boldsymbol{d}_{ijk}^{syn} - \boldsymbol{d}_{ijk}^{obs} \right) \right\|^2 \right) + \frac{\beta}{2} \| R(m - m_{ref}) \|^2 \\ &+ \sum_{k=1}^{n_f} \sum_{i=1}^{n_s} \sum_{l=1}^{n_{\kappa_z}} \left(e_{ik}^l \left(\hat{E}_{z,ik}^l, \hat{H}_{z,ik}^l, m \right), \lambda_{ik}^l \right), \end{aligned} \tag{5.20}$$

where we introduce a Lagrange multiplier λ_{ik}^l for each set of PDEs corresponding to each $ik-th$ experiment and to each $l-th$ κ_z parameter value.

5.4 Constrained optimization with a SQP method using SNOPT

In the previous sections we introduced the general framework for the PDE-constrained optimization strategy in the full-space and we derived a particular Lagrangian for the isotropic 2.5-D CSEM PDEs. Our problem is especially complex, the solution of the PDEs are not directly the observables and we need to include the PDEs for a set of wavenumber values to correctly represent the observable variables. To simplify the Lagrangian, we only consider an in-line horizontal electric dipole and a specific observable: the in-line electric field component, E_x.

Now, we will use the elements given in the previous sections to derive a formulation of a PDE-constrained optimization scheme in the full-space for the particular Lagrangian in equation (5.20). This formulation is implemented by using the COMSOL-MATLAB programming structure and a general-purpose optimization algorithm, SNOPT (Gill et al., 2002, 2005). SNOPT solves the PDE-constrained optimization problem using an implementation of a Sequential Quadratic Programming (SQP) method and it is included in the COMSOL package. SQP methods are equivalent to the previously introduced Newton's method (e.g. Boggs and Tolle, 1995).

The essential idea of the SQP method is to solve the nonlinearly constrained minimization problem using a sequence of QP subproblems. In each iteration the QP subproblem minimizes a quadratic approximation to the Lagrangian function, subject to the linearization of the constraints in the original problem. The solution of the QP subproblem is used as a search direction to update the model for the next iteration. The main advantage of using a QP subproblem is that it is relatively easy to solve and yet, it is assumed to reflect

in some way the local properties of the original problem (Boggs and Tolle, 1995).

A SQP method is one of the most effective methods to solve nonlinearly constrained optimization problems (Nocedal and Wright, 1999) and SNOPT is a robust and efficient optimization solver. However, we use it through COMSOL and we do not have access to the source code, thus we can not exploit the particular matrix structures arising from our problem which could improve the performance. Due to the complexity of the formulation of such a constrained scheme, at present we have limited our program to the implementation with COMSOL. This allows us to validate the problem formulation and to realize preliminary studies on its performance, as a first step towards a more efficient implementation.

In this section, we will derive the problem formulation, describe the basic algorithm of a SQP method and the principal techniques that SNOPT uses to implement it. Finally, we validate the performance of the inversion results for two synthetic models.

5.4.1 Problem formulation for the 2.5-D CSEM isotropic PDEs

We assume a *discretize-optimize* strategy (Haber et al., 2004) to formulate the 2.5-D CSEM PDE-constrained optimization problem in the full-space, because this form is required for implementation in the COMSOL-MATLAB structure and SNOPT optimization solver.

We start with the objective function (5.7) in a FE discretized form:

$$F\left(\left\{\boldsymbol{U}^l\right\},\boldsymbol{m}\right)=\frac{1}{2}\left(\boldsymbol{d}^{syn}\left(\left\{\boldsymbol{U}^l\right\},\boldsymbol{m}\right)-\boldsymbol{d}^{obs}\right)^T\boldsymbol{W}_d^T\boldsymbol{W}_d\boldsymbol{\eta}\left(\boldsymbol{d}^{syn}\left(\left\{\boldsymbol{U}^l\right\},\boldsymbol{m}\right)-\boldsymbol{d}^{obs}\right)+\frac{\beta}{2}R\left(\boldsymbol{m}-\boldsymbol{m}^{ref}\right), \tag{5.21}$$

where the observed data, $\boldsymbol{d}^{obs}$, is a vector of $n_d=n_f\times n_s\times n_r$ values and the synthetic data, $\boldsymbol{d}^{syn}$, is a vector with the same dimensions, which depends on the elementwise discretized model parameter $\boldsymbol{m}$ and on a set of vectors $\boldsymbol{U}^l$ with block elements $\boldsymbol{U}^l_{ik}$, which at the same time are vectors containing the FE discretized fields $\left(\hat{E}^l_{ik},\hat{H}^l_{ik}\right)^T_j$ on each node j, associated with the $ik-th$ experiment and with the $l-th$ κ_z parameter value. The matrices $\boldsymbol{\eta}$ and $\boldsymbol{W}_d$ are $n_d\times n_d$ diagonal matrices as defined in (5.8) and (5.9), respectively, note however, that the frequency weighting is constant for all data at a specific frequency but varying source and receiver position.

To form the Lagrangian function associated with the objective function above, we use the discretized FE system (2.60) as state equation for the isotropic 2.5-D CSEM PDEs, and we include them for each $ik-th$ experiment and each $l-th$ κ_z parameter value, since they all constrain the state variables and also indirectly the observables:

$$\mathcal{L}=\frac{1}{2}\left(\boldsymbol{d}^{syn}\left(\left\{\boldsymbol{U}^l\right\},m\right)-\boldsymbol{d}^{obs}\right)^T\boldsymbol{W}_d^T\boldsymbol{W}_d\boldsymbol{\eta}\left(\boldsymbol{d}^{syn}\left(\left\{\boldsymbol{U}^l\right\},m\right)-\boldsymbol{d}^{obs}\right)+\frac{\beta}{2}R\left(\boldsymbol{m}-\boldsymbol{m}^{ref}\right)+\sum_{k=1}^{n_f}\sum_{i=1}^{n_s}\sum_{l=1}^{n_{\kappa_z}}\left(\boldsymbol{\lambda}^l_{ik}\right)^T\left[\boldsymbol{A}^l_{ik}(m)\boldsymbol{U}^l_{ik}-\boldsymbol{F}^l_{ik}(m)\right]. \tag{5.22}$$

Individual state equations and variables do not couple across experiments, therefore the Lagrangian above can be written as:

$$\mathcal{L} = \frac{1}{2}\left(\boldsymbol{d}^{syn}(\boldsymbol{U},m) - \boldsymbol{d}^{obs}\right)^T \boldsymbol{W}_d^T \boldsymbol{W}_d \boldsymbol{\eta}\left(\boldsymbol{d}^{syn}(\boldsymbol{U},m) - \boldsymbol{d}^{obs}\right) + \frac{\beta}{2} R\left(\boldsymbol{m} - \boldsymbol{m}^{ref}\right) + \boldsymbol{\lambda}^T\left[\boldsymbol{A}(m)\boldsymbol{U} - \boldsymbol{F}(m)\right], \tag{5.23}$$

where we have redefined $\boldsymbol{A}$ as a block diagonal matrix with block elements, $\boldsymbol{A}_{ik}^l$, the vector $\boldsymbol{U}$ is composed of block vectors $\boldsymbol{U}_{ik}^l$, the vector $\boldsymbol{F}$ is composed of block vectors $\boldsymbol{F}_{ik}^l$, and the vector of the Lagrange multipliers $\boldsymbol{\lambda}^T$ is formed by block vectors $\boldsymbol{\lambda}_{ik}^l$.

Without loss of generality but for sake of simplicity, in the following we only consider one experiment, that is the data corresponding to a single transmitter position and operating at a single frequency. Then, the matrices in the state equations are:

$$\boldsymbol{A} = \text{diag}\left(\boldsymbol{A}^l\right); \quad l = 1,\ldots,n_{\kappa_z}, \tag{5.24}$$

$$\boldsymbol{A}^l = \{\boldsymbol{A}_{ij}^l\}; \quad i,j = 1,\ldots,n, \tag{5.25}$$

where n is the number of nodes of the discretized FE mesh, and:

$$\boldsymbol{U} = \{\boldsymbol{U}^l\}; \quad l = 1,\ldots,n_{\kappa_z}, \tag{5.26}$$

$$\boldsymbol{U}^l = \{\boldsymbol{U}_j^l\} = \left\{\begin{pmatrix}\hat{E}_j^l & \hat{H}_j^l\end{pmatrix}^T\right\}; \quad j = 1,\ldots,n, \tag{5.27}$$

$$\boldsymbol{F} = \{\boldsymbol{F}^l\}; \quad l = 1,\ldots,n_{\kappa_z}, \tag{5.28}$$

$$\boldsymbol{F}^l = \{\boldsymbol{F}_i^l\}; \quad i = 1,\ldots,n. \tag{5.29}$$

The Lagrange multipliers $\boldsymbol{\lambda}$ are also discretized in the following form:

$$\boldsymbol{\lambda} = \{\boldsymbol{\lambda}^l\}; \quad l = 1,\ldots,n_{\kappa_z}, \tag{5.30}$$

$$\boldsymbol{\lambda}^l = \{\boldsymbol{\lambda}_j^l\} = \left\{\begin{pmatrix}\lambda_{E,j}^l & \lambda_{H,j}^l\end{pmatrix}^T\right\}; \quad j = 1,\ldots,n, \tag{5.31}$$

and the relation between $\boldsymbol{d}^{syn}$ and $\{\boldsymbol{U}^l\}$ is, in discretized form:

$$\boldsymbol{d}^{syn} = \boldsymbol{P}\boldsymbol{E}_x; \tag{5.32}$$

$$\boldsymbol{E}_x = \sum_{l=1}^{n_{\kappa_z}} \nu^l \hat{\boldsymbol{E}}_{\boldsymbol{x}}^l, \tag{5.33}$$

$$\hat{\boldsymbol{E}}_{\boldsymbol{x}}^l = \bar{\boldsymbol{D}}^l(m)\left[\bar{\boldsymbol{C}}^l\boldsymbol{U}^l - \bar{\boldsymbol{S}}\right], \tag{5.34}$$

where $\boldsymbol{P}$ is an operator that projects the solution to the receiver locations, $\boldsymbol{E}_x$ and $\hat{\boldsymbol{E}}_{\boldsymbol{x}}^l$ are vectors with length, the number of nodes n, and $\bar{\boldsymbol{D}}^l(m)$ and $\bar{\boldsymbol{C}}^l$ are $n \times n$ diagonal matrices from the discretization in equation (5.17) of $(\kappa_e^l)^{-2}$ and of the derivative operator with c_k^l, respectively. The vector $\bar{\boldsymbol{S}}$ contains the source term, thus, it is sparse.

As explained at the beginning of this chapter, a stationary point $\{\boldsymbol{U},m\}$ of the La-

grangian needs to fulfill the first-order conditions (5.4), which in the discretized case and for our particular problem considering a single experiment, expand as:

$$\mathcal{L}_{\hat{E}_z^l} = \left(\boldsymbol{P}\nu^l\bar{\boldsymbol{D}}^l\bar{\boldsymbol{C}}^l\mathbf{1}_{10}\right)^T\boldsymbol{W}_d^T\boldsymbol{W}_d\left(\boldsymbol{d}^{syn}-\boldsymbol{d}^{obs}\right)+(\boldsymbol{A}^l\mathbf{1}_{10})^T\boldsymbol{\lambda}^l, \tag{5.35a}$$

$$\mathcal{L}_{\hat{H}_z^l} = \left(\boldsymbol{P}\nu^l\bar{\boldsymbol{D}}^l\bar{\boldsymbol{C}}^l\mathbf{1}_{01}\right)^T\boldsymbol{W}_d^T\boldsymbol{W}_d\left(\boldsymbol{d}^{syn}-\boldsymbol{d}^{obs}\right)+(\boldsymbol{A}^l\mathbf{1}_{01})^T\boldsymbol{\lambda}^l, \tag{5.35b}$$

$$\begin{aligned}\mathcal{L}_m = \left(\boldsymbol{P}\sum_{s=1}^{n_{\kappa_z}}\nu^s\nabla_m\bar{\boldsymbol{D}}^s\left[\bar{\boldsymbol{C}}^s\boldsymbol{U}^s-\bar{\boldsymbol{S}}\right]\right)^T\boldsymbol{W}_d^T\boldsymbol{W}_d\left(\boldsymbol{d}^{syn}-\boldsymbol{d}^{obs}\right)+\frac{\beta}{2}\nabla_m R(\boldsymbol{m}-\boldsymbol{m}^{ref})\\ +\sum_{s=1}^{n_{\kappa_z}}[\nabla_m\boldsymbol{A}^s\boldsymbol{U}^s-\nabla_m\boldsymbol{F}^s]^T\boldsymbol{\lambda}^s,\end{aligned} \tag{5.35c}$$

$$\mathcal{L}_{\lambda_E^l} = \mathbf{1}_{10}^T(\boldsymbol{A}^l\boldsymbol{U}^l-\boldsymbol{F}^l), \tag{5.35d}$$

$$\mathcal{L}_{\lambda_H^l} = \mathbf{1}_{01}^T(\boldsymbol{A}^l\boldsymbol{U}^l-\boldsymbol{F}^l), \tag{5.35e}$$

$$\tag{5.35f}$$

where $\mathbf{1}_{10}$ and $\mathbf{1}_{01}$ are vectors of n block elements with a $\begin{pmatrix}1 & 0\end{pmatrix}^T$ vector and a $\begin{pmatrix}0 & 1\end{pmatrix}^T$ vector in each block, respectively.

To form the Newton step (5.5), we derive the second derivatives of the Lagrangian:

$$\mathcal{L}_{\hat{E}_z^l\hat{E}_z^l} = \left(\boldsymbol{P}\nu^l\bar{\boldsymbol{D}}^l\bar{\boldsymbol{C}}^l\mathbf{1}_{10}\right)^T\boldsymbol{W}_d^T\boldsymbol{W}_d\left(\boldsymbol{P}\nu^l\bar{\boldsymbol{D}}^l\bar{\boldsymbol{C}}^l\mathbf{1}_{10}\right), \tag{5.36}$$

$$\mathcal{L}_{\hat{E}_z^l\hat{H}_z^l} = \left(\boldsymbol{P}\nu^l\bar{\boldsymbol{D}}^l\bar{\boldsymbol{C}}^l\mathbf{1}_{10}\right)^T\boldsymbol{W}_d^T\boldsymbol{W}_d\left(\boldsymbol{P}\nu^l\bar{\boldsymbol{D}}^l\bar{\boldsymbol{C}}^l\mathbf{1}_{01}\right), \tag{5.37}$$

$$\mathcal{L}_{\hat{E}_z^l\hat{E}_z^n} = \left(\boldsymbol{P}\nu^l\bar{\boldsymbol{D}}^l\bar{\boldsymbol{C}}^l\mathbf{1}_{10}\right)^T\boldsymbol{W}_d^T\boldsymbol{W}_d\left(\boldsymbol{P}\nu^n\bar{\boldsymbol{D}}^n\bar{\boldsymbol{C}}^n\mathbf{1}_{10}\right), \tag{5.38}$$

$$\mathcal{L}_{\hat{E}_z^l\hat{H}_z^n} = \left(\boldsymbol{P}\nu^l\bar{\boldsymbol{D}}^l\bar{\boldsymbol{C}}^l\mathbf{1}_{10}\right)^T\boldsymbol{W}_d^T\boldsymbol{W}_d\left(\boldsymbol{P}\nu^n\bar{\boldsymbol{D}}^n\bar{\boldsymbol{C}}^n\mathbf{1}_{01}\right), \tag{5.39}$$

$$\begin{aligned}\mathcal{L}_{\hat{E}_z^l m} = \left(\boldsymbol{P}\nu^l\bar{\boldsymbol{D}}^l\bar{\boldsymbol{C}}^l\mathbf{1}_{10}\right)^T\boldsymbol{W}_d^T\boldsymbol{W}_d\left(\boldsymbol{P}\sum_{s=1}^{n_{\kappa_z}}\nu^s\nabla_m\bar{\boldsymbol{D}}^s\left[\bar{\boldsymbol{C}}^s\boldsymbol{U}^s-\bar{\boldsymbol{S}}\right]\right)\\ +\nabla_m\left(\boldsymbol{P}\nu^l\bar{\boldsymbol{D}}^l\bar{\boldsymbol{C}}^l\mathbf{1}_{10}\right)^T\boldsymbol{W}_d^T\boldsymbol{W}_d\left(\boldsymbol{d}^{syn}-\boldsymbol{d}^{obs}\right)+\nabla_m(\boldsymbol{A}^l\mathbf{1}_{10})^T\boldsymbol{\lambda}^l,\end{aligned} \tag{5.40}$$

$$\mathcal{L}_{\hat{E}_z^l\lambda_E^l} = (\boldsymbol{A}^l\mathbf{1}_{10})^T\mathbf{1}_{10}, \tag{5.41}$$

$$\mathcal{L}_{\hat{E}_z^l\lambda_H^l} = (\boldsymbol{A}^l\mathbf{1}_{10})^T\mathbf{1}_{01}, \tag{5.42}$$

$$\mathcal{L}_{\hat{E}_z^l\lambda^n} = 0, \tag{5.43}$$

$$\mathcal{L}_{\hat{H}_z^l\hat{E}_z^l} = \left(\boldsymbol{P}\nu^l\bar{\boldsymbol{D}}^l\bar{\boldsymbol{C}}^l\mathbf{1}_{01}\right)^T\boldsymbol{W}_d^T\boldsymbol{W}_d\left(\boldsymbol{P}\nu^l\bar{\boldsymbol{D}}^l\bar{\boldsymbol{C}}^l\mathbf{1}_{10}\right), \tag{5.44}$$

$$\mathcal{L}_{\hat{H}_z^l\hat{H}_z^l} = \left(\boldsymbol{P}\nu^l\bar{\boldsymbol{D}}^l\bar{\boldsymbol{C}}^l\mathbf{1}_{01}\right)^T\boldsymbol{W}_d^T\boldsymbol{W}_d\left(\boldsymbol{P}\nu^l\bar{\boldsymbol{D}}^l\bar{\boldsymbol{C}}^l\mathbf{1}_{01}\right), \tag{5.45}$$

$$\mathcal{L}_{\hat{H}_z^l\hat{E}_z^n} = \left(\boldsymbol{P}\nu^l\bar{\boldsymbol{D}}^l\bar{\boldsymbol{C}}^l\mathbf{1}_{01}\right)^T\boldsymbol{W}_d^T\boldsymbol{W}_d\left(\boldsymbol{P}\nu^n\bar{\boldsymbol{D}}^n\bar{\boldsymbol{C}}^n\mathbf{1}_{10}\right), \tag{5.46}$$

$$\mathcal{L}_{\hat{H}_z^l\hat{H}_z^n} = \left(\boldsymbol{P}\nu^l\bar{\boldsymbol{D}}^l\bar{\boldsymbol{C}}^l\mathbf{1}_{01}\right)^T\boldsymbol{W}_d^T\boldsymbol{W}_d\left(\boldsymbol{P}\nu^n\bar{\boldsymbol{D}}^n\bar{\boldsymbol{C}}^n\mathbf{1}_{01}\right), \tag{5.47}$$

$$\mathcal{L}_{\hat{H}_z^l m} = \left(\boldsymbol{P}\nu^l \bar{\boldsymbol{D}}^l \bar{\boldsymbol{C}}^l \mathbf{1}_{01}\right)^T \boldsymbol{W}_d^T \boldsymbol{W}_d \left(\boldsymbol{P}\sum_{s=1}^{n_{\kappa_z}} \nu^s \nabla_m \bar{\boldsymbol{D}}^s \left[\bar{\boldsymbol{C}}^s \boldsymbol{U}^s - \bar{\boldsymbol{S}}\right]\right) + \nabla_m \left(\boldsymbol{P}\nu^l \bar{\boldsymbol{D}}^l \bar{\boldsymbol{C}}^l \mathbf{1}_{01}\right)^T \boldsymbol{W}_d^T \boldsymbol{W}_d \left(\boldsymbol{d}^{syn} - \boldsymbol{d}^{obs}\right) + \nabla_m \left(\boldsymbol{A}^l \mathbf{1}_{01}\right)^T \boldsymbol{\lambda}^l, \tag{5.48}$$

$$\mathcal{L}_{\hat{H}_z^l \lambda_E^l} = (\boldsymbol{A}^l \mathbf{1}_{01})^T \mathbf{1}_{10}, \tag{5.49}$$

$$\mathcal{L}_{\hat{H}_z^l \lambda_H^l} = (\boldsymbol{A}^l \mathbf{1}_{01})^T \mathbf{1}_{01}, \tag{5.50}$$

$$\mathcal{L}_{\hat{H}_z^l \lambda^n} = 0, \tag{5.51}$$

$$\mathcal{L}_{m\hat{E}_z^l} = \left(\boldsymbol{P}\sum_{s=1}^{n_{\kappa_z}} \nu^s \nabla_m \bar{\boldsymbol{D}}^s \left[\bar{\boldsymbol{C}}^s \boldsymbol{U}^s - \bar{\boldsymbol{S}}\right]\right)^T \boldsymbol{W}_d^T \boldsymbol{W}_d \left(\boldsymbol{P}\nu^l \bar{\boldsymbol{D}}^l \bar{\boldsymbol{C}}^l \mathbf{1}_{10}\right) + \left(\boldsymbol{d}^{syn} - \boldsymbol{d}^{obs}\right)^T \boldsymbol{W}_d^T \boldsymbol{W}_d \left(\boldsymbol{P}\nu^l \nabla_m \bar{\boldsymbol{D}}^l \bar{\boldsymbol{C}}^l \mathbf{1}_{10}\right) + (\boldsymbol{\lambda}^l)^T \nabla_m \boldsymbol{A}^l \mathbf{1}_{10}, \tag{5.52}$$

$$\mathcal{L}_{m\hat{H}_z^l} = \left(\boldsymbol{P}\sum_{s=1}^{n_{\kappa_z}} \nu^s \nabla_m \bar{\boldsymbol{D}}^s \left[\bar{\boldsymbol{C}}^s \boldsymbol{U}^s - \bar{\boldsymbol{S}}\right]\right)^T \boldsymbol{W}_d^T \boldsymbol{W}_d \left(\boldsymbol{P}\nu^l \bar{\boldsymbol{D}}^l \bar{\boldsymbol{C}}^l \mathbf{1}_{01}\right) + \left(\boldsymbol{d}^{syn} - \boldsymbol{d}^{obs}\right)^T \boldsymbol{W}_d^T \boldsymbol{W}_d \left(\boldsymbol{P}\nu^l \nabla_m \bar{\boldsymbol{D}}^l \bar{\boldsymbol{C}}^l \mathbf{1}_{01}\right) + (\boldsymbol{\lambda}^l)^T \nabla_m \boldsymbol{A}^l \mathbf{1}_{01}, \tag{5.53}$$

$$\mathcal{L}_{mm} = \left(\boldsymbol{P}\sum_{s=1}^{n_{\kappa_z}} \nu^s \nabla_m \bar{\boldsymbol{D}}^s \left[\bar{\boldsymbol{C}}^s \boldsymbol{U}^s - \bar{\boldsymbol{S}}\right]\right)^T \boldsymbol{W}_d^T \boldsymbol{W}_d \left(\boldsymbol{P}\sum_{s=1}^{n_{\kappa_z}} \nu^s \nabla_m \bar{\boldsymbol{D}}^s \left[\bar{\boldsymbol{C}}^s \boldsymbol{U}^s - \bar{\boldsymbol{S}}\right]\right) + \frac{\beta}{2} \nabla_m \left(\nabla_m R(\boldsymbol{m} - \boldsymbol{m}^{ref})\right) + \sum_{s=1}^{n_{\kappa_z}} \nabla_m \left[\nabla_m \boldsymbol{A}^s \boldsymbol{U}^s - \nabla_m \boldsymbol{F}^s\right]^T \boldsymbol{\lambda}^s, \tag{5.54}$$

$$\mathcal{L}_{m\lambda_E^l} = \left(\nabla_m \boldsymbol{A}^l \boldsymbol{U}^l - \nabla_m \boldsymbol{F}^l\right)^T \mathbf{1}_{10} \tag{5.55}$$

$$\mathcal{L}_{m\lambda_H^l} = \left(\nabla_m \boldsymbol{A}^l \boldsymbol{U}^l - \nabla_m \boldsymbol{F}^l\right)^T \mathbf{1}_{01} \tag{5.56}$$

$$\mathcal{L}_{\lambda_E^l \hat{E}_z^l} = \mathbf{1}_{10}^T \boldsymbol{A}^l \mathbf{1}_{10}, \tag{5.57}$$

$$\mathcal{L}_{\lambda_E^l \hat{H}_z^l} = \mathbf{1}_{10}^T \boldsymbol{A}^l \mathbf{1}_{01}, \tag{5.58}$$

$$\mathcal{L}_{\lambda_E^l \hat{E}_z^n} = 0, \tag{5.59}$$

$$\mathcal{L}_{\lambda_E^l \hat{H}_z^n} = 0, \tag{5.60}$$

$$\mathcal{L}_{\lambda_E^l m} = \mathbf{1}_{10}^T \left(\nabla_m \boldsymbol{A}^l \boldsymbol{U}^l - \nabla_m \boldsymbol{F}^l\right), \tag{5.61}$$

$$\mathcal{L}_{\lambda_E^l \lambda_E^l} = 0, \tag{5.62}$$

$$\mathcal{L}_{\lambda_E^l \lambda_H^l} = 0, \tag{5.63}$$

$$\mathcal{L}_{\lambda_E^l \lambda_E^n} = 0, \tag{5.64}$$

$$\mathcal{L}_{\lambda_E^l \lambda_H^n} = 0, \tag{5.65}$$

$$\mathcal{L}_{\lambda_H^l \hat{E}_z^l} = \mathbf{1}_{01}^T \boldsymbol{A}^l \mathbf{1}_{10}, \tag{5.66}$$

$$\mathcal{L}_{\lambda_H^l \hat{H}_z^l} = \mathbf{1}_{01}^T \boldsymbol{A}^l \mathbf{1}_{01}, \tag{5.67}$$

$$\mathcal{L}_{\lambda_H^l \hat{E}_z^n} = 0, \tag{5.68}$$

$$\mathcal{L}_{\lambda_H^l \hat{H}_z^n} = 0, \tag{5.69}$$

$$\mathcal{L}_{\lambda_H^l m} = \mathbf{1}_{01}^T \left(\nabla_m \boldsymbol{A}^l \boldsymbol{U}^l - \nabla_m \boldsymbol{F}^l\right), \tag{5.70}$$

$$\mathcal{L}_{\lambda_H^l \lambda_E^l} = 0, \tag{5.71}$$

$$\mathcal{L}_{\lambda_H^l \lambda_H^l} = 0, \tag{5.72}$$

$$\mathcal{L}_{\lambda_H^l \lambda_E^n} = 0, \tag{5.73}$$

$$\mathcal{L}_{\lambda_H^l \lambda_H^n} = 0. \tag{5.74}$$

Accordingly, the Newton step for our particular problem can be written as:

$$\begin{pmatrix} \mathcal{L}_{\boldsymbol{u}^1\boldsymbol{u}^1} & \dots & \mathcal{L}_{\boldsymbol{u}^1\boldsymbol{u}^{n_{\kappa_z}}} & \mathcal{L}_{\boldsymbol{u}^1\boldsymbol{m}} & \mathcal{L}_{\boldsymbol{u}^1\boldsymbol{\lambda}^1} & \dots & \mathcal{L}_{\boldsymbol{u}^1\boldsymbol{\lambda}^{n_{\kappa_z}}} \\ \vdots & \vdots & \vdots & \vdots & \vdots & & \vdots \\ \mathcal{L}_{\boldsymbol{u}^{n_{\kappa_z}}\boldsymbol{u}^1} & \dots & \mathcal{L}_{\boldsymbol{u}^{n_{\kappa_z}}\boldsymbol{u}^{n_{\kappa_z}}} & \mathcal{L}_{\boldsymbol{u}^{n_{\kappa_z}}\boldsymbol{m}} & \mathcal{L}_{\boldsymbol{u}^{n_{\kappa_z}}\boldsymbol{\lambda}^1} & \dots & \mathcal{L}_{\boldsymbol{u}^{n_{\kappa_z}}\boldsymbol{\lambda}^{n_{\kappa_z}}} \\ \mathcal{L}_{\boldsymbol{m}\boldsymbol{u}^1} & \dots & \mathcal{L}_{\boldsymbol{m}\boldsymbol{u}^{n_{\kappa_z}}} & \mathcal{L}_{\boldsymbol{m}\boldsymbol{m}} & \mathcal{L}_{\boldsymbol{m}\boldsymbol{\lambda}^1} & \dots & \mathcal{L}_{\boldsymbol{m}\boldsymbol{\lambda}^{n_{\kappa_z}}} \\ \mathcal{L}_{\boldsymbol{\lambda}^1\boldsymbol{u}^1} & \dots & \mathcal{L}_{\boldsymbol{\lambda}^1\boldsymbol{u}^{n_{\kappa_z}}} & \mathcal{L}_{\boldsymbol{\lambda}^1\boldsymbol{m}} & \mathcal{L}_{\boldsymbol{\lambda}^1\boldsymbol{\lambda}^1} & \dots & \mathcal{L}_{\boldsymbol{\lambda}^1\boldsymbol{\lambda}^{n_{\kappa_z}}} \\ \vdots & \vdots & \vdots & \vdots & \vdots & & \vdots \\ \mathcal{L}_{\boldsymbol{\lambda}^{n_{\kappa_z}}\boldsymbol{u}^1} & \dots & \mathcal{L}_{\boldsymbol{\lambda}^{n_{\kappa_z}}\boldsymbol{u}^{n_{\kappa_z}}} & \mathcal{L}_{\boldsymbol{\lambda}^{n_{\kappa_z}}\boldsymbol{m}} & \mathcal{L}_{\boldsymbol{\lambda}^{n_{\kappa_z}}\boldsymbol{\lambda}^1} & \dots & \mathcal{L}_{\boldsymbol{\lambda}^{n_{\kappa_z}}\boldsymbol{\lambda}^{n_{\kappa_z}}} \end{pmatrix} \begin{pmatrix} \delta\boldsymbol{u}^1 \\ \vdots \\ \delta\boldsymbol{u}^{n_{\kappa_z}} \\ \delta\boldsymbol{m} \\ \delta\boldsymbol{\lambda}^1 \\ \vdots \\ \delta\boldsymbol{\lambda}^{n_{\kappa_z}} \end{pmatrix} = - \begin{pmatrix} \mathcal{L}_{\boldsymbol{u}^1} \\ \vdots \\ \mathcal{L}_{\boldsymbol{u}^{n_{\kappa_z}}} \\ \mathcal{L}_{\boldsymbol{m}} \\ \mathcal{L}_{\boldsymbol{\lambda}^1} \\ \vdots \\ \mathcal{L}_{\boldsymbol{\lambda}^{n_{\kappa_z}}} \end{pmatrix} \tag{5.75}$$

where the blocks in the matrix above are also matrices of the second derivatives of the Lagrangian with the subscripts $\boldsymbol{u}^l$ referring to $\hat{E}_z^l$ and $\hat{H}_z^l$ with all combinations given in (5.36) – (5.74), and the subscripts $\boldsymbol{\lambda}^l$ referring to λ_E^l and λ_H^l with all possible combinations given by the same set of equations. Therefore, we can identify transposed terms, and terms that are null, so that the system above results in:

$$\begin{pmatrix} \mathcal{L}_{\boldsymbol{u}^1\boldsymbol{u}^1} & \dots & \mathcal{L}_{\boldsymbol{u}^1\boldsymbol{u}^{n_{\kappa_z}}} & \mathcal{L}_{\boldsymbol{u}^1\boldsymbol{m}} & \mathcal{L}_{\boldsymbol{u}^1\boldsymbol{\lambda}^1} & 0 & 0 \\ \vdots & \vdots & \vdots & \vdots & 0 & \ddots & 0 \\ \mathcal{L}^T_{\boldsymbol{u}^1\boldsymbol{u}^{n_{\kappa_z}}} & \dots & \mathcal{L}_{\boldsymbol{u}^{n_{\kappa_z}}\boldsymbol{u}^{n_{\kappa_z}}} & \mathcal{L}_{\boldsymbol{u}^{n_{\kappa_z}}\boldsymbol{m}} & 0 & 0 & \mathcal{L}_{\boldsymbol{u}^{n_{\kappa_z}}\boldsymbol{\lambda}^{n_{\kappa_z}}} \\ \mathcal{L}^T_{\boldsymbol{u}^1\boldsymbol{m}} & \dots & \mathcal{L}^T_{\boldsymbol{u}^{n_{\kappa_z}}\boldsymbol{m}} & \mathcal{L}_{\boldsymbol{m}\boldsymbol{m}} & \mathcal{L}_{\boldsymbol{m}\boldsymbol{\lambda}^1} & \dots & \mathcal{L}_{\boldsymbol{m}\boldsymbol{\lambda}^{n_{\kappa_z}}} \\ \mathcal{L}^T_{\boldsymbol{u}^1\boldsymbol{\lambda}^1} & 0 & 0 & \mathcal{L}^T_{\boldsymbol{m}\boldsymbol{\lambda}^1} & 0 & \dots & 0 \\ 0 & \ddots & 0 & \vdots & \vdots & \ddots & \vdots \\ 0 & 0 & \mathcal{L}^T_{\boldsymbol{u}^{n_{\kappa_z}}\boldsymbol{\lambda}^{n_{\kappa_z}}} & \mathcal{L}^T_{\boldsymbol{m}\boldsymbol{\lambda}^{n_{\kappa_z}}} & 0 & \dots & 0 \end{pmatrix} \begin{pmatrix} \delta\boldsymbol{u}^1 \\ \vdots \\ \delta\boldsymbol{u}^{n_{\kappa_z}} \\ \delta\boldsymbol{m} \\ \delta\boldsymbol{\lambda}^1 \\ \vdots \\ \delta\boldsymbol{\lambda}^{n_{\kappa_z}} \end{pmatrix} = - \begin{pmatrix} \mathcal{L}_{\boldsymbol{u}^1} \\ \vdots \\ \mathcal{L}_{\boldsymbol{u}^{n_{\kappa_z}}} \\ \mathcal{L}_{\boldsymbol{m}} \\ \mathcal{L}_{\boldsymbol{\lambda}^1} \\ \vdots \\ \mathcal{L}_{\boldsymbol{\lambda}^{n_{\kappa_z}}} \end{pmatrix}. \tag{5.76}$$

The next step in the solution of the inverse problem using a PDE-constrained optimization approach is to solve the above system for $\delta\boldsymbol{u}^1, \dots, \delta\boldsymbol{u}^{n_{\kappa_z}}, \delta\boldsymbol{m}, \delta\boldsymbol{\lambda}^1, \dots, \delta\boldsymbol{\lambda}^{n_{\kappa_z}}$ and use the solution as a search direction for the new update.

5.4.2 Essentials of the SQP method

Sequential Quadratic Programming (SQP) methods solve the nonlinearly constrained minimization problem using a sequence of Quadratic Programming (QP) subproblems. In the QP subproblem the objective function is a quadratic approximation of the Lagrangian function in (5.3) (or in 5.23), subject to the linearization of the constraints of the original

problem. Therefore, the QP subproblem at an iterate $y_k = \{u_k, m_k\}$, λ_k is stated as:

$$\begin{aligned} &\min_y \mathcal{L}_q(y, y_k, \lambda_k) \\ &\text{subject to} \quad e_L(y, y_k) = 0, \end{aligned} \tag{5.77}$$

where $\mathcal{L}_q$ is the quadratic approximation to $\mathcal{L}$ at y_k:

$$\mathcal{L}_q(y, y_k, \lambda_k) = \mathcal{L}(y_k, \lambda_k) + (\nabla_y \mathcal{L})^T(y_k, \lambda_k)\delta y + \frac{1}{2}\delta y^T \nabla_y^2 \mathcal{L}(y_k, \lambda_k)\delta y, \tag{5.78}$$

and e_L is the linearization of the constraints e at y_k:

$$e_L(y, y_k) = e(y_k) + (\nabla_y e(y_k))^T \delta y. \tag{5.79}$$

Note that the constraints are included in the objective function ($\mathcal{L}_q$) for this equivalent problem and, in this formulation we only consider the equality PDE-constraints to simplify the presentation, however, the method allows to include both equality and inequality constraints in a similar way (see e.g. Boggs and Tolle, 1995; Nocedal and Wright, 1999). Although the optimal multipliers are not known, approximations λ_k to the multipliers can be maintained as part of the iterative process.

Iterations in SQP methods are distinguished in major and minor iterations. The major iterations generate a sequence of y_k, that satisfy the linear constraints and converge to a point y, which satisfies the nonlinear constraints and the first-order conditions for optimality. On the other hand, at each major iteration the solution of the QP subproblem is calculated through a sequence of minor iterations, and provides a new search direction.

SQP methods are particularly suitable to solve problems with nonlinear constraints. The reason is that using these methods neither the initial point nor the different points in the solution process need to be feasible, that is, need to satisfy all of the constraints. This is advantageous in problems with nonlinear constraints since in these cases finding a feasible point can be a difficult task. Additionally, SQP methods can be easily modified so that linear constraints are always satisfied.

On the other hand, SQP methods, like Newton's method and steepest descent, are only guaranteed to find a local solution of the optimization problem. An important issue of the method is to assure global convergence to this local minimum, that is to assure that, under suitable conditions, the method will converge to some local solution from any remote starting point.

The iterates generated by the QP subproblem (5.77) are identical to those generated by Newton's method when applied to the system composed of the KKT conditions and the constraints equations. This means that the SQP method would have theoretically, local convergence properties similar to Newton's method. However, the need for a globally convergent algorithm requires an approximation of the Hessian, $\nabla_x^2 \mathcal{L}$, that fulfills certain properties (see e.g. Boggs and Tolle, 1995), in spite of the convergence properties.

Let H_k be an approximation to $\nabla^2\mathcal{L}$ at the point (y_k, λ_k), we can rewrite the problem as:

$$\begin{aligned} &\min_{u,m} F_k + g_k^T \delta y + \frac{1}{2}\delta y^T H_k \delta y \\ &\text{subject to} \quad e_k + J_k^T \delta y = 0, \end{aligned} \tag{5.80}$$

where the subindex k indicates an evaluation at y_k, or at (y_k, λ_k) for the Hessian, and g is the gradient of the objective function, $\nabla_y F$, and J is the Jacobian, $\nabla_y e(y)$. Note that we applied that $\nabla_y e_k \delta y$ is constant.

Then, the first-order optimality conditions for the QP subproblem are:

$$g_k + H_k \delta y_k - J_k^T \pi_k = 0, \tag{5.81a}$$

$$e_k + J_k^T \delta y_k = 0, \tag{5.81b}$$

with δy_k the optimal point, and π_k the optimal multiplier of the QP subproblem (5.80) at the $k-th$ iteration. The solution δy_k is used to generate a new iterate y_{k+1}, by taking a step from y_k in the direction of δy_k. However, a new estimate of the multiplier λ_k is also required to continue to the next iteration. A possible choice is to use the optimal multipliers π_k of the QP subproblem as the new estimate λ_{k+1}. Then, the vectors δy_k and π_k can be identified with the solution of the Newton step (5.5) with $\pi_k = \lambda_{k+1}$.

Defining $\delta\lambda_k$ as $\delta\lambda_k = \pi_k - \lambda_k$, then:

$$\lambda_{k+1} = \pi_k = \lambda_k + \delta\lambda_k, \tag{5.82}$$

and substituting this expression and rearranging terms, the system of equations (5.81) becomes:

$$H_k \delta y_k - J_k^T \delta\lambda_k = -g_k + J_k^T \lambda_k, \tag{5.83a}$$

$$J_k^T \delta y_k = -e(y_k). \tag{5.83b}$$

The solution of this system for δy_k and $\delta\lambda_k$ is used to generate the new iterates, using a line search procedure to determine the steplength in the search directions. To decide if the step for the new iterate should be accepted, the line search method uses a merit function, ψ. The length of the step is modified so that the step from y_k to y_{k+1} reduces the value of ψ. If the merit function is properly chosen, the reduction implies that acceptable progress towards the solution is being made, and global convergence can be achieved.

In the unconstrained minimization a natural merit function is the objective function itself. Contrarily, in the constrained optimization, the merit function has to balance the drive to decrease the objective function with the need to satisfy the constraints, since the iterates are generally infeasible. This balance is often controlled by a parameter in ψ that weights a measure of the infeasibility against the value of either the objective function or the Lagrangian function (Boggs and Tolle, 1995).

Finally, the new iterates are used to evaluate the problem functions and derivatives and to calculate the prescribed choice of H_{k+1}.

The basic algorithm underlying the SQP method can be summarized as:

Algorithm 1 Local SQP algorithm (modified from Nocedal and Wright, 1999)

1: Choose an initial pair (y_0, λ_0); set $k \leftarrow 0$;
2: **repeat**
3: Evaluate $F(y_k)$, $g(y_k)$, $e(y_k)$, $J(y_k)$ and form $H(y_k, \lambda_k)$.
4: Solve the QP subproblem, (5.80), to obtain δy_k and π_k (or $\delta\lambda_k$);
5: Choose steplength α so that $\psi(y_k + \alpha\delta y_k) < \psi(y_k)$.
6: Set $y_{k+1} \leftarrow y_k + \alpha\delta y_k$ and $\lambda_{k+1} \leftarrow \pi_k$;
7: Set $k \leftarrow k + 1$;
8: **until** a convergence test is satisfied

5.4.3 SNOPT: A general-purpose large-scale SQP algorithm

SNOPT (Sparse Nonlinear OPTimizer; Gill et al., 2002, 2005) is an established general-purpose optimization software package which implements a SQP method for large-scale problems. In this thesis, we use the $7th$ version of SNOPT (Gill et al., 2006) through the COMSOL-MATLAB programming structure.

In the SQP method, SNOPT approximates the Hessian of the Lagrangian by a limited-memory quasi-Newton method and it uses a reduced-Hessian semidefinite QP solver for the QP subproblems. The algorithm accepts problems with general inequality constraints both linear and nonlinear, using an active-set strategy and includes several additional advanced techniques to deal, adaptively with specific problem features. Details on SNOPT implementation are fully described in Gill et al. (2005).

In this section, we expose briefly the basis of the different approximations implemented in SNOPT, following Gill et al. (2005) and Gill and Wong (2012). In some points the algorithm has more than one method to solve the problem; here we only describe the ones that are suitable for the characteristics of our problem.

Firstly, SNOPT uses a modified Lagrangian function associated with (5.77), given by:

$$\mathcal{L}(y, y_k, \lambda_k) = F(y) - \lambda_k^T (e(y) - \hat{e}_k(y)), \tag{5.84}$$

where $\hat{e}_k(y)$ denotes the vector of linearized constraints functions (state equations and other constraints), $\hat{e}_k(y) = e(y_k) + J(y_k)(y - y_k)$, and $e(y) - \hat{e}_k(y)$ is the departure from the linearity (Gill and Wong, 2012). Then the first and second derivatives from the modified Lagrangian are given by:

$$\nabla\mathcal{L}(y, y_k, \lambda_k) = g(y) - (J(y) - J(y_k))^T \lambda_k \tag{5.85a}$$

$$\nabla^2\mathcal{L}(y, y_k, \lambda_k) = \nabla^2 F(y) - \sum_{i=1}^{m} \lambda_{k,i} \nabla^2 e_i(y). \tag{5.85b}$$

The Hessian of the modified Lagrangian is independent of y_k and coincides with the Hessian of the conventional Lagrangian. Also, $\mathcal{L}(y, y_k, \lambda_k)|_{y=y_k} = F(y_k)$, and $\nabla\mathcal{L}(y, y_k, \lambda_k)|_{y=y_k} = g(y_k)$. Thus, the quadratic objective function in (5.80), defines also a local quadratic model at $y = y_k$ of this modified version of the Lagrangian.

The Hessian above is approximated ensuring positive definiteness, and it is updated using the BFGS quasi-Newton method:

$$H_{k+1} = H_k + \theta_k(\Delta L_k)(\Delta L_k)^T - \Gamma_k q_k q_k^T, \tag{5.86}$$

where

$$\begin{aligned}
\theta_k &= 1/(\Delta L_k)^T \Delta y_k, \\
\Gamma_k &= 1/q_k^T \Delta y_k, \\
q_k &= H_k \Delta y_k, \\
\Delta y_k &= y_{k+1} - y_k, \\
\Delta L_k &= \nabla\mathcal{L}(y_{k+1}, y_k, \pi) - \nabla\mathcal{L}(y_k, y_k, \pi).
\end{aligned}$$

When H_k is positive definite, H_{k+1} is positive definite if and only if the approximate curvature $(\Delta L_k)^T \Delta y_k$ is positive. Note that $\mathcal{L}$ is function of a π vector. There are several possibilities for this vector, for example the least-squares multipliers λ_k. However, SNOPT uses the updated multipliers π_{k+1} from the line search, because they result in short steps in the search and are available at no cost. Then, from the expression of $\nabla\mathcal{L}$ in (5.85a), ΔL_k results in:

$$\begin{aligned}
\Delta L_k &= \nabla\mathcal{L}(y_{k+1}, y_k, \pi_{k+1}) - \nabla\mathcal{L}(y_k, y_k, \pi_{k+1}) \\
&= g_{k+1} - g_k - (J_{k+1} - J_k)^T \pi_{k+1}.
\end{aligned} \tag{5.87}$$

In fact, the Hessian of the modified Lagrangian at the optimal point is only required to be positive definite on a subspace, and the approximate curvature, $(\Delta L_k)^T \Delta y_k$, can be negative or very small at points close to the optimal point. The program incorporates a criteria to decide if $(\Delta L_k)^T \Delta y_k$ is sufficiently positive, and it modifies the update when it is not (see Gill et al., 2005).

To treat the problems where the number of nonlinear variables is very large, SNOPT uses a limited-memory approach, in which H_k is not a result of k updates, but of a limited number of updates. Considering N the number of nonlinear variables, and let r and k denote two major iterations such that $r \leq k \leq r + p$, with p a preassigned value. At iteration k the Hessian is approximated by the BFGS method and can be expressed in terms of p updates to a positive-definite H_r:

$$H_k = H_r + \sum_{j=r}^{k-1} \left(\theta_j (\Delta L_j)(\Delta L_j)^T - \Gamma_j q_j q_j^T \right). \tag{5.88}$$

The quantities $\{\Delta L_j, q_j, \theta_j, \Gamma_j\}$ are stored for each j. During the major iteration k, the QP solver accesses H_k by requesting products of the form $H_k v$:

$$H_k v = H_r v + \sum_{j=r}^{k-1} \Big(\theta_j \Big((\Delta L_j)^T v\Big)(\Delta L_j) - \Gamma_j \Big(q_j^T v\Big) q_j\Big). \tag{5.89}$$

In SNOPT, the SQP structure is extended to incorporate general equality and inequality constraints and nonlinear constraints which are linearized. In the solution process, SNOPT estimates at each iteration a subset of constraints that are binding (are active) at a QP solution, the so-called working set, W. Then, it solves the QP subproblem imposing the constraints in the working set as equalities and all other constraints are ignored.

For the solution of the QP subproblem, SNOPT uses a reduced-Hessian method to obtain δy_k in the KKT system (5.81), with e_k all the constraints in the working set at the current iteration. Examining this system of equations, the part of the step δy_k in the range space of J_k^T is completely determined by the second block row $J_k^T \delta y_k = -e_k$. The Lagrangian Hessian, H_k, affects only the part of δy_k in the orthogonal subspace, namely the null-space of J_k (Nocedal and Wright, 1999). Then, using a reduced-Hessian technique, quasi-Newton methods (e.g. BFGS method) are applied to find approximations to only the part containing the Hessian.

The derivation of reduced-Hessian method passes by defining matrices Y_k and Z_k whose columns span the range space of J_k^T and the null-space of J_k, respectively. Then, the search direction, solution of (5.81) can be written as (Nocedal and Wright, 1999):

$$\delta y_k = Y_k p_y + Z_k p_z, \tag{5.90}$$

and substituting it in (5.81), the following system is obtained:

$$\Big(Z_k^T H_k Z_k\Big) p_z = -\Big(Z_k^T H_k Y_k\Big) p_y - Z_k^T g_k, \tag{5.91a}$$

$$(J_k Y_k)\, p_y = -e_k. \tag{5.91b}$$

The system above can be simplified dropping the cross term $\Big(Z_k^T H_k Y_k\Big) p_y$, yielding the simpler system:

$$\Big(Z_k^T H_k Z_k\Big) p_z = -Z_k^T g_k. \tag{5.92}$$

Removing the cross term is justified when $Z_k^T H_k Z_k$ is replaced by a quasi-Newton approximation, because the normal component p_y usually converges to zero faster than the tangential component p_z (Nocedal and Wright, 1999).

There are several possibilities to solve the above system with SNOPT, but because our system is very large we will use the CG method, which is applicable here since the QP Hessians, H_k, are by construction positive definite or semidefinite.

Once the QP solution is determined in a certain iteration, new estimates of a solution of the optimization problem are computed using a line search method and an augmented

Lagrangian merit function.

Finally, the convergence criteria for SNOPT is based on satisfying the first-order optimality conditions to within certain tolerances.

5.4.4 Synthetic examples

In this section we show the inversion results of two synthetic marine CSEM models obtained using a FE PDE-constrained optimization scheme and SNOPT solver package, described in the section above. Although SNOPT is a robust and efficient general-purpose program, we access it through the COMSOL-MATLAB programming structure as a black-box, which complicates to adequately tune performance to our particular problem. A more efficient application of the PDE-constrained optimization scheme could be built by using an open-source package since then the particular problem structure could be exploited. Further investigation opportunities in this direction will be discussed in Chapter 7. Nevertheless, it is insightful to develop a first implementation using SNOPT, to verify the applicability of a PDE-constrained optimization scheme to the 2.5-D CSEM inverse problem and to investigate its performance for this particular case.

As inversion data in the objective function we use the natural logarithm of amplitudes and the phases of the in-line electric field component E_x. The model parameter is the decadal logarithm, $\log_{10}$, of the conductivity. Inverting for the logarithm of the amplitudes instead of for the amplitudes directly, gives a better scaling of all data corresponding to different receivers, since amplitudes vary orders of magnitude with the distance to the source. To calculate correctly the phase misfit, taking into account periodicity we use the following expression:

$$\Phi_{E_x}^{obs} - \Phi_{E_x}^{syn} = -i \log\Big(\exp\Big(i\Big(\Phi_{E_x}^{obs}[\text{rad}] - \Phi_{E_x}^{syn}[\text{rad}]\Big)\Big)\Big).$$

In the examples presented in this section we do not include a regularization term in the objective function. A smoothing regularization function of the form of a gradient of the model parameter is singular at element interfaces when using a FE formulation with elementwise constant shape functions for the conductivity variable, thus it can not be directly incorporated in the objective function. A proposed solution is a reformulation in terms of a primal-dual FE formulation as developed in Schwarzbach and Haber (2013). However, we have not implemented it in this thesis to not over-complicate the problem in this first stage. In the following examples we use another strategy to deal with the ill-posedness of the inverse problem, consisting of the use of different meshes for the control variable (conductivity parameter variable) and for the state variables (variables solution of the modeling PDEs, $\hat{E}_z$ and $\hat{H}_z$). The main idea is to compute the EM fields in a suitable unstructured mesh that is finer in the vicinity of the sources and coarser with the distance, and to calculate the control variable in a coarser mesh, even regular if the initial geometry allows. Applying this strategy we model properly the fields on one hand, and on the other hand, we reduce the number of conductivity unknowns (elementwise conductivity)

reducing the ill-posedness of the problem and the computational time.

The communication between meshes is established defining a coupling operator. In our implementation we use a predefined coupling operator from COMSOL. It is defined in the control variable mesh (source map) and given the model parameter variable as argument. When the value of the coupling operator is required in some location within the state variable mesh (destination map), its argument is first evaluated in the source mesh and thereafter mapped to the destination mesh.

In the first example, we want to recover the spatial distribution of the conductivity for the canonical 2-D model, Figure 4.27, introduced in Chapter 4. Although we invert for the conductivity model parameter, in this section we show results of the resistivity (inverse of the conductivity), since the model in Figure 4.27 is given in resistivities.

The 'real' data is calculated first, modeling the EM fields in the 2-D canonical model. The mesh used for these computations is finer than the state variable mesh used for the inversion to avoid the inverse crime. The EM fields are excited by an $x-$directed horizontal electric dipole at $100m$ above the seafloor, and are calculated for three different horizontal positions of this transmitter: $x = -1km, 0$ and $1km$. For all the positions, the transmitter is located above the reservoir, which extends from $x = -3km$ to $3km$. The operating frequency is $0.25Hz$, a suitable frequency to resolve the $100\Omega \cdot m$ reservoir embedded in $1\Omega \cdot m$ sediments at $1km$ depth, below the seafloor. The receivers are located along an $x-$directed profile, extending from $-10km$ to $10km$, every $500m$, and on the seafloor (at $0.5m$ above the seafloor).

The initial model for the inversion is homogeneous, with a control variable value of 0.01, and with the air and the sea layers of the 'real' model. The size of the whole model where the fields are calculated is $60km \times 40km$ with center in $(0, 0)$, and the inversion domain, where the conductivity is a parameter coupled to the control variable in the control variable model, is $22km \times 4km$ and centered at $(0, -3km)$. The FE mesh for this model has 2624 elements, with 662 elements in the inversion domain, and the same mesh is used for all the wavenumber parameter values and for all the transmitter positions. Although in this thesis we have shown that the accuracy of the solution when modeling the EM fields depends on the mesh design, and this should be adapted to the different wavenumber parameter values and transmitter positions, this would further complicate the problem, so at present, in this example we consider a unique mesh for all these situations. The shape functions for the EM fields are quadratic Lagrange shape functions, which results in 5311 DOFs for $\hat{E}_z^l$ and 5311 DOFs for $\hat{H}_z^l$, for each wavenumber parameter value and for each transmitter position.

The model for the control variable has the size of the inversion domain in the state variables model, and a coarser mesh since it does not need to accommodate the variations of the fields closed to the source, but fine enough to resolve the thin, $100m$, reservoir. The total number of elements in this mesh is 582, and coincides with the number of DOFs of the control variable, since it is modeled with constant elementwise shape functions. To better constrain the inversion process, we give bounds to the control variable, an upper

bound $m^u = 1$, and a lower bound $m^l = -2$.

The PDE system of equations is assembled for a set of wavenumber parameter values and for the three transmitter positions, since we want a multi-experiment inversion using a PDE-constrained optimization. The set of wavenumber parameter values consists of 23 values distributed logarithmically from 1×10^{-4} to $5 \times 10^{-2} m^{-1}$ and 0. Taking into account the number of DOFs of the problem, for $\hat{E}_z$ and $\hat{H}_z$, for each wavenumber parameter value and for each frequency, the resulting FE system of linear equations is huge, with a total number of $(5311\hat{E}_z + 5311\hat{H}_z) \times 24\kappa_z \times 3T_x = 764784$ DOFs. Adding the DOFs associated to the control variable, 582, the total number of DOFs is 765366.

In each major iteration of the SQP solver, it is necessary to evaluate the gradient of the objective function, $\nabla_{\boldsymbol{m}} F(\boldsymbol{u}, \boldsymbol{m})$:

$$\nabla_{\boldsymbol{m}} F(\boldsymbol{u}, \boldsymbol{m}) = \frac{\partial F}{\partial \boldsymbol{m}} + \frac{\partial F}{\partial \boldsymbol{u}} \cdot \left(\frac{\partial \boldsymbol{e}}{\partial \boldsymbol{u}} \right)^{-1} \cdot \frac{\partial \boldsymbol{e}}{\partial \boldsymbol{m}}. \tag{5.93}$$

We use the adjoint method to calculate the gradient. This method introduces and defines an adjoint solution $\boldsymbol{u}^*$ as:

$$\boldsymbol{u}^* = \frac{\partial F}{\partial \boldsymbol{u}} \left(\frac{\partial \boldsymbol{e}(\boldsymbol{u})}{\partial \boldsymbol{u}} \right)^{-1}. \tag{5.94}$$

This expression is then multiplied in the RHS by the term $\partial \boldsymbol{e}/\partial \boldsymbol{u}$ and transposed, obtaining a single system of linear equations:

$$\left(\frac{\partial \boldsymbol{e}}{\partial \boldsymbol{u}} \right)^T \cdot \boldsymbol{u}^* = \frac{\partial F}{\partial \boldsymbol{u}}. \tag{5.95}$$

Then, the gradient of the objective function can be calculated solving this additional system of equations and substituting $\boldsymbol{u}^*$ with $(\partial F/\partial \boldsymbol{u})(\partial \boldsymbol{e}/\partial \boldsymbol{u})^{-1}$ in equation (5.93). Using MUMPS direct solver, this system can be solved at the cost of a back-substitution, since it is the transpose of the last linearization needed for solving the forward problem. The main inconvenience of using this strategy is that considering a PDE-constrained optimization scheme, our system matrix is huge and requires lot of memory, thus other strategies should be investigated.

In this first example, we set to stop the SNOPT optimization solver when it reaches an optimality tolerance of 1×10^{-3} with a maximum number of objective evaluations of 34. As mentioned before, the optimality tolerance is the level of accuracy to which we want the final iterate of SNOPT fulfill the first-order optimality conditions. Our choice for the values of these parameters is based on trial and error, after performing several tests and can still be improved upon.

Figure 5.1 displays the final resistivity model in the control variable and in the state variable meshes. The inversion program recovers the reservoir block in the correct position and approximately with the correct shape and resistivity of $100\Omega \cdot m$ with some lower values in some of the elements forming the reservoir. However, some small artifacts can

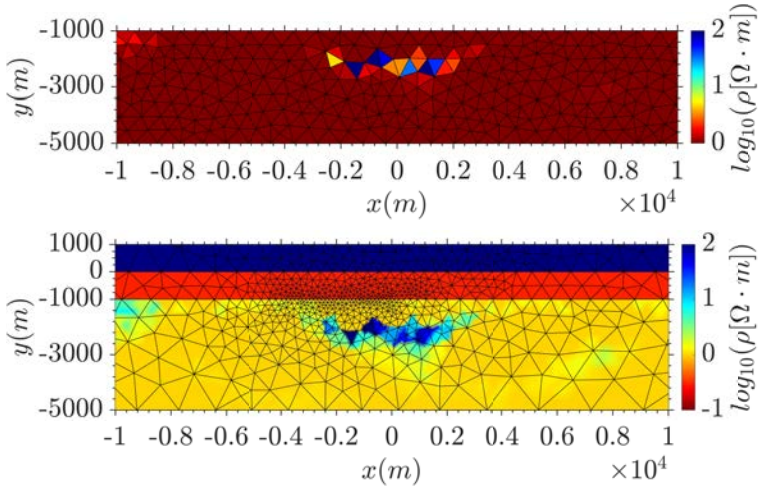

Figure 5.1: *Resistivity model ($log_{10}\rho(x,y)$) resulting from the inversion of the 2-D canonical model in-line electric field data. Top: Resistivity model in the model parameter (control variable) mesh. Bottom: Resistivity model in the mesh used for the electric field calculations. The model domain of the control variable coincides with the inversion domain. It is a $22km \times 4km$ rectangle centered at $x = 0, y = -3km$. The model domain where the electric field is calculated is larger, a $60 \times 40km$ rectangle, and includes the inversion domain and the sea and the air layers. The control variable mesh has 582 elements and the state variables mesh, 662 in the inversion domain and 2624 elements in total. Both meshes are fixed during the inversion process. The initial model was homogeneous, with $0.9772\Omega \cdot m$, and with the air and the sea layers, and we inverted for the E_x amplitude and phase data corresponding to three different transmitter locations, at $x = -1000m, 0$ and $1000m$ and $y = -900m$, and operating at a $0.25Hz$, with receivers along the $x-$axis from $-10km$ to $10km$, every $500m$ and on the seafloor. The results have been obtained without a regularization function. Information of the quality of the results is given in Figure 5.3.*

be observed in the LHS of the model, below the receivers.

The corresponding amplitude and phase of the 'real' in-line electric field data together with the inversion predicted data for the three different experiments with different transmitter positions are plotted in Figure 5.2 as a function of the receivers positions. According to the plots, the mismatch is small in both amplitudes and phases, and for all three experiments, however, it is notable in the phases for large offsets, at receivers located at distances larger than approximately $7km$ to the source.

Information of the optimization process and of the quality of the solution is given in Figure 5.3 where the evolution of the objective function value and of the error with the number of major iterations is provided. This error is an estimate of the degree of non-optimality; further details can be found in (Gill et al., 2006). The same Figure illustrates the number of minor iterations in each major iteration as bar graph.

Observing the evolution of the objective function, it is between the second and the third major iterations that the decay is stronger. It passes from a value of 22 to a value of 6. In the next iterations, the decay continues but with a smoother slope. The decay behavior changes again after the $8th$ major iteration, the slope gets smaller indicating a slow decrease of the objective function value. It passes from a value of 3.2 in the $8th$ major iteration to a value of 1.9 in the last iteration, the $31st$ one.

The evolution of the error with the major iterations is related to the one of the objective

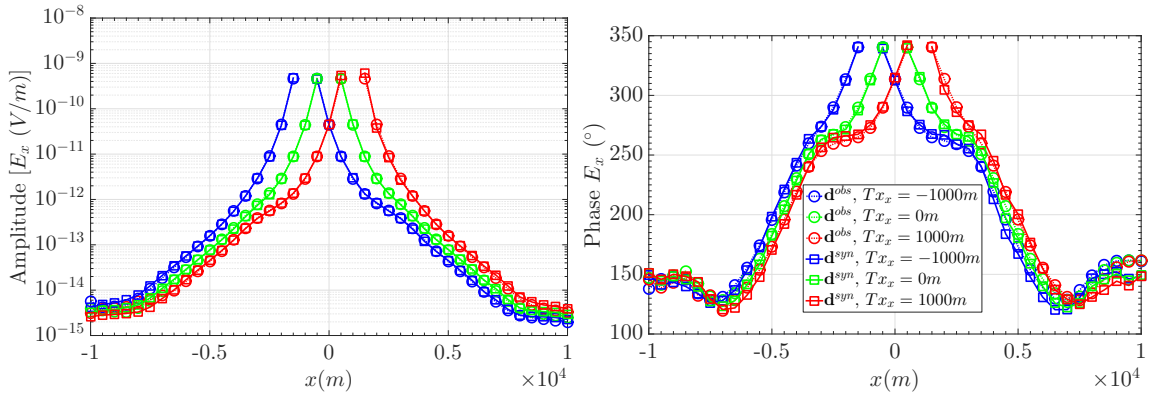

Figure 5.2: *'Real' data of the canonical 2-D model and data predicted by the inversion for three different positions of the transmitter. 'Observed' (circles) and predicted (squares) amplitudes (left) and phases (right) of the in-line electric field, E_x, as a function of the receiver locations, and for three different transmitter positions: $-1km$ (blue), 0 (green) and $1km$ (red).*

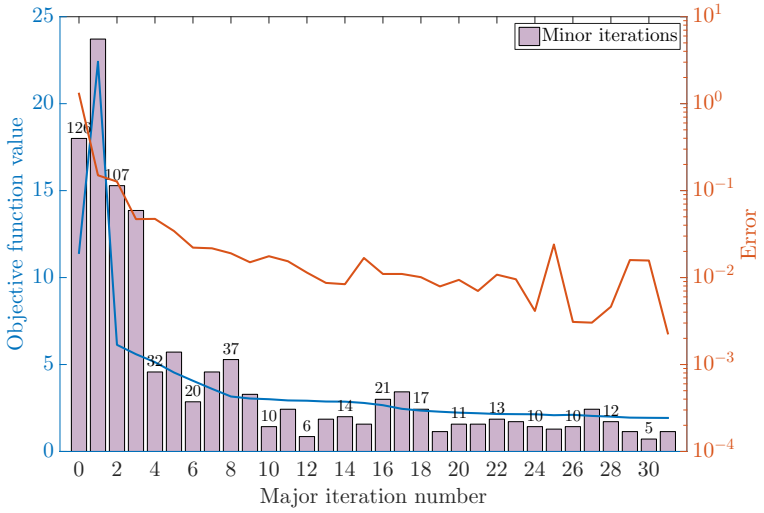

Figure 5.3: *Data from the PDE-constrained optimization process using SNOPT solver for the inversion of the 2-D canonical model electric field data. The left axis corresponds to the objective function value (blue) and the right axis to the first-order optimality error (orange), which are plotted as a function of the major iteration number. The bar graph plots the number of minor iterations required by the program to solve the QP subproblem at each major iteration.*

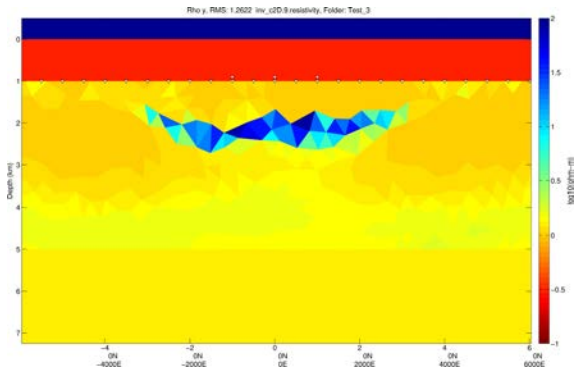

Figure 5.4: *Resistivity model resulting from the inversion of the 2-D canonical model in-line electric field data for three different transmitter positions, computed using MARE2DEM, a FE modeling program with an implementation of the well-established Occam's inversion method. To obtain these results we used the default parameters of MARE2DEM. We inverted for three sets of E_x amplitude and phase data corresponding to three different transmitter positions, at $-1km, 0$ and $1km$.*

function, thus it shows similar decay stages. It starts with a value of 1.3 which decreases to a value of 4.7×10^{-2} in the $3rd$ major iteration. Then the decay is smoother reaching a value of 2×10^{-3} at the last iteration.

These different phases of decay of the objective function and the error are also followed by the number of minor iterations. Initially, in each major iterations it is required a large number of minor iterations, around 100, to solve the QP subproblem and continue to the next major iteration. After the third major iteration, the number of minor iterations per major iteration is smaller, around 30, and it changes again for major iterations after the $8th$ with a number of minor iterations per major iteration between 20 and 5.

The required time to run this example was $41min$ and $52s$ with an INTEL i7 3.2 GHz quad-core processor and 16 GB RAM desktop computer, and the memory used was: $4.89GB$ of physical memory and $10.23GB$ of virtual memory. It is a high demand of computational resources for a simple model. Thus the inversion scheme should be improved investigating techniques to reduce the memory required to solve the problem and consequently to improve the time efficiency.

Finally, we have calculated the solution of the inverse problem for this example using the extensively tested MARE2DEM program (Key and Ovall, 2011; Key, 2012), with the goal to verify qualitatively the validity of our solution. The resulting resistivity model is plotted in Figure 5.4 and it is very similar to the one we obtained using SNOPT (Figure 5.1).

The inversion algorithm MARE2DEM implements the well-established Occam's method (Key, 2012), which does not solve the PDE-constrained optimization problem directly. It would be interesting to compare the different performance between the inversion scheme of MARE2DEM and the one under study, however because of the big differences already on the problem formulation, it is not a trivial task, and we consider it out of the scope of this thesis.

As a second example, we invert data from a marine model represented in Figure 5.5. It

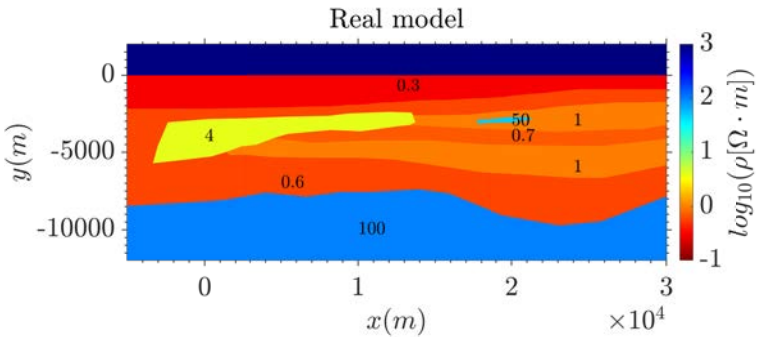

Figure 5.5: *Marine resistivity model with bathymetry and with two bodies, with resistivities of* $4\Omega \cdot m$ *and* $50\Omega \cdot m$*, embedded in a stratified media with more conductive materials. This model is taken from the example model included in the MARE2DEM open source and freely available version program. The color scale is the logarithm of the resistivity and the numbers in the image are the resistivity in* $\Omega \cdot m$*.*

consists in a model with an air layer and a sea layer, with bathymetry and with a stratified subseafloor of $1, 0.7$ and $0.6\Omega \cdot m$, where two bodies with larger resistivities of $4\Omega \cdot m$ and $50\Omega \cdot m$ are embedded at approximately $1 - 2km$ below the seafloor. The model has also a $100\Omega \cdot m$ basement, which is only possible to resolve with MT. This model is taken from the example given in the freely available version of MARE2DEM[1]. It is designed to test the program for both CSEM and MT methods, independently and jointly. Here, we use it only for CSEM, thus it is not possible with an inversion to recover the entire model structures, because the method is not sensitive to all of them. However, we use it to validate our inversion scheme and to check that although not recovering the complete model, our result is similar to the one of MARE2DEM.

As in the example before, we invert for the natural logarithm of the amplitudes and for the phases of the in-line electric field component, and the model parameter is also logarithmic conductivity. The 'real' data we use in the inversion is calculated importing the model (Figure 5.5) given in the MARE2DEM package to our program, and using a different mesh (finer) than the one we will use in the inversion. This data is calculated for eight experiments, with four different transmitter positions, at $(0, -2140)$, $(5208.33, -2053.79)$, $(10416.67, -1855.01)$ and $(15625, -1586.17)m$, and for two different frequencies of 0.25 and $0.75Hz$. The transmitter is, as in the example above, an in-line horizontal electric dipole, and the receivers are located on the seafloor, following the bathymetry, every $1km$ from $x = 1km$ to $x = 25km$.

The initial model is an homogeneous model with $\log_{10} \sigma_0 = 1 \times 10^{-3}$, and with the air and sea layers, and the bathymetry of the 'real' model. We use again different meshes and models for the state variables and for the control variable. The model of the state variables contain the entire initial model, and the size of the whole model is $200km \times 200km$, centered in $(0, 0)$. In this model the inversion domain is defined as a polygon enclosing the area comprised between $x = 0$ to $x = 25km$, and $y = -10km$ to $y \approx -2.2km$ on the LHS, and $y = -10km$ to $y \approx -0.93km$ on the RHS of the domain, with the upper horizontal boundary

[1] MARE2DEM version downloaded in 2015 from `http://mare2dem.ucsd.edu/`

coinciding with the bathymetry of the model. The model for the control variable is just the area defined by this polygon.

The number of elements of the state variable mesh is 8490, with 2896 elements meshing the inversion domain. This same mesh is used for all the wavenumbers, frequencies and transmitter positions, and it is fixed during the inversion process. The number of DOFs, using quadratic Lagrange shape functions, is 17053 for $\hat{E}_z$ and 17053 for $\hat{H}_z$, for each wavenumber, frequency and transmitter position.

The mesh of the control variable has 2724 elements. It is not much coarser than the mesh of the inversion domain in the state variable mesh because the control variable model also includes the bathymetry, which requires a fine meshing. The control variable is discretized using constant elementwise shape functions, hence the number of DOFs is the same as the number of elements: 2724. We also include bounds to the control variable in the optimization process, with an upper bound of $m^u = 1$ and a lower bound of $m^l = -2$.

The wavenumber parameter, κ_z, values are the same as in the previous model, thus the total number of DOFs are: $(17053\hat{E}_z + 17053\hat{H}_z) \times 24\kappa_z \times 4T_x \times 2freq. = 6548352$ DOFs. If we add the number of DOFs of the control variable, the total number is 6551076. Thus the system matrix of the state equations is huge, and lot of memory will be required to operate with it.

The inversion parameter settings are an optimality tolerance of 1×10^{-4} and a maximum number of objective function evaluations of 200.

Figure 5.6 displays the resistivity model resulting from the inversion in the control variable and in the state variable meshes. The inversion recovers the two resistive bodies, the big and the small one, and with approximately the correct value of resistivity, slightly overestimated in the big body, and underestimated in the small body. It also finds a more conductive sediment above and below the small body, with a resistivity smaller than $1\Omega\cdot m$, and between the two bodies, coinciding with the structure in the 'real' model.

The 'observed' and predicted amplitude and phase data associated to these models is plotted in Figure 5.7 for the different transmitter positions and for the two different frequencies. Qualitatively, the amplitude mismatch between the 'observed' and the predicted data is acceptable for all transmitters and frequencies. On the other hand, the phase mismatch is acceptable for the $0.25Hz$ frequency, but a bit too large for the phases at $0.75Hz$ frequency and for large offsets, although it does not seem to affect significantly the resistivity model result.

Figure 5.8 displays the evolution of the objective function value and of the error with the number of major iterations, and the number of minor iterations in each major iteration for this inversion example. Initially, the objective function value is about 8 and in the next iterations oscillate between 8 and 4. In the $4th$ major iteration, the objective function value starts to grow reaching a value of 20 at the $7th$ iteration, that does not decay significantly until the $11th$ iteration to a value of 18, and to a value of about 2 in the $12th$ iteration. In the next major iterations, the decrease of the objective function value continues, but more slowly and it is 0.2 in the last iteration, the $53rd$.

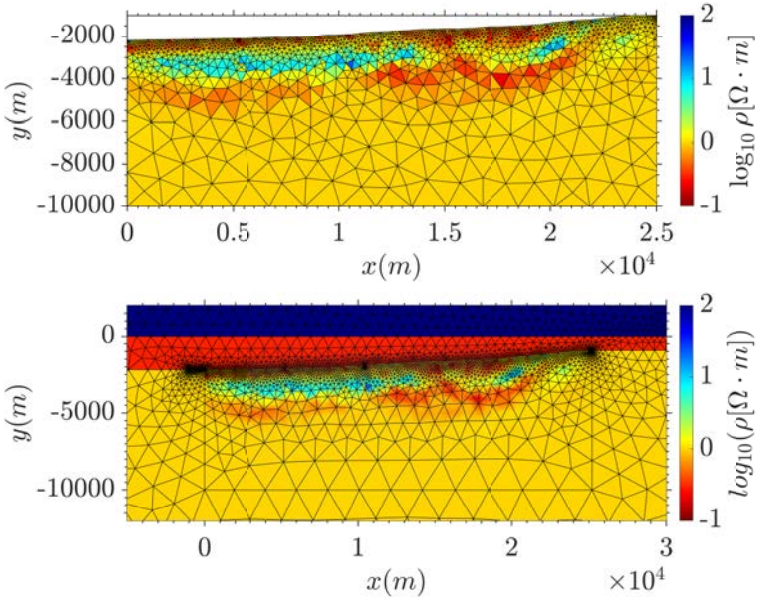

Figure 5.6: *Resistivity model ($log_{10}\rho(x,y)$) resulting from the inversion of the in-line electric field data for the marine model in Figure 5.5, for eight sets of data corresponding to four transmitter positions and two frequencies. Top: Resistivity model in the model parameter (control variable) mesh. Bottom: Resistivity model in the mesh used for the electric field calculations. The model domain of the control variable coincides with the inversion domain in the electric field model. It is a polygon enclosing the area comprised between $x = 0$ to $x = 25km$, and $y = -10km$ to $y \approx -2.2km$ on the LHS, and $y = -10km$ to $y \approx -0.93km$ on the RHS of the domain, with the upper horizontal boundary coinciding with the bathymetry of the model. The model domain where the electric field is calculated is larger than the domain of the control variable, it is a $200km \times 200km$ square, and includes the inversion domain and an air and a sea layers. The control variable mesh has 2724 elements and the state variables mesh, 2896 in the inversion domain and 8490 elements in total. Both meshes are fixed during the inversion process. The initial model was homogeneous, with $0.9977\Omega \cdot m$ ($\log_{10}\sigma_0 = 1 \times 10^{-3}$), and with the air and the sea layers, and we inverted for the E_x amplitude and phase data corresponding to four different transmitter locations, at $(x,y) = (0,-2140),(5208.33,-2053.79),(10416.67,-1855.01)$ and $(15625,-1586.17)m$, and for two frequencies of 0.25 and $0.75Hz$, with receivers along the $x-$axis from $1km$ to $25km$, every $1km$, and on the seafloor following the bathymetry. The results have been obtained without a regularization function. Information of the quality of the results is given in Figure 5.8.*

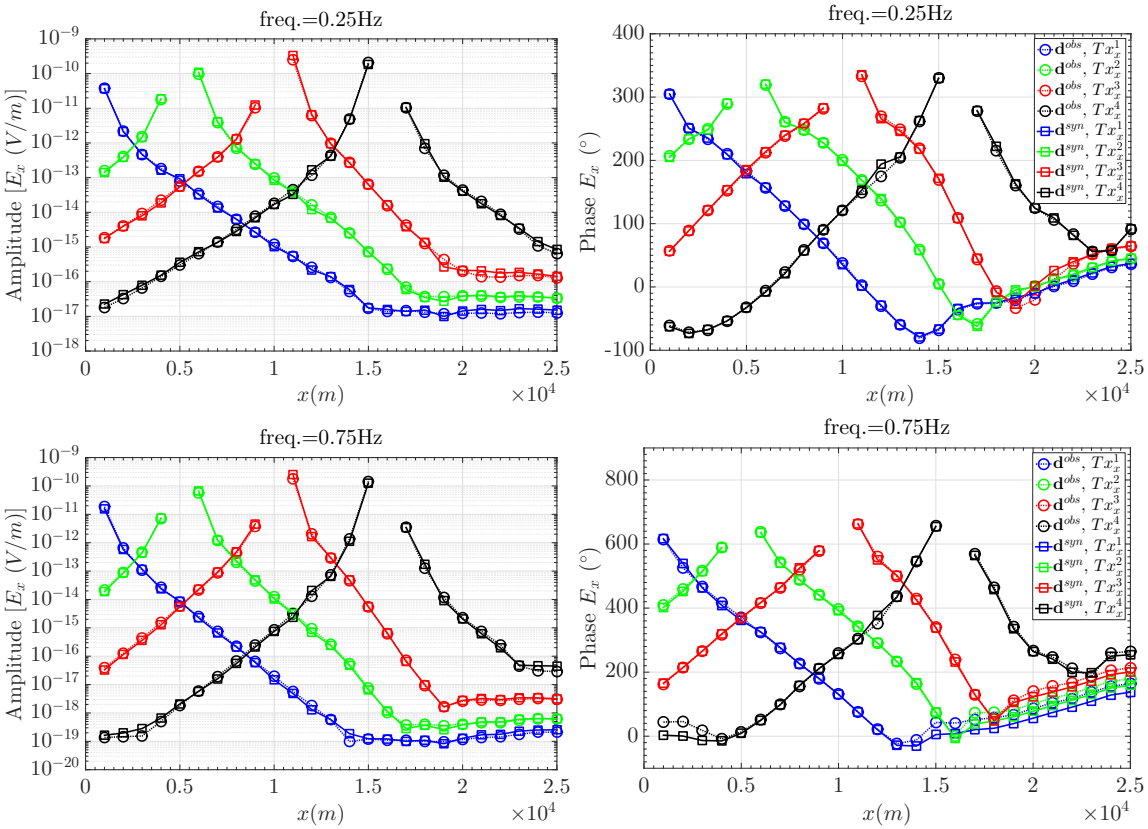

Figure 5.7: *'Real' data of the marine model in Figure 5.5 and data predicted by the inversion for four different positions of the transmitter and for two different frequencies. 'Observed' (circles) and predicted (squares) amplitudes (left) and phases (right) of the in-line electric field E_x as a function of the receiver locations, and for four different transmitter positions, $Tx_x^1 = (0, -2140), Tx_x^2 = (5208.33, -2053.79), Tx_x^3 = (10416.67, -1855.01)$ and $Tx_x^4 = (15625, -1586.17)m$, and for two different frequencies, $0.25Hz$ (top) and $0.75Hz$ (bottom).*

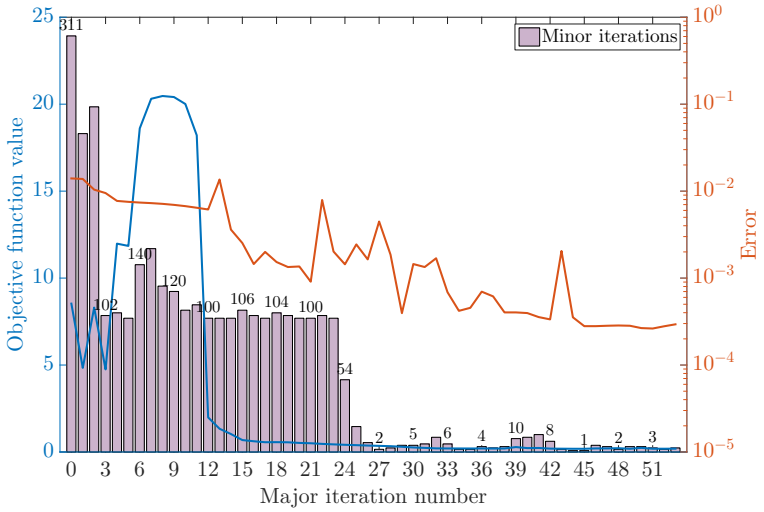

Figure 5.8: *Data from the PDE-constrained optimization process using SNOPT solver for the inversion of the electric field data of the marine model in Figure 5.5. The left axis corresponds to the objective function value (blue) and the right axis to the first-order optimality error (orange), which are plotted as a function of the major iteration number. The bar graph plots the number of minor iterations required by the program to solve the QP subproblem at each major iteration.*

The decay of the error has a more constant slope, it starts with a value of 1×10^{-2} and it is 2.9×10^{-4} at the final major iteration.

Observing the evolution of the number of minor iterations with the major iterations, we can distinguish three phases. At the beginning, and in the first two major iterations the number of minor iterations per major iteration is approximately between 200 and 300. This phase coincides with the initial oscillations of the objective function value. A second phase occurs between the $3rd$ and the $23rd$ major iterations, with about 100 minor iterations per major iteration, without an appreciable relation with the objective function value. Finally, the third phase is between the $24th$ major iteration and the final one, with a small number of minor iterations per major iteration, between 1 and 13. This behavior of the number of minor iterations coincides with the small variations behavior of the objective function values at these last major iterations.

The time to run this example was $19h22m3s$ with an INTEL i7 3.2 GHz quad-core processor and 32 GB RAM desktop computer, and the memory used was: $26.18GB$ of physical memory and $34.77GB$ of virtual memory. Both time and memory are very high since in this inversion scheme we introduce all the equations for all wavenumbers, frequencies and transmitters in the same matrix.

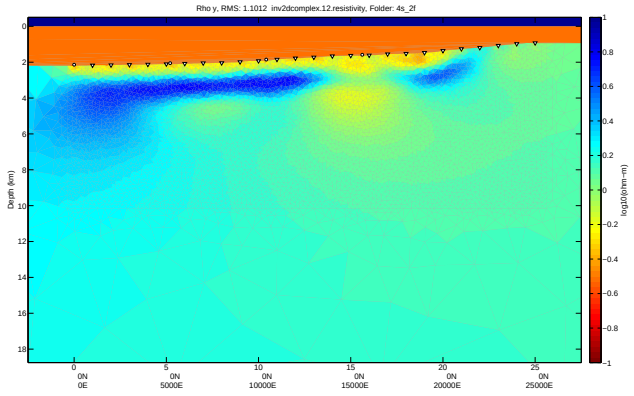

Figure 5.9: *Resistivity model resulting from the inversion of the in-line electric field data for the marine model in Figure 5.5, using MARE2DEM, a FE modeling program with an implementation of the well-established Occam's inversion method. To obtain these results we used the default parameters of MARE2DEM. We inverted for eight sets of E_x amplitude and phase data corresponding to four different transmitter positions along the model and for two frequencies of 0.25 and $0.75Hz$.*

Finally, in Figure 5.9 we show the resistivity model obtained from solving the inverse problem of this example with MARE2DEM. We observe a similar solution to the one we showed in Figure 5.6, but smoother since MARE2DEM uses a regularization functional. The recovered model shows the two resistive bodies and a more conductive region in the sediments between them, and above the small resistive body.

5.5 Optimize-discretize 2.5-D CSEM constrained optimization

In the previous section we have derived a formulation for the constrained optimization problem in the full-space following a *discretize-optimize* strategy, that is starting with the discretized state equations and variables and then deriving the first-order optimality conditions and the Newton's step for the Lagrangian. We have also described a first implementation of this scheme using the COMSOL-MATLAB programming structure and SNOPT optimization solver.

Our next goal is to investigate a FE *all-at-once* approach formulation that should open the possibility to implement an inversion code with adaptive FE meshes for the state and control variables. Advantages of a program implementing this formulation would be, on one hand, a significant reduction of the numerical effort needed to solve the inverse problem, and on the other hand, to better pose the problem by choosing a discretization mesh coarser where we lack information in the control variable mesh or where a fine mesh is not required for accuracy in the state variable mesh (Bangerth, 2008).

To derive such a formulation we consider an *optimize-discretize* approach, because with a *discretize-optimize* approach, as already presented in this chapter, the discretization can not be changed by adapting the FE mesh between nonlinear iterations, and the potential to reduce the numerical cost by taking into account the spatial structure of the solutions is lost. The explanation is that a change in the discretization changes the size of the finite dimensional problems, and then, norms used to estimate the error in adaptive mesh refinement techniques, become meaningless (Bangerth, 2008).

The *optimize-discretize* approach, derives all the optimization problem in continuous function spaces before discretizing it into numerical systems. This strategy gives more flexibility in discretizing as iterations in the optimization process advance and resolve all scaling issues related to different mesh sizes (Bangerth, 2008).

The use of adaptive FE meshes in a PDE constrained optimization scheme is a very recent area of research. To formulate the basic problem, we have followed the mathematical works of Bangerth (2002, 2008); Günther (2010) and the works on applications of Joshi et al. (2004); Bangerth and Joshi (2008); Wang et al. (2013). To derive the inverse problem in a variational form, we have also followed the work of Petra and Stadler (2011).

In this section, we first formulate the Lagrangian optimization problem with PDE constraints for the 2.5-D CSEM PDEs in variational form, and second, we discretize the Newton step using FE on independent meshes.

5.5.1 State equations

To derive the formulation of the constrained optimization problem for the 2.5-D CSEM data, we start with the strong form of the 2.5-D CSEM PDEs for the isotropic problem (2.15). To formulate the problem we need to include the overall set of PDEs corresponding to the set of κ_z parameter values, $\{\kappa_z^l\}$, with $l = 1,\ldots,n_{\kappa_z}$, used in the Fourier inverse

transform.

Without loss of generality but for sake in exposition, we consider a single experiment, with the transmitter at a single position ($i = 1$) and operating at a single frequency ($k = 1$). Additionally, as in the section above, we suppose a particular case of a $x-$directed HEPD transmitter. Then, for each κ_z^l, the state equations are:

$$-\nabla\cdot\left(\hat{y}(\kappa_e^l)^{-2}\nabla\hat{E}_z^l\right) - i\kappa_z^l\nabla\cdot\left((\kappa_e^l)^{-2}\mathbf{R}\nabla\hat{H}_z^l\right) + \hat{y}\hat{E}_z^l = +i\kappa_z^l\nabla\cdot\left((\kappa_e^l)^{-2}\hat{\mathbf{J}}_t^s\right) \tag{5.96a}$$

$$-\nabla\cdot\left(\hat{z}(\kappa_e^l)^{-2}\nabla\hat{H}_z^l\right) + i\kappa_z^l\nabla\cdot\left((\kappa_e^l)^{-2}\mathbf{R}\nabla\hat{E}_z^l\right) + \hat{z}\hat{H}_z^l = -\hat{z}\nabla\cdot\left((\kappa_e^l)^{-2}\mathbf{R}\hat{\mathbf{J}}_t^s\right) \quad \text{in } \Omega \tag{5.96b}$$

$$\hat{E}_z^l, \hat{H}_z^l = 0 \text{ on } \partial\Omega, \tag{5.96c}$$

where

$$\hat{z} = i\mu_0\omega, \quad \hat{y} = \sigma, \quad (\kappa_e^l)^{-2} = \left((\kappa_z^l)^2 + \hat{z}\hat{y}\right)^{-1}, \quad \nabla = (\partial_x, \partial_y), \quad \hat{\mathbf{J}}_t^s = (\hat{J}_x^s, 0), \quad \mathbf{R} = \begin{pmatrix} 0 & -1 \\ 1 & 0 \end{pmatrix}.$$

The equations above can be rewritten in a more compact form as:

$$-\nabla\cdot(C_E^l\nabla\hat{E}_z^l) - \nabla\cdot(\boldsymbol{D}^l\nabla\hat{H}_z^l) + \hat{y}\hat{E}_z^l = \nabla\cdot(\boldsymbol{D}^l\boldsymbol{R}^T\hat{\mathbf{J}}_t^s) \tag{5.97a}$$

$$-\nabla\cdot(C_H^l\nabla\hat{H}_z^l) + \nabla\cdot(\boldsymbol{D}^l\nabla\hat{E}_z^l) + \hat{z}\hat{H}_z^l = -\nabla\cdot(C_H^l\mathbf{R}\hat{\mathbf{J}}_t^s), \tag{5.97b}$$

where

$$\begin{aligned} C_E^l &= C_E^l(\kappa_z^l, \sigma, \omega) = \hat{y}(\kappa_e^l)^{-2}, \\ C_H^l &= C_H^l(\kappa_z^l, \sigma, \omega) = \hat{z}(\kappa_e^l)^{-2}, \\ \boldsymbol{D}^l &= \boldsymbol{D}^l(\kappa_z^l, \sigma, \omega) = i\kappa_z^l(\kappa_e^l)^{-2}\boldsymbol{R}. \end{aligned}$$

5.5.2 Variational form

In Chapter 2 we derived the variational or weak form for the equations above (equation 2.50); here, we write them for a particular case of a $x-$directed HEPD transmitter, for a κ_z^l parameter value, and using the variables C_E^l, C_H^l and $\boldsymbol{D}^l$ defined above:

$$\int_\Omega \left(\nabla\vec{v}_1^l\cdot(C_E^l\nabla\hat{E}_z^l) + \nabla\vec{v}_1^l\cdot(\boldsymbol{D}^l\nabla\hat{H}_z^l) + \vec{v}_1^l\hat{y}\hat{E}_z^l\right)d^2r = -\int_\Omega \nabla\vec{v}_1^l\cdot(\boldsymbol{D}^l\boldsymbol{R}^T\hat{\mathbf{J}}_t^s)d^2r \tag{5.98a}$$

$$\int_\Omega \left(\nabla\vec{v}_2^l\cdot(C_H^l\nabla\hat{H}_z^l) - \nabla\vec{v}_2^l\cdot(\boldsymbol{D}^l\nabla\hat{E}_z^l) + \vec{v}_2^l\hat{z}\hat{H}_z^l\right)d^2r = \int_\Omega \nabla\vec{v}_2^l\cdot(C_H^l\mathbf{R}\hat{\mathbf{J}}_t^s)d^2r, \tag{5.98b}$$

where the variables $\hat{E}_z^l, \hat{H}_z^l$ and the test functions v_1^l, v_2^l are from the space $\mathcal{H}^l \subset \mathcal{H} = [H_0^1(\Omega)]^2$, the Sobolev space of functions with square integrable first-order weak derivatives in Ω, and that vanish in the outer boundary $\partial\Omega$. We can rewrite the equations above

in a more compact form, with $(\cdot,\cdot)$ denoting the $L^2(\Omega)$ inner product (equation 2.38):

$$(C_E^l \nabla \hat{E}_z^l, \nabla v_1^l) + (\boldsymbol{D}^l \nabla \hat{H}_z^l, \nabla v_1^l) + (\hat{y}\hat{E}_z^l, v_1^l) = -(\boldsymbol{D}^l \boldsymbol{R}^T \hat{\mathbf{J}}_t^s, \nabla v_1^l) \tag{5.99a}$$

$$(C_H^l \nabla \hat{H}_z^l, \nabla v_2^l) - (\boldsymbol{D}^l \nabla \hat{E}_z^l, \nabla v_2^l) + (\hat{z}\hat{H}_z^l, v_2^l) = (C_H^l \mathbf{R}\hat{\mathbf{J}}_t^s, \nabla v_2^l), \tag{5.99b}$$

or

$$A_E^l(\kappa_z^l; \sigma; [\hat{E}_z^l, \hat{H}_z^l])(v_1^l) = 0, \tag{5.100a}$$

$$A_H^l(\kappa_z^l; \sigma; [\hat{E}_z^l, \hat{H}_z^l])(v_2^l) = 0, \tag{5.100b}$$

with

$$A_E^l(\kappa_z^l; \sigma; [\hat{E}_z^l, \hat{H}_z^l])(v_1^l) = (C_E^l \nabla \hat{E}_z^l, \nabla v_1^l) + (\boldsymbol{D}^l \nabla \hat{H}_z^l, \nabla v_1^l) + (\hat{y}\hat{E}_z^l, v_1^l) + (\boldsymbol{D}^l \boldsymbol{R}^T \hat{\mathbf{J}}_t^s, \nabla v_1^l) \tag{5.101a}$$

$$A_H^l(\kappa_z^l; \sigma; [\hat{E}_z^l, \hat{H}_z^l])(v_2^l) = (C_H^l \nabla \hat{H}_z^l, \nabla v_2^l) - (\boldsymbol{D}^l \nabla \hat{E}_z^l, \nabla v_2^l) + (\hat{z}\hat{H}_z^l, v_2^l) - (C_H^l \mathbf{R}\hat{\mathbf{J}}_t^s, \nabla v_2^l), \tag{5.101b}$$

where the semilinear forms A_E^l and A_H^l are nonlinear in their first set of arguments, but are linear in the test functions, and include partial differential operators and inhomogeneous forcing terms (transmitter terms).

5.5.3 Problem statement

The PDE-constrained optimization problem (5.1) can be stated as:

$$\text{minimize} \quad F(\{\hat{E}_{z,ik}^l, \hat{H}_{z,ik}^l\}, m) = \left(\sum_{k=1}^{n_f} \eta_k \sum_{i=1}^{n_s} \sum_{j=1}^{n_r} \frac{1}{2} \left\| W_{ijk}^d \left(\left(PO\left(\left\{ \hat{E}_{z,ik}^l, \hat{H}_{z,ik}^l \right\} \right) \right)_{ijk} - d_{ijk}^{obs} \right) \right\|^2 \right) + \frac{\beta}{2} \|R(m - m_{ref})\|^2,$$

$$\text{subject to} \quad A_{E,ik}^l(\kappa_z^l; m; [\hat{E}_{z,ik}^l, \hat{H}_{z,ik}^l])(v_{1,ik}^l) = 0, \quad A_{H,ik}^l(\kappa_z^l; m; [\hat{E}_{z,ik}^l, \hat{H}_{z,ik}^l])(v_{2,ik}^l) = 0, \tag{5.102}$$
$$\forall v_{1,ik}^l, v_{2,ik}^l \in \mathcal{H}^{l,e}, \quad \text{and for} \quad l = 1, \ldots, n_{\kappa_z}, \quad k = 1, \ldots, n_f, \quad i = 1, \ldots, n_s,$$

with the objective function from (5.7) and the variational form of the PDEs from (5.100), for the multi-experiment case, and with $\mathcal{H}^{l,e} \subset \mathcal{H}^l$ the space of the $l-th$ shape functions of the $e-th$ experiment (or $ik-th$ experiment). In the equations above the model parameter is m, which can be σ or a function of it, e.g. $\log_{10}\sigma$, since the conductivity varies orders of magnitude in a model. The space of m is $\mathcal{M} = \{m \in L^\infty(\Omega) : m_l \leq m(x,y) \leq m_u\}$, where m_l and m_u are lower and upper bounds, respectively.

Let us consider a single experiment ($i = 1, k = 1$), for which we want to solve the constrained minimization problem:

$$\text{minimize} \quad F(\{\hat{E}_z^l, \hat{H}_z^l\}, m) = \sum_{j=1}^{n_r} \frac{1}{2} \left\| W_j^d \left(\left(PO\left(\left\{ \hat{E}_z^l, \hat{H}_z^l \right\} \right) \right)_j - d_j^{obs} \right) \right\|^2 + \frac{\beta}{2} \|R(m - m_{ref})\|^2,$$

$$\text{subject to } \; A_E^l(\kappa_z^l; m; [\hat{E}_z^l, \hat{H}_z^l])(v_1^l) = 0, \;\; A_H^l(\kappa_z^l; m; [\hat{E}_z^l, \hat{H}_z^l])(v_2^l) = 0, \tag{5.103}$$
$$\forall v_1^l, v_2^l \in \mathcal{H}^l, \;\; \text{and for } \; l = 1, \ldots, n_{\kappa_z}.$$

To characterize the solutions of the minimization problem, we vectorize the variables $\{u^l\} = \{\hat{E}_z^l, \hat{H}_z^l\}$ resulting in $\boldsymbol{u}$, and we introduce a set of Lagrange multipliers $\lambda_E^l, \lambda_H^l \in \mathcal{H}^l$, which we also vectorize and denote the joint set of all variables by $x = \{\boldsymbol{u}, \boldsymbol{\lambda}_E, \boldsymbol{\lambda}_H, m\} \in \mathcal{X}_m = \boldsymbol{\mathcal{H}} \times \boldsymbol{\mathcal{H}} \times \mathcal{M}$, where $\boldsymbol{\mathcal{H}} = \{\mathcal{H}^l\}$.

The Lagrangian function $\mathcal{L} : \mathcal{X}_m \to \mathbb{R}$, (5.3), for the 2.5-D CSEM problem is then:

$$\mathcal{L}(x) = F(\boldsymbol{u}, m) + \sum_{l=1}^{n_{\kappa_z}} \Big(A_E^l(\kappa_z^l; m; u^l)(\lambda_E^l) + A_H^l(\kappa_z^l; m; u^l)(\lambda_H^l) \Big), \tag{5.104}$$

which couples the objective function $F : \boldsymbol{\mathcal{H}} \times \mathcal{M} \to \mathbb{R}^+$, defined above, and the state equations constraints, through the Lagrange multipliers, $\lambda_E^l, \lambda_H^l \in \mathcal{H}^l$. Note that in the Lagrangian, different state equations for different experiments would be included in the sum with different $\lambda_{E,ik}^l, \lambda_{H,ik}^l$.

Deriving the optimality conditions (5.4), where $\mathcal{L}_x : \mathcal{X}_m \times \mathcal{X}_m \to \mathbb{R}$, for our particular problem and taking the Gâteaux derivatives of $\mathcal{L}$ at the optimal solution x in the perturbation direction $\tilde{x}$ we obtain:

$$\mathcal{L}_{\hat{E}_z^l}(\tilde{E}_z^l) = \left(d^{syn} - d^{obs}, \frac{\partial d^{syn}}{\partial E_x} \nu^l (-i\kappa_z^l)(\kappa_e^{-2})^l \partial_x \tilde{E}_z^l \right) + (C_E^l \nabla \tilde{E}_z^l, \nabla \lambda_E^l) + (\hat{y} \tilde{E}_z^l, \lambda_E^l) - (\boldsymbol{D}^l \nabla \tilde{E}_z^l, \nabla \lambda_H^l) = 0, \tag{5.105a}$$

$$\mathcal{L}_{\hat{H}_z^l}(\tilde{H}_z^l) = \left(d^{syn} - d^{obs}, \frac{\partial d^{syn}}{\partial E_x} \nu^l \hat{z} (\kappa_e^{-2})^l \partial_y \tilde{H}_z^l \right) + (C_H^l \nabla \tilde{H}_z^l, \nabla \lambda_H^l) + (\hat{z} \tilde{H}_z^l, \lambda_H^l) + (\boldsymbol{D}^l \nabla \tilde{H}_z^l, \nabla \lambda_E^l) = 0, \tag{5.105b}$$

$$\begin{aligned} \mathcal{L}_m(\tilde{m}) = &\left(d^{syn} - d^{obs}, \frac{\partial d^{syn}}{\partial E_x} \sum_{l=1}^{n_{\kappa_z}} \nu^l \frac{\partial \hat{E}_x^l}{\partial m} \tilde{m} \right) + \beta (\nabla m, \nabla \tilde{m}) + \sum_{l=1}^{n_{\kappa_z}} \Big((\partial_m C_E^l \tilde{m} \nabla \hat{E}_z^l, \nabla \lambda_E^l) \\ &+ (\partial_m \boldsymbol{D}^l \tilde{m} \nabla \hat{H}_z^l, \nabla \lambda_E^l) + (\partial_m \hat{y} \tilde{m} \hat{E}_z^l, \lambda_E^l) + (\partial_m \boldsymbol{D}^l \boldsymbol{R}^T \tilde{m} \hat{\mathbf{j}}_t^{s,l}, \nabla \lambda_E^l) + (\partial_m C_H^l \tilde{m} \nabla \hat{H}_z^l, \nabla \lambda_H^l) \\ &- (\partial_m \boldsymbol{D}^l \tilde{m} \nabla \hat{E}_z^l, \nabla \lambda_H^l) - (\partial_m C_H^l \tilde{m} \mathbf{R} \hat{\mathbf{j}}_t^{s,l}, \nabla \lambda_H^l) \Big) = 0, \end{aligned} \tag{5.105c}$$

$$\mathcal{L}_{\lambda_E^l}(\tilde{\lambda}_E^l) = (C_E^l \nabla \hat{E}_z^l, \nabla \tilde{\lambda}_E^l) + (\boldsymbol{D}^l \nabla \hat{H}_z^l, \nabla \tilde{\lambda}_E^l) + (\hat{y} \hat{E}_z^l, \tilde{\lambda}_E^l) + (\boldsymbol{D}^l \boldsymbol{R}^T \hat{\mathbf{j}}_t^{s,l}, \nabla \tilde{\lambda}_E^l) = 0, \tag{5.105d}$$

$$\mathcal{L}_{\lambda_H^l}(\tilde{\lambda}_H^l) = (C_H^l \nabla \hat{H}_z^l, \nabla \tilde{\lambda}_H^l) - (\boldsymbol{D}^l \nabla \hat{E}_z^l, \nabla \tilde{\lambda}_H^l) + (\hat{z} \hat{H}_z^l, \tilde{\lambda}_H^l) - (C_H^l \mathbf{R} \hat{\mathbf{j}}_t^{s,l}, \nabla \tilde{\lambda}_H^l) = 0, \tag{5.105e}$$

for $l = 1 \ldots n_{\kappa_z}$, where we have used the definitions of the measurement variable d^{syn}, we have chosen $j = 1$ for ease of exposition, and we have used a particular choice for the regularization functional $R(m) = (\nabla m, \nabla m)$.

In the resulting equations, (5.105a) and (5.105b) can be identified as the adjoint equations in variational form, defining λ_E^l and λ_H^l, equation (5.105c) is the control equation, and equations (5.105d) and (5.105e) are state equations in a variational form for $l = 1 \ldots n_{\kappa_z}$.

5.5.4 Search directions and discretization

We formulate the solution of the coupled system of nonlinear equations above, using Newton's method in equation (5.5), for a search direction:

$$\delta x = \{\delta\hat{E}_z^1, \delta\hat{H}_z^1, \ldots, \delta\hat{E}_z^{n_{\kappa_z}}, \delta\hat{H}_z^{n_{\kappa_z}}, \delta m, \delta\lambda_E^1, \delta\lambda_H^1, \ldots, \delta\lambda_E^{n_{\kappa_z}}, \delta\lambda_H^{n_{\kappa_z}}\}.$$

Newton's method requires second-order derivatives of the Lagrangian (the Hessian of the Lagrangian), $\mathcal{L}_{xx}(\delta x, \tilde{x})$, which expanded read as:

$$\mathcal{L}_{\hat{E}_z^l\hat{E}_z^l}(\delta\hat{E}_z^l, \tilde{E}_z^l) = \left(\frac{\partial d^{syn}}{\partial E_x}\nu^l(-i\kappa_z^l)(\kappa_e^{-2})^l\partial_x\delta\hat{E}_z^l, \frac{\partial d^{syn}}{\partial E_x}\nu^l(-i\kappa_z^l)(\kappa_e^{-2})^l\partial_x\tilde{E}_z^l\right), \tag{5.106}$$

$$\mathcal{L}_{\hat{E}_z^l\hat{H}_z^l}(\delta\hat{H}_z^l, \tilde{E}_z^l) = \left(\frac{\partial d^{syn}}{\partial E_x}\nu^l\hat{z}(\kappa_e^{-2})^l\partial_y\delta\hat{H}_z^l, \frac{\partial d^{syn}}{\partial E_x}\nu^l(-i\kappa_z^l)(\kappa_e^{-2})^l\partial_x\tilde{E}_z^l\right), \tag{5.107}$$

$$\mathcal{L}_{\hat{E}_z^l\hat{E}_z^n}(\delta\hat{E}_z^n, \tilde{E}_z^l) = \left(\frac{\partial d^{syn}}{\partial E_x}\nu^n(-i\kappa_z^n)(\kappa_e^{-2})^n\partial_x\delta\hat{E}_z^n, \frac{\partial d^{syn}}{\partial E_x}\nu^l(-i\kappa_z^l)(\kappa_e^{-2})^l\partial_x\tilde{E}_z^l\right), \tag{5.108}$$

$$\mathcal{L}_{\hat{E}_z^l\hat{H}_z^n}(\delta\hat{H}_z^n, \tilde{E}_z^l) = \left(\frac{\partial d^{syn}}{\partial E_x}\nu^n\hat{z}(\kappa_e^{-2})^n\partial_y\delta\hat{H}_z^n, \frac{\partial d^{syn}}{\partial E_x}\nu^l(-i\kappa_z^l)(\kappa_e^{-2})^l\partial_x\tilde{E}_z^l\right), \tag{5.109}$$

$$\begin{aligned}\mathcal{L}_{\hat{E}_z^l m}(\delta m, \tilde{E}_z^l) &= \left(\frac{\partial d^{syn}}{\partial E_x}\sum_{l=1}^{n_r}\nu^l\frac{\partial\hat{E}_x^l}{\partial m}\delta m, \frac{\partial d^{syn}}{\partial E_x}\nu^l(-i\kappa_z^l)(\kappa_e^{-2})^l\partial_x\tilde{E}_z^l\right)\\ &+\left(d^{syn}-d^{obs}, \frac{\partial d^{syn}}{\partial E_x}\nu^l\partial_m((\kappa_e^{-2})^l)\delta m(-i\kappa_z^l)\partial_x\tilde{E}_z^l\right)+(\partial_m C_E^l\delta m\nabla\tilde{E}_z^l, \nabla\lambda_E^l)\\ &+(\partial_m\hat{y}\delta m\tilde{E}_z^l, \lambda_E^l)-(\partial_m\boldsymbol{D}^l\delta m\nabla\tilde{E}_z^l, \nabla\lambda_H^l),\end{aligned} \tag{5.110}$$

$$\mathcal{L}_{\hat{E}_z^l\lambda_E^l}(\delta\lambda_E^l, \tilde{E}_z^l) = (C_E^l\nabla\tilde{E}_z^l, \nabla\delta\lambda_E^l)+(\hat{y}\tilde{E}_z^l, \delta\lambda_E^l), \tag{5.111}$$

$$\mathcal{L}_{\hat{E}_z^l\lambda_H^l}(\delta\lambda_H^l, \tilde{E}_z^l) = -(\boldsymbol{D}^l\nabla\tilde{E}_z^l, \nabla\delta\lambda_H^l), \tag{5.112}$$

$$\mathcal{L}_{\hat{E}_z^l\lambda_E^n}(\delta\lambda_E^n, \tilde{E}_z^l) = 0, \tag{5.113}$$

$$\mathcal{L}_{\hat{E}_z^l\lambda_H^n}(\delta\lambda_H^n, \tilde{E}_z^l) = 0, \tag{5.114}$$

$$\mathcal{L}_{\hat{H}_z^l\hat{E}_z^l}(\delta\hat{E}_z^l, \tilde{H}_z^l) = \left(\frac{\partial d^{syn}}{\partial E_x}\nu^l(-i\kappa_z^l)(\kappa_e^{-2})^l\partial_x\delta\hat{E}_z^l, \frac{\partial d^{syn}}{\partial E_x}\nu^l\hat{z}(\kappa_e^{-2})^l\partial_y\tilde{H}_z^l\right), \tag{5.115}$$

$$\mathcal{L}_{\hat{H}_z^l\hat{H}_z^l}(\delta\hat{H}_z^l, \tilde{H}_z^l) = \left(\frac{\partial d^{syn}}{\partial E_x}\nu^l\hat{z}(\kappa_e^{-2})^l\partial_y\delta\hat{H}_z^l, \frac{\partial d^{syn}}{\partial E_x}\nu^l\hat{z}(\kappa_e^{-2})^l\partial_y\tilde{H}_z^l\right), \tag{5.116}$$

$$\mathcal{L}_{\hat{H}_z^l\hat{E}_z^n}(\delta\hat{E}_z^n, \tilde{H}_z^l) = \left(\frac{\partial d^{syn}}{\partial E_x}\nu^n(-i\kappa_z^n)(\kappa_e^{-2})^n\partial_x\delta\hat{E}_z^n, \frac{\partial d^{syn}}{\partial E_x}\nu^l\hat{z}(\kappa_e^{-2})^l\partial_y\tilde{H}_z^l\right), \tag{5.117}$$

$$\mathcal{L}_{\hat{H}_z^l\hat{H}_z^n}(\delta\hat{H}_z^n, \tilde{H}_z^l) = \left(\frac{\partial d^{syn}}{\partial E_x}\nu^n\hat{z}(\kappa_e^{-2})^n\partial_y\delta\hat{H}_z^n, \frac{\partial d^{syn}}{\partial E_x}\nu^l\hat{z}(\kappa_e^{-2})^l\partial_y\tilde{H}_z^l\right), \tag{5.118}$$

$$\begin{aligned}\mathcal{L}_{\hat{H}_z^l m}(\delta m, \tilde{H}_z^l) &= \left(\frac{\partial d^{syn}}{\partial E_x}\sum_{l=1}^{n_{\kappa_z}}\nu^l\frac{\partial\hat{E}_x^l}{\partial m}\delta m, \frac{\partial d^{syn}}{\partial E_x}\nu^l\hat{z}(\kappa_e^{-2})^l\partial_y\tilde{H}_z^l\right)\\ &+\left(d^{syn}-d^{obs}, \frac{\partial d^{syn}}{\partial E_x}\nu^l\partial_m((\kappa_e^{-2})^l)\delta m\hat{z}\partial_y\tilde{H}_z^l\right)+(\partial_m C_H^l\delta m\nabla\tilde{H}_z^l, \nabla\lambda_H^l)\\ &+(\partial_m\boldsymbol{D}^l\delta m\nabla\tilde{H}_z^l, \nabla\lambda_E^l),\end{aligned} \tag{5.119}$$

$$\mathcal{L}_{\hat{H}_z^l \lambda_E^l}(\delta\lambda_E^l, \tilde{H}_z^l) = (\boldsymbol{D}^l \nabla \tilde{H}_z^l, \nabla \delta\lambda_E^l), \tag{5.120}$$

$$\mathcal{L}_{\hat{H}_z^l \lambda_H^l}(\delta\lambda_H^l, \tilde{H}_z^l) = (C_H^l \nabla \tilde{H}_z^l, \nabla \delta\lambda_H^l) + (\hat{z}\tilde{H}_z^l, \delta\lambda_H^l), \tag{5.121}$$

$$\mathcal{L}_{\hat{H}_z^l \lambda_E^n}(\delta\lambda_E^n, \tilde{H}_z^l) = 0, \tag{5.122}$$

$$\mathcal{L}_{\hat{H}_z^l \lambda_H^n}(\delta\lambda_H^n, \tilde{H}_z^l) = 0, \tag{5.123}$$

$$\begin{aligned}\mathcal{L}_{m\hat{E}_z^l}(\delta\hat{E}_z^l, \tilde{m}) = &\left(\frac{\partial d^{syn}}{\partial E_x}\nu^l(-i\kappa_z^l)(\kappa_e^{-2})^l\partial_x\delta\hat{E}_z^l, \frac{\partial d^{syn}}{\partial E_x}\sum_{l=1}^{n_{\kappa_z}}\nu^l\frac{\partial \hat{E}_x^l}{\partial m}\tilde{m}\right)\\ &+\left(d^{syn}-d^{obs}, \frac{\partial d^{syn}}{\partial E_x}\nu^l\partial_m((\kappa_e^{-2})^l)\tilde{m}(-i\kappa_z^l)\partial_x\delta\hat{E}_z^l\right) + (\partial_m C_E^l\tilde{m}\nabla\delta\hat{E}_z^l, \nabla\lambda_E^l)\\ &+ (\partial_m\hat{y}\tilde{m}\delta\hat{E}_z^l, \lambda_E^l) - (\partial_m\boldsymbol{D}^l\tilde{m}\nabla\delta\hat{E}_z^l, \nabla\lambda_H^l),\end{aligned} \tag{5.124}$$

$$\begin{aligned}\mathcal{L}_{m\hat{H}_z^l}(\delta\hat{H}_z^l, \tilde{m}) = &\left(\frac{\partial d^{syn}}{\partial E_x}\nu^l\left(\hat{z}(\kappa_e^{-2})^l\partial_y\delta\hat{H}_z^l\right), \frac{\partial d^{syn}}{\partial E_x}\sum_{l=1}^{n_{\kappa_z}}\nu^l\frac{\partial \hat{E}_x^l}{\partial m}\tilde{m}\right)\\ &+\left(d^{syn}-d^{obs}, \frac{\partial d^{syn}}{\partial E_x}\nu^l\partial_m((\kappa_e^{-2})^l)\tilde{m}\hat{z}\partial_y\delta\hat{H}_z^l\right) + (\partial_m\boldsymbol{D}^l\tilde{m}\nabla\delta\hat{H}_z^l, \nabla\lambda_E^l)\\ &+ (\partial_m C_H^l\tilde{m}\nabla\delta\hat{H}_z^l, \nabla\lambda_H^l),\end{aligned} \tag{5.125}$$

$$\mathcal{L}_{mm}(\delta m, \tilde{m}) = \left(\frac{\partial d^{syn}}{\partial E_x}\sum_{l=1}^{n_{\kappa_z}}\nu^l\frac{\partial \hat{E}_x^l}{\partial m}\delta m, \frac{\partial d^{syn}}{\partial E_x}\sum_{l=1}^{n_{\kappa_z}}\nu^l\frac{\partial \hat{E}_x^l}{\partial m}\tilde{m}\right) + \beta(\nabla\delta m, \nabla\tilde{m}), \tag{5.126}$$

$$\begin{aligned}\mathcal{L}_{m\lambda_E^l}(\delta\lambda_E^l, \tilde{m}) = &(\partial_m C_E^l\tilde{m}\nabla\hat{E}_z^l, \nabla\delta\lambda_E^l) + (\partial_m\boldsymbol{D}^l\tilde{m}\nabla\hat{H}_z^l, \nabla\delta\lambda_E^l) + (\partial_m\hat{y}\tilde{m}\hat{E}_z^l, \delta\lambda_E^l)\\ &+ (\partial_m\boldsymbol{D}^l\boldsymbol{R}^T\tilde{m}\hat{\mathbf{J}}_t^{s,l}, \nabla\delta\lambda_E^l),\end{aligned} \tag{5.127}$$

$$\begin{aligned}\mathcal{L}_{m\lambda_H^l}(\delta\lambda_H^l, \tilde{m}) = &(\partial_m C_H^l\tilde{m}\nabla\hat{H}_z^l, \nabla\delta\lambda_H^l) - (\partial_m\boldsymbol{D}^l\tilde{m}\nabla\hat{E}_z^l, \nabla\delta\lambda_H^l)\\ &- (\partial_m C_H^l\tilde{m}\mathbf{R}\hat{\mathbf{J}}_t^{s,l}, \nabla\delta\lambda_H^l),\end{aligned} \tag{5.128}$$

$$\mathcal{L}_{\lambda_E^l \hat{E}_z^l}(\delta\hat{E}_z^l, \tilde{\lambda}_E^l) = (C_E^l\nabla\delta\hat{E}_z^l, \nabla\tilde{\lambda}_E^l) + (\hat{y}\delta\hat{E}_z^l, \tilde{\lambda}_E^l), \tag{5.129}$$

$$\mathcal{L}_{\lambda_E^l \hat{H}_z^l}(\delta\hat{H}_z^l, \tilde{\lambda}_E^l) = (\boldsymbol{D}^l\nabla\hat{H}_z^l, \nabla\tilde{\lambda}_E^l), \tag{5.130}$$

$$\mathcal{L}_{\lambda_E^l \hat{E}_z^n}(\delta\hat{E}_z^n, \tilde{\lambda}_E^l) = 0, \tag{5.131}$$

$$\mathcal{L}_{\lambda_E^l \hat{H}_z^n}(\delta\hat{H}_z^n, \tilde{\lambda}_E^l) = 0, \tag{5.132}$$

$$\begin{aligned}\mathcal{L}_{\lambda_E^l m}(\delta m, \tilde{\lambda}_E^l) = &(\partial_m C_E^l\delta m\nabla\hat{E}_z^l, \nabla\tilde{\lambda}_E^l) + (\partial_m\boldsymbol{D}^l\delta m\nabla\hat{H}_z^l, \nabla\tilde{\lambda}_E^l) + (\partial_m\hat{y}\delta m\hat{E}_z^l, \tilde{\lambda}_E^l)\\ &+ (\partial_m\boldsymbol{D}^l\boldsymbol{R}^T\delta m\hat{\mathbf{J}}_t^{s,l}, \nabla\tilde{\lambda}_E^l),\end{aligned} \tag{5.133}$$

$$\mathcal{L}_{\lambda_E^l \lambda_E^l}(\delta\lambda_E^l, \tilde{\lambda}_E^l) = 0, \tag{5.134}$$

$$\mathcal{L}_{\lambda_E^l \lambda_H^l}(\delta\lambda_H^l, \tilde{\lambda}_E^l) = 0, \tag{5.135}$$

$$\mathcal{L}_{\lambda_E^l \lambda_E^n}(\delta\lambda_E^n, \tilde{\lambda}_E^l) = 0, \tag{5.136}$$

$$\mathcal{L}_{\lambda_E^l \lambda_H^n}(\delta\lambda_H^n, \tilde{\lambda}_E^l) = 0, \tag{5.137}$$

$$\mathcal{L}_{\lambda_H^l \hat{E}_z^l}(\delta\hat{E}_z^l, \tilde{\lambda}_H^l) = -(\boldsymbol{D}^l\nabla\delta\hat{E}_z^l, \nabla\tilde{\lambda}_H^l), \tag{5.138}$$

$$\mathcal{L}_{\lambda_H^l \hat{H}_z^l}(\delta\hat{H}_z^l, \tilde{\lambda}_H^l) = (C_H^l\nabla\delta\hat{H}_z^l, \nabla\tilde{\lambda}_H^l) + (\hat{z}\delta\hat{H}_z^l, \tilde{\lambda}_H^l), \tag{5.139}$$

$$\mathcal{L}_{\lambda_H^l \hat{E}_z^n}(\delta\hat{E}_z^n, \tilde{\lambda}_H^l) = 0, \tag{5.140}$$

$$\mathcal{L}_{\lambda_H^l \hat{H}_z^n}(\delta\hat{H}_z^n, \tilde{\lambda}_H^l) = 0, \tag{5.141}$$

$$\begin{aligned}\mathcal{L}_{\lambda_H^l m}(\delta m, \tilde{\lambda}_H^l) = (\partial_m C_H^l \delta m \nabla\hat{H}_z^l, \nabla\tilde{\lambda}_H^l) - (\partial_m \boldsymbol{D}^l \delta m \nabla\hat{E}_z^l, \nabla\tilde{\lambda}_H^l) \\ + (\partial_m C_H^l \delta m \boldsymbol{R}\hat{\mathbf{J}}_t^{s,l}, \nabla\tilde{\lambda}_H^l),\end{aligned} \tag{5.142}$$

$$\mathcal{L}_{\lambda_H^l \lambda_E^l}(\delta\lambda_E^l, \tilde{\lambda}_H^l) = 0, \tag{5.143}$$

$$\mathcal{L}_{\lambda_H^l \lambda_H^l}(\delta\lambda_H^l, \tilde{\lambda}_H^l) = 0, \tag{5.144}$$

$$\mathcal{L}_{\lambda_H^l \lambda_E^n}(\delta\lambda_E^n, \tilde{\lambda}_H^l) = 0, \tag{5.145}$$

$$\mathcal{L}_{\lambda_H^l \lambda_H^n}(\delta\lambda_H^n, \tilde{\lambda}_H^l) = 0. \tag{5.146}$$

Then, the update direction for the $k-th$ iteration, δx_k, is determined from equation (5.5) with equations (5.106) – (5.146) as the second derivatives and equations (5.105) as the first derivatives evaluated at x_k, obtaining a system of equations that represent one condition for each variable in δx_k.

The formulation of the optimization problem until this point is derived in function spaces. To actually compute finite-dimensional approximations to x, we have to discretize both the state and adjoint variables, as well as the model parameters.

We discretize Newton's step with the FE method, and choose as basis functions of a finite dimensional space, piecewise quadratic shape functions on triangular meshes, $\{\phi_i\}_{i=1}^{N_u}$, $\forall\phi_i \in \mathcal{H}_h$, for the state and adjoint variables:

$$\tilde{E}_z^l = \sum_{i=1}^{N_u}\phi_i; \quad \tilde{H}_z^l = \sum_{i=1}^{N_u}\phi_i; \quad \delta\hat{E}_z^l = \sum_{i=1}^{N_u}\delta E_i^l\phi_i; \quad \delta\hat{H}_z^l = \sum_{i=1}^{N_u}\delta H_i^l\phi_i; \tag{5.147a}$$

$$\tilde{\lambda}_E^l = \sum_{i=1}^{N_u}\phi_i; \quad \tilde{\lambda}_H^l = \sum_{i=1}^{N_u}\phi_i; \quad \delta\lambda_E^l = \sum_{i=1}^{N_u}\delta\lambda_{E,i}^l\phi_i; \quad \delta\lambda_{H,i}^l = \sum_{i=1}^{N_u}\delta\lambda_{H,i}^l\phi_i; \tag{5.147b}$$

$$\text{for} \quad l = 1,\ldots,n_{\kappa_z},$$

and piecewise constant discontinuous functions, $\{\chi_i\}_{i=1}^{N_m}$, $\forall\chi_i \in \mathcal{M}_h$, for the model parameter:

$$\tilde{m} = \sum_{i=1}^{N_m}\chi_i; \quad \delta m = \sum_{i=1}^{N_m}\delta m_i\chi_i. \tag{5.148}$$

In the equations above we have chosen the same function spaces for the state and adjoint variables and for all the variables corresponding to different wavenumber parameter values. This simplifies the problem, since we do not see any advantage of using different spaces for these variables. However, from a mathematical point of view we could have chosen different spaces.

Substituting these expressions in (5.105), (5.106) – (5.146) and rearranging terms, and

evaluating them at x_k we obtain a discretized Newton's step:

$$\begin{pmatrix} \boldsymbol{B}_{EE} & \boldsymbol{B}_{EH} & \boldsymbol{C}_{Em} & \boldsymbol{D}_{E\lambda_E} & \boldsymbol{D}_{E\lambda_H} \\ \boldsymbol{B}_{EH}^T & \boldsymbol{B}_{HH} & \boldsymbol{C}_{Hm} & \boldsymbol{D}_{H\lambda_E} & \boldsymbol{D}_{H\lambda_H} \\ \boldsymbol{C}_{Em}^T & \boldsymbol{C}_{Hm}^T & \boldsymbol{C}_{mm} & \boldsymbol{C}_{m\lambda_E} & \boldsymbol{C}_{m\lambda_H} \\ \boldsymbol{D}_{E\lambda_E}^T & \boldsymbol{D}_{H\lambda_E}^T & \boldsymbol{C}_{m\lambda_E}^T & \boldsymbol{0} & \boldsymbol{0} \\ \boldsymbol{D}_{E\lambda_H}^T & \boldsymbol{D}_{H\lambda_H}^T & \boldsymbol{C}_{m\lambda_H}^T & \boldsymbol{0} & \boldsymbol{0} \end{pmatrix} \begin{pmatrix} \boldsymbol{\delta E}_k \\ \boldsymbol{\delta H}_k \\ \boldsymbol{\delta m}_k \\ \boldsymbol{\delta \lambda}_k^{\boldsymbol{E}} \\ \boldsymbol{\delta \lambda}_k^{\boldsymbol{H}} \end{pmatrix} = - \begin{pmatrix} \boldsymbol{G_E} \\ \boldsymbol{G_H} \\ \boldsymbol{G_m} \\ \boldsymbol{G}_{\lambda_E} \\ \boldsymbol{G}_{\lambda_H} \end{pmatrix} \tag{5.149}$$

where

$$\boldsymbol{B}_{EE} = \begin{pmatrix} \mathcal{L}_{\hat{E}_z^1 \hat{E}_z^1} & \dots & \mathcal{L}_{\hat{E}_z^1 \hat{E}_z^{n_{\kappa_z}}} \\ \vdots & \ddots & \vdots \\ \mathcal{L}_{\hat{E}_z^{n_{\kappa_z}} \hat{E}_z^1} & \dots & \mathcal{L}_{\hat{E}_z^{n_{\kappa_z}} \hat{E}_z^{n_{\kappa_z}}} \end{pmatrix}, \quad \boldsymbol{B}_{EH} = \begin{pmatrix} \mathcal{L}_{\hat{E}_z^1 \hat{H}_z^1} & \dots & \mathcal{L}_{\hat{E}_z^1 \hat{H}_z^{n_{\kappa_z}}} \\ \vdots & \ddots & \vdots \\ \mathcal{L}_{\hat{E}_z^{n_{\kappa_z}} \hat{H}_z^1} & \dots & \mathcal{L}_{\hat{E}_z^{n_{\kappa_z}} \hat{H}_z^{n_{\kappa_z}}} \end{pmatrix},$$

$$\boldsymbol{B}_{HH} = \begin{pmatrix} \mathcal{L}_{\hat{H}_z^1 \hat{H}_z^1} & \dots & \mathcal{L}_{\hat{H}_z^1 \hat{H}_z^{n_{\kappa_z}}} \\ \vdots & \ddots & \vdots \\ \mathcal{L}_{\hat{H}_z^{n_{\kappa_z}} \hat{H}_z^1} & \dots & \mathcal{L}_{\hat{H}_z^{n_{\kappa_z}} \hat{H}_z^{n_{\kappa_z}}} \end{pmatrix},$$

$$\boldsymbol{C}_{Em} = \begin{pmatrix} \mathcal{L}_{\hat{E}_z^1 m} \\ \vdots \\ \mathcal{L}_{\hat{E}_z^{n_{\kappa_z}} m} \end{pmatrix}, \quad \boldsymbol{C}_{Hm} = \begin{pmatrix} \mathcal{L}_{\hat{H}_z^1 m} \\ \vdots \\ \mathcal{L}_{\hat{H}_z^{n_{\kappa_z}} m} \end{pmatrix}, \quad \boldsymbol{C}_{m\lambda_E} = \begin{pmatrix} \mathcal{L}_{m\lambda_E^1} \\ \vdots \\ \mathcal{L}_{m\lambda_E^{n_{\kappa_z}}} \end{pmatrix}, \quad \boldsymbol{C}_{m\lambda_H} = \begin{pmatrix} \mathcal{L}_{m\lambda_H^1} \\ \vdots \\ \mathcal{L}_{m\lambda_H^{n_{\kappa_z}}} \end{pmatrix}; \quad \boldsymbol{C}_{mm} = \mathcal{L}_{mm},$$

$$\boldsymbol{D}_{E\lambda_E} = \begin{pmatrix} \mathcal{L}_{\hat{E}_z^1 \lambda_E^1} & 0 & \dots & 0 \\ 0 & \mathcal{L}_{\hat{E}_z^2 \lambda_E^2} & \dots & 0 \\ \vdots & \vdots & \ddots & \vdots \\ 0 & 0 & 0 & \mathcal{L}_{\hat{E}_z^{n_{\kappa_z}} \lambda_E^{n_{\kappa_z}}} \end{pmatrix}, \quad \boldsymbol{D}_{E\lambda_H} = \begin{pmatrix} \mathcal{L}_{\hat{E}_z^1 \lambda_H^1} & 0 & \dots & 0 \\ 0 & \mathcal{L}_{\hat{E}_z^2 \lambda_H^2} & \dots & 0 \\ \vdots & \vdots & \ddots & \vdots \\ 0 & 0 & 0 & \mathcal{L}_{\hat{E}_z^{n_{\kappa_z}} \lambda_H^{n_{\kappa_z}}} \end{pmatrix},$$

$$\boldsymbol{D}_{H\lambda_E} = \begin{pmatrix} \mathcal{L}_{\hat{H}_z^1 \lambda_E^1} & 0 & \dots & 0 \\ 0 & \mathcal{L}_{\hat{H}_z^2 \lambda_E^2} & \dots & 0 \\ \vdots & \vdots & \ddots & \vdots \\ 0 & 0 & 0 & \mathcal{L}_{\hat{H}_z^{n_{\kappa_z}} \lambda_E^{n_{\kappa_z}}} \end{pmatrix}, \quad \boldsymbol{D}_{H\lambda_H} = \begin{pmatrix} \mathcal{L}_{\hat{H}_z^1 \lambda_H^1} & 0 & \dots & 0 \\ 0 & \mathcal{L}_{\hat{H}_z^2 \lambda_H^2} & \dots & 0 \\ \vdots & \vdots & \ddots & \vdots \\ 0 & 0 & 0 & \mathcal{L}_{\hat{H}_z^{n_{\kappa_z}} \lambda_H^{n_{\kappa_z}}} \end{pmatrix},$$

$$\boldsymbol{\delta E}_k = \begin{pmatrix} \boldsymbol{\delta \hat{E}}_{z,k}^1 \\ \vdots \\ \boldsymbol{\delta \hat{E}}_{z,k}^{n_{\kappa_z}} \end{pmatrix}, \quad \boldsymbol{\delta H}_k = \begin{pmatrix} \boldsymbol{\delta \hat{H}}_{z,k}^1 \\ \vdots \\ \boldsymbol{\delta \hat{H}}_{z,k}^{n_{\kappa_z}} \end{pmatrix}, \quad \boldsymbol{\delta \lambda}_k^{\boldsymbol{E}} = \begin{pmatrix} \boldsymbol{\delta \lambda}_{E,k}^1 \\ \vdots \\ \boldsymbol{\delta \lambda}_{E,k}^{n_{\kappa_z}} \end{pmatrix}, \quad \boldsymbol{\delta \lambda}_k^{\boldsymbol{H}} = \begin{pmatrix} \boldsymbol{\delta \lambda}_{H,k}^1 \\ \vdots \\ \boldsymbol{\delta \lambda}_{H,k}^{n_{\kappa_z}} \end{pmatrix},$$

$$\boldsymbol{G_E} = \begin{pmatrix} \mathcal{L}_{\hat{E}_z^1} \\ \vdots \\ \mathcal{L}_{\hat{E}_z^{n_{\kappa_z}}} \end{pmatrix}, \quad \boldsymbol{G_H} = \begin{pmatrix} \mathcal{L}_{\hat{H}_z^1} \\ \vdots \\ \mathcal{L}_{\hat{H}_z^{n_{\kappa_z}}} \end{pmatrix}, \quad \boldsymbol{G_m} = \mathcal{L}_m, \quad \boldsymbol{G}_{\lambda_H} = \begin{pmatrix} \mathcal{L}_{\lambda_H^1} \\ \vdots \\ \mathcal{L}_{\lambda_H^{n_{\kappa_z}}} \end{pmatrix}, \quad \boldsymbol{G}_{\lambda_H} = \begin{pmatrix} \mathcal{L}_{\lambda_H^1} \\ \vdots \\ \mathcal{L}_{\lambda_H^{n_{\kappa_z}}} \end{pmatrix},$$

and where the individual blocks ij of the second derivatives matrices above are:

$$\left[\mathcal{L}_{\hat{E}_z^l \hat{E}_z^l}\right]_{ij}(\boldsymbol{x}_k) = \left(\frac{\partial d^{syn}}{\partial E_x} \nu^l (-i\kappa_z^l)(\kappa_e^l(m_k))^{-2} \partial_x \phi_j, \frac{\partial d^{syn}}{\partial E_x} \nu^l (-i\kappa_z^l)(\kappa_e^l(m_k))^{-2} \partial_x \phi_i \right), \tag{5.150}$$

$$\left[\mathcal{L}_{\hat{E}_z^l \hat{H}_z^l}\right]_{ij}(\boldsymbol{x}_k) = \left(\frac{\partial d^{syn}}{\partial E_x}\nu^l \hat{z}(\kappa_e^l(m_k))^{-2}\partial_y\phi_j, \frac{\partial d^{syn}}{\partial E_x}\nu^l(-i\kappa_z^l)(\kappa_e^l(m_k))^{-2}\partial_x\phi_i\right), \tag{5.151}$$

$$\left[\mathcal{L}_{\hat{E}_z^l \hat{E}_z^n}\right]_{ij}(\boldsymbol{x}_k) = \left(\frac{\partial d^{syn}}{\partial E_x}\nu^n(-i\kappa_z^n)(\kappa_e^n(m_k))^{-2}\partial_x\phi_j, \frac{\partial d^{syn}}{\partial E_x}\nu^l(-i\kappa_z^l)(\kappa_e^l(m_k))^{-2}\partial_x\phi_i\right), \tag{5.152}$$

$$\left[\mathcal{L}_{\hat{E}_z^l \hat{H}_z^n}\right]_{ij}(\boldsymbol{x}_k) = \left(\frac{\partial d^{syn}}{\partial E_x}\nu^n \hat{z}(\kappa_e^n(m_k))^{-2}\partial_y\phi_j, \frac{\partial d^{syn}}{\partial E_x}\nu^l(-i\kappa_z^l)(\kappa_e^l(m_k))^{-2}\partial_x\phi_i\right), \tag{5.153}$$

$$\begin{aligned}\left[\mathcal{L}_{\hat{E}_z^l \boldsymbol{m}}\right]_{ij}(\boldsymbol{x}_k) &= \left(\frac{\partial d^{syn}}{\partial E_x}\sum_{s=1}^{n_{\kappa_z}}\nu^s \partial_m \hat{E}_x^s\Big|_{m_k}\chi_j, \frac{\partial d^{syn}}{\partial E_x}\nu^l(-i\kappa_z^l)(\kappa_e^l(m_k))^{-2}\partial_x\phi_i\right)\\ &+\left(d_k^{syn} - d^{obs}, \frac{\partial d^{syn}}{\partial E_x}\nu^l \partial_m(\kappa_e^l)^{-2}\Big|_{m_k}(-i\kappa_z^l)\partial_x\phi_i\chi_j\right) + \left(\partial_m C_E^l\Big|_{m_k}\chi_j\nabla\phi_i, \nabla\lambda_{E,k}^l\right)\\ &+\left(\partial_m\hat{y}\Big|_{m_k}\phi_i\chi_j, \lambda_{E,k}^l\right) - \left(\partial_m \boldsymbol{D}^l\Big|_{m_k}\nabla\phi_i\chi_j, \nabla\lambda_{H,k}^l\right),\end{aligned} \tag{5.154}$$

$$\left[\mathcal{L}_{\hat{E}_z^l \lambda_E^l}\right]_{ij}(\boldsymbol{x}_k) = \left(C_E^l(m_k)\nabla\phi_i, \nabla\phi_j\right) + \left(\hat{y}(m_k)\phi_i, \phi_j\right), \tag{5.155}$$

$$\left[\mathcal{L}_{\hat{E}_z^l \lambda_H^l}\right]_{ij}(\boldsymbol{x}_k) = -\left(\boldsymbol{D}^l(m_k)\nabla\phi_i, \nabla\phi_j\right), \tag{5.156}$$

$$\left[\mathcal{L}_{\hat{E}_z^l \lambda_E^n}\right]_{ij}(\boldsymbol{x}_k) = 0, \tag{5.157}$$

$$\left[\mathcal{L}_{\hat{E}_z^l \lambda_H^n}\right]_{ij}(\boldsymbol{x}_k) = 0, \tag{5.158}$$

$$\left[\mathcal{L}_{\hat{H}_z^l \hat{E}_z^l}\right]_{ij}(\boldsymbol{x}_k) = \left(\frac{\partial d^{syn}}{\partial E_x}\nu^l(-i\kappa_z^l)(\kappa_e^l(m_k))^{-2}\partial_x\phi_j, \frac{\partial d^{syn}}{\partial E_x}\nu^l \hat{z}(\kappa_e^l(m_k))^{-2}\partial_y\phi_i\right), \tag{5.159}$$

$$\left[\mathcal{L}_{\hat{H}_z^l \hat{H}_z^l}\right]_{ij}(\boldsymbol{x}_k) = \left(\frac{\partial d^{syn}}{\partial E_x}\nu^l \hat{z}(\kappa_e^l(m_k))^{-2}\partial_y\phi_j, \frac{\partial d^{syn}}{\partial E_x}\nu^l \hat{z}(\kappa_e^l(m_k))^{-2}\partial_y\phi_i\right), \tag{5.160}$$

$$\left[\mathcal{L}_{\hat{H}_z^l \hat{E}_z^n}\right]_{ij}(\boldsymbol{x}_k) = \left(\frac{\partial d^{syn}}{\partial E_x}\nu^n(-i\kappa_z^n)(\kappa_e^n(m_k))^{-2}\partial_x\phi_j, \frac{\partial d^{syn}}{\partial E_x}\nu^l \hat{z}(\kappa_e^l(m_k))^{-2}\partial_y\phi_i\right), \tag{5.161}$$

$$\left[\mathcal{L}_{\hat{H}_z^l \hat{H}_z^n}\right]_{ij}(\boldsymbol{x}_k) = \left(\frac{\partial d^{syn}}{\partial E_x}\nu^n \hat{z}(\kappa_e^n(m_k))^{-2}\partial_y\phi_j, \frac{\partial d^{syn}}{\partial E_x}\nu^l \hat{z}(\kappa_e^l(m_k))^{-2}\partial_y\phi_i\right), \tag{5.162}$$

$$\begin{aligned}\left[\mathcal{L}_{\hat{H}_z^l \boldsymbol{m}}\right]_{ij}(\boldsymbol{x}_k) &= \left(\frac{\partial d^{syn}}{\partial E_x}\sum_{s=1}^{n_{\kappa_z}}\nu^s \partial_m \hat{E}_x^s\Big|_{m_k}\chi_j, \frac{\partial d^{syn}}{\partial E_x}\nu^l \hat{z}(\kappa_e^l(m_k))^{-2}\partial_y\phi_i\right)\\ &+\left(d_k^{syn} - d^{obs}, \frac{\partial d^{syn}}{\partial E_x}\hat{z}\nu^l \partial_m(\kappa_e^l)^{-2}\Big|_{m_k}\partial_y\phi_i\chi_j\right) + \left(\partial_m C_H^l\Big|_{m_k}\nabla\phi_i\chi_j, \nabla\lambda_{H,k}^l\right)\\ &+\left(\partial_m \boldsymbol{D}^l\Big|_{m_k}\nabla\phi_i\chi_j, \nabla\lambda_{E,k}^l\right),\end{aligned} \tag{5.163}$$

$$\left[\mathcal{L}_{\hat{H}_z^l \lambda_E^l}\right]_{ij}(\boldsymbol{x}_k) = \left(\boldsymbol{D}^l(m_k)\nabla\phi_i, \nabla\phi_j\right), \tag{5.164}$$

$$\left[\mathcal{L}_{\hat{H}_z^l \lambda_H^l}\right]_{ij}(\boldsymbol{x}_k) = \left(C_H^l(m_k)\nabla\phi_i, \nabla\phi_j\right) + \left(\hat{z}\phi_i, \phi_j\right), \tag{5.165}$$

$$\left[\mathcal{L}_{\hat{H}_z^l \lambda_E^n}\right]_{ij}(\boldsymbol{x}_k) = 0, \tag{5.166}$$

$$\left[\mathcal{L}_{\hat{H}_z^l \lambda_H^n}\right]_{ij}(\boldsymbol{x}_k) = 0, \tag{5.167}$$

$$\left[\mathcal{L}_{\boldsymbol{m}\hat{\boldsymbol{E}}_z^l}\right]_{ij}(\boldsymbol{x}_k)=\left(\frac{\partial d^{syn}}{\partial E_x}\nu^l(-i\kappa_z^l)(\kappa_e^l(m_k))^{-2}\partial_x\phi_j,\frac{\partial d^{syn}}{\partial E_x}\sum_{s=1}^{n_{\kappa_z}}\nu^s\partial_m\hat{E}_x^s\Big|_{m_k}\chi_i\right)$$
$$+\left(d_k^{syn}-d^{obs},\frac{\partial d^{syn}}{\partial E_x}\nu^l\partial_m((\kappa_e^l)^{-2})\Big|_{m_k}(-i\kappa_z^l)\chi_i\partial_x\phi_j\right)+\left(\partial_m C_E^l\Big|_{m_k}\chi_i\nabla\phi_j,\nabla\lambda_{E,k}^l\right) \tag{5.168}$$
$$+\left(\partial_m\hat{y}\Big|_{m_k}\chi_i\phi_j,\lambda_{E,k}^l\right)-\left(\partial_m\boldsymbol{D}^l\Big|_{m_k}\chi_i\nabla\phi_j,\nabla\lambda_{H,k}^l\right),$$

$$\left[\mathcal{L}_{\boldsymbol{m}\hat{\boldsymbol{H}}_z^l}\right]_{ij}(\boldsymbol{x}_k)=\left(\frac{\partial d^{syn}}{\partial E_x}\nu^l\hat{z}(\kappa_e^l(m_k))^{-2}\partial_y\phi_j,\frac{\partial d^{syn}}{\partial E_x}\sum_{s=1}^{n_{\kappa_z}}\nu^s\partial_m\hat{E}_x^s\Big|_{m_k}\chi_i\right)$$
$$+\left(d_k^{syn}-d^{obs},\frac{\partial d^{syn}}{\partial E_x}\hat{z}\nu^l\partial_m(\kappa_e^l)^{-2}\Big|_{m_k}\chi_i\partial_y\phi_j\right)+\left(\partial_m\boldsymbol{D}^l\Big|_{m_k}\chi_i\nabla\phi_j,\nabla\lambda_{E,k}^l\right) \tag{5.169}$$
$$+\left(\partial_m C_H^l\Big|_{m_k}\chi_i\nabla\phi_j,\nabla\lambda_{H,k}^l\right),$$

$$[\mathcal{L}_{\boldsymbol{mm}}]_{ij}(\boldsymbol{x}_k)=\left(\frac{\partial d^{syn}}{\partial E_x}\sum_{l=1}^{n_{\kappa_z}}\nu^l\partial_m\hat{E}_x^l\Big|_{m_k}\chi_j,\frac{\partial d^{syn}}{\partial E_x}\sum_{l=1}^{n_{\kappa_z}}\nu^l\partial_m\hat{E}_x^l\Big|_{m_k}\chi_i\right)+\beta\left(\nabla\chi_j,\nabla\chi_i\right), \tag{5.170}$$

$$\left[\mathcal{L}_{\boldsymbol{m}\lambda_E^l}\right]_{ij}(\boldsymbol{x}_k)=\left(\partial_m C_E^l\Big|_{m_k}\nabla\hat{E}_{z,k}^l\chi_i,\nabla\phi_j\right)+\left(\partial_m\boldsymbol{D}^l\Big|_{m_k}\nabla\hat{H}_{z,k}^l\chi_i,\nabla\phi_j\right)$$
$$+\left(\partial_m\hat{y}\Big|_{m_k}\hat{E}_{z,k}^l\chi_i,\phi_j\right)+\left(\partial_m\boldsymbol{D}^l\Big|_{m_k}\boldsymbol{R}^T\hat{\mathbf{J}}_t^{s,l}\chi_i,\nabla\phi_j\right), \tag{5.171}$$

$$\left[\mathcal{L}_{\boldsymbol{m}\lambda_H^l}\right]_{ij}(\boldsymbol{x}_k)=\left(\partial_m C_H^l\Big|_{m_k}\nabla\hat{H}_{z,k}^l\chi_i,\nabla\phi_j\right)-\left(\partial_m\boldsymbol{D}^l\Big|_{m_k}\nabla\hat{E}_{z,k}^l\chi_i,\nabla\phi_j\right)$$
$$+\left(\partial_m C_H^l\Big|_{m_k}\mathbf{R}\hat{\mathbf{J}}_t^{s,l}\chi_i,\nabla\phi_j\right), \tag{5.172}$$

$$\left[\mathcal{L}_{\lambda_E^l\hat{\boldsymbol{E}}_z^l}\right]_{ij}(\boldsymbol{x}_k)=\left(C_E^l(m_k)\nabla\phi_j,\nabla\phi_i\right)+\left(\hat{y}(m_k)\phi_j,\phi_i\right), \tag{5.173}$$

$$\left[\mathcal{L}_{\lambda_E^l\hat{\boldsymbol{H}}_z^l}\right]_{ij}(\boldsymbol{x}_k)=\left(\boldsymbol{D}^l(m_k)\nabla\phi_j,\nabla\phi_i\right), \tag{5.174}$$

$$\left[\mathcal{L}_{\lambda_E^l\hat{\boldsymbol{E}}_z^n}\right]_{ij}(\boldsymbol{x}_k)=0, \tag{5.175}$$

$$\left[\mathcal{L}_{\lambda_E^l\hat{\boldsymbol{H}}_z^n}\right]_{ij}(\boldsymbol{x}_k)=0, \tag{5.176}$$

$$\left[\mathcal{L}_{\lambda_E^l\boldsymbol{m}}\right]_{ij}(\boldsymbol{x}_k)=\left(\partial_m C_E^l\Big|_{m_k}\nabla\hat{E}_{z,k}^l\chi_j,\nabla\phi_i\right)+\left(\partial_m\boldsymbol{D}^l\Big|_{m_k}\nabla\hat{H}_{z,k}^l\chi_j,\nabla\phi_i\right)$$
$$+\left(\partial_m\hat{y}\Big|_{m_k}\hat{E}_{z,k}^l\chi_j,\phi_i\right)+\left(\partial_m\boldsymbol{D}^l\Big|_{m_k}\boldsymbol{R}^T\hat{\mathbf{J}}_t^{s,l}\chi_j,\nabla\phi_i\right), \tag{5.177}$$

$$\left[\mathcal{L}_{\lambda_E^l\lambda_E^l}\right]_{ij}(\boldsymbol{x}_k)=0, \tag{5.178}$$

$$\left[\mathcal{L}_{\lambda_E^l\lambda_H^l}\right]_{ij}(\boldsymbol{x}_k)=0, \tag{5.179}$$

$$\left[\mathcal{L}_{\lambda_E^l\lambda_E^n}\right]_{ij}(\boldsymbol{x}_k)=0, \tag{5.180}$$

$$\left[\mathcal{L}_{\lambda_E^l\lambda_H^n}\right]_{ij}(\boldsymbol{x}_k)=0, \tag{5.181}$$

$$\left[\mathcal{L}_{\lambda_H^l\hat{\boldsymbol{E}}_z^l}\right]_{ij}(\boldsymbol{x}_k)=\left(-\boldsymbol{D}^l(m_k)\nabla\phi_j,\nabla\phi_i\right), \tag{5.182}$$

$$\left[\mathcal{L}_{\lambda_H^l \hat{\boldsymbol{H}}_z^l}\right]_{ij}(\boldsymbol{x}_k) = \left(C_H^l(m_k)\nabla\phi_j, \nabla\phi_i\right) + \left(\hat{z}\phi_j, \phi_i\right), \tag{5.183}$$

$$\left[\mathcal{L}_{\lambda_H^l \hat{\boldsymbol{E}}_z^n}\right]_{ij}(\boldsymbol{x}_k) = 0, \tag{5.184}$$

$$\left[\mathcal{L}_{\lambda_H^l \hat{\boldsymbol{H}}_z^n}\right]_{ij}(\boldsymbol{x}_k) = 0, \tag{5.185}$$

$$\begin{aligned}\left[\mathcal{L}_{\lambda_H^l \boldsymbol{m}}\right]_{ij}(\boldsymbol{x}_k) = &\left(\partial_m C_H^l\Big|_{m_k} \nabla\hat{H}_{z,k}^l \chi_j, \nabla\phi_i\right) - \left(\partial_m \boldsymbol{D}^l\Big|_{m_k} \nabla\hat{E}_{z,k}^l \chi_j, \nabla\phi_i\right) \\ &+ \left(\partial_m C_H^l\Big|_{m_k} \boldsymbol{R}\hat{\mathbf{J}}_t^{s,l} \chi_j, \nabla\phi_i\right),\end{aligned} \tag{5.186}$$

$$\left[\mathcal{L}_{\lambda_H^l \lambda_E^l}\right]_{ij}(\boldsymbol{x}_k) = 0, \tag{5.187}$$

$$\left[\mathcal{L}_{\lambda_H^l \lambda_H^l}\right]_{ij}(\boldsymbol{x}_k) = 0, \tag{5.188}$$

$$\left[\mathcal{L}_{\lambda_H^l \lambda_E^n}\right]_{ij}(\boldsymbol{x}_k) = 0, \tag{5.189}$$

$$\left[\mathcal{L}_{\lambda_H^l \lambda_H^n}\right]_{ij}(\boldsymbol{x}_k) = 0, \tag{5.190}$$

and of the first derivatives:

$$\begin{aligned}\left[\mathcal{L}_{\hat{\boldsymbol{E}}_z^l}\right]_i(\boldsymbol{x}_k) = &\left(d_k^{syn} - d^{obs}, \frac{\partial d^{syn}}{\partial E_x} \nu^l (-i\kappa_z^l)(\kappa_e^l(m_k))^{-2} \partial_x \phi_i\right) \\ &+ \left(C_E^l(m_k)\nabla\phi_i, \nabla\lambda_{E,k}^l\right) + \left(\hat{y}(m_k)\phi_i, \lambda_{E,k}^l\right) - \left(\boldsymbol{D}^l(m_k)\nabla\phi_i, \nabla\lambda_{H,k}^l\right),\end{aligned} \tag{5.191a}$$

$$\begin{aligned}\left[\mathcal{L}_{\hat{\boldsymbol{H}}_z^l}\right]_i(\boldsymbol{x}_k) = &\left(d_k^{syn} - d^{obs}, \frac{\partial d^{syn}}{\partial E_x} \nu^l \hat{z}(\kappa_e^l(m_k))^{-2} \partial_y \phi_i\right) + \left(C_H^l(m_k)\nabla\phi_i, \nabla\lambda_{H,k}^l\right) \\ &+ \left(\hat{z}\phi_i, \lambda_{H,k}^l\right) + \left(\boldsymbol{D}^l(m_k)\nabla\phi_i, \nabla\lambda_{E,k}^l\right),\end{aligned} \tag{5.191b}$$

$$\begin{aligned}[\mathcal{L}_{\boldsymbol{m}}]_i(\boldsymbol{x}_k) = &\left(d_k^{syn} - d^{obs}, \frac{\partial d^{syn}}{\partial E_x} \sum_{l=1}^{n_{\kappa_z}} \nu^l \partial_m \hat{E}_x^l\Big|_{m_k} \chi_i\right) + \beta\left(\nabla m\Big|_{m_k}, \nabla\chi_i\right) \\ &+ \sum_{l=1}^{n_{\kappa_z}} \left(\left(\partial_m C_E^l\Big|_{m_k} \nabla\hat{E}_{z,k}^l \chi_i, \nabla\lambda_{E,k}^l\right) + \left(\partial_m \boldsymbol{D}^l\Big|_{m_k} \nabla\hat{H}_{z,k}^l \chi_i, \nabla\lambda_{E,k}^l\right)\right. \\ &+ \left(\partial_m \hat{y}\Big|_{m_k} \hat{E}_{z,k}^l \chi_i, \lambda_{E,k}^l\right) + \left(\partial_m \boldsymbol{D}^l\Big|_{m_k} \boldsymbol{R}^T \hat{\mathbf{J}}_t^{s,l} \chi_i, \nabla\lambda_{E,k}^l\right) + \left(\partial_m C_H^l\Big|_{m_k} \nabla\hat{H}_{z,k}^l \chi_i, \nabla\lambda_{H,k}^l\right) \\ &\left. - \left(\partial_m \boldsymbol{D}^l\Big|_{m_k} \nabla\hat{E}_{z,k}^l \chi_i, \nabla\lambda_{H,k}^l\right) - \left(\partial_m C_H^l\Big|_{m_k} \mathbf{R}\hat{\mathbf{J}}_t^{s,l} \chi_i, \nabla\lambda_{H,k}^l\right)\right),\end{aligned} \tag{5.191c}$$

$$\begin{aligned}\left[\mathcal{L}_{\lambda_E^l}\right]_i(\boldsymbol{x}_k) = &\left(C_E^l(m_k)\nabla\hat{E}_{z,k}^l, \nabla\phi_i\right) + \left(\boldsymbol{D}^l(m_k)\nabla\hat{H}_{z,k}^l, \nabla\phi_i\right) + \left(\hat{y}(m_k)\hat{E}_{z,k}^l, \phi_i\right) \\ &+ \left(\boldsymbol{D}^l(m_k)\boldsymbol{R}^T\hat{\mathbf{J}}_t^{s,l}, \nabla\phi_i\right),\end{aligned} \tag{5.191d}$$

$$\begin{aligned}\left[\mathcal{L}_{\lambda_H^l}\right]_i(\boldsymbol{x}_k) = &\left(C_H^l(m_k)\nabla\hat{H}_{z,k}^l, \nabla\phi_i\right) - \left(\boldsymbol{D}^l(m_k)\nabla\hat{E}_{z,k}^l, \nabla\phi_i\right) + \left(\hat{z}\hat{H}_{z,k}^l, \phi_i\right) \\ &- \left(C_H^l(m_k)\mathbf{R}\hat{\mathbf{J}}_t^{s,l}, \nabla\phi_i\right),\end{aligned} \tag{5.191e}$$

with the subscripts i, j iterating over all DOFs and l over all wavenumber parameters.

Note that the system (5.149) in the multi-experiment case, would not couple equations and variables across experiments and the Hessian of this system would be a block matrix

of a larger diagonal matrix including all experiments. The solution of the system (5.149) is the search direction δx_k to update x_k. The system (5.149) is huge and indefinite, i.e. it has negative and positive eigenvalues, thus solving it directly is not possible and it is necessary to use an approximation method, for example GN with CG method.

On the other hand, in the formulation above, we have chosen different function spaces for the state and adjoint variables and for the control variable. To include adaptive mesh refinement techniques in the optimization process, we would additionally choose entirely independent grids for the state variables and the control variables and apply mesh refinement independently to each one of them. For the adaptive mesh refinement, investigation should be done to determine an appropriate error indicator for each mesh case.

References

A. Abubakar, T. M. Habashy, V. L. Druskin, L. Knizhnerman, and D. Alumbaugh. 2.5D forward and inverse modeling for interpreting low-frequency electromagnetic measurements. *Geophysics*, 73(4):F165–F177, 2008.

D. Avdeev and A. Avdeeva. 3D magnetotelluric inversion using a limited-memory quasi-newton optimization. *Geophysics*, 74(3):F45–F57, 2009.

D. B. Avdeev. Three-dimensional electromagnetic modelling and inversion from theory to application. *Surveys in Geophysics*, 26:767–799, 2005.

W. Bangerth. *Adaptive finite element methods for the identification of distributed parameters in partial differential equations*. PhD thesis, University of Heidelberg, 2002.

W. Bangerth. A framework for the adaptive finite element solution of large-scale inverse problems. *SIAM Journal on Scientific Computing*, 30(6):2965–2989, 2008.

W. Bangerth and A. Joshi. Adaptive finite element methods for the solution of inverse problems in optical tomography. *Inverse problems*, 24:034011, 2008.

G. Biros and O. Ghattas. Parallel Lagrange-Newton–Krylov–Schur methods for PDE-constrained optimization. Part I: The Krylov–Schur solver. *SIAM Journal on Scientific Computing*, 27(2):687–713, 2005.

P. T. Boggs and J. W. Tolle. Sequential quadratic programming. *Acta Numerica*, 4:1–51, 1995.

M. Commer and G. A. Newman. New advances in three-dimensional controlled-source electromagnetic inversion. *Geophysical Journal International*, 172:513–535, 2008.

S. C. Constable, R. L. Parker, and C. G. Constable. Occam's inversion: A practical algorithm for generating smooth models from electromagnetic sounding data. *Geophysics*, 52(3): 289–300, 1987.

C. deGroot Hedlin and S. Constable. Occam's inversion to generate smooth, two-dimensional models from magnetotelluric data. *Geophysics*, 55(12):1613–1624, 1990.

G. D. Egbert and A. Kelbert. Computational recipes for electromagnetic inverse problems. *Geophysical Journal International*, 189:251–267, 2012.

C. G. Farquharson and D. W. Oldenburg. Approximate sensitivities for the electromagnetic inverse problem. *Geophysical Journal International*, 126:235–252, 1996.

P. E. Gill and E. Wong. *Mixed Integer Nonlinear Programming*, volume 154 of *The IMA Volumes in Mathematics and its Applications*, chapter Sequential quadratic programming methods, pages 147–224. Springer Verlag, 2012.

P. E. Gill, W. Murray, and M. A. Saunders. SNOPT: An SQP algorithm for large-scale constrained optimization. *SIAM Journal on Optimization*, 12(4):979–1006, 2002.

P. E. Gill, W. Murray, and M. A. Saunders. SNOPT: An SQP algorithm for large-scale constrained optimization. *SIAM Review*, 47(1):99–131, 2005.

P. E. Gill, W. Murray, and M. A. Saunders. *User's Guide for SNOPT Version 7: Software for Large-Scale Nonlinear Programming*. Systems Optimization Laboratory (SOL), Stanford University, 2006.

P. E. Gill, M. A. Saunders, and E. Wong. *Modeling and Optimization: Theory and Applications*, volume 147 of *Springer Proceedings in Mathematics and Statistics*, chapter On the performance of SQP methods for nonlinear programming, pages 95–123. Springer Verlag, 2015.

A. V. Grayver. Parallel three-dimensional magnetotelluric inversion using adaptive finite-element method. Part I: theory and synthetic study. *Geophysical Journal International*, 202:584–603, 2015.

A. V. Grayver, R. Streich, and O. Ritter. Three-dimensional parallel distributed inversion of CSEM data using a direct forward solver. *Geophysical Journal International*, 193:1432–1446, 2013.

A. Günther. *Structure exploiting Galerkin schemes for optimal control of PDEs with constraints on the involved variables*. PhD thesis, University of Hamburg, 2010.

E. Haber. Quasi-Newton methods for large-scale electromagnetic inverse problems. *Inverse Problems*, 21:305–323, 2005.

E. Haber. Model problems in PDE-constrained optimization, 2007.

E. Haber, U. M. Ascher, and D. W. Oldenburg. On optimization techniques for solving nonlinear inverse problems. *Inverse Problems*, 16:1263–1280, 2000.

E. Haber, U. M. Ascher, and D. W. Oldenburg. Inversion of 3D electromagnetic data in frequency and time domain using an inexact all-at-once approach. *Geophysics*, 69(5): 1216–1228, 2004.

R. Herzog. *Lectures notes, Algorithms and preconditioning in PDE-constrained optimization*. [PDF Document]. Retrieved from Course Notes Online Website, 2010. URL `https://www.tu-chemnitz.de/mathematik/part_dgl/talks/Lecture_Notes_Algorithms_and_Preconditioning.pdf`. Last accessed 9th May 2016.

R. Herzog and K. Kunisch. Algorithms for PDE-constrained optimization. *GAMM-Mitteilungen*, 33:163–176, 2010.

M. Hinze, R. Pinnau, M. Ulbrich, and S. Ulbrich. *Optimization with PDE constraints*, volume 23 of *Mathematical Modelling: Theory and Applications*. Springer, 2009.

J. Huber. *Interior-point methods for PDE-constrained optimization*. PhD thesis, University of Basel, 2013.

A. Joshi, W. Bangerth, and E. M. Sevick-Muraca. Adaptive finite element based tomography for fluorescence optical imaging in tissue. *Optics Express*, 12(22):5402–5417, 2004.

K. Key. Marine EM inversion using unstructured grids: a 2D parallel adaptive finite element algorithm. In *2012 SEG Annual Meeting*. Society of Exploration Geophysicists, 2012.

K. Key and J. Ovall. A parallel goal-oriented adaptive finite element method for 2.5-D electromagnetic modelling. *Geophysical Journal International*, 186:137–154, 2011.

R. L. Mackie and T. R. Madden. Three-dimensional magnetotelluric inversion using conjugate gradients. *Geophysical Journal International*, 115:215–229, 1993.

G. A. Newman and D. L. Alumbaugh. Three-dimensional magnetotelluric inversion using non-linear conjugate gradients. *Geophysical Journal International*, 140:410–424, 2000.

J. Nocedal and S. J. Wright. *Numerical Optimization*. Springer-Verlag, 1999.

N. Petra and G. Stadler. Model variational inverse problems governed by partial differential equations. Technical report, ICES REPORT 11-05, 2011.

W. Rodi and R. L. Mackie. Nonlinear conjugate gradients algorithm for 2-D magnetotelluric inversion. *Geophysics*, 66(1):174–187, 2001.

Y. Sasaki. Full 3-D inversion of electromagnetic data on PC. *Journal of Applied Geophysics*, 46:45–54, 2001.

C. Schwarzbach and E. Haber. Finite element based inversion for time-harmonic electromagnetic problems. *Geophysical Journal International*, 193:615–634, 2013.

W. Siripunvaraporn. Three-dimensional magnetotelluric inversion: An introductory guide for developers and users. *Surveys in Geophysics*, 33:5–27, 2012.

W. Siripunvaraporn, G. Egbert, Y. Lenbury, and M. Uyeshima. Three-dimensional magnetotelluric inversion: data-space method. *Physics of the Earth and Planetary Interiors*, 150: 3–14, 2004.

J. T. Smith and J. R. Booker. Rapid inversion of two- and three-dimensional magnetotelluric data. *Journal of Geophysical Research*, 96(B3):3905–3922, 1991.

A. N. Tikhonov and V. Y. Arsenin. Methods for solving ill-posed problems. *New York, Wiley*, 1977.

F. Tröltzsch. *Optimal control of Partial Differential Equations: Theory, methods and applications*, volume 112 of *Graduate Studies in Mathematics*. American Mathematical Society, 2010.

D. Wang, R. M. Kirby, R. S. MacLeod, and C. R. Johnson. Inverse electrocardiographic source localization of ischemia: An optimization framework and finite element solution. *Journal of Computational Physics*, 250:403–424, 2013.

W. Wilhelms, R.-U. Börner, and K. Spitzer. Preparation for a 3D magnetotelluric inversion - specific characteristics of the all-at-once approach. In *5th International Symposium on Three-Dimensional Electromagnetics*, 2013.

CHAPTER 6

Summary and Discussions

6.1 Adaptive FE modeling of anisotropic 2-D CSEM and MT

FE formulation of the CSEM and MT problems

We derived the governing equations of the frequency-domain 2.5-D CSEM problem and applied a Fourier transformation to the strike-directed spatial coordinate, z, of the 3-D Maxwell's equations onto the wavenumber domain κ_z. As a result, we obtained a set of coupled PDEs with variables the transformed electric and magnetic field components and with second-order derivatives in the 2-D conductivity model plane. The 2.5-D approximation allows to simulate correctly the 3-D controlled-sources and EM fields in a 2-D conductivity model, but the problem needs to be solved for a set of κ_z wavenumber parameter values in order to transform the EM fields back to the spatial domain. The derivations of the governing PDEs for the CSEM and MT methods are for a total field approximation, and the MT fields are excited through boundary conditions.

Next, we derived the FE Galerkin formulation for the frequency-domain 2.5-D CSEM problem in the electrically isotropic and anisotropic cases. The FE formulation transforms the infinite dimensional problem to a finite dimensional one by firstly, expressing the problem in its weak form, introducing test functions, and secondly, discretizing the geometry in finite elements and approximating the variables and the test functions as a linear combination of trial functions and subsequently of elementwise defined shape functions. This formulation reduces in one the order of the derivatives. We have chosen as test functions and shape functions Lagrange polynomials. The Lagrange shape functions are defined in the nodes, and then, since the problem variables are the strike-directed transformed components, the continuity conditions on the normal components are fulfilled by construction. The continuity conditions on the tangential EM field components in interior boundaries are imposed as natural boundary conditions in the FE derivation.

The result is a large and sparse linear system of discretized equations with unknowns the wavenumber-domain transformed strike-directed electric and magnetic field components in the nodes of the FE mesh, and with the matrix operator composed of elementwise integrals of products between the shape functions and its derivatives. We also provided

the corresponding form for arbitrary oriented electric and magnetic sources. The formulation for the electrically anisotropic problem has been derived considering four DOFs in the conductivity tensor, which can describe the dipping anisotropic case.

We obtained the MT TE and TM modes equations as a particular case of the 2.5-D CSEM problem equations when the source terms and the wavenumber parameter are null. We derived the FE formulation and the linear system of discretized equations for both the isotropic and anisotropic cases, using again Lagrange shape functions.

A contribution from this thesis is the derivation of a compact form for the FE discretized PDEs, for the frequency-domain CSEM method in a dipping electrically anisotropic media and using a total field approach.

Program implementation using state-of-the-art numerical packages

We implemented the derived FE formulation for the CSEM and MT modeling problems in the COMSOL FE software, in particular we use the COMSOL-MATLAB interface in an object-oriented programming environment. COMSOL offers a number of benefits related with the wide variety of powerful libraries it includes. But even though, implementing a physical problem in COMSOL may seem easy at first, however, it swiftly complicates as soon as there is no suitable pre-defined interface readily available or when complete programs are to be implemented. Another drawback is the impossibility to access the different library source codes. Despite these inconveniences, the robust an efficient libraries included in COMSOL in combination with the object-oriented programming of MATLAB result in a high performance program suitable for testing new approaches quickly once the physical formulation is set up in the COMSOL environment.

The program we developed is prepared to model arbitrary oriented electric and magnetic sources with finite-length. It uses the MUMPS direct solver for the solution of the FE system, which is intrinsically efficient since the factorization of the system matrix can be reused for the computations of the adjoint solution and for multiple transmitter sources which result in multiple right-hand-side vectors.

For MT, the program excites the model through boundary conditions. It calculates analytically 1-D MT fields for the left and the right hand sides of the model independently and assumes these field values as given boundary conditions to the left and right hand side of the model, respectively.

The program also includes the possibility to use different shape function orders and unstructured meshes and an automated adaptive mesh refinement algorithm based on an *a posteriori* error estimator to control the quality of the solution.

The accuracy of the solution scales with the size of the mesh elements, thus it can be improved by refining the mesh. Refining the whole mesh would result in a large system that would increase the memory and computational time unnecessarily. Automated adaptive mesh refinement methods increase the solution accuracy by iteratively refining the grid. At each iteration, an elementwise estimation of the error contribution to the solu-

tion error is calculated and used to select a subset of elements for refinement. Then, *a posteriori* error estimator methods calculate an estimate of the error contribution of each element using the FE solution in a certain iteration or computing an auxiliary solution. In our program it is possible to use two different *a posteriori* error estimator methods. One is a global error estimator and the other one a goal-oriented error estimator. The global error estimator method uses the FE solution to estimate the error contribution of each element to the global error. On the other hand, the goal-oriented error estimator method estimates the elementwise error contribution to a goal function. In the program, the goal-oriented error estimator is an implementation of a dual-weighted residual (DWR) method. Using this method the error contribution is calculated as a product of the residual and the dual solutions.

When modeling CSEM with our program, all the transformed EM field components are calculated first in the wavenumber domain and transformed after onto the spatial domain using fast sine and cosine digital filters and a set of positive wavenumber values. To use these filters, the parity of the EM field components is first determined depending on the source-receivers geometry. When the configuration is not in-line or broad-side, the EM field component is decomposed into its even and odd parts, and the inverse Fourier transform is calculated using the digital filters and a set of positive and negative wavenumber values.

The capabilities of our modeling program are similar to the ones of the free state-of-the-art MARE2DEM program (Key and Ovall, 2011; Key, 2012), being our program superior with the option to employ different shape function orders and to define a more general conductivity tensor. However, MARE2DEM is much faster for a multiexperiment because it is efficiently parallelized.

Influence of the model dimensions and mesh design on the solution accuracy

Model dimensions and mesh design influence the solution accuracy. Bounds to these parameters can be extracted from the operating frequency and from the wavenumber parameter values (for CSEM). Because we use Dirichlet boundary conditions, the model dimensions have to be large enough, so that the EM fields are sufficiently attenuated at the boundaries. In EM induction methods, an indicative value of this attenuation is given by the skin depth. Other studies suggest that locating the external boundaries of the model at a few times the skin depth usually ensures sufficient attenuation. The expression of the skin depth is inversely related to the frequency, thus lower frequencies require larger models. In contrast, the higher frequencies provide a lower bound on the smallest reasonable mesh element size because not more than the minimum skin depth can be resolved.

In CSEM modeling, the wavenumber parameter, κ_z, is related to the mesh element size. Mitsuhata (2000) demonstrated that in order to obtain accurate results, the node spacing has to be smaller than the inverse of the largest κ_z.

We conducted numerical experiments to revisit these relations and to illustrate which

orders of magnitude are typical for MT and CSEM models. These experiments were performed on 1-D models in order to validate our results with analytical and semi-analytical solutions.

In MT, we studied the solution accuracy when varying the model dimensions and mesh element size for a wide range of frequencies, varying from 1×10^{-5} to $1\times10^{1}Hz$. We found that for accuracy at all the frequencies, it is necessary a mesh element size of $250m$ and a model size of $5\times10^{6}m$ side. The mesh element size coincides with two times the skin depth at the highest frequency and the model size is some orders of magnitude smaller than the skin depth in the air layer and larger than the skin depth in the receiver locations layer, at the lowest frequency.

Moreover, we studied the influence of model dimensions and mesh design in a 1-D CSEM model, a marine 1-D reservoir canonical model proposed by Weiss and Constable (2006). First, we computed the solution for three different meshes using quadratic Lagrange shape functions, and verified that the relation given by Mitsuhata (2000) is a good indicator of the necessary mesh element size to obtain accurate solutions for a given set of wavenumber values. When this relation was not fulfilled, and the wavenumber values were larger than the inverse of the node spacing, the plotted transformed in-line electric field component as a function of the wavenumber values was oscillating.

Second, we computed, for the same model, the solution for different values of the shape function order, $1st$, $2nd$ and $3rd$, for the same mesh and compared with the previous results, varying the mesh and for a fixed quadratic polynomial order. When increasing the order of the Lagrange shape functions by one, nodes are added in the midpoints of the previous FE mesh. Therefore, similar results are expected between a finer mesh and a larger polynomial order. We found that the reduction of the mesh element size, has more effect for receivers closer to the source, where the EM fields change faster, and that if the mesh in these positions is fine enough, the polynomial order is not particularly important. In contrast, for larger offsets the polynomial order has more influence in the solution accuracy than the mesh element size. The results verify, in general, that increasing the polynomial order or reducing the element size decreases the error. However, when the mesh element size is sufficiently small and the polynomial is quadratic, the error does not change significantly if we reduce the size of the elements or increase the order of the polynomial. The reason is that for a mesh with sufficiently small elements the error is not anymore related to the FE approximation but to the perturbation error.

Lastly, we compared the solution accuracy between different tests, varying the model dimensions and the air layer thickness. The errors were similar and small for receivers at short offsets and they increased with the distance to the source in all cases. Best accuracy was achieved for models with a $20km$ thick air layer, a value much smaller than the skin depth in the air, because of high attenuation in the sea layer.

Adaptive mesh refinement: validation and robustness

In a general 2-D case, a semi-analytical solution of a model does not exist, thus, we can not measure the error of the numerical solution in the same way as for a 1-D model. Automated adaptive mesh refinement techniques provide a measure of FE approximation errors and use it to iteratively refine, globally or locally, the FE grid to enhance the solution accuracy. In the results discussed here we used the DWR method to estimate the error of a goal function: the gradient of the transformed strike-directed electric and magnetic fields in the receivers locations.

Different frequencies and wavenumber parameter values require different mesh designs. Computing the optimal mesh for each configuration of parameters would be computationally very expensive. In our program, we split the different parameters in groups of nearby values and calculate the suitable mesh applying the adaptive mesh refinement algorithm for representative values of the parameters of each group. This strategy is adopted from Key and Ovall (2011). Then, the resulting optimal mesh is used for the computation of the solution using the rest of parameters values of the groups. We refer to each of these groups as 'mesh group', because the parameter values of each group shear the same refined mesh.

We conducted several tests on the 1-D canonical model for CSEM, using the adaptive mesh refinement algorithm to validate its performance, comparing the resulting numerical solution with a semi-analytical solution. We distributed the set of wavenumber values in 5 mesh groups. The adaptive mesh refinement was applied for the midvalue of each group.

In a first stage, the program calculates for the midvalue parameter of each group, the primal solution, the residual and the dual solution for the goal function and calculates the elementwise error indicator as a product of the residual and the dual solution. In each iteration of the adaptive mesh refinement algorithm a fraction of elements with the worst error indicator is selected for refinement. In a second stage, the mesh obtained from the first stage for each group is used for the calculation of the solution for the rest of parameter values in the group.

We observed that initially, at small wavenumber values, the dual solution is larger at the receiver locations and the residual is larger around the source, extending some kilometers laterally and in depth. This behavior is expected because on one hand, the functional we are using to calculate the dual solution is defined in the receiver locations, and on the other hand, the accuracy of the primal solution, related with the residual, is lower around the source position, where a coarse mesh can not accommodate the strong variations of the EM fields. The error indicator resulting from an elementwise product of these two solutions was consequently larger at the receivers locations and around the source position.

At the first iterations of the adaptive mesh refinement algorithm, both the region around the source and the receivers positions are refined. After some mesh refinement steps, the error in the region around the source is sufficiently low and the refinement concentrates in the receivers positions. At larger wavenumber values the largest errors are more con-

centrated at the source position. As the mesh refinement algorithm proceeds, the error, at these wavenumber values, decreases faster at the receiver positions and needs more iterations to decrease at the source position. The reason of these observations is that the transformed fields for which we are computing the error are faster attenuated at large wavenumbers than at small ones, thus the error is more concentrated on the source position where the fields are larger.

To study the evolution of the solution accuracy during the adaptive mesh refinement process, we investigated the error of the amplitudes and of the phases of the in-line electric field component between our solution and the semi-analytical solution for different mesh refinement steps. We observed that the error decay for the amplitudes occurs mostly at the early iterations, whereas the error decay for the phases is more monotone with the mesh refinement steps.

We analyzed the run time of the program, to compute the discussed solutions, as a function of the number of DOFs. The computer used in the experiments was a desktop computer with an INTEL i7 4 GHz quad-core processor and 16 GB RAM. The time to factorize and solve the primal solution, the residual and the dual solution, used to compute the error indicator is about 2 to 6s for 87093 to 2.9×10^5 DOFs, including the DOFs of the dependent variables and of the adjoint variables. The total run time is 80s for an initial mesh of about 5.5×10^4 DOFs and up to 300s for a final mesh after 5 adaptive mesh refinement steps, with an increase of about 2×10^5 number of DOFs from the initial value. This total run time in the last refinement step includes the goal-oriented adaptive mesh refinement process time, for 5 iterations and 5 mesh groups, the time for the computation of the solution for each of the parameter values of each group (3 groups with 9 wavenumbers values and 2 groups with one wavenumber value) and the time for mesh refinements in each iteration for each group. This sums up to approximately 243.5s. The remaining time until 300s includes, among other things, the loading of all the inputs (e.g. the model geometry and the initial mesh), the generation of mesh groups, the data transfer in several parts between COMSOL structure and MATLAB, and the calculation of the Fourier inverse transform. The time efficiency of the program could be improved by parallelizing the computations of the mesh groups since they are independent.

Adaptive mesh refinement: shape function order and error estimator

We studied the influence of the shape function order on the performance of the adaptive mesh refinement method using again the 1-D canonical model for CSEM. We varied the order of the shape functions from quadratic to linear and cubic ($p = 1$ and 3).

First, we estimated the normalized error as a function of the number of DOFs (or adaptive mesh refinement iterations) for different mesh groups corresponding to different wavenumber values and we fixed the shape function order to $p = 2$. The normalization of the error was for each group to the value of the error in the initial mesh. We observed that in the first two iterations the decrease of the error is very small, and that it is after

the third step, when the model is about two times the initial number of DOFs, that the decrease is important. We also observed a different behavior after the third refinement step, between the mesh groups of smaller wavenumbers and the mesh groups of larger ones. At the smallest wavenumbers, the error decay after the third refinement step is small. Contrarily, at the largest wavenumbers the decrease of the error, after the third refinement step, is very steep and reaches values some orders of magnitude smaller than the ones reached at the same refinement level by smaller wavenumbers. We interpret these observations as an indication that after the third refinement step, the size of the elements at the receiver locations is sufficiently small for large wavenumbers to fulfill the relation of the maximum wavenumber value being smaller than the inverse of the node separation. Moreover, the EM fields for these wavenumbers are very small and it takes longer for them to converge, which explains the large error variation between iterations.

Second, we examined the normalized error estimate as a function of the number of DOFs for different order of the polynomial shape functions $p = 1, 2$ and 3, and for a fixed mesh group with a small wavenumber value. The error estimate was normalized for each p by its value in the initial mesh. The main differences were observed between the decay of the error curves for $p = 1$ and for $p = 2, 3$. The initial mesh for $p = 1$ has smaller number of DOFs than for $p = 2$ and 3, and for the first 10 mesh refinement steps, the decay of the error with the number of DOFs is very small, since the increment of DOFs in each step is also small. Models using $p = 2$ and $p = 3$ start with many more number of DOFs, and their error decay after a few iterations is much more abrupt than the one for $p = 1$. Comparing the error decay between $p = 2$ and $p = 3$, for $p = 3$ the decay is more abrupt, but it starts with a larger number of DOFs and in each iteration the increment of DOFs is larger than for $p = 2$. Comparing the error curves for a particular number of DOFs, after a certain number of mesh refinement steps, different for each p case, we observed that the error for $p = 2$ is smaller than for $p = 1$ and for $p = 3$, and that the differences are larger when compared to $p = 1$.

Third, we analyzed the error between the numerical and semi-analytical solution as a function of the number of DOFs for different shape function orders at different receivers positions. The results for a receiver at a short offset, $x = 1km$, and for $p = 1, 2$ and 3 with the goal-oriented error estimator, were similar to the described ones for the error indicator. The error corresponding to data calculated with the adaptive mesh refinement using a global error estimator and $p = 2$ showed a similar behavior to the error corresponding to data calculated with the goal-oriented error estimator and $p = 2$, but the slope of the curve was smoother for the first one. Therefore, for the same number of DOFs, the error for the global error estimator method was larger than for the goal-oriented method. Comparing these results with the error for the mesh refined entirely in each step and with $p = 2$, its evolution with the number of DOFs was also similar to the other cases with $p = 2$, but in each refinement step the increment of the number of DOFs was very large, and the slope of the error curve was smaller than the one for the adaptive mesh refinement cases.

Our interpretation of these results is that the goal-oriented method with $p = 1$ starts

with a very low number of DOFs and needs many mesh refinement steps to increase them before it is be able to accommodate the strong variations of the EM fields closed to the source. The goal-oriented method with $p = 2$ starts with more DOFs than $p = 1$, and actually in the first iterations the error is larger than the one of $p = 1$ for the same number of DOFs. However, since for $p = 2$ each element has more DOFs, the goal-oriented method refines the appropriate elements and in a few iterations the error decays to a lower value than for $p = 1$, even though with the same total number of DOFs. Then, the solution converges and although performing more mesh refinement steps, the error does not decrease. A similar interpretation is valid for $p = 3$, but in comparison to $p = 2$, it needs more DOFs to converge, since it has more DOFs per element. Comparing the adaptive mesh refinement process between using the global or the goal-oriented error estimators, the differences in the amplitude error are not very notable at this receiver location, but the slightly better performance of the goal-oriented method could indicate that there are some elements that are not located where the residual is higher, that are affecting the solution accuracy in the receiver location, and the goal-oriented method is refining them whereas the global error estimator not. On the other hand, the uniform mesh refinement increases faster the number of DOFs, because in each refinement step it refines all the elements (in the domain), instead of only the elements with a large estimated error. At the same time, it only refines elements in this domain and does not take into account elements from other domains that could be affecting the error at the receivers locations.

The performance of the error is similar for data at larger offsets. At $5km$ offset, the initial error for $p = 2$ and $p = 3$ is smaller, and the error for $p = 1$ decays faster than at shorter offsets. The error for $p = 2$ also converges faster than at shorter offsets, and the slope of $p = 3$ is smoother. We interpret the lower initial error for $p = 2, 3$, and the fast decay at this location, for $p = 1, 2$, because the EM fields do not vary as strongly as at a short offset, and the same error values can be reached with less number of DOFs. For the same reason the curve for $p = 3$ is smoother, since the error at the beginning is already small, and a mesh refinement step increases largely the number of DOFs, to values where the error is not anymore dominated by the approximation error but by the perturbation error.

At a $9km$ offset, the initial error for $p = 1$ and 2 is similar to the one at $5km$, and the error for $p = 3$ is smaller. The curves are smoother, and require more number of DOFs to decrease the error. Our interpretation of the changes in the curves at $x = 9km$ regarding the curves at $x = 1,5km$ are that the goal-oriented method although is refining elements in this location, refines more elements at $x = 5km$ which is closer to the source, for this reason some more refinement steps are necessary at this location for $p = 1$ and $p = 2$ than at $x = 5km$ to reach the same error values. It is possible that another goal function in the adaptive mesh refinement method, which better weights the receivers locations, could improve these results. The different behavior of the adaptive method using the global error estimator has also a similar cause but much more accentuated than the goal-oriented method, since the larger residual is at the source location and this method is not weighted.

From these tests we find an outperformance of the goal-oriented adaptive mesh refinement method with $p = 2$ compared to the same method with $p = 1$ and $p = 3$, and compared to both, the uniform refinement and the adaptive mesh refinement with a global error estimator.

Modeling complex geometries: 2-D CSEM model with topography

We checked the flexibility of the modeling program to accommodate the topography in a CSEM model and we examined the changes in its efficiency when varying the polynomial order to $p = 1, 2, 3$ in a flat and in the topography models.

We considered as a first model, the 2-D canonical model with a flat seafloor and as a second model, a variant of the 2-D canonical model where the only difference is an undulating seafloor topography with amplitude $Y = 100m$ and wavelength $\lambda = 4000m$. We computed the EM field responses for the flat and the bathymerty 2-D canonical models and for different order of the polynomial shape functions, $p = 1, 2$ and 3. For both, the flat and the bathymetry models, the final number of elements and number of DOFs is larger for lower p, and the initial number of DOFs is larger for larger p, by construction. The differences of the initial and final number of elements and number of DOFs between the flat and the bathymetry models, for each p, are small, and in general slightly larger for the bathymetry model, since some extra elements are required to accommodate the smooth topography. Thus, the adaptive FE method using triangular unstructured grids accommodates efficiently the topography, decreasing the element size towards the sea-Earth interface and retaining well-shaped elements, while maintaining the size of the elements in the rest of the mesh, resulting in a total number of elements very similar to the flat model. On the other hand, varying the shape functions order in the bathymetry model does not show an improvement compared to varying the shape functions order in the flat model.

Using the same models we studied the distortion of CSEM data caused by the undulating seafloor topography, restricting the analysis to the in-line electric field component (E_x). In this analysis we fixed the shape function order to quadratic. Additionally to the original 2-D canonical model with flat seafloor and $1km$ sea layer, and the variant with bathymetry of wavelength $\lambda = 4km$, we considered three more models, also variants of the 2-D canonical model: 1) the 2-D canonical model with a flat seafloor and a thicker sea layer of $1.2km$, 2) the 2-D canonical model with bathymetry, but changing the wavelength of the harmonic interface to $\lambda = 1km$ 3) the flat 2-D canonical model without the reservoir.

We examined the in-line electric field component as a function of the receiver locations for these 5 models calculating the error between the responses from: a) the bathymetry model with $\lambda = 4km$ and the flat model with $1km$ sea layer, b) the bathymetry model with $\lambda = 4km$ and the flat model with $1.2km$ sea layer, c) the bathymetry model with $\lambda = 1km$ and the flat model with $1km$ sea layer, d) the flat model with $1km$ sea layer and the homogeneous model.

Comparing d) with a), b) and c), we found that the anomaly caused by the reservoir

is larger than the distortion caused by the bathymetry, in both amplitudes and phases. However, the distortion caused by the bathymetry is also significant.

In a) we could see the effect of the $\lambda = 4km$ bathymetry, with the receiver positions in the reference flat model coinciding with receiver positions over the ridges in the bathymetry model. We observed a correspondence between the location of the maximums and minimums of the error in the amplitude with the ridge and valley topography. We interpreted the distortion of the amplitudes caused by a combination of inductive and galvanic effects for receivers close to the source and over the reservoir, and by the geometry for receivers at a longer distance. The phase distortion seemed mainly affected by a geometry effect.

To verify this interpretation, in b) we calculated the error between the responses of the same bathymetry model and the responses of a flat reference model with receiver positions coinciding with receiver positions on the valleys of the bathymetry model. In this case, we observed a larger error (bathymetry distortion) than in the previous case for all receivers. Similarly to the first test, we interpreted the origin of the variations of the error, as an inductive-galvanic effect for positions close to the source and as a geometric effect for positions at large offsets. However, in this case, this association at large offsets was not so clear as in the previous case, because the magnitude of the error at all the receiver positions is much larger and masks slightly the variations. The phases in this second test showed, as in the first test, a geometric effect at large offsets.

Finally, in c) we analyzed the bathymetry distortion on a $\lambda = 1km$ undulating bathymetry model, comparing the responses to the ones of a flat reference model, with all the receivers in the bathymetry model located on the ridges and in the same positions as in the flat reference model. The distortion associated to this model is larger for the amplitudes and similar for the phases to the distortion observed in the model with a $\lambda = 4km$ undulating bathymetry. We observed that the distortion close to the source and above the reservoir is larger than at receivers at larger offsets. We explained the large error at all positions as caused by an inductive-galvanic effect, larger than in the $\lambda = 4km$ undulating bathymetry model, because of a more rough bathymetry in this last test. Further, we explained the larger error close to the source and above the reservoir because of an interaction between the bathymetry distortion and the reservoir distortion.

Modeling complex geometries: 2-D MT graben-like model

To validate our program on a 2-D MT model with a complex geometry, we considered the graben-like model introduced in the COMMEMI project (Zhdanov et al., 1997) and referred to as the COMMEMI model 2D-4. To compute the FE solution, we applied the goal-oriented adaptive mesh refinement algorithm and we observed large values of the error indicator in the air layer. Examining the residual and the dual solutions, we found that both have large errors in the air layer. We explained these observations with the large EM fields in this region. In MT we excite the model by giving boundary conditions on the EM fields in the top of the model. In the air the EM fields have a similar value as in the

top boundary, and the diffusion is only significant when penetrating the Earth. Thus, the large values in the air yield a large residual. On the other hand, the largest values of the dual solution in the air could be explained partly for the same reason but also because of the strong variation of the conductivity values in the air-Earth interface, which affect the accuracy of the solution in the receiver locations.

As a consequence of the large errors in the air, the mesh refinement concentrates in this region, augmenting largely the number of elements before decreasing the error in the receiver locations, therefore the adaptive mesh refinement algorithm is not efficient in this case and other error estimator methods should be investigated for MT.

Comparing our results to the responses computed with MARE2DEM (Key and Ovall, 2011) and to the corresponding solutions from the COMMEMI project (Zhdanov et al., 1997), we concluded that our numerical results are accurate. The program models accurately the abrupt changes in the apparent resistivities and phases which coincide with jumps in the resistivity due to the geological structure, and the apparent resistivities and phases corresponding to the inclined plane forming the graben-structure. The thin layers at the upper part of the subsurface model are well resolved by the highest frequencies. We also observe a better accuracy of the TE mode with respect the TM mode. However, the COMMEMI TM mode error bars are also larger than the TE mode error bars, indicating more variability in the TM mode results between different programs. The explanation is that the TM mode is more sensitive to the air layer, and consequently the solution is less stable.

Oriented and finite-length 3-D sources

In order to benchmark the source modeling component of our program and to demonstrate the importance of considering realistic sources in certain experimental scenarios we analyzed land and marine CSEM models for different orientation and geometry of the sources.

First, we considered a land CSEM model grossly simulating the geology at the carbon sequestration site in Ketzin, Germany, proposed by Streich et al. (2011) and Streich and Becken (2011). We studied two variants of this model, a 1-D approach that we could compare to a semi-analytical solution and a 2-D approach simulating a more realistic geology. Additionally, we considered four different source cases: 1) an in-line (90° azimuth) horizontal electric point dipole, 2) a 120° azimuth oriented horizontal electric point dipole, 3) an in-line straight $1km$ length grounded wire, and 4) a 120° azimuth oriented grounded wire, $1km$ length.

We found that, the solution of the 1-D Ketzin model for all source cases and at a frequency of $0.1Hz$ is accurate compared to the semi-analytical solution calculated using DIPOLE1D (Key, 2009), which allows oriented sources with finite length on 1-D models.

We examined the different source approximation effects in the in-line electric field component, by calculating the error between the responses of the in-line HEPD in the Ketzin model and the responses of: a) a model without the reservoir layer and with the

same source, b) the same model with a 120° azimuth oriented HEPD, c) the same model with an in-line $1km$ length HED and d) the same model with a 120° azimuth oriented, $1km$ length HED. The error calculated with a) highlights the effect of the reservoir, with b), the effect of the orientation is isolated, with c), we observe the longitude effect and with d), we show both the longitude and orientation effects.

We observe that the error due to the reservoir is larger at the receivers approximately above the boundaries of the reservoir. The difference between modeling the orientation of the point dipole (120° azimuth) or approximating it as an in-line directed point dipole gives a relative error in the amplitude of the same order of magnitude as the error caused by the storage layer. The largest errors are caused by the differences between modeling the longitude of the grounded wire or approximating it as a point dipole. Finally, the differences between modeling the source with its longitude and orientation or modeling it as an in-line point dipole, results in errors similar to the effect of the longitude. We find that the phases are also distorted by the reservoir and the source approximation but in a lower order, thus showing less sensitivity to these effects. According to these results, in this model it is necessary to simulate both the orientation and geometry of the source since the errors caused in the amplitudes and phases by a simpler approach are similar or even larger than the caused by the target layer.

We extended the study of the source approximations to the Ketzin 2-D model, considering again the same source variants and 3 different frequencies of: $0.01, 0.1$ and $1Hz$ and computed the error of the in-line electric field component between modeling the orientation and geometry of the CSEM source or modeling an in-line point dipole approximation for different frequencies. We found that the error in the amplitude caused by the different sources is similar for all frequencies and similar to the 1-D case. The distortion of the field due to the source approximation is larger at short offsets and larger than the reservoir anomaly. Because the small targets of the Ketzin 2-D model require short offsets for detection, it is necessary to consider a realistic approximation of the source.

Second, we analyzed a marine CSEM experiment with a $100m$ floating wire, typical for marine CSEM commercial hydrocarbon exploration, oriented with an azimuth and dip angles, which is a practical problem in marine surveys, where the water currents distort the source shape and orientation. In these tests, we considered the canonical 1-D model and four different source approximation cases: 1) an in-line HEPD, 2) an in-line $100m$ HED, 3) a 120° azimuth oriented HEPD, and 4) a 120° azimuth oriented HEPD with orientation also in the vertical direction, with 20° dip angle. The operating frequency was $0.25Hz$. Again, we validated the results by comparing our responses to the semi-analytical solutions and examined the results by comparing the effects of the source geometry and orientation. We observed that the reservoir layer for this model is appreciable at almost all the receivers positions and that the error between considering the length of the source or approximating it as a point dipole is very small, indicating that for this model a point dipole is a good approximation. In contrast, we observed that the error approximation of not modeling the orientation, both the azimuth or dip, is large. From these results we conclude that a point

dipole approximation is accurate in a marine scenario with a source of $100m$ length and with the target reservoir at a large distance to the source, compared to the region influenced by the dipole geometry. However, we confirm that in the same scenarios, slightly different orientation of the source results in significant differences of the electric field response, that extend several kilometers from the source location and that can be of the same order of magnitude as the electric field anomaly indicating the presence of the target reservoir.

CSEM modeling of vertical and dipping anisotropy

We validated our FE implementation of the anisotropic CSEM problem, simulating and analyzing the responses of models with vertical anisotropy (TIV) and dipping anisotropy (TTI). The models used in the experiments were a 1-D model with a sea layer and a TIV resistivity half-space and two 2-D models, one with a sea layer and a reservoir embedded in TIV resistivity sediments, and another one also with the sea layer and the TIV resistivity sedimented subsurface, but with the reservoir embedded in an additional anticline structure simulated as two bulk-tilted anisotropic (TTI) structures. The TIV half-space model has a vertical resistivity of $\rho_v = 2\Omega \cdot m$ and a horizontal resistivity of $\rho_h = 1\Omega \cdot m$. The transmitter was, for all the experiments, an horizontal electric point dipole located $50m$ above the seafloor, and we considered it at different locations, and for the in-line and broad-side configurations. The operating frequencies were $0.05, 0.25$ and $1Hz$.

First, we compared the EM fields responses of the TIV resistivity half-space model with the EM fields responses of two isotropic half-space models with resistivities coinciding with ρ_v and ρ_h. The CSEM responses of a layered model with TIV resistivity is well understood, thus, it is appropriate to benchmark our algorithm. For in-line configuration fields, the responses of the anisotropic model were almost identical to the responses of the $2\Omega \cdot m$ isotropic model at all frequencies and for all offsets. Contrarily, for broad-side configuration, the fields from the anisotropic model were almost identical to the ones from the $1\Omega \cdot m$ isotropic model. The explanation of this behavior is that the in-line configuration electric fields are in the model plane and propagate in the seafloor with a significant vertical component, thus in the vertical anisotropic model they are more sensitive to the vertical resistivity component of $2\Omega \cdot m$, and the responses approach to the ones of an isotropic model with this resistivity. On the other hand, in the broad-side configuration the electric fields are purely azimuthal and largely horizontal, thus in the vertical anisotropic model they are more sensitive to the horizontal component of the resistivity of $1\Omega \cdot m$, and the responses approach the ones of an isotropic model with this resistivity. The obtained modeled results of the EM fields for a TIV 1-D model are consistent with the expected response behavior and validated our implementation.

Second, we simulated the responses of a 2-D model with an isotropic reservoir embedded in vertical anisotropic sediments with the same $\rho_v = 2\Omega \cdot m$ and $\rho_h = 1\Omega \cdot m$. In the in-line configuration, we observed the effect of the reservoir in the amplitude as a maximum in the reservoir boundaries locations. On the other hand, the effect of the TIV

sediments consisted of a large increase of the amplitude, much larger than the one caused by the reservoir at all frequencies. Therefore, we concluded that fitting an isotropic model to in-line data that contains vertical anisotropy could mask the reservoir or indicate a different location, dimensions and resistivity value. On the other hand, for the broad-side configuration, we observed reservoir effects similar to the ones observed in the in-line configuration, an increase of the amplitude, but with a smaller magnitude.

From these results, we concluded that the vertical anisotropy effect can be observed in both in-line and broad-side configurations, but the effect is larger for the in-line disposition. This can be explained because the isotropic sediments of the 2-D model we used for the normalization are $1\Omega \cdot m$, the same resistivity value as the horizontal component, ρ_h, in the anisotropic case, and as we discussed in the previous experiments with a half-space TIV model, the broad-side configuration is more sensitive to the horizontal component of the resistivity and the in-line configuration to the vertical component of the resistivity.

Comparing our results, for the TIV 2-D model, to the responses computed for the same model using MARE2DEM, we find a good agreement between both solutions.

Third, we examined a 2-D model where the resistive reservoir is embedded in an anticline structure surrounded by vertical anisotropic sediments. The anticline structure is simulated with two blocks, located at $1.6km$ depth, $600m$ below the seafloor, with anisotropic resistivities of TTI type. The TTI resistivities of these blocks are $\rho_h = 1\Omega \cdot m$ and $\rho_v = 2\Omega \cdot m$, and we consider two different cases, one with a dip angle of $\alpha_d = 20°$, in the right block, and $\alpha_d = -20°$, in the left block, and another one with a dip angle of $\alpha_d = 40°$, in the right block, and $\alpha_d = -40°$, in the left block. The sediments surrounding these blocks are assumed with TIV resistivity, with the same $\rho_h = 1\Omega \cdot m$ and $\rho_v = 2\Omega \cdot m$.

In the in-line configuration, we observed the anticline anomaly as a decay of the amplitude to values smaller than one. This decay was larger for higher frequencies and for the model with dip angles $\pm 40°$. For the same source-receivers configuration, we also examined the isolated effect of the anticline and the reservoir together. The normalized amplitude curves were very similar to the ones of the anticline anomaly, and the main differences were that the maximum and minimum values were slightly smaller in this last case.

For the broad-side configuration, the effect of the anticline was very similar to the observed in the in-line configuration, with a drop of the amplitude, larger for larger dip angle and for higher frequencies, but with slightly smaller magnitude than in the in-line configuration. On the other hand, the isolated effect of the anticline and the reservoir together, was also similar to the observed in the in-line configuration.

Our interpretation of these results is that the anticline structure anomaly dominates the responses, when isolated from the vertical anisotropy distortion, but its effect is weighted by the effect of the reservoir, thus reducing its magnitude compared to the effect of the anticline alone.

The observed TIV seafloor anomalies of a large increment of the amplitude which mask the reservoir anomaly are in agreement with the results by Li and Dai (2011) and Davydy-

cheva and Frenkel (2013). The distortion effect of the anticline consisting in a drop of the amplitude which masks the reservoir is also observed by Davydycheva and Frenkel (2013).

6.2 2.5-D CSEM PDE-constrained optimization

In the last years, there has been a rise in FE modeling programs that simulate the EM fields in 2-D and 3-D models. However, these modeling codes have not been transferred onto inversion codes, and only very recently, investigations in this direction have appeared.

We investigated a FE framework for the inversion of CSEM data and formulated for the first time the 2.5-D CSEM inverse problem as a PDE-constrained optimization in full-space (all-at-once approach) and using FE. Most of the inversion programs for EM are developed in the reduced space, that is eliminating the state variables from the inversion using equality constraints and solving the optimization problem only for the model parameters. There are alternative approaches that do not eliminate the state variables and treats the state and model parameters variables as independent optimization variables which are coupled through the PDEs constraints. These methods are referred to *all-at-once* or full-space.

Our interest on the application of these approaches to the solution of the CSEM inverse problem is justified for several reasons. First, using this approach it is not necessary to repeatedly compute the costly solution of the PDEs for each evaluation of the objective function and of the adjoint equation, to evaluate the sensitivities and the gradients, because it only requires to solve exactly the solution of the state equation at the end of the optimization process. Second, the approach can handle techniques with convergences rates higher than linear and third, the combination of the PDE-constrained optimization in the full-space with a FE discretization can include adaptive FE meshes in the inversion process.

We derived this formulation in two different ways: using a *discretize-optimize* strategy and an *optimize-discretize* strategy. In the *discretize-optimize* strategy the problem is considered in discretized form and the Lagrangian optimization conditions and the Newton's step are derived on it. We followed this scheme for the derivation and we implemented the resulting problem in the COMSOL-MATLAB structure using a general-purpose optimization program, SNOPT, which is an implementation of a SQP method.

We showed two synthetic examples of application of this implementation: a canonical reservoir model and a more realistic marine model with topography. We did not use a regularization function in the examples, but a different mesh for the control variables and for the state variables. In this way, the mesh for the control variables can be coarser than the mesh for the state variables and the problem is better posed, behaving similar to a regularization functional. In both cases the program recovered the main structures of the model within an acceptable data misfit. However, the performance of the program is not efficient, it requires much memory and time. In the *all-at-once* approach the system matrix is sparse but also very large, because the same system matrix includes the discretized equations for all the wavenumbers, frequencies and transmitters, thus, increasing the time and memory

demands of the program. Furthermore, it is difficult to improve the performance of our program since using SNOPT through COMSOL does not grant access to the system matrix structure and thus prohibits problem specific performance optimizations. To extract further conclusions on the inversion scheme performance, we should implement the problem directly from MATLAB, avoiding the use of the general-purpose optimizer.

Finally, we have formulated the 2.5-D CSEM inverse problem as a PDE-constrained optimization in full-space using an *optimize-discretize* strategy and FE, as a first step of an inversion scheme using adaptive FE.

References

S. Davydycheva and M. Frenkel. The impact of 3D tilted resistivity anisotropy on marine CSEM measurements. *The Leading Edge*, 32(11):1374–1381, 2013.

K. Key. 1D inversion of multicomponent, multifrequency marine CSEM data: Methodology and synthetic studies for resolving thin resistive layers. *Geophysics*, 74(2):F9–F20, 2009.

K. Key. Marine EM inversion using unstructured grids: a 2D parallel adaptive finite element algorithm. In *2012 SEG Annual Meeting*. Society of Exploration Geophysicists, 2012.

K. Key and J. Ovall. A parallel goal-oriented adaptive finite element method for 2.5-D electromagnetic modelling. *Geophysical Journal International*, 186:137–154, 2011.

Y. Li and S. Dai. Finite element modelling of marine controlled-source electromagnetic responses in two-dimensional dipping anisotropic conductivity structures. *Geophysical Journal International*, 185(2):622–636, 2011.

Y. Mitsuhata. 2-D electromagnetic modeling by finite-element method with a dipole source and topography. *Geophysics*, 65(2):465–475, 2000.

R. Streich and M. Becken. Electromagnetic fields generated by finite-length wire sources: comparison with point dipole solutions. *Geophysical Prospecting*, 59:361–374, 2011.

R. Streich, M. Becken, and O. Ritter. 2.5D controlled-source EM modeling with general 3D source geometries. *Geophysics*, 76(6):F387–F393, 2011.

C. J. Weiss and S. Constable. Mapping thin resistors and hydrocarbons with marine EM methods, Part II – Modeling and analysis in 3D. *Geophysics*, 71(6):G321–G332, 2006.

M. S. Zhdanov, I. M. Varenstov, J. T. Weaver, N. G. Golubev, and V. A. Krylov. Methods for modelling electromagnetic fields. Results from COMMEMI - the international project on the comparison of modelling methods for electromagnetic induction. *Journal of Applied Geophysics*, 37:133–271, 1997.

CHAPTER 7

Conclusions and Outlook

7.1 Conclusions

We developed a robust and versatile adaptive unstructured mesh FE program for 2-D modeling of CSEM and MT data. The CSEM modeling problem is formulated with a 2.5-D approximation that considers a 2-D conductivity model and realistic 3-D EM sources. The FE formulation uses nodal shape functions for both methods and allows to simulate the EM fields on isotropic and anisotropic conductivity models. Though, the anisotropic case is not general, it includes vertical and dipping anisotropy. The FE formulations are derived for the total field and for arbitrary oriented 3-D sources when modeling CSEM. The derived formulation of the FE 2.5-D CSEM anisotropic problem for the total field and for general sources is a contribution of this thesis.

The program is implemented through COMSOL and MATLAB software using modern libraries and a high-quality mesh generator. It is prepared to model arbitrary oriented electric and magnetic sources with finite-length. The program solves the FE system using a fast and robust direct solver which allows to reuse the factorization of the FE system matrix to compute, for example, the adjoint solution. The accuracy of the solution is controlled and improved by an adaptive mesh refinement algorithm. In this algorithm there is the possibility to use two different *a posteriori* error estimator functions: a global error estimator and a goal-oriented error estimator. The global error estimator, estimates the error contribution of each element to the solution error using the residual of the FE approximation. On the other hand, the goal-oriented error estimator, estimates the error contribution of each element to a goal function using a DWR method which necessitate the residual of the FE primal solution and the dual solution. The Fourier inverse transform required by the 2.5-D CSEM approximation is calculated using fast sine and cosine digital filters methods.

The influence of the model dimensions and mesh design on the solution accuracy is validated by revisiting the known relations with the frequency and the wavenumber parameters, and demonstrates the importance of a proper mesh design to obtain accurate responses.

The program is verified for both, CSEM and MT, methods and for land and marine

environments by comparing the numerical solution with an analytical or semi-analytical one, finding good accuracy in all cases. The 2-D modeling results are benchmarked versus the MARE2DEM program and compared to published results. Time efficiency has been demonstrated, obtaining times for the factorization and solution of the problem of a few seconds for a number of DOFs of 1×10^5 and quadratic shape functions. The run time grows to hundreds of seconds, for the CSEM modeling which requires the solution for different wavenumber values and when the adaptive mesh refinement process is applied. The time efficiency could be improved by parallelizing the program for different wavenumbers, frequencies and sources.

The program allows to use high-order shape functions in contrast to most of the state-of-the-art algorithms which uses linear shape functions. We used this advantage to study the influence of the shape function order on the solution accuracy, finding an outperformance of the quadratic shape functions compared to linear and cubic ones.

The performance difference of the two adaptive mesh refinement methods, included in the program for CSEM modeling, are compared and yield similar results for receivers at short offsets and differentiate more for farther offsets, with superiority of the goal-oriented method over the global error estimator method. The reason is because the global error estimator method refines the regions that contribute larger to the solution error in the whole model, using the residual of the FE equations, and these are around the source where the EM fields vary strongly. Therefore, after some refinement steps, the solution is accurate at short offsets, but not at large distances. Contrarily, the goal-oriented method calculates the error contribution of each element to a goal function, in our case a gradient of the dependent variables defined on the receivers locations, using a dual weighted residual method. Thus, the refinement occurs around the source and at the receivers positions, and the solution is more accurate at large offsets than the solution calculated using the global error estimator. Nevertheless, we found that the performance of the goal function could be still improved experimenting with different goal functions, that better weight the data at all receivers.

We used the high capabilities of the program to study synthetically different physical problems that are often encountered in realistic models and experimental situations, but that can not always be modeled properly because of program limitations. In particular, we addressed three main physical situations: a marine CSEM model with seafloor topography, a land and a marine model with oriented and finite length sources and a marine model with a reservoir embedded in a vertical anisotropic structure and in an anticline structure. We conclude that anomalies caused by any of these physical phenomena can be of the order or larger than typical target anomalies, therefore, appropriate modeling should be considered.

In recent years, FE modeling programs emerged that simulate the EM fields in 2-D and 3-D models. However, these modeling codes are rarely employed in inversion codes, and only very recently, investigation in this direction has begun. We have formulated for the first time the 2.5-D CSEM inverse problem as a PDE-constrained optimization in full-space

(*all-at-once* approach) that uses FE, in contrast to the reduced-space approach underlying most available inversion programs for EM. The *all-at-once* approach can use techniques with convergences rates higher than linear and at the same time avoid the repeated costly calculation of sensitivities and gradients at each iteration. Another advantage of combining a PDE-constrained optimization scheme in the full-space with a FE discretization is that it can be included the possibility of adaptive FE meshes in the inversion process.

We have derived this formulation for the *all-at-once* approach in two different ways: using a *discretize-optimize* strategy and an *optimize-discretize* strategy. In the *discretize-optimize* strategy the inverse problem is considered discretized and the Lagrangian optimization conditions as well as the Newton's step are derived from this form. The resulting inverse problem is implemented in the COMSOL-MATLAB structure using the general-purpose optimization program SNOPT, which is an implementation of a SQP method. Two synthetic examples verify the approach: a canonical reservoir model and a more realistic marine model with topography. Though regularization is not explicitly applied, it is shown that using a different mesh for the control variables and for the state variables has a similar effect as regularization if the mesh for the control variable is coarser than the mesh for the state variable. In both examples the program recovered the main structures of the model with an acceptable data misfit. However, the performance of the program is not efficient, it requires lot of memory and time. This is because in the *all-at-once* approach the system matrix is sparse but also extremely large. The same system matrix includes the discretized equations for all the wavenumbers, frequencies and transmitters.

Finally, we have formulated the 2.5-D CSEM inverse problem as a PDE-constrained optimization in full-space using an *optimize-discretize* strategy and FE, as a first step towards an inversion scheme using adaptive FE.

7.2 Outlook

In the development of this thesis we found many points that deserve further investigation.

First of all, the derived FE formulation for an electrically anisotropic media is limited to a four component tensor. To extend anisotropy in this formulation is quite complex for CSEM because of the 2.5-D approach but can be achieved. To our knowledge, a general anisotropic formulation has only been derived for MT but not yet for 2.5-D CSEM.

Secondly, the function in the goal-oriented adaptive mesh refinement should be further investigated. In this thesis we compared the goal-oriented method to the global one, but we left open to study the performance of different goal functions. However, we realized that goal functions using a DWR method could be interesting to investigate since they better scale all the receivers.

The modeling program presented in this thesis is quite efficient when it is only necessary to solve the problem for one value of the parameters wavenumber, frequency and transmitter. However, for 2.5-D CSEM it is always necessary to calculate the solution for a set of wavenumber values, and typical MT and CSEM experiments are for several fre-

quencies and transmitter positions. Therefore, a parallelization of the program for these parameters is desirable.

Further the inclusion of even more general transmitters is a possibility. Our implementation includes arbitrary oriented sources with finite-length, but the finite length transmitters are restricted to a straight shape. However, in real surveys, the long transmitters used for land CSEM are often not straight, due to environmental or anthropogenic reasons, and it has been demonstrated that a straight line approximation can distort the data.

In the inversion part of this thesis, we only present the first steps towards an adaptive FE inversion program using an *all-at-once* approach. Hence, it provides a set of new ideas for further research.

First, the presented formulation using the *discretize-optimize* strategy, that we tested with the SNOPT general-purpose optimization program, could be directly implemented in the COMSOL-MATLAB structure and solved with a Gauss-Newton approximation, which is similar to SQP, but may be easier to implement. Then, appropriate open-source libraries to solve the resulting system could be used to avoid the limitations caused by proprietary software.

Even more interesting would be to implement the *optimize-discretize* formulation in the COMSOL-MATLAB structure using a Gauss-Newton approximation. This could open the possibility to use adaptive FE meshes in the inversion, so that the FE meshes optimize in each iteration independently for the control and the state variables.

Finally, due to the complication of the problem we restricted the formulation to the in-line electric field component, E_x, observable. A more general formulation should be derived that includes other observables, and a formulation for the MT problem.